Estudio y Mitigación del Envejecimiento por Radiación de las Cámaras de Deriva del Detector CMS en el LHC

Study and Mitigation of the Radiation Aging of the Drift Tube Chambers of the Compact Muon Solenoid at the Large Hadron Collider

UNIVERSIDAD
COMPLUTENSE
MADRID

Facultad de Ciencias Físicas

TESIS DOCTORAL

Memoria que presenta para optar al título de Doctor en Física

David Daniel Redondo Ferrero

Dirigida por los Doctores

Cristina Fernández Bedoya e Ignacio Redondo Fernández

Estudio y Mitigación del Envejecimiento por Radiación de las Cámaras de Deriva del Detector CMS en el LHC

Study and Mitigation of the Radiation Aging of the Drift Tube Chambers of the Compact Muon Solenoid at the Large Hadron Collider

UNIVERSIDAD
COMPLUTENSE
MADRID

Facultad de Ciencias Físicas

TESIS DOCTORAL

Memoria que presenta para optar al título de Doctor en Física

David Daniel Redondo Ferrero

Dirigida por los Doctores

Cristina Fernández Bedoya e Ignacio Redondo Fernández

Abstract

Over the last decades, the LHC (Large Hadron Collider) at CERN and its experiments have contributed significantly to some of the most groundbreaking results in particle physics, being the only worldwide facility available nowadays to study the Higgs and, with great precision, the energy frontier. To extend the sensitivity for new physics searches, a major upgrade of the LHC was approved, the High Luminosity LHC (HL-LHC), in which a tenfold increase of luminosity is planned extending another 10 years the operation of the machine up to a total of more than 30 years of running.

This thesis is part of the necessary activities to ensure the optimal performance of the CMS (Compact Muon Solenoid) experiment in preparation for the HL-LHC phase. In particular, it focuses on ensuring the identification and detection of muons in the central region of CMS, which is covered by the gaseous detectors Drift Tube (DT) chambers.

The DT detector is critical for the operation of the CMS experiment due to its role in the precise identification and tracking of muons, which are key particles in high-energy physics experiments. Muons, being much heavier than electrons and less likely to interact with matter, can travel through dense detector components, making them ideal for probing the interactions that occur during particle collisions. In CMS, muons serve as important signatures for many physics processes, including those related to the Higgs boson, searches for new particles, and tests of the Standard Model.

Ensuring a reliable operation of the DT detector is mandatory for running during HL-LHC and this implies that all of the systems need to operate satisfactorily, while minimizing the cost. The two key components of the DT detector are the gaseous detector and its electronics, particularly the one sitting inside the experimental cavern. Both need to survive in aggressive experimental conditions (radiation, magnetic field, low dissipation, high reliability) and with few or none yearly maintenance since they are embedded in the iron yoke of the CMS barrel wheels. The main goal of this thesis is to study the reliability of the operation of the DT system for HL-LHC and take the necessary actions to ensure its optimal performance.

Beyond longevity related to the lifetime of the parts, which was studied during construction, the main concern for the future is the tolerance to radiation of the full system, particularly when the intensity is expected to increase factors 5 to 7.5 the nominal instantaneous luminosity for which the detectors were designed. Studying the impact of this radiation in the HL-LHC detectors is a critical step to guarantee its reliable operation and is, therefore, what has been intended in this document through a detailed study of the future performance of the CMS DT detector.

Accordingly, the thesis main goal can been subdivided in several lower level objectives:

- Evaluate the radiation field expected and the fluxes and doses that can be expected in HL-LHC and understand the impact of the radiation both in gaseous detectors and in its electronics. This topic has been covered in Chapter 2.

- Investigate and study the longevity of the DT detector under the expected accumulated charge. This includes the realization of long irradiation campaigns with DT chambers at the GIF++ (Gamma Irradiation Facility ++) at CERN where irradiation of large detectors and muon test beams can be performed. This activity, the analysis performed and its corresponding results are detailed in Chapter 3.

- Study the loss of performance observed and modeling the behaviour of the detector. The hypothesis and model to describe the aging process is compared with the detector data obtained at GIF++ in Chapter 4.

- Plan and study mitigating actions to alleviate the potential performance loss. A highlight is the addition of a shielding layer on the top most exposed DT chambers at CMS. Work performed included the construction and installation of this shielding but also the simulation of the radiation field reduction thanks to this shielding has been performed using the software GAMOS. Description is contained in Chapter 5.

- Investigate the radiation tolerance of the electronic prototypes designed for operation at HL-LHC. This included performing radiation tests at the CHARM facility at CERN and analyzing the resulting expected behaviour of the system. The description of the tests and the results and extrapolations to HL-LHC are included in Chapter 6.

In summary, the impact of the increase of radiation expected by the operation at HL-LHC is addressed in this document for what concerns the

CMS DT detector. An effort has been made to provide the broadest possible perspective on all the variables and effects that could affect the detector's performance, while ensuring that actions were taken to guarantee its optimal operation. An effort has also been made to propose a model consistent with the multitude of results obtained from the various radiation tests, allowing for a reasonable estimation of the expected performance under HL-LHC conditions.

The work performed in this thesis has been critical to provide insight into the expected performance of the CMS DT, and take informed decisions on the weak points to attack. Besides enlarging the know-how on gaseous detectors and the particular performance of the DT chambers under radiation damage, we have obtained one good piece of news, that is, by replacing the detector's electronics, the operation of the detector is expected to be satisfactory throughout HL-LHC.

Resumen

Durante la últimas décadas, el LHC (Gran Colisionador de Hadrones) del CERN y sus experimentos han contribuido significativamente a algunos de los resultados más innovadores en física de partículas, siendo hoy en día la única instalación mundial disponible para estudiar el bosón de Higgs y, con gran precisión, la frontera de la energía. Con el fin de ampliar la sensibilidad para las búsquedas de nueva física, se aprobó una importante mejora del LHC, el LHC de Alta Luminosidad (HL-LHC), en el que se prevé multiplicar por diez la luminosidad, extendiendo otros 10 años el funcionamiento de la máquina hasta un total de más de 30 años de funcionamiento.

Esta tesis forma parte de las actividades necesarias para asegurar el funcionamiento óptimo del experimento CMS (Compact Muon Solenoid) en preparación para la fase HL-LHC. En particular, se centra en asegurar la identificación y detección de muones en la región central de CMS, que está cubierta por las cámaras del detector gaseoso Drift Tube (DT).

El detector DT es crítico para el funcionamiento del experimento CMS debido a su papel en la identificación y seguimiento precisos de los muones, que son partículas clave en los experimentos de física de altas energías. Los muones, al ser mucho más pesados que los electrones y menos susceptibles de interaccionar con la materia, pueden viajar a través de los densos componentes del detector, lo que los hace ideales para sondear las interacciones que se producen durante las colisiones de partículas. En CMS, los muones sirven como firmas importantes para muchos procesos físicos, incluidos los relacionados con el bosón de Higgs, las búsquedas de nuevas partículas y las pruebas del Modelo Estándar.

En consecuencia, el objetivo principal de la tesis puede subdividirse en varios objetivos de nivel inferior:

- Evaluar el campo de radiación esperado y los flujos y dosis que pueden esperarse en el HL-LHC y comprender el impacto de la radiación tanto en los detectores gaseosos como en su electrónica. Este tema se ha tratado en el Capítulo 2.

- Investigar y estudiar la longevidad del detector DT bajo la carga acumulada esperada. Esto incluye la realización de largas campañas de irradiación con cámaras de DT en el GIF++ (Gamma Irradiation Facility ++) del CERN, donde se puede llevar a cabo la irradiación de grandes detectores y haces de prueba de muones. Esta actividad, el análisis realizado y sus correspondientes resultados se detallan en el Capítulo 3.

- Estudiar la pérdida de rendimiento observada y modelizar el comportamiento del detector. La hipótesis y el modelo para describir el proceso de envejecimiento se comparan con los datos del detector obtenidos en GIF++ en el Capítulo 4.

- Planificar y estudiar acciones paliativas para reducir la posible pérdida de rendimiento. Destaca la adición de una capa de blindaje en las cámaras DT más expuestas del CMS. El trabajo realizado incluye la construcción e instalación de este blindaje, pero también la simulación de la reducción del campo de radiación gracias a este blindaje se ha realizado utilizando el software GAMOS. La descripción figura en el Capítulo 5.

- Investigar la tolerancia a la radiación de los prototipos electrónicos diseñados para su funcionamiento en el HL-LHC. Esto incluyó la realización de pruebas de radiación en la instalación CHARM en el CERN y el análisis del comportamiento esperado resultante del sistema. La descripción de las pruebas y los resultados y extrapolaciones al HL-LHC se incluyen en el Capítulo 6.

En resumen, el impacto del aumento de radiación esperado por la operación en el HL-LHC se aborda en este documento para lo que concierne al detector CMS DT. Se ha realizado un esfuerzo para proporcionar una perspectiva lo más amplia posible de todas las variables y efectos que podrían afectar al funcionamiento del detector, asegurando al mismo tiempo que se han tomado las acciones necesarias para garantizar su funcionamiento óptimo. También se ha propuesto un modelo consistente con la multitud de resultados obtenidos en las distintas pruebas de radiación, permitiendo una estimación razonable del rendimiento esperado en las condiciones del HL-LHC.

El trabajo realizado en esta tesis ha sido crítico para proporcionar una visión del rendimiento esperado del DT de CMS, y tomar decisiones informadas sobre los puntos débiles a atacar. Además de ampliar el conocimiento sobre detectores gaseosos y el rendimiento particular de las cámaras de DT

y su electrónic bajo daño por radiación, se ha podido establecer un alto nivel de confianza que sustituyendo la electrónica del detector, se espera que el funcionamiento del detector sea satisfactorio a lo largo del HL-LHC.

Index

Abstract **vii**

Resumen **xi**

1 Particle Physics, the LHC and CMS **1**
1.1 The Standard Model of Particle Physics 2
1.2 Interaction of radiation with matter 5
1.2.1 Photons interaction with matter 5
1.2.2 Charged particles interactions with matter 5
1.2.3 Neutrons interactions with matter 8
1.3 The LHC collider 9
1.3.1 LHC Luminosity 12
1.3.2 The CMS Experiment at the LHC 15
1.3.3 The CMS Drift Tube Chambers 22
1.3.4 Electronics of the DT Chamber 25

2 Radiation hardness of the CMS Drift Tubes in HL-LHC **31**
2.1 High Luminosity LHC 31
2.1.1 CMS Phase 2 at HL-LHC 34
2.2 Expected background radiation at CMS 35
2.3 Radiation damage on gaseous detectors 38
2.4 Radiation damage on electronics 44
2.4.1 Total Ionizing Dose 45
2.4.2 Displacement Damage Dose 46
2.4.3 Single Event Effects 46
2.4.4 SOFT ERRORS (Non-Destructive) 46
2.4.5 HARD ERRORS (Destructive) 47
2.4.6 Radiation effects in FPGAs 49
2.5 Drift Tubes at HL-LHC 50

2.5.1 Estimation of the particle fluxes of DT at HL-LHC . . 50
2.5.2 Study on the longevity of ROB electronics 53
2.5.3 DT upgrade for HL-LHC 55
2.6 Summary and Conclusions 59

3 Studies of the Longevity of DT Chambers at GIF++ 61
3.1 Baseline considerations about aging of DT chambers at construction 62
3.2 DT aging campaigns at GIF++ 63
3.2.1 The GIF++ Facility at CERN 63
3.2.2 Dosimetry at GIF++ 65
3.3 Current and gain measurements 70
3.3.1 2015 MB1 Irradiation 70
3.4 Investigation Plan at GIF++ 73
3.4.1 2016 MB1 Irradiation 76
3.5 2017-2019 Irradiation Campaign 85
3.5.1 Integrated Dose 86
3.5.2 Hit Efficiency analysis 87
3.5.3 High Voltage Scans 89
3.5.4 Results from operation in a Muon Test Beam 90
3.6 Summary and Conclusions 91

4 Interpretation and modelling of GIF++ results 95
4.1 Baseline hypothesis for aging 96
4.2 Modeling of the voltage in an aged wire 97
4.2.1 Voltage versus the distance to the wire's center 100
4.2.2 Electric field versus the distance to the wire's center . . 102
4.2.3 Effect of the dimensions of the outer cylinder 103
4.2.4 Gain as a function of the electric field 104
4.2.5 Comparison of the gain model with GIF++ data . . . 109
4.2.6 Hypothesis for the dynamic variation of the gain with the dose rate 113
4.3 Summary and conclusions 120

5 Mitigation of the DT Chambers aging 123
5.1 Operational adjustments 123
5.2 Gas system modifications 126
5.3 Drift Tubes Radiation Shielding 127
5.3.1 Shielding Installation 127

5.4 Shielding Performance Evaluation 129
5.4.1 GAMOS Simulations 130
5.4.2 Shielding Configurations 132
5.5 Summary and Conclusions 139

6 Radiation Hardness of the DT electronics at CHARM 141
6.1 Radiation hardness measurement of phase 2 prototypes at CHARM 142
6.1.1 The OBDTv1 Board 142
6.1.2 The CHARM facility 144
6.1.3 Test Setup 146
6.1.4 Dosimetry online and offline at CHARM 152
6.2 Results of the Irradiation Campaign 153
6.2.1 Results from the performance of the fans 156
6.2.2 Results from the Power Supply distribution 156
6.2.3 Result from the Optical Transceivers 158
6.2.4 Results from the FPGA performance in the reference test 160
6.2.5 Results from the FPGA performance in the final firmware test 162
6.2.6 Results of the Microsemi Polarfire Remote Reprogramming Firmware 164
6.3 Summary and Conclusions 165

Conclusions 167

A Evaluation of using a Half-Filter for the source at GIF++ 173

B Online Dose Monitoring for the CHARM Facility 175

References 181

List of Figures

1.1 The particles of the Standard Model separated in fermions (quarks and leptons) and bosons. Its mass, charge and spin appear indicated. 3

1.2 Diagram of the CERN accelerator's complex. The LHC is the last ring in a complex chain of particle accelerators. The smaller machines are used in a chain to help boost the particles to their final energies and provide beams to a whole set of smaller experiments at CERN. 11

1.3 Cross Sections for specific physics processes, from the ATLAS TDR (2003) [6]. The dotted lines show the energies of two hadron colliders (the Tevatron at 1.96 TeV, and the LHC at 14 TeV). 13

1.4 CMS layout and overall characteristics. 16

1.5 The CMS coordinate system. 17

1.6 Longitudinal cut of a quarter of the CMS Muon spectrometer as originally designed. 21

1.7 Cross-sectional and longitudinal view of CMS with the subdivision into wheels and sectors. 23

1.8 Diagram of a transversal section of a DT cell where the electrodes and the field lines can be seen. 24

1.9 Schematic view of a DT chamber with the two outer Superlayers that measure the ϕ coordinate and the inner Superlayer that measures the θ coordinate. The staggering of cells between layers allows to discriminate which side of the wire the track went through. 25

1.10 Integrated luminosity delivered and recorded by CMS up to mid 2024 29

2.1 Timeline for the LHC and High-Luminosity LHC 32

2.2 Radiation Field inside the CMS Experiment. A complete view of the CMS experiment is illustrated in (a). The dose map (b) has been determined for 10 years operation of the machine while charged hadrons (c) and neutron (d) fluxes have been calculated for normal operational conditions [25]. 37

2.3 Absorbed dose estimated for different muon stations in central and forward part of CMS detector using FLUKA simulations of proton-proton collisions at 7 TeV per beam with a Phase 2 geometry model. Results are normalized to an integrated luminosity of 3000 fb^{-1} assuming an inelastic scattering cross section of 80 mb [25]. 38

2.4 FLUKA simulations of proton-proton collisions at 7 TeV per beam with a Phase 2 geometry model for different muon station in central and forward part of CMS detector. Results are normalized for an instantaneous luminosity of $5 \times 10^{34}\ cm^{-2}s^{-1}$ assuming an inelastic scattering cross section of 80 mb [25]. . . 39

2.5 Simulation (CERN fluka 4-1.1) of the energy spectra of the particles in the volumes covered by the MB1 chambers of Wheel-2 for the CMS Phase 2 detectors during HL-LHC. Fluxes are normalized to a single pp-collision [26]. 40

2.6 Simulation (CERN fluka 4-1.1) of the energy spectra of the particles in the volumes covered by the MB4 chambers of Wheel-2 for the CMS Phase 2 detectors during HL-LHC. Fluxes are normalized to a single pp-collision [26]. 41

2.7 Progressive degradation of a Geiger Counter while being exposed to radiation. Curve 4 is the singles counting rate vs voltage measured after 10^8 counts. 42

2.8 Chemical reaction occurring in the anodes of a gaseous detector that leads to radiation aging. 43

2.9 Rate per DT chamber channel in Hz/cm^2 for each of the DT chambers in the CMS detector calculated at an average luminosity of $4.645 \cdot 10^{33} cm^{-2}s^{-1}$ 52

2.10 Extrapolation of the background rates measured in MB4 chambers for luminosities up to 10^{35} $cm^{-2}s^{-1}$. 53

2.11 Relationship between L1A rate and the number of hit's processed without error. 54

2.12 Diagram of the new architecture for the CMS Phase 2 DT systems that will be installed for operation during HL-LHC. GMT is the Global Muon Trigger system that receives the DT Trigger Primitives. DAQ refers to the Data Acquisition system that receives the readout data. DSS is the CMS Detector Safety System. UXC is the CMS experimental cavern and USC is the CMS Service cavern. BX refers to LHC bunch crossing which represents a unit of time of 25 ns. 56
2.13 Image of an OBDT-theta and Testpulse-theta boards fixed to the mechanical frame that connects them to the Minicrate. . . 59

3.1 Layout of the Gamma Irradiation Facility ++ 63
3.2 MB1 chamber installed at GIF++ seen from the position of the source 65
3.3 Portable dosimeter Automess 6150 AD 67
3.4 Conversion factors [48] between dose units 69
3.5 Irradiation flux simulation inside the GIF++ bunker [44]. . . . 70
3.6 Two-dimensional dose rate distribution on the DT chamber installed at GIF++. 72
3.7 CMS DT spare chamber (rectangular detector with green outline) placement in the GIF++ bunker, shadowed by a CSC chamber (red outline). 73
3.8 Currents as a function of time for the three Superlayers during the 2015 irradiation of an MB1 chamber. 74
3.9 Analysis of a DT wire. 77
3.10 Integrated dose and dose rate as a function of time for the 2016 irradiation. 78
3.11 Current as a function of time for 2016 data taken with the newly installed wires on the MB1 chamber 79
3.12 Current per dose rate per wire as a function of integrated dose in the replaced wires of the MB1 80
3.13 Corrected current per dose rate as a function of integrated dose in the replaced wires of the MB1 81
3.14 HV current dependence on instantaneous luminosity in MB1 (left) and MB4 (right) as a function of the sector number, i.e. azimuthal angle, where 4 and 10 correspond to the top and bottom sectors, respectively, from [23] 82
3.15 Current per instantaneous luminosity as a function of the integrated luminosity of the replaced and old wires 83

3.16 Estimated gain as a function of the integrated luminosity for the MB1 YB ±2 chamber at HL-LHC 85
3.17 Current as a function of time for the VDC and MB1 chamber at GIF++ 86
3.18 Integrated dose [mGy] as a function of time for the 2017-2019 irradiation at GIF++. The axis on the right shows the equivalent expected luminosity for MB1 chambers in the external wheels for the HL-LHC as discussed in 3.4.1.3 88
3.19 Illustration of a DT chamber and a reconstructed track segment with 4 associated hits in SL3 extrapolated to SL1 89
3.20 Hit efficiency for cosmic muons as a function of integrated luminosity for the aged layers (SL1L1 and SL1L4) at 3550 V with a front-end threshold of 30 mV during the 2017-2018 campaign on an MB2 chamber. 90
3.21 Hit efficiency for cosmic muons as a function of HV for the aged layers (SL1L1 and SL1L4) when the source is off and the front-end threshold 30 mV for different values of the integrated luminosity 91
3.22 Hit efficiency for cosmic muons as a function of HV for the aged layers (SL1L1 and SL1L4) when the source is off and the front-end threshold values of 20 and 30 mV 92
3.23 Hit efficiency for test-beam muons as a function of dose rate for the aged layers (SL1L1 and SL1L4) and the non-irradiated layer SL1L3 93

4.1 Representation of the equipotential lines inside the drift cell with the anode at 3600 V, the strips at 1800 V and the cathode at -1200 V. 98
4.2 Diagram of a wire of radius a inside a cylinder of radius b (left) and representation of the electrical field between the anode and the cathode. This is the typical construction of a drift tube. . 99
4.3 Representation of the assembly of cylindrical wires through which we model the inner of the DT cell when coating has been attached to the wire. 99
4.4 Representation of the two capacitors in series through which the DT cell with its wire and its coating are modeled. 100
4.5 Voltage at each position inside the simulated DT cell versus the distance to the center of the wire. Four different configurations of wire diameter are represented, having all of them a similar behaviour. 102

4.6 Voltage at each position inside the simulated DT cell versus the distance to the center of the wire. Region close to the wire has been enlarged for easier visualization. Different configurations of wire diameter are represented. 103

4.7 Electric field for different configurations of the wire diameter as a function of the position versus the wire center. As can be seen the maximum electric field gets very much reduced as one moves away from the wire's center. 103

4.8 Voltage as a function of the distance to the center of the anode wire for different diameters and voltages of the outer cylinder. As can be seen the effect of the strip is to smooth the voltage drop inside the DT cell. 104

4.9 Equipotential lines inside a simulated Drift Cell in Garfield with the wire at 3550 V (50 μm diameter), the cathodes at -1200 V (11.5 mm wide) and the strips at 1800 V (16 mm wide).108

4.10 Drift velocity in a simulated DT cell in GARFIELD++ as a function of the electric field. As can be seen, for the region of 1 kV/cm to 10 kV/cm, the drift velocity is constant, as expected in our cells. 109

4.11 Electrical field in a simulated DT cell in GARFIELD++. . . . 110

4.12 Townsend coefficient as a function of the electric field for the DT gas mixture. 110

4.13 Values obtained for the gain of a DT cell (to be multiplied by 10^5) as a function of the radius using the Townsend coefficients obtained from Garfield++. 111

4.14 Hit efficiency for cosmic muons as a function of HV for the aged layers (SL1L1 and SL1L4) when the source is off and the front-end threshold 30 mV for different values of the integrated luminosity. The separation in voltage between the curves of different accumulated dose is overlaid. 112

4.15 In light blue, it is represented the dependence of the wire gain on the wire's voltage for a fixed value of strips 1800 V and cathodes at -1200 V as obtained experimentally at CERN ([51]). Overlaid are the values of the gain at 50% hit efficiency (green) which is a common gain for any aged scenario. In orange, the line for the aged chamber that reaches 50% hit efficiency at 3480 V which means that its gain at 3550 V corresponds to approximately 1.3 10^5. 114

4.16 Equivalent circuit of the DT cell under gamma flux irradiation. The current I_i represents the current due to the gamma flux for different dose rates "i" and assumed to be after the avalanche. 115

4.17 Currents per wire versus de dose rate of the gamma flux at GIF++ for different wires and with different levels of aging. . 116

4.18 Ratio of the current per wire versus the dose rate for different intensities of the gamma flux at GIF++ as a function of the current in the wire. This ratio is proportional to the gain of the DT cell, since it relates the number of electrons collected for a given number of gammas. Different levels of aging in the wire are represented. It can be seen that the larger the aging, the lower the gain. It can also be seen that this drop of gain is not flat versus the wire current. 117

4.19 Calculated gain (natural log) as a function of its wire current for each of the three cases. In blue is the wires that have not aged, in red the wire that has aged 338 mGy and in green the wire that has aged 845 mG. 118

5.1 In the left plot the hit efficiency of each station in each wheel is plotted as the average path a high energy particle coming from the interaction point. The right plot depicts the HV values after final optimization in 2018. 124

5.2 In the left plot the concentration of O_2 and H_20 is shown during a change from closed to open loop. The right plot shows the impact of air leaks on the drift velocity. 127

5.3 Integral of the signals generated in the chamber during collisions as measured by the High Voltage current per instantaneous luminosity unit (left). The top chambers of the outer wheels (W±2) were covered with prototype shields. Sectors covered in LS2 installation (right) 129

5.4 Occupancy of the MB4 chambers displayed as a function of the sector and wheel extrapolated to a luminosity of 10^{34} cm^{-2} s^{-1}. The lower values around sector 10 correspond to chambers close to the floor of the cavern. 130

5.5 Ratio between occupancy for the MB4 chambers before and after shielding installation. Wheel 0 chambers were only shielded in a fraction of their surface due to mechanical integration problems. 131

5.6 3D representation of the simulation of 100 neutrons (in yellow) reaching the shielding from the left, with secondary photons are represented in green. 132
5.7 Background segments reconstructed in the MB1 station were propagated in the z-R plane in order to observe their position and direction. Figure from [65]. 134
5.8 Realistic energy distribution of fast protons and neutrons in MB1 Wh±2. 135
5.9 GAMOS simulations of 2 cm thick shields using incident protons(left) and neutrons(right) with a flat energy distribution. . 136
5.10 GAMOS simulations of 2 cm thick shields using incident protons(left) and neutrons(right) with a realistic energy distribution of the fast particles in MB1 Wh±2. 137

6.1 Drawing of the OBDTv1 functionality and main components. . 144
6.2 Image of the OBDTv1 board top and bottom. 145
6.3 CHARM facility layout. The location of the Overhead Conveyor is indicated. 146
6.4 Image of the Overhead Conveyor with our setup inside the CHARM facility. 147
6.5 Drawing of the Test Stand interconnections for the main test. OBDT and PUFO are located inside CHARM while VC707 is in the Control Room. 149
6.6 Drawing of a flip-flop chain. 4096 elements were used to detect a potential SEU under different logic conditions. 152
6.7 Accumulated number of power cycles and reconfigurations performed during the irradiation at CHARM. 155
6.8 Temperatures of all of the OBDT and PUFO board sensors during all the irradiation period. 156
6.9 Voltages at the output of the linear regulators MIC69502WR in the OBDT and PUFO board during all the irradiation . . . 157
6.10 Temperatures read from the optical transceivers in the OBDT and PUFO. The temperature sensors of the QSFP are internal to the transceivers and are read through an I^2C interface. . . 158
6.11 Temperatures, currents and voltages in the PUFO board when an increase in current was observed. All the boards functionalities were working properly and the origin of this increase is believed to be in the FTL410QD4C device. 159
6.12 Results of the number of SEUs measured in the test stand versus the integrated dose. 163

A.1 Dose rate as a function of the distance to the center of the bunker 174

B.1 Drawing of the CHARM facility aerial view with the irradiation locations. 176
B.2 Representation of the full dataset of the 822 proportional counter information as recorded in TIMBER during the OBDTv1 irradiation period of November 3rd to November 12th 2021. . . . 177
B.3 Figure 3: Zoom in of the TIMBER data for the 822 proportional counter. 178
B.4 Histogram of the values of the 822 proportional counter detector as read by TIMBER during all of the radiation period between November 3rd to November 12th 2021. 178
B.5 The number of spills over threshold versus time is represented together with the dose recorded by the two RADMON sensors. As can be seen the behaviour of both measurements is very similar. 179
B.6 Representation of the number of spills selected from TIMBER versus the integrated dose provided by RADMON. 179
B.7 Representation of the number of spills selected from TIMBER versus the integrated dose provided by RADMON for the period without shielding and the linear fit included. 180

List of Tables

1.1 LHC Collider Main Parameters 15

3.1 Simulated flux [$\frac{counts}{s \cdot cm^2}$] downstream and upstream attenuators open (from [44]). 68

3.2 Percentage of total flux in D4 position (from [44]), conversion coefficients according to energy range from [48] and conversion factor normalized to the percentage of total flux. 71

3.3 Estimated integrated charge in mC/cm up to the end of HL-LHC operations (3000 fb^{-1}) based on measured currents as a function of instantaneous luminosity. 81

4.1 Gain (to be multiplied by 10^5) calculated from the Garfield++'s Townsend coefficients for different voltages and different values of the wire radius. 108

4.2 Gain comparison between the model presented in the thesis and the data measured at GIF++ for the MB1 and MB2 chamber. 113

4.3 Calculation of the resistivity of the wires and its coating . . . 120

5.1 GAMOS simulation results in % for the listed configurations launching 1000 neutrons or photons perpendicular to the shield. 132

6.1 List of the main components that are part of the OBDTv1 and PUFO boards and that have been irradiated. 150

6.2 Optical transceivers used in the OBDTv1 and PUFO boards during irradiation. 150

6.3 Configuration used during the irradiation in the two periods and doses and fluences received. 153

6.4 Total dose and fluence received at CHARM during the irradiation period. 154

6.5 Average variation of the test stand currents throughout the irradiation period. 157
6.6 Table with the values of Loss of Signal and RX_data_error corrected in the three commercial optical transceivers 160
6.7 Cross sections calculated for the SEU reference test both in the OBDT and PUFO board. Average values are calculated . 160
6.8 Cross sections in the RAMs calculated for the SEU reference test both in the OBDT and PUFO board. Average values are calculated. 161
6.9 Dose and fluences accumulated when the SEU reference test was operational. 161
6.10 Comparison of the cross sections in the SEU reference test performed by us at CHARM and by other groups at different facilities. 162
6.11 Extrapolation of the number of failures due to SEUs in the OBDT board expected during HL-LHC if we separate the contribution of each chamber type which has very different expected fluence. 165

Chapter 1

Particle Physics, the LHC and CMS

Particle physics, the branch of physics that studies the fundamental constituents of matter and their interactions, is the basis of the current understanding of nature at the smallest scales. The field's evolution has been marked by groundbreaking discoveries, the development of sophisticated theoretical frameworks, and the construction of monumental experimental systems.

The theoretical framework is described in the so-called "Standard Model (SM)" [1] and it provides a comprehensive and highly successful theory for understanding the fundamental particles and forces that constitute the universe, except for gravity. It predicts with large precision a wide array of experimental results and has been validated by numerous experiments.

One of these experiments which has contributed to complete our understanding of the SM, through the discovery of the Higgs boson, is the CMS (Compact Muon Solenoid) [2] experiment at the LHC (Large Hadron Collider) [3] at CERN (European Center for Nuclear Research).

This thesis is framed in the investigations and activities that will allow to continue the operation of the CMS experiment during the 10 years of a new high luminosity regime that is referred to as High Luminosity LHC (HL-LHC) [4]. The focus is ensuring the reliable operation of the muon detector in the central region of the CMS experiment and overcoming the limitations that can be found due to the increase of radiation dose and flux, occupancy, throughput, trigger rate and, after more than 20 years of operation, also aging.

In this chapter, an introduction to the theoretical framework that justifies the construction of these huge and sophisticated detectors, a description of

the experiments themselves and the constrains for operation under HL-LHC will be covered.

1.1 The Standard Model of Particle Physics

The history of the SM of particle physics goes back more than a century and its starting point can be considered the discovery of the electron by J.J. Thomson in 1897 which was followed by the consequent development of quantum mechanics that over the decades expanded with significant contributions from many physicists. The Standard Model is one of the most robust and extensively tested theories in modern science.

The SM describes the fundamental particles that make up the Universe and the forces that govern their interactions. It consists of seventeen types of fundamental particles which are classified into two categories: fermions and bosons. Fermions constitute the building blocks of matter, while bosons are force carriers that mediate interactions between particles.

Fermions are half-integer spin particles which means, they obey the Pauli exclusion principle, and they can be subdivided in two types: quarks and leptons. Each of these fermions has its anti-particle, which has the same mass, but opposite quantum numbers. The twelve fermions comprise three generations of leptons: the electron, the muon and the tau leptons, with their counterpart neutrinos; and quarks, with different flavors: up and down, strange and charm, and top and bottom. Each extra generation is an exact copy of the first one, apart from the increasing particle mass. An overview of all fermions, leptons and quarks, is given in Figure 1.1.

Quarks are never observed isolated, they are always found combined to form hadrons. Two quark hadrons (quark and antiquark) are called mesons while three quark hadrons are called baryons, being the most stable of them the well known neutrons and protons, made of quarks up and down, and constituting the nucleus of every atom in the period table of elements. Electrons, on their side, surround the nucleus of all ordinary matter.

The interactions between particles that are described by the SM include three of the four known fundamental forces in the universe: the electromagnetic force, the weak nuclear force, and the strong nuclear force, but it excludes gravity. The relative strengths of the strong, electromagnetic, weak and gravitational forces are of the order $(1, 1/137, 10^{-6}, 10^{-39})$.

The electromagnetic force, mediated by photons, is responsible for interactions between charged particles and is described in the theory of Quantum Electrodynamics (QED). The weak nuclear force, mediated by W and Z

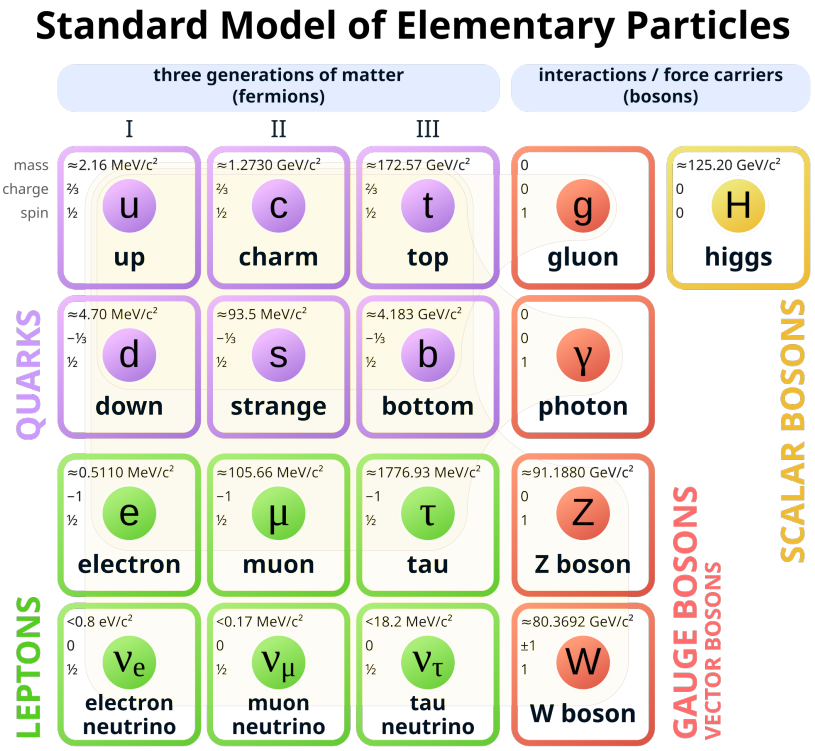

Figure 1.1: The particles of the Standard Model separated in fermions (quarks and leptons) and bosons. Its mass, charge and spin appear indicated.

bosons, governs radioactive decay and neutrino interactions. The strong nuclear force, mediated by gluons, binds quarks together within protons and neutrons, and holds nuclei together. These bosons, which are fundamental force carriers, are spin 1 particles, and thus, obey Bose-Einstein statistics.

As a gauge theory, the SM is described by a Lagrangian that is invariant under local transformations of the $SU(3)_C \otimes SU(2)_L \otimes U(1)_Y$ symmetry group. The $SU(3)_C$ is the color gauge group, the fundamental symmetry group of quantum chromodynamics (QCD). This theory describes the strong interaction between quarks as mediated by the exchange of eight massless gluons, also carriers of the color charge. QCD explains the confinement of quarks within hadrons, the fact that quarks cannot exist in isolation is explained by the growth of the interaction strength towards large scales. Quarks are only "free" at high energies.

The $SU(2)_L \times U(1)_Y$ gauge group describes the electroweak interactions,

a unified description of the electromagnetic and weak forces, where L denotes that only left-handed (negative helicity) particles participate in the interaction and the label Y refers to the weak hypercharge. This unification of the electromagnetic and weak forces into a single framework known as electroweak theory was a significant milestone in the development of the Standard Model.

Before electroweak-symmetry breaking, SU(2) is mediated by three weak isospin, massless bosons W_μ, and U(1) by a weak hypercharge massless boson, B0. The latter, weak hypercharge, relates the electrical charge and the third component of the weak isospin. After electroweak symmetry breaking, these gauge bosons are recombined and give raise to the massive carriers of weak force (W^+, W^-, Z) and the massless photon, carrier of the electromagnetic interaction. This process requires the introduction in the model of a scalar field, the Higgs field.

The Higgs mechanism is a fundamental process in the Standard Model of particle physics that serves to explain how particles acquire mass. It describes the existence of the Higgs field, a pervasive field that permeates all of space. When particles interact with this field, they acquire mass proportional to the strength of their interaction. This mechanism is facilitated by the Higgs boson, a scalar particle with spin 0, which is a quantum excitation of the Higgs field.

The Higgs boson, discovered at the LHC at CERN in 2012, provides particles with mass through the Higgs mechanism. This discovery confirmed the last missing piece of the SM and was a monumental achievement in particle physics.

The SM has been extensively validated through numerous experiments over several decades and is considered to be an effective theory up to the TeV range. The SM as a whole theory requires 26 free parameters that can be measured experimentally: 3 gauge couplings, 6 mixing angles, 12 masses (6 of the quarks and 6 of the leptons), 2 boson masses, 2 CP-violating phases, and 1 CP-violating angle.

High-energy particle colliders, such as the LHC, have been instrumental in testing the predictions of the Standard Model. These experiments have consistently confirmed the existence of predicted particles and their properties, reinforcing the validity of the theory. However, certain phenomena, such as neutrino oscillations, have hinted at physics beyond the Standard Model. The SM also does not incorporate gravity, which is described separately by General Relativity. Additionally, the SM cannot explain the nature of Dark Matter and Dark Energy, which constitute most of the universe's mass and energy, nor explains the asymmetry between matter and antimatter. These

limitations point to the need for a more comprehensive theory that can unify all fundamental forces and account for all observed phenomena.

1.2 Interaction of radiation with matter

In what follows, a summary of radiation-matter interactions will be given.

1.2.1 Photons interaction with matter

Photons include gamma rays (γ), ultra-violet rays (UV), X-rays, etc., all of them transport electromagnetic radiation at the speed of light and have no mass or charge. The electro-magnetic effects caused by this kind of radiation can be photoelectric absorption, pair production or Compton scattering:

- Photoelectric absorption: the incident photon energy is transferred to an electron, which is ejected from the atom.
- Compton scattering: Photons interact with an electron in the material losing energy and glance off with a different wavelength.
- Pair production: As the incoming photon energy exceeds twice the energy corresponding to the electron rest mass, i.e. 1.02 MeV, the production of an electron and positron pair becomes possible. The photon is absorbed, and its energy is used to create an electron-positron pair. This process is intimately related to the bremsstrahlung process.

Gamma rays can also participate in nuclear reactions.

1.2.2 Charged particles interactions with matter

Energetic charged particles interact with matter by electrical (i.e., coulombic) forces and lose kinetic energy via excitation, ionization , and radiative losses. Excitation and ionization occur when charged particles lose energy by interacting with orbital electrons in the medium. These interactional, or collisional, losses occur due to the coulombic forces exerted on charged particles when they pass in proximity to the electric field generated by the atoms' electrons and protons. Excitation is the transfer of some of the incident particles' energy to electrons in the absorbing material, promoting them to a different orbital with a higher energy level. In excitation, the energy transferred to an electron does not exceed its binding energy. Following excitation, the electron will return to a lower energy level, with the emission of the excitation

energy in the form of electromagnetic radiation. This process is referred to as de-excitation. If the transferred energy exceeds the binding energy of the electron, ionization occurs, whereby the electron is ejected from the atom. The result of ionization is an ion pair consisting of the ejected electron and the positively charged atom.

Charged particles (such as protons and electrons/positrons) going through matter can interact both with the nuclei -via the nuclear interaction and the Coulomb interaction- and with the electron cloud -via the Coulomb interaction (electromagnetic interaction). Although the effects of a collision with the light electron is going to affect the colliding particle much less than an impact with the heavy nucleus, the probability of such a collision is much higher.

1.2.2.1 Electromagnetic Interactions

Charged particles interact with the electrons and nuclei of materials primarily through Coulomb forces. Electromagnetic interactions dominate at most energies and result in the scattering of the charged particle, leading to energy loss and deflection. The energy lost by the particle through these interactions can cause excitation and ionization of atoms within the material, altering its properties and structure. If the transferred energy is sufficient to overcome the binding energy of an electron, ionization occurs, resulting in the ejection of the electron. If the energy is insufficient for ionization but enough to elevate the electron to a higher energy state, excitation occurs.

The energy loss of charged particles in materials is described by the Bethe-Bloch equation, which quantifies the stopping power of the material. This equation takes into account factors such as the charge and velocity of the particle and the electron density of the material. The stopping power is a measure of the energy loss per unit path length and is needed to predict the range and penetration depth of the particle.

The Bethe-Bloch equation for the stopping power, $-\frac{dE}{dx}$, of a charged particle moving through a medium is given by:

$$-\frac{dE}{dx} = \frac{4\pi e^4 z^2}{m_e c^2 \beta^2} \left(\frac{nZ}{A}\right) \left[\ln\left(\frac{2m_e c^2 \beta^2 \gamma^2 T_{max}}{I^2}\right) - 2\beta^2 - \frac{\delta}{2}\right]$$

where:

- e is the elementary charge.
- z is the charge of the particle.

- m_e is the electron mass.
- c is the speed of light.
- $\beta = \frac{v}{c}$ is the velocity of the particle relative to the speed of light.
- $\gamma = \frac{1}{\sqrt{1-\beta^2}}$ is the Lorentz factor.
- n is the electron density of the medium.
- Z is the atomic number of the medium.
- A is the atomic mass of the medium.
- I is the mean excitation potential of the medium.
- T_{max} is the maximum kinetic energy transferable to a free electron in a single collision.
- δ is the density effect correction.

The energy loss described by the Bethe-Bloch equation is highly dependent on the velocity of the charged particle. At low velocities, the stopping power increases as the velocity increases. This increase continues until the particle reaches a velocity corresponding to a minimum in the stopping power, known as the Bethe-Bloch minimum. Beyond this point, as the velocity increases further, the stopping power decreases slightly and then increases again due to relativistic effects.

The stopping power is proportional to the square of the charge of the incident particle (ζ^2). This means that particles with higher charges, such as alpha particles, experience significantly higher energy loss compared to singly charged particles like protons. Electrons and positrons lose energy by collisions while traversing an absorber, just as massive charged particles do. In addition, because of their small mass and depending on their kinetic energy, they will undergo a significant energy-loss by radiative emission, i.e., by the so-called bremsstrahlung emission. This happens beyond a few tens of MeV for electrons and beyond hundreds of GeV for muons.

It is worth mentioning the emission of electromagnetic radiation, so-called Cherenkov Radiation that occurs when charged particles travel through a material faster than the speed of light in that medium. This phenomenon occurs due to the polarization of the medium and the subsequent emission of light as the medium returns to its ground state. Cherenkov radiation is used in particle detectors to identify the presence and velocity of high-energy charged particles.

1.2.2.2 Nuclear Interactions

At high energies, charged particles can interact with the nuclei of atoms in the material.

Charged particles may undergo multiple scattering events as they pass through a material. These scattering events can be elastic or inelastic. Elastic scattering involves the deflection of the charged particle without a significant loss of energy, while inelastic scattering involves a transfer of energy to the material's electrons or nuclei. The cumulative effect of these scattering events determines the overall trajectory and dispersion of the particle beam.

If the charged particle has sufficient energy, it can induce nuclear reactions, which can result in the production of new isotopes, the emission of neutrons, protons, alpha particles, etc. These interactions can result in nuclear reactions, such as spallation, fragmentation, or fusion reactions.

1.2.3 Neutrons interactions with matter

Neutrons are particles without charge and, therefore, they are more likely to interact with the nucleus of an atom than with the electrons outside of it. Therefore neutron interactions with matter are dominated by nuclear interactions. Coulombian interactions, which is the dominating energy loss mechanism for charged particles, do not affect neutrons. There are three main possible interactions involving neutrons depending on their energy:

- Elastic scattering: After the interaction the total kinetic energy of the system is conserved, the maximum energy transfer is reached when the nucleus has similar mass as the neutron, such as hydrogen nuclei. The process of reducing the initial high speed of fast neutrons to low energy neutrons (thermal neutrons) is called moderation or thermalization.

- Inelastic scattering: After the neutron interacts with the nucleus there is a change of the kinetic energy of the system and the nucleus reaches an excited state, which causes the emission of the excess energy in some form of radiation.

- Neutron capture: A nuclear reaction in which a target nucleus absorbs a neutron and then emits electromagnetic energy such as a photon. The initial nucleus and the result of the capture are isotopes of the same element.

The neutron passing through the material loses energy until the neutron is captured by an atom and the energy is emitted in the form of gamma rays.

A thermal neutron is a free neutron with a kinetic energy corresponding to the average energy of the particles in the ambient materials. They are relatively slow and have low energy but have large cross-section in fission processes. Also thermal neutrons are more easily captured by materials based on Cadmium and Boron (Boron's neutron capture cross-section is 2000 times more than hydrogen.).

The effects of neutrons on matter depend on their energy and as such, they are classified as epithermal if it has a kinetic energy of below 1 MeV. Fast neutrons which are those with energy above 1 MeV, and below 20 MeV and ultra-fast neutrons that are neutrons with energy greater than 20 MeV. The small kinetic energy of epithermal neutrons makes them exchange energy through elastic scattering with the nucleus, in addition, epithermal neutrons will sometimes get absorbed. Fast and ultra-fast neutrons have greater energy and deposit more energy when interacting with the nucleus. They are particularly relevant to account for the amount of Single Event Upsets (SEUs) in an electronic component.

The construction of shielding targeting neutrons is more complicated than in the case of charged particles because of the more complicated nature of nuclear interactions.

1.3 The LHC collider

The LHC was built with the goal of testing the predictions of several particle physics theories, among them, study the nature of electroweak symmetry breaking, presumed to be governed by the Higgs mechanism. Also it was aimed to expand the search of new particles predicted by different theories such as Supersymmetry (SUSY), and to study other unresolved questions in particle physics such as the nature of Dark Matter or the asymmetry between matter and antimatter in the visible universe.

The LHC allows to study the fundamental constituents of matter by colliding particles at extremely high energies. The kinetic energy of these colliding particles can be converted into mass of new, heavier particles. In this way, physicists can recreate conditions similar to those just after the Big Bang, allowing them to study the building blocks of the universe at the smallest scales.

The LHC is the most powerful collider ever made, with a circumference of 26.7 km, built 100 m underground beneath the French-Swiss border in the existing tunnel made for the previous Large Electron-Positron (LEP) collider [5]. In the LHC tunnel, two beams of protons, or heavy ions, circulate in

opposite directions inside two vacuum pipes forming two concentric rings. The circulating beams collide at four interaction points where the four main experiments are located. ATLAS (A Toroidal LHC Apparatus) [6] and CMS (Compact Muon Solenoid) are both general purpose experiments designed to fulfill similar physics programs with different architecture for increased redundancy. They are situated in opposing points in the LHC ring. ALICE (A Large Ion Collider Experiment) [7] studies quark-gluon plasma properties through heavy ion collisions and LHCb (Large Hadron Collider beauty) [8] focuses on matter-antimatter asymmetry and CP-symmetry violation.

Particles cannot be accelerated directly to energies of the order of TeV, such as those of the LHC design. Therefore, it is required to follow a series of coordinated boosts in a collider chain, as shown in Figure 1.2. Starting with a single bottle of hydrogen gas, an electric field removes the electrons from the hydrogen atoms. These protons are accelerated up to 50 MeV with a linear accelerator (LINAC 2) and injected into a circular accelerator (Booster) where they reach an energy of 1.4 GeV. Next, they are injected into the Proton Synchrotron (PS) and the Super Proton Synchrotron (SPS), increasing their energies up to 25 and 450 GeV, respectively. The final step is the injection into the LHC, where a total of 2808 bunches, separated by 25 ns and containing $\sim 1.1 \times 10^{11}$ protons each, are boosted to final energies of 6.5 TeV, circling the perimeter 11245 times per second. The 25 ns separation is determined by the LHC frequency, 40.08 MHz, a clock that synchronizes all systems around the ring.

One of the main advantages of a circular accelerator is that the energy of the particles can be increased gradually each loop they travel inside the same pipe. However, this also poses one of the major challenges, such as containing the beams in a closed trajectory without significant loss of energy. Synchrotron radiation is a phenomenon where charged particles, such as electrons or protons, moving at high speeds emit electromagnetic radiation due to their acceleration following a curved path. This radiation reduces the energy from the particles, causing them to lose momentum and, consequently, reducing the efficiency of particle acceleration in colliders.

Thousands of magnets of different varieties and sizes are used to direct the beams around the accelerator, keeping them stable and precisely aligned. These include 1232 dipole magnets, 15 meters in length, which bend the beams, and 392 quadrupole magnets, each 5-7 meters long, which focus the beams. Just prior to collision, insertion magnets are used to "squeeze" the particles closer together to increase the chances of collisions. The main dipoles generate powerful 8.3 T magnetic fields, 100000 times more powerful than the Earth's magnetic field, which is only possible when a current of

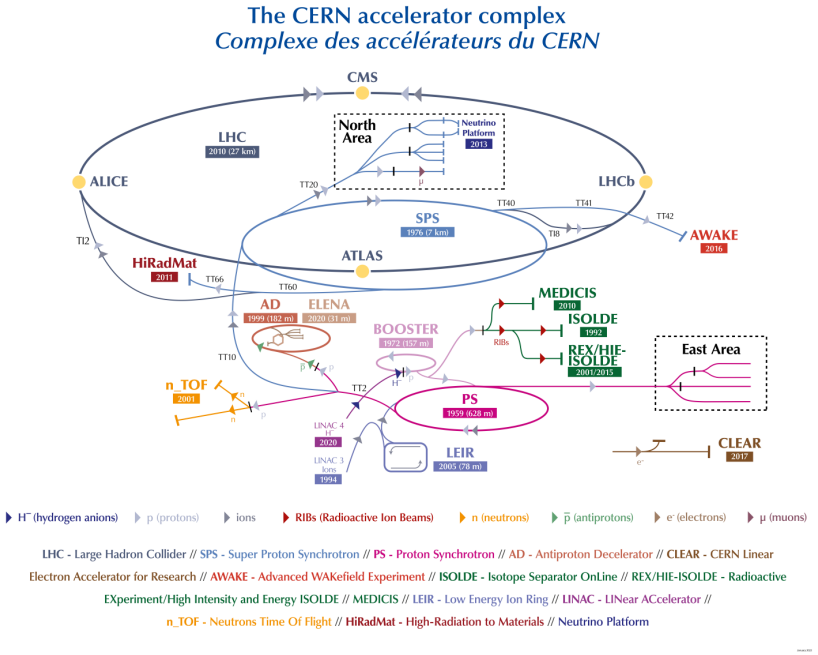

Figure 1.2: Diagram of the CERN accelerator's complex. The LHC is the last ring in a complex chain of particle accelerators. The smaller machines are used in a chain to help boost the particles to their final energies and provide beams to a whole set of smaller experiments at CERN.

11080 amperes flows through a superconducting coil. The need for a high beam intensity, not reachable with anti-proton beams, made necessary to have independent cavities along the ring, one for each proton beam.

The LHC superconducting magnets operate at very low temperatures to allow conducting this large current without resistance. The LHC is the largest cryogenic system in the world and one of the coldest places on Earth, operating at a temperature of 1.9 K (-271.3 °C), colder than outer space. The superconducting coils of niobium-titanium (NbTi) are kept at those temperatures by a closed circuit of superfluid liquid helium.

Moreover, proton beams must travel along the accelerator without interacting with any other material that would cause scattering of the energy. Accordingly, LHC pipes are kept at ultra-high vacuum in the order of 10^{-10} to 10^{-11} mbar.

In the LHC, during Run 2, two 6.5 TeV proton beams collide every 25 ns for a total of 13 TeV collision energy, the highest in any accelerator ever built. Acceleration to top energies at the LHC is achieved using supercon-

ducting radio frequency (RF) cavity systems. Each beam travels through eight cavities made of niobium sputtered on copper performing at maximum accelerating voltage of 2MV at 400 MHz. These oscillating fields also tighten the proton beams into the up to 2808 discrete bunches that circulate inside the collider.

1.3.1 LHC Luminosity

Luminosity, often denoted by the symbol L, quantifies the number of particle collisions that occur in a given area over a specified period. It is expressed in units of inverse centimeters squared per second ($cm^{-2}s^{-1}$). High luminosity means a higher rate of collisions, which increases the probability of observing rare physical processes.

The number of events produced per unit time is described in equation 1.1:

$$N = L \cdot \sigma \tag{1.1}$$

where:

- N is the total number of events,
- L is the integrated luminosity, that is, total luminosity integrated during the data-taking period
- σ is the cross section of the process.

The integrated luminosity (L) is the total number of collisions that occur over a period, usually expressed in inverse femtobarns (fb^{-1}). It is obtained by integrating the instantaneous luminosity (L_i) over time as in equation 1.2. Higher integrated luminosity means more data, which is essential for making statistically significant discoveries.

$$L = \int L_i \cdot dt \tag{1.2}$$

Therefore, in order to maximize the probability of finding rare processes, with low cross section, it is imperative to have as high luminosity as possible. An example of the cross section of the different processes that can happen in the LHC is shown in Figure 1.3.

On the other hand, the instantaneous Luminosity L_i refers to the collision rate at a specific moment in time. It depends on factors such as the number of particles in each beam, their density, and the beam's focus at the interaction

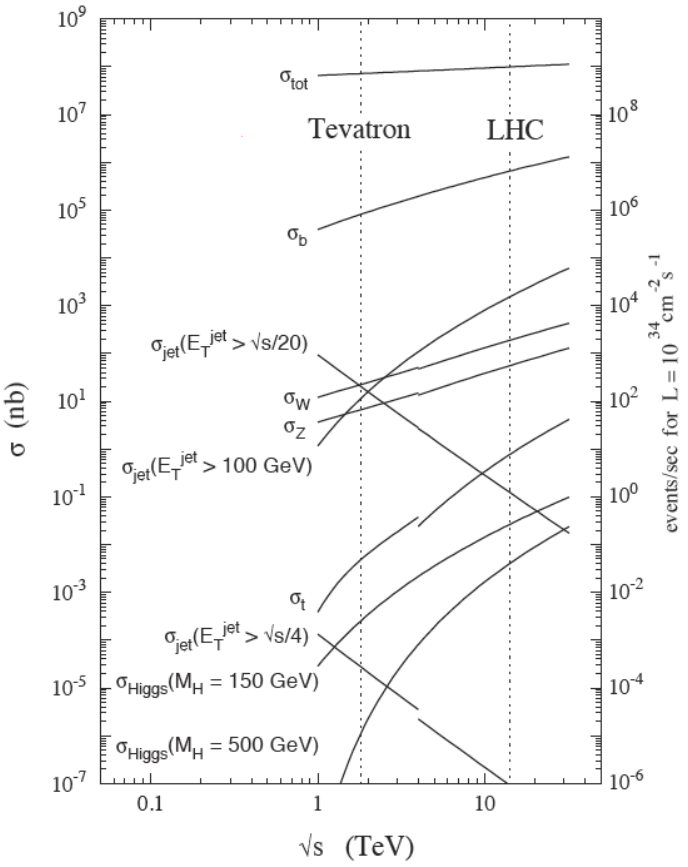

Figure 1.3: Cross Sections for specific physics processes, from the ATLAS TDR (2003) [6]. The dotted lines show the energies of two hadron colliders (the Tevatron at 1.96 TeV, and the LHC at 14 TeV).

points. It can be written for a Gaussian transverse beam profile distribution as in equation 1.3:

$$L = \frac{N_b^2 \; n_b \, f_r \; \gamma_r}{4 \; \pi \; \epsilon_r \; \beta^*} \tag{1.3}$$

where:

- N_b is the number of particles per bunch,
- n_b the number of bunches per beam,
- f_r the revolution frequency,

- γ_r the relativistic gamma factor,

- ϵ_r is the normalized transverse beam emittance, defined as the product of the RMS of the particles positions distribution, times the RMS of the particle momenta distribution. It gives an idea of the spatial and the momentum dispersion of the beam. This parameter is constant for all the beam life and the goal of the injection procedure is to introduce a beam with the lowest beam emittance in the collider.

- β^*, the beta function at the collision point. Contrary to ϵ_r, β^* can be reduced along the ring length, with dedicated magnetic optics which squeezes the beams in the Interaction Point (IP). Note that a lower β^* means a higher spread in the particle momenta.

The above expression assumes round beams with equal beam parameters for both proton beams. The exploration of rare events in the LHC collisions requires both high beam energies and high beam intensities. All these parameters and other design characteristics of the accelerator are summarized in Table 1.1.

Under nominal operating conditions, LHC had 2808 bunches in each beam, with around 10^{11} protons per bunch. The size of the bunch at the interaction points is approximately 16 μm which increases the probability of proton-proton collisions.

The LHC began operation in 2009 and has been operating since, alternating running periods and shutdowns to perform reparations or upgrades. Three running periods of several years have been gone so far, interleaved with two Long Shutdowns (LS).

Run 1 provided proton collisions at a centre-of-mass energy, $\sqrt{s}$, of 7 TeV in 2010 and $\sqrt{s} = 8$ TeV in 2011 and 2012. The Long Shutdown 1 (LS1) period (2013-2014) took place in order to update and upgrade the machine and increase its energy. In 2015 a new data-taking period started, Run 2, which increased the energy in the center of mass up to 13 TeV, providing collisions until 2018. After that, the Long Shutdown 2 (LS2) (2019-2021) took place, followed by a new era, Run 3, with collisions at $\sqrt{s} = 13.6$ TeV and expected to reach 14 TeV.

The design luminosity of the LHC was $10^{34}\ cm^{-2}s^{-1}$ but it soon became clear that increasing this value was relatively easily achievable, at least, easier than increasing the energy. Accordingly, a program for upgrading the LHC and its detectors was laid down as a way to increase the potential for discovery of rare particles and new phenomena. This program included several steps of upgrades that took place during the LS2 and allowed achieving more than a

Table 1.1: LHC Collider Main Parameters

Quantity	**Number**
Circumference	26 659 m
Dipole operating temperature	1.9 K (-271.3Â°C)
Number of magnets	9593
Number of main dipoles	1232
Number of main quadrupoles	392
Number of RF cavities	8 per beam
Nominal energy, protons	6.5 TeV
Nominal energy, ions	2.56 TeV/u (energy per nucleon)
Nominal energy, protons collisions	13 TeV
Time between collisions	25 ns
Bunch Crossing Rate f_r	40.08 MHz
No. of bunches per proton beam	2808
No. of protons per bunch (at start)	1.2×10^{11}
Number of turns per second	11245
Number of collisions per second	1 billion
ϵ_r	3.75 μm
Transverse beam size at IP5	16.7 μm
β^* IP5 beta value	0.55 m
Crossing angle	285 μrad
E_{stored} Stored energy	362 MJ
Design instantaneous luminosity	10^{34} cm^{-2}s^{-1}
Average number of collisions per crossing	20

factor 2 of the nominal luminosity. Next step is the so-called HL-LHC, which will be prepared during Long Shutdown 3 (LS3)and will allow achieving factor 5 instantaneous luminosities with respect to the nominal, and up to a factor 10 the integrated luminosity.

1.3.2 The CMS Experiment at the LHC

The CMS experiment is one of the two multi-purpose detectors operating at the LHC. It is located in an experimental cavern 100 m underground at the LHC point 5, near the french village of Cessy. The experiment has a cylindrical shape with a length of 21.6 m and a diameter of 14.6 m. CMS is approximately half the size of ATLAS but weighs twice as much, around 14000 tons, thus the word Compact in its name.

The central feature of the CMS apparatus is a superconducting solenoid of

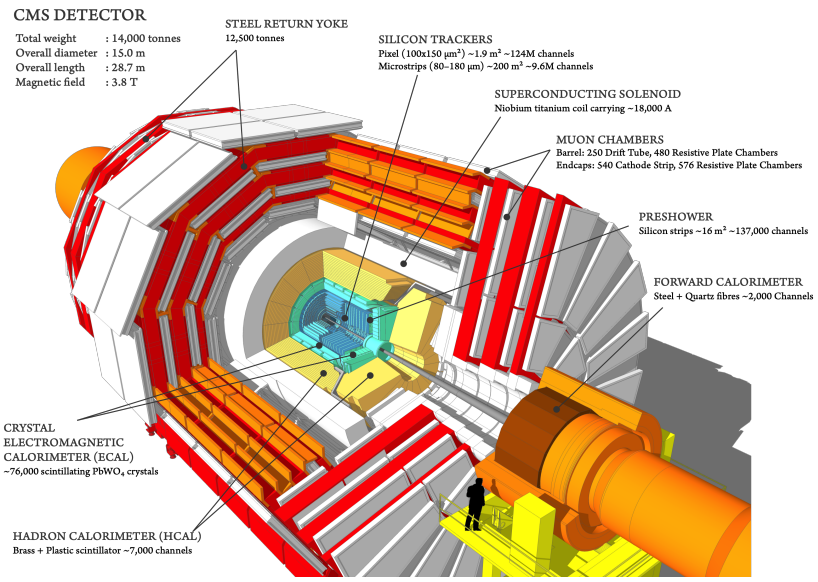

Figure 1.4: CMS layout and overall characteristics.

6 m internal diameter, providing a magnetic field of 3.8 T. The CMS magnet is made of a niobium-titanium superconducting solenoid operating at 4.5 K. The steel return yoke of the magnet serves as support for the chambers of the muon system.

Within the solenoid volume are a silicon pixel and strip tracker, a lead-tungstate crystal electromagnetic calorimeter, and a brass and scintillator hadron calorimeter, each composed of a barrel and two endcap sections. Forward calorimeters extend the coverage provided by the barrel and endcap detectors. Muons are measured in gas-ionization detectors embedded in the steel flux-return yoke outside the solenoid.

The CMS layout can be seen in Figure 1.4. The central zone called barrel is divided in five cylindrical slices called wheels, numbered from -2 to +2, with wheel 0 situated in the center around the interaction point. The barrel is surrounded on both sides by two endcaps.

First of all, we should define the coordinate system we are going to use throughout the document. The CMS detector is designed over a Cartesian right-handed system, with its origin centered at the nominal collision point as can be seen in Figure 1.5. The x axis points radially inward toward the center of the LHC and the y axis points vertically upward, defining the transverse x-y plane perpendicular to the beam direction. Therefore, the z axis points along the beam direction toward the Jura mountains from LHC Point 5 or

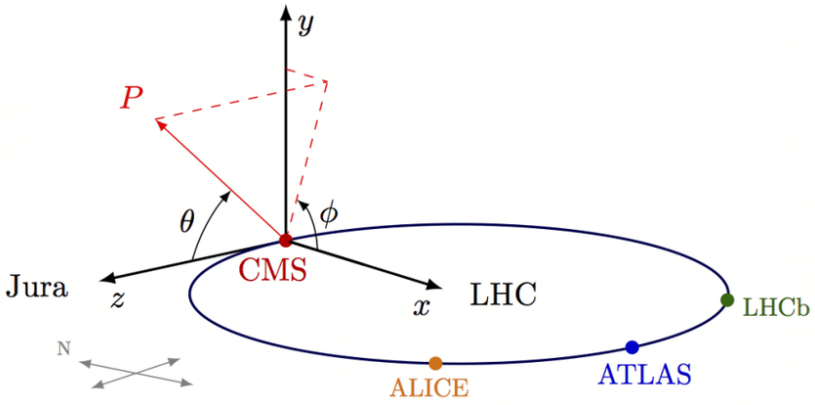

Figure 1.5: The CMS coordinate system.

counterclockwise in the geographical map. Moreover, the geometry of CMS encourages to define a set of cylindrical coordinates maintaining the z axis. We can then measure the azimuthal angle ϕ from the x axis in the x-y plane and the polar angle θ from the z axis. A more convenient notation for the polar angle is the pseudorapidity, defined as $\eta = -ln[tan(\theta/2)]$, where η is zero in the x-y plane and $\pm\infty$ in the beam axis, $\eta = 1$ corresponds to $\theta \simeq 40$ and $\eta = 2.5$ to 10.

If we define the transverse momentum of the particle as $p_T = \sqrt{(p_x^2 + p_y^2)}$, we can express the four vector of any particle using (E, p_T, η, ϕ) as well as (E, p_x, p_y, p_z) through the transformation:

- $p_x = p_T \cdot cos\phi$
- $p_y = p_T \cdot sin\phi$
- $p_z = p_T \cdot sinh(\eta)$.

The detector requirements for CMS design to meet the goals of the LHC physics programme are described as follows:

- Good muon identification and momentum resolution over a wide range of momenta and angles, good dimuon mass resolution ($\sim$ 1% at 100 GeV), and the ability to determine unambiguously the charge of muons with p $<$ 1 TeV;
- Good charged-particle momentum resolution and reconstruction efficiency in the inner tracker. Efficient triggering and offline tagging of τ's and b-jets, requiring pixel detectors close to the interaction region;

- Good electromagnetic energy resolution, good diphoton and dielectron mass resolution (∼1% at 100 GeV), wide geometric coverage, π^0s rejection, and efficient photon and lepton isolation at high luminosities;

- Good missing transverse energy and dijet mass resolution, requiring hadron calorimeters with a large hermetic geometric coverage and with fine lateral segmentation.

To comply with these requirements, the following detectors were designed and constructed:

The silicon tracker is placed in the innermost part of the CMS detector and it has been designed to provide precise measurements of the trajectories of charged particles produced in high-energy proton-proton collisions. It has a length of 5.8 m and a diameter of 2.5 m and is composed of multiple silicon layers which provide very high granularity and good spatial resolution. It consists of two main parts: the pixel detector, which is closest to the IP and provides the highest granularity, and the strip detector, which covers a larger area and provides additional tracking layers. This combination ensures that the tracker can handle the high particle densities typical of LHC collisions while maintaining excellent spatial resolution. It is made up of 3 pixel layers and 10 microstrips in the central region and 2 pixel layers and 9 microstrips in the low angle regions. Charged particles that cross the tracker volume deposit their energy while creating electron-hole pairs that drift to the electrodes creating a signal that can be measured. There are 67 million channels for the pixel detector and 10 million for the microstrip, distributed in an area of 220 m^2 silicon sensors with an average precision of around 20 μm.

The Electromagnetic Calorimeter (ECAL) is a critical component designed to precisely measure the energy of electrons and photons and is situated between the silicon tracker and the hadron calorimeter (HCAL) to ensure that it captures and measures the energy of electromagnetic particles before they interact with the denser materials in the HCAL. It is made of more than 75000 lead tungstate ($PBWO_4$) scintillating crystals. These crystals generate light when photons or electrons reach them and that scintillation light is collected by photodetectors glued to the back of each of the crystals. The amount of light produced in the crystals is directly proportional to the energy of the incoming particle, allowing for precise energy measurements. To maximize its performance, the ECAL is divided into several sections: the barrel (EB), which surrounds the beam pipe in a cylindrical layout, and the endcaps (EE), which cover the detector's ends. Additionally, there is a preshower detector (ES) in front of the endcaps to improve photon identification and provide further energy resolution. The high granularity of the

ECAL ensures excellent spatial resolution, allowing for precise determination of the position and energy of particles.

The Hadron Calorimeter (HCAL) measures the energy of hadrons such as protons, neutrons, and pions, produced in high-energy proton-proton collisions. HCAL provides precise measurements of hadronic energy, which is essential for reconstructing the energy and momentum of jets (clusters of particles resulting from quark and gluon fragmentation). This capability is critical for identifying and analyzing complex events, such as those involving top quarks or potential signals of new physics. The HCAL is structured into several layers of dense absorber material, such as brass or steel, interspersed with active plastic scintillator layers. When hadrons pass through the HCAL, they interact with the dense absorber material, creating a shower of secondary particles. These secondary particles then pass through the scintillator layers, which emit light in response to the energy deposited by the particles. Photodetectors collect this light and convert it into electrical signals, which are then used to calculate the energy of the incoming hadrons. The HCAL is divided into four main sections: the Barrel HCAL (HB), the Endcap HCAL (HE), the Outer HCAL (HO), and the Forward HCAL (HF). The HB surrounds the ECAL in a cylindrical arrangement, while the HE covers the regions at the ends of the barrel. The HO is situated outside the solenoid magnet, providing additional detection capabilities for particles that escape the inner calorimeters. The HF, located at the extreme forward and backward regions of CMS, is designed to detect particles produced at small angles to the beam line, capturing information about highly energetic collisions.

The Muon detectors [9] of the CMS experiment are an essential component designed to identify and measure the properties of muons. Muons are particularly significant in particle physics because they can penetrate deep into matter without interacting much, while at the same time they are heavy charged particles which can leave a track in the detectors, making them crucial for studying high-energy collisions in particle physics. Many of the processes that LHC aims to study, including the Higgs boson decay, have muons in their final state. The cleanest channel for the Higgs boson is it's decay in two Z^0 bosons, each of them decaying in two opposing charge muons. Therefore, muon detectors are an essential part of CMS and a robust and redundant system with precise tracking capabilities and large coverage was designed.

Muon identification is guaranteed due to the calorimeters and the iron yoke which provide sufficient containment for hadronic showers with a thickness of 11.8 interaction lengths (λ) and filter all particles except muons and

neutrinos, which pass undetected. Charge and momentum measurements take advantage of the curvature of the tracks due to the magnetic field present.

There are three different muon sub-detectors installed in CMS which are organized into two main regions the barrel and the endcaps ensuring comprehensive coverage of the entire detector. Drift Tubes Chambers (DTs) are used in the barrel, up to $|\eta| < 1.2$, where the background rate is low and the magnetic field homogeneous. DTs are described in detail in the following section.

The endcaps, $0.8 < |\eta| < 2.4$, are instead equipped with Cathode Strip Chambers (CSCs), chosen to cope with the high particle flux and non uniformity of the magnetic field. CSC are proportional chambers consisting of a gaseous volume between two cathodes, one of them segmented in aluminum strips. Perpendicularly there is a series of wires acting as anodes. When a charged particle ionizes de gas, the resulting positive ions drift towards the cathodes, while the electrons drift towards the anode. Near the wire, an electron avalanche is produced, which induces a signal distributed along the cathode strips, thus providing a measurement of both coordinates describing the movement of the muon. Each CSC is trapezoidal in shape and consists of 6 gas gaps, each gap having a plane of radial cathode strips and a plane of anode wires running almost perpendicularly to the strips.

All CSCs, except those in the innermost station, are overlapped to avoid gaps in the muon acceptance. There are 36 chambers in each ring of a muon station, except for the innermost rings starting from the second station which have 18 chambers. Information about the position of the incoming particle is collected both in the anode wire and on a group of finely segmented cathode strips. The latter allows to perform centre of gravity measurements ensuring high position resolution, while the former is characterized by a fast signal suitable for trigger purposes. The resolution measurements with the strips varies from approximately 70 μm for the innermost stations to approximately 150 μm for the outermost ones, while r can be determined with a precision of approximately 0.5 cm.

Both CSC and DT are complemented by specific trigger detectors called Resistive Plate Chambers (RPC), which provide coarser position information but excellent temporal resolution ($\sim$2 ns) and are used as a redundant system to ensure a robust trigger.

RPC chambers consist of two planes of high resistivity material separated by 2 mm of gas. The plates are covered in the external side by graphite electrodes that generate a strong electric field inside the gas by applying a voltage around 9 kV. When a particle crosses the gas volume an electron

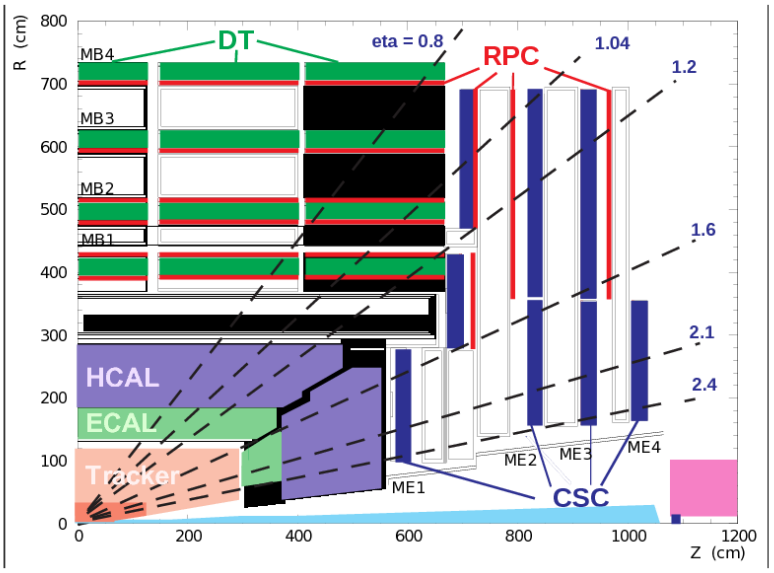

Figure 1.6: Longitudinal cut of a quarter of the CMS Muon spectrometer as originally designed.

avalanche is produced and the associated electric signal is collected by strips placed in the external part of the electrodes.

A total of 6 layers of RPCs are embedded in the barrel muon system, 2 in each of the first 2 stations, and 1 in each of the last 2 stations. The redundancy in the first 2 stations guarantees that the trigger algorithm works even for low p_T tracks, that may not reach the outer 2 stations. In the endcap region, there is a plane of RPCs in each of the first 3 stations in order for the trigger to use the coincidences between stations to reduce background, to improve the time resolution for bunch crossing identification, and to achieve a good p_T resolution at trigger level.

In order to cover all possible events, the muon spectrometer needs very high acceptance and redundancy. To achieve this, the muon sub-detectors are distributed as can be seen in Figure 1.6.

The final piece of the CMS experiment is the trigger and Data Acquisition System (DAQ). This system is designed to select the most interesting events ensuring high data recording efficiency for a wide range of physics objects and events topologies, while applying online selective requirements to reduce the incoming 40 MHz event rate to an output rate of about 100 Hz, allowing the permanent storage of the events.

The CMS trigger system reduces the event rate in two steps: the Level 1

(L1) and the High Level Trigger (HLT) algorithms. The former is designed to achieve a maximum output rate of 100 kHz and consists of custom-designed, programmable electronics while the HLT is based on software algorithms running on a large cluster of commercial processors, the event filter farm.

The L1 trigger system uses only coarsely segmented data from the muon system and the calorimeters while the full granularity data are stored in the detector frontend electronics waiting for the L1 decision (L1A, Level 1 Accept). This has to be taken within a latency time of 3.2 μs, that is, after 128 bunch crossings and is based on the decision of local, regional and global trigger components. If the event is accepted, a trigger signal L1A is sent to all the the data acquisition electronics on CMS which has been storing the full detector data in the meantime. This validated information of the corresponding event is then transferred to the Data Acquisition (DAQ) chain, that is, the HLT.

The full detector information ($\sim$1 MB) is read out by the Data Acquisition (DAQ) system at a rate of up to 100 kHz, considering that the average size of an event is approximately 1 Mbyte, the data storage rate reaches values around 1 Terabyte per day. The HLT has access to the complete read-out data and can perform complex calculations similar to those made in the offline analysis software. The Trigger menus are composed of a set of trigger paths, each path addressing a specific physics object selection.

1.3.3 The CMS Drift Tube Chambers

The DT chambers are used in the barrel region of the CMS detector for muon identification, triggering and precise muon trajectory reconstruction.

The muon barrel detector contains 250 DT chambers arranged inside the magnet return yoke of CMS. They are subdivided in the 5 iron barrel wheels. Every wheel consists of four concentric rings of chambers, called stations and named respectively MB1/2/3/4, where MB stands for Muon Barrel. Each ring is segmented in 12 azimuthal sectors, each one covering an angular region of 30°. Thus, each ring contains 12 DT chambers with the exception of MB4 which consists of 14 of them, as can be seen in Figure 1.7.

The basic detector element is a rectangular drift cell with a transversal size of 4.2 cm x 1.3 cm and a variable length between 2 and 4 meters, depending on the position in the CMS barrel. DT chambers are filled with a 85%/15% Ar/CO2 gas mixture.

The cell is delimited by aluminum (Al) beams on the sides where cathodes are located and aluminum plates on the top and bottom and Al plates delimiting each of the detection layers. Attached to these plates through a

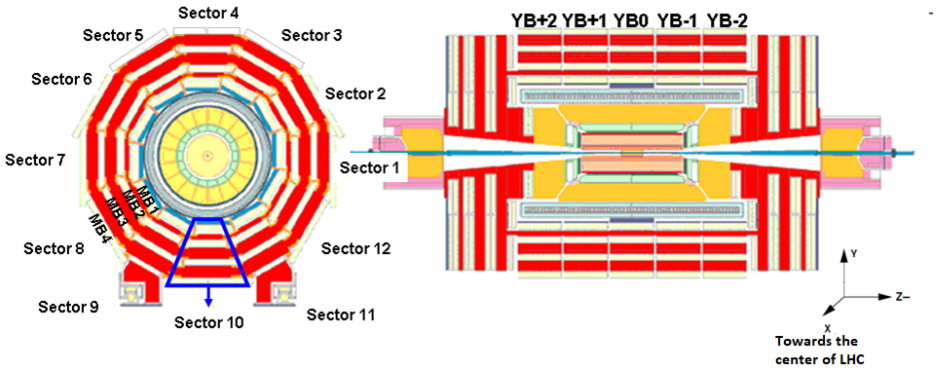

Figure 1.7: Cross-sectional and longitudinal view of CMS with the subdivision into wheels and sectors.

mylar insulation, aluminum strip electrodes shape the electric field to achieve constant drift velocity along the cell [9].

Inside each of these cells there is a 50 μm diameter gold-plated steel wire that acts as the anode. The standard operating voltage for the anode, cathode and strips are +3600 V, -1200 V and +1800 V respectively.

DT cells form layers, and stacks of four layers, staggered by half a cell, are assembled to form a Superlayer (SL). A DT chamber is made of a block of two SLs measuring the ϕ coordinate plus one SL measuring the z or θ coordinate. The only exception to this rule applies to the MB4 stations where only the two ϕ SL are present. A schematic layout of a single DT chamber is shown in Figure 1.8 and a sketch of a full constructed chamber can be seen in Figure 1.9. The total number of sensitive cells is around 172000.

When a particle passes through the chamber it ionizes the gas and the resulting electrons and ions move towards the anode and cathode respectively. Close to the anode, electron avalanches are generated and the multiplied charge induces a current pulse in the electrodes and results in an electric signal that is processed by the electronics of the detector.

The main advantage of the chamber is that, at a given electric field and pressure, the drift velocity is constant in the gas volume and, therefore, the position of the particle when it crossed the detector can be obtained from the value of the time information of the received hit.

The operating drift velocity is 54.3 μm/ns which gives a maximum drift time of 400 ns, much larger than the time between bunch crossings. The single cell time resolution is of the order of 4 ns.

The muon trajectory can be reconstructed by fitting the hits from each SL

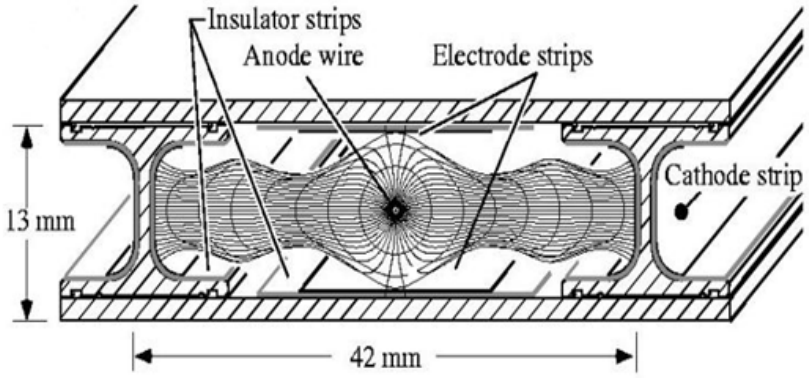

Figure 1.8: Diagram of a transversal section of a DT cell where the electrodes and the field lines can be seen.

into track segments. In the offline reconstruction, where the bunch crossing from which the muon came from is known, the procedure is rather straight forward. Each hit's time information gets corrected to represent only the drift time, which can be translated to drift distance through the constant drift velocity. The main uncertainty is the laterality of the hit with respect to the anode wire. In general, all combinations are exercised and the track that produces a fit with the smaller χ^2 error is selected.

As mentioned before, the DT system is used also for triggering muons, which means, that out of the hits information, not only the track needs to be reconstructed but also the bunch crossing needs to be assigned unequivocally. Therefore, not only the laterality but also the time of the arrival of the muon is used as a free parameter. The uncertainty in the time of the hit is large, as can be deduced from the fact that the drift time in each cell can correspond to up to 16 LHC bunch crossings. When the good time is used, the hits are aligned into a straight track, but several ghosts tracks can be created in the process. The DT trigger system needs to perform this reconstruction and provide the correct bunch crossing of the event in real time (total CMS Trigger latency needs to be smaller than 3 μs).

From the offline system, the target chamber resolution is 100 μm in the r-phi plane and 150 μm in the z direction. This is achieved by 8 track points measured in the two (r-phi) SL, provided the maximum deviation from linearity of the cell space-time relation be less than 100-150 μm and being the wire resolution better than 250 μm. This can be achieved if the DT cell time resolution is $\sim$4 ns. A precise alignment system is used in CMS

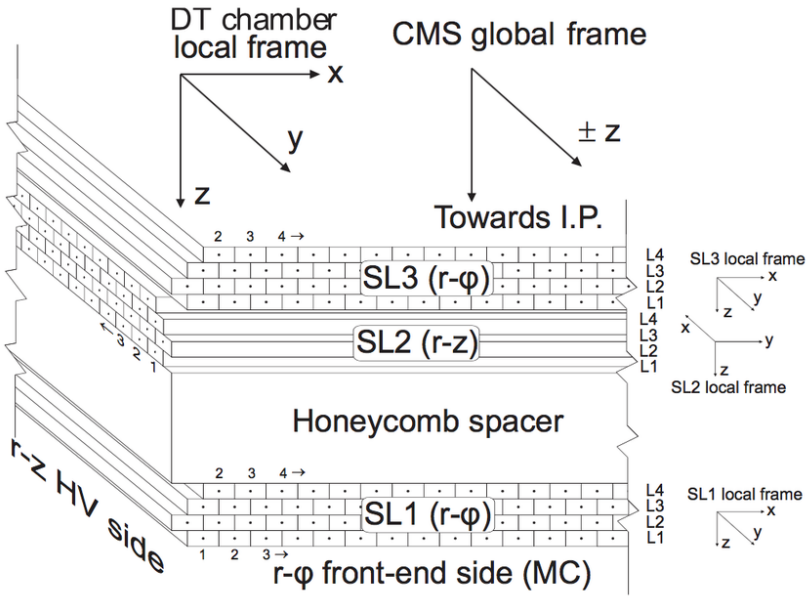

Figure 1.9: Schematic view of a DT chamber with the two outer Superlayers that measure the ϕ coordinate and the inner Superlayer that measures the θ coordinate. The staggering of cells between layers allows to discriminate which side of the wire the track went through.

as a way to ensure a well known position of all the DT chambers and its relation to the tracker.

1.3.4 Electronics of the DT Chamber

1.3.4.1 High Voltage distribution

The High Voltage system of the DT chambers is based in the CAEN SY4527 [10] universal multichannel power supply system. The final modules are the CAEN A877 modules that power the anode, cathode and strips of each cell. All cathode and strips of each DT layer (between 50 and 100 DT cells per layer) are connected to a single channel of the A877 power supply, while the anode wires are split in two channels named Wire 0 and Wire 1. In the smaller MB1 and MB2 chambers, which are the ones chosen to be irradiated, as will be described later, Wire 0 wires are the ones from cell 1 to 32 while the rest go to Wire 1.

1.3.4.2 DT FEB: Front-End Board

The signals coming from the wires are processed by the Front-End Boards (FEB), which are built around the MAD ASIC designed by the INFN Padova [11]. The FEB conditions the signals through an analogic process of amplification and threshold comparison so the output is a logic signal that can be sent to the nearby trigger and readout electronics.

Analog signal processing must use a short shaping time to achieve a high spatial resolution while introducing minimal noise; this allows low-gain operation of the drift tubes, thus improving reliability and chamber lifetime.

In order to get response times independent from the amplitude of the signals as well as uniformity across the different channels, the comparator must be fast and precise. Channel masking functionality was required to avoid performance issues due to noisy channels. The resulting custom front-end application specific integrated circuit chip (ASIC), named MAD, was developed using 0.8 mm BiCMOS technology with a total power consumption of 100 mW (25 mW/ch).

Each analog chain at the MAD begins with a charge preamplifier that uses a single gain stage, folded/unfolded cascode, having a Gain-Bandwith product (GBW) in excess of 1 GHz (result from simulation). For the analog section an average gain of about 3.4 mV/fC is obtained with $(1850 \pm 60)/pF$ electrons of noise. The feedback time constant is 33 ns while input impedance is approximately 100 ohms in the range 5-200 MHz, to match the DT cell one. The dead time of the FEB is around 150 ns, which should be acceptable. The rate capability of the MAD ASIC largely exceeds demand: 800 fC charge pulses (just below saturation) at 2 MHz rate do not affect the efficiency in detecting 5 fC interleaved signals, so there is a wide safety margin with respect to the total rate (about 10 kHz) expected per drift tube during CMS operation.

The output driver is also very fast, and delivering differential levels (pseudo-LVDS [12]) that minimize mutual interferences and can be transmitted through low-cost cables.

1.3.4.3 Legacy DT Readout system

The DT read out system [13] is organized in several levels, merging data from all chamber channels to the CMS global DAQ system in the control room.

The ROB (Read Out Boards) are the first level of the CMS DT chambers data acquisition system. They are responsible for the time digitization of the incoming chamber signals in order to allow further reconstruction of charged particle tracks. The ROB boards, designed and developed at CIEMAT, re-

ceive the 50 ns pseudo-LVDS signals coming from the FEB electronics, store them in internal buffers and measure its time of arrival with respect to the Level 1 Accept signal.

ROBs are built around a 32-channel HPTDC ASIC [14] developed by the CERN EP/MIC group. This device supplies the basic time elements to reconstruct muon tracks, that is, the relative time to a common trigger for every hit produced on chamber wires. One of its main advantages is its multi hit capability and its high programmability. ROBs are located inside the so-called Minicrate, attached to the DT chambers. The Minicrates are aluminum structures supporting the on-detector DT electronics and cool them through conduction to embedded circulating water. They host up to 17 boards per chamber together with a large number of interconnecting cables. The system is complex and has a relatively large power consumption (up to 100 W per chamber).

Each ROB performs the time digitization of 128 chamber channels. Between 3 and 7 ROB boards are installed per Minicrate in order to perform the full read out of one DT chamber, totaling 1500 ROBs in the system.

The output signal from the ROBs is through a copper LVDS cable that transmits its digital data through a 240 Mbps National Instruments serializer (DS92LV1021 [15]) to the next level of the data acquisition chain, which originally was made out of the Read Out Server (ROS) boards in the CMS wheel's tower racks. As the LHC instantaneous luminosity increased, the ROS boards needed to be extracted from the CMS cavern and they were replaced by some custom copper to optical converters that could extend the ROB transmission link for another 60 meters up to the counting room. There, a new electronics, so-called, uROS system, receives the ROB information, merges it into event fragments and sends it to the CMS global DAQ.

The uROS board is based in a common design with the second level of the CMS DT Phase 1 upgrade Trigger system. A common uTCA-based board called TM7 [16] was developed by INFN for the DT trigger (TwinMux) and readout (uROS) second-level electronics upgrade. The TM7 is a single-slot double-width and full-height Advanced Mezzanine Card (AMC) [17] based around a Xilinx Virtex-7 FPGA [18] that includes optical transceivers for slow-speed inputs and high-speed data transmission up to 13 Gbps. Different firmwares were developed by different groups to implement either the readout or the trigger functionality. The uROS boards receive the 1500 readout links from the ROB boards at UXC, process the data in Virtex-7 FPGAs, and deliver it to the DAQ system through the AMC13 boards [19]. They contain up to 72 optic fiber input links (grouped in 12-fibre MTP connectors) routed to general input/output pins of the FPGA. The readout links are 240 Mbps

pseudo DC balanced following DS90LV1021 protocol. Specific deserialization has been implemented to ensure reliable data reception. The uROS system was installed in 2017 to cope with the increased luminosity expected in Run 2 and Run 3, and in order to solve the slow processing capability of the original ROS boards in view of the luminosity increase.

1.3.4.4 Legacy DT Trigger system

The electronics of the DT local trigger consists of four basic components: Bunch and Track Identifiers (BTI), Track Correlators (TRACO), Trigger Servers (TS) [20], all of them assembled together with the ROB boards inside the Minicrates.

The ROB boards transfer the hit signals to the BTIs, mounted on the Trigger Boards (TB) where they reconstruct SL track segments, assigning a candidate bunch crossing. The association of hits is based on a mean-timer technique [21], which uses the fact that there is a fixed relation between the drift times of any three adjacent planes. These tracks are transferred to the TRACO ASIC which correlates the tracks from both phi SLs. If a correlation can be found, the TRACO defines a new segment, enhancing the angular resolution and producing a quality hierarchy. TRACO segments are sent to the TS, whose purpose is to perform a track selection in a multitrack environment and forward it through a copper link at 480 Mbps through the National Instruments serializer (DS92LV1021) to the CUOF boards in the balconies and from there, through optical fiber, to the TwinMux boards in the control room.

The TwinMux boards are also TM7 boards but with a different firmware for the reception of both the DT trigger links and the RPC links. The TwinMux board primary role is to achieve the merging of several 480 Mb/s trigger links to higher speed serial links and compensate delays to provide BX alignment of the trigger data coming from the different inputs. The Twinmux arranges and fans-out the slow input optical links coming from the TRBs into faster links (10 Gbps) to the next level of the CMS Trigger chain, the BMTF (Barrel Muon Track Finder) [22]. The BMTF is in charge of fitting the DT segments to track trajectories and assigning a transverse momentum to the muons. Additionally, the TwinMux implements the Superprimitives algorithm to enhance the DT trigger primitives with the use of the RPC hits information.

The DT system has been operating satisfactorily throughout the years in the different running periods. The amount of dead channels $<1\%$ and the dead time during data taking has been basically insignificant. It has been a very robust system, as expected from construction and the different

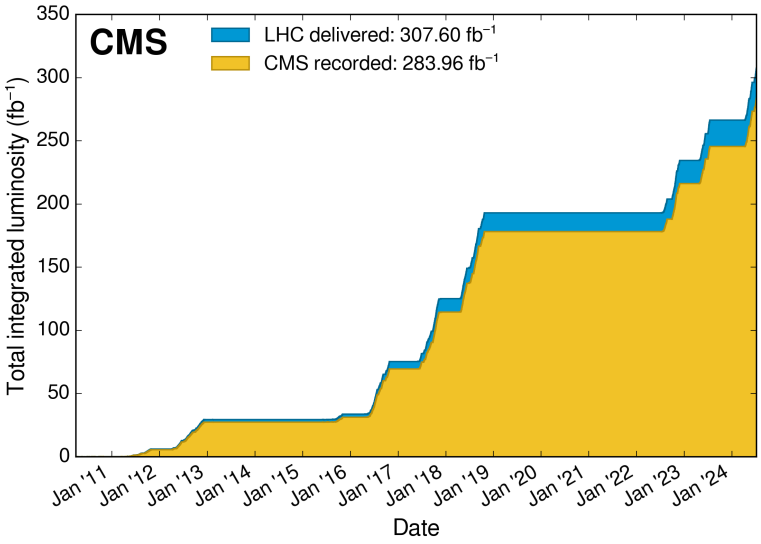

Figure 1.10: Integrated luminosity delivered and recorded by CMS up to mid 2024

upgrades have performed very nicely. The total luminosity accumulated so far at CMS is $\sim$285 fb^{-1} as can be seen in Figure 1.10 and the expectation is that the DT detector can continue taking data so satisfactorily during all the HL-LHC period.

Chapter 2

Radiation hardness of the CMS Drift Tubes in HL-LHC

Providing an answer to the reliability of operation of the Drift Tubes detector for HL-LHC requires understanding the impact that the radiation will have both on the detector and its electronics. In this chapter the present knowledge on this field is summarized, focusing on its impact in our particular detector. Moreover, the knowledge of the radiation field present nowadays at CMS during LHC will be used to estimate the future environmental conditions and also, estimate detector performance at HL-LHC. These studies have helped shape the definition of the upgrade program for the Drift Tubes detector and this upgrade program baseline plan will also be summarized.

2.1 High Luminosity LHC

The LHC project was designed to accumulate a total integrated luminosity of 300 fb^{-1}. The various upgrades throughout the years, will allow to increase this number up to 500 fb^{-1} by the end of the present Run 3 (2022-2025). To extend the sensitivity for new physics searches, a major upgrade is being built, HL-LHC. The HL-LHC aims to achieve an instantaneous luminosity of $5 \times 10^{34}\ cm^{-2}s^{-1}$ initially and up to $7.5 \times 10^{34}\ cm^{-2}s^{-1}$ later in its operation. Integrated luminosity is expected to reach up to 4000 fb^{-1} over its lifetime, a tenfold increase with respect to the original LHC's design. The center-of-mass energy for proton-proton collisions is expected to be raised from the current 13.6 up to 14 TeV.

This upgrade programme is necessary to fully exploit the physics potential of the LHC. Many search channels are statistics limited and their sensitivity will increase with the integrated luminosity. For many proposed scenarios,

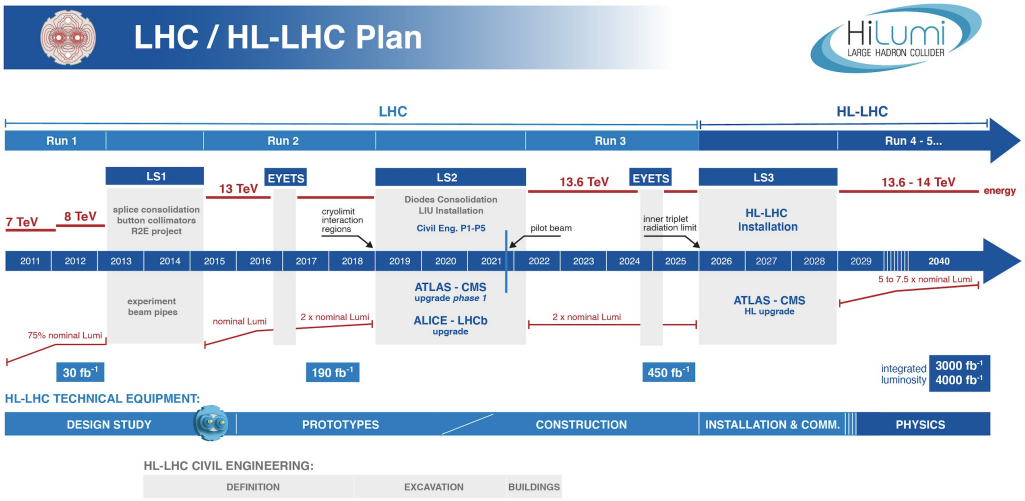

Figure 2.1: Timeline for the LHC and High-Luminosity LHC

including Supersymmetry and new heavy gauge bosons, the attainable mass range can be improved at HL-LHC to at least one TeV. The properties of the discovered Higgs boson will be measured with higher precision, which will allow searches for new physics associated with the Higgs sector. Also the accuracy for many SM tests will improve dramatically; in particular, the sensitivity to rare processes increases linearly with luminosity. The searches for new physics will be extended to exotic models, with challenging signatures from the experimental point of view: long-lived particles decaying leptonically, final states with low p_T muons, heavy slowly moving charged particles, or highly boosted dimuons, requiring improved muon detection and trigger capabilities.

To achieve this luminosity increase, several elements in the LHC collider need to be upgraded. Stronger superconducting magnets will be needed to increase the collision rates, including quadrupole magnets with a higher magnetic field to focus the proton beams more tightly at the collision points. Special radio-frequency cavities, known as crab cavities, need to be installed to tilt the proton bunches as they collide, ensuring more head-on collisions and thus higher luminosity. These modifications of the machine will take place during the LS3 technical stop that is planned for 2026-2029, resuming operation in 2030. The LHC schedule can be seen in Figure 2.1.

This increase of luminosity has important consequences on the LHC detectors requiring substantial upgrades and innovations. Higher luminosity

results in a greater number of proton-proton collisions per second, leading to a denser particle environment. This increase in the particle rate implies:

- Radiation damage on the detectors: the integrated dose that will be received by the detectors will be ten times larger, and not all materials and detectors have been designed to stand these doses. Accordingly, material radiation tolerance needs to be assessed and the performance of the detectors needs to be verified at the expected doses.

- Radiation damage on the electronics: Similarly, the electronics systems performance that are located inside the experimental cavern need to be verified for the new doses and for the expected fluxes, which, even in the absence of accumulated damage, can suffer a failure rate which makes them non-operational.

- Higher occupancy: the increased particle rate will manifest as an increase of both the signals and the noise in the detectors. The signal to noise ratio in the detectors needs to be maintained, no dead time effects need to be ensured and the buffers in the different parts of the electronic chains as well as the bandwidth of the communication links have to be increased.

- Pile up: the luminosity increase will not be accompanied by an increase of the LHC clock, but instead through better focusing and larger currents injection. Accordingly, the number of bunch crossings is expected to be the same but the amount of collisions expected on each bunch crossing will be larger. This is known as pile-up and implies that on each bunch crossing, the number of events that may need to be reconstructed will increase significantly from the present 45 events up to 200 events.

- Trigger system implications: The trigger system, responsible for deciding online which collision events to record, must be significantly enhanced to manage the increased data rates and event complexity. The new system will incorporate more sophisticated algorithms and greater processing power to ensure that interesting events are captured efficiently despite the higher background noise. The planned L1A rate will increase from present 100 kHz to a peak of 750 kHz and the amount of time allowed for taking the L1A decision needs to be enlarged from 4 μs to 12.5 μs. These changes have profound consequences in all of the CMS electronics chain, implying a replacement of most of the systems.

2.1.1 CMS Phase 2 at HL-LHC

To withstand the challenging environmental conditions in HL-LHC, maintaining equivalent physics object performance, all of the CMS subdetectors need to go through an intense upgrade program. This upgrade program is called Phase 2 Upgrade. The details are described here [23] but they can be summarized as:

Firstly, the inner tracker of CMS will be entirely replaced with a more advanced silicon-based system. The upgraded tracker will provide more precise measurements of particle trajectories, helping to improve vertex reconstruction and particle identification, even in the presence of higher levels of pile-up events. Additionally, the new tracker will have extended coverage in the forward region, enhancing the detector's overall efficiency and will include the possibility to participate with the outer layers in the Level 1 trigger, greatly enhance the p_T measurement at the trigger level.

A MIP (Minimum Ionizing Particle) Timing Detector (MTD) will be installed, providing timing information for minimum ionizing particles, enhancing the ability to distinguish between closely spaced collision events and improving overall event reconstruction and particle identification under pile-up.

Both ECAL and HCAL will undergo significant enhancements to maintain its performance under higher radiation and particle flux conditions with particular emphasis to the replacement of the full HCAL endcap region by the so-called HGCAL (High Granularity Calorimeter). HGCAL features high spatial and temporal resolution through the use of finely segmented silicon sensors and scintillators. This will allow for precise energy measurements and detailed 3D imaging of particle showers using particle flow techniques.

Finally, the Muon System will see the addition of new gas detectors, such as Gas Electron Multipliers (GEMs) which will be installed to extend the coverage in the most forward region, particularly the ME0 detector that will cover the pseudorapidity range $2.03 < |\eta| < 2.80$ which is not covered by any muon detector so far. In the pseudorapidity range $1.80 < |\eta| < 2.40$, presently covered only by CSC chambers, improved Resistive Plate Chambers (iRPCs) with better timing resolution will be installed increasing the redundancy.

For the DT system in the barrel, extensive studies have been performed (some of them reported in this thesis), to understand which parts of the system will need replacement. Several items need to be taken into consideration, being one of the more relevant the radiation damage both in the detector and its electronics.

2.2 Expected background radiation at CMS

As mentioned, the radiation damage of the detectors and its electronics is a critical aspect for the operation under HL-LHC that needs to be addressed. As a starting point, it is important to gain knowledge on the expected radiation environment.

High-energy experiments are exposed to the adverse radiation environment that results from the interactions, with surrounding materials, of particles produced by high rate collisions of incoming beams with target or head-on collisions of particle beams at high luminosity. As a result, a varied energy spectra of all different types of radiation (charged and neutral hadrons, electrons and photons) are present in the experimental cavern going through all the different processes of radiation interacting with matter. Since most of the radiation originates at the interaction point (IP), there is a clear dependency on the particle spectra with the distance to the IP.

High-energy particles from the IP begin to cascade when entering the material of surrounding detectors. If the material is thick, the cascade development will continue until most of the charged particles are stopped. Particles backscattered from the calorimeters and cascades leaking out the calorimeters produce neutrons, photons and electrons through their interactions with surrounding material and equipment located in the experimental hall. While electromagnetic cascades are rapidly absorbed, neutrons will travel long distances losing their energy gradually. Therefore, the neutron fluence dominates the radiation environment at larger radii and long times from the collision. Nuclear capture of thermal neutrons frequently results in the production of photons. Large amounts of photons also result from excited-state decay of spallation products and from fast neutron interactions with atomic nuclei. Photons, produced deep inside the material, are rapidly absorbed. Only photons, produced close to the surface of material, have a chance to produce electrons and positrons and are responsible for a low-energy electron component in the environment. As some of the particles or excited nuclei have long decaying times, this mixed field of neutrons, photons and electrons constitutes a background with no time structure. The numerous scatterings of neutrons and photons before their capture yield a uniform and isotropic field of low-energy background particles. The radiation type, energy and level induced on detector material and equipment will depend on the position of the detector with respect to the collision point and creates activation of materials at the regions closer to the IP.

Appart from the background of particles coming from the IP, at the CMS detector there is also a very large particle flux due to energetic particles gen-

erated at high eta (i.e. close to the beam line) in the region between the Hadronic Forward calorimeter (HF) and the Target Absorber Secondaries (TAS). In the present CMS design, the Forward Shielding is designed to reduce the flux of these particles, whilst allowing access to the beam-pipe components whenever needed for maintenance or repair activity. This important shielding is made of the called Fixed Iron Nose (FIN) and a double-hinged rotable element (the Rotating Shielding). Still, there is a large amount of background noise present in the outermost layers of the detector which has been proved to be coming from this region. Shielding materials would have to be added to the present shielding to suppress most of the existing background noise. Yet the mechanism of the Rotating Shielding has reached its loading maximum capacity and other integration aspects prevent any substantial improvement to the present Forward Shielding. In addition, from Run 4, when High Luminosity LHC will be in operation, the background noise will dramatically increase, if no action is taken.

Overall, the radiation field that can be encountered inside the CMS experimental cavern differs from space applications, radiation protection, medicine, etc. This complex radiation field is composed of charged hadrons and leptons, neutrons and photons, being the large flux of high energy neutrons an intrinsic characteristic of the LHC. Extensive simulations have been performed in the past to study the expected radiation field, and some details can be seen in Figure 2.2. These Fluka [24] Monte Carlo simulations allow obtaining a first and coarse information regarding the Total Ionizing Dose (TID) and the time-integrated particle flux per unit surface also called the particle fluence, both of them with undesired effects in the detectors.

As it is to be expected, the radiation expected in the area where the DT detector is located is expected to be low, particularly compared with the other subdetectors. This has opened the door to using technologies that are not intrinsically radiation hard, although the necessity of testing becomes even more critical. The expected fluxes from these Fluka simulations in the area of the DT chambers can be seen in Figures 2.4a and 2.4b. The total dose expected in the region of the DT chambers throughout the 10 years of HL-LHC operation can be seen in Figure 2.3

In addition, the energy spectra of the different particle types observed in different locations inside the CMS detector has also been simulated, taking into account the different material's composition and volumes in the detector. The results are shown in Figures 2.5 and 2.6. The neutron spectrum ranges from 1 GeV down to 1 MeV and is characterized by three peaks and a rather flat plateau between the second and third peak. Starting at the high energy end of the spectrum, the first peak, around 70 MeV, corresponds to the

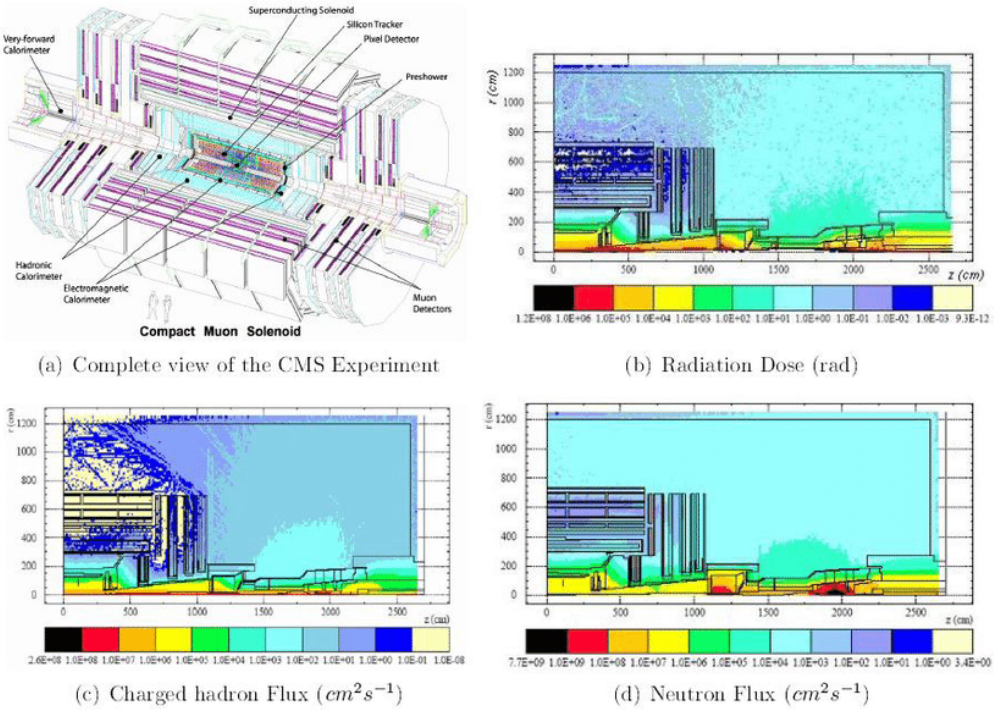

(a) Complete view of the CMS Experiment

(b) Radiation Dose (rad)

(c) Charged hadron Flux ($cm^2 s^{-1}$)

(d) Neutron Flux ($cm^2 s^{-1}$)

Figure 2.2: Radiation Field inside the CMS Experiment. A complete view of the CMS experiment is illustrated in (a). The dose map (b) has been determined for 10 years operation of the machine while charged hadrons (c) and neutron (d) fluxes have been calculated for normal operational conditions [25].

minimum in neutron-nucleus cross section, where the neutron absorption in the calorimeters and iron yoke is lowest, we will call these the fast neutrons. The second peak is broad and consists of several resonances, it ranges from 10 keV to 1 MeV and is likely due to resonances in the scattering cross section. The third peak is located at 0.03-0.050 eV, which corresponds to the thermal limit (293 K = 0.025 eV). The nearly flat plateau towards the thermal limit is due to very slow energy loss of non-thermal neutrons since they only scatter elastically. It is interesting to note that the spectra of the neutron, photon, and electron/positron species are very similar in the different locations in the muon spectrometer, except for the MB4 chambers, where the peak of fast neutrons (10-100 MeV) is absent. This prediction from simulation indicates that, although very few neutrons are created at this location, the detectors are still within a gas of low-energy neutrons created elsewhere.

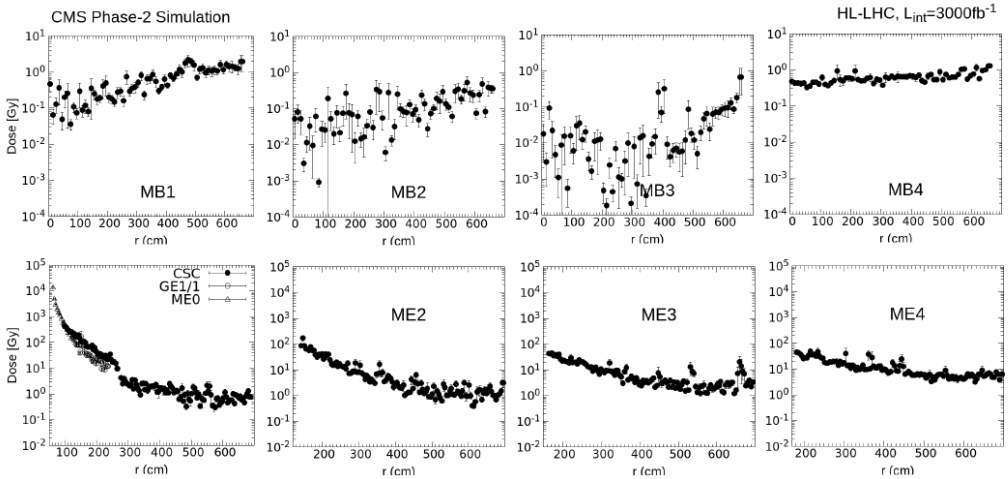

Figure 2.3: Absorbed dose estimated for different muon stations in central and forward part of CMS detector using FLUKA simulations of proton-proton collisions at 7 TeV per beam with a Phase 2 geometry model. Results are normalized to an integrated luminosity of 3000 fb^{-1} assuming an inelastic scattering cross section of 80 mb [25].

2.3 Radiation damage on gaseous detectors

Deterioration of performance of gas detectors under irradiation has been observed since the start of their use in particle physics experiments [27]. In general, the observed damage depends on the amount of incident radiation but other aspects such as gas composition, gas quality, material of the detector and type and rate of radiation, affect the final performance in a different way.

This degradation is commonly referred to as "aging". Detector lifetimes are expressed in terms of integrated charge per wire (or electrode) length, of O(1 mC/cm). They can also be expressed in terms of a surface O(mC/cm^2). The observed phenomenology included the appearance of local and permanent damages detected as self-sustained discharges, excessive currents, gradual loss of energy resolution and decrease and non-uniformity of the gas gain.

Even in the early ages of the field, devices such as the Geiger-Müller (GM) tubes after prolonged exposure to radiation showed changes in the gas amplification characteristics. Over time, the gas amplification would decrease, leading to reduced sensitivity and efficiency of the GM tube. Further studies found that the reason behind the degradation of performance was caused by

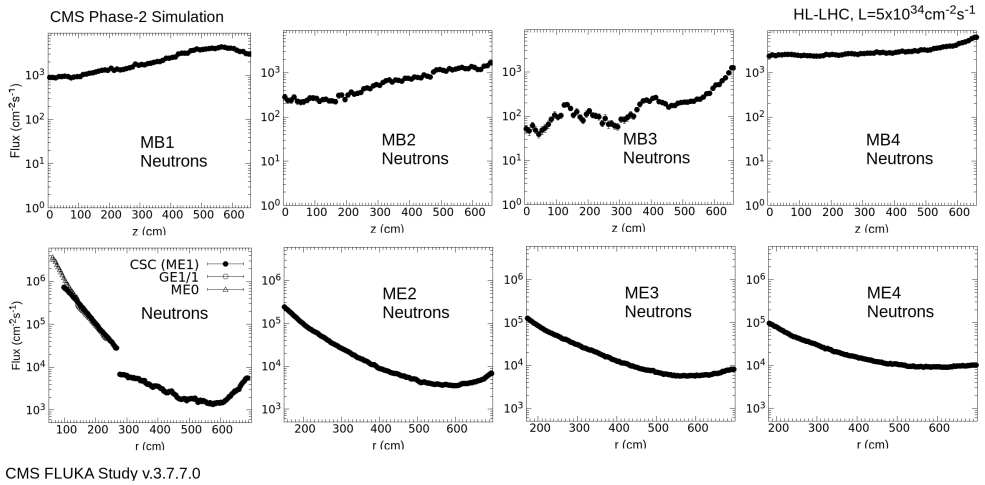

(a) Neutron particle flux

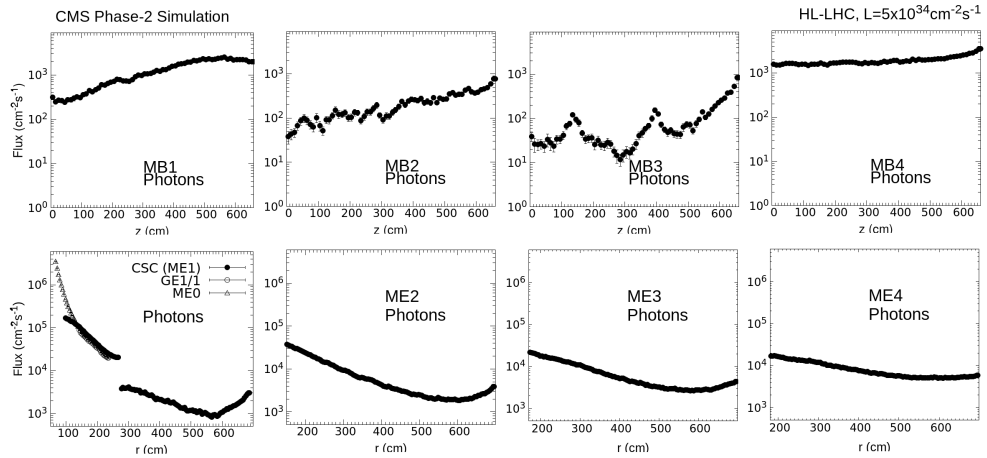

(b) Photon particle flux

Figure 2.4: FLUKA simulations of proton-proton collisions at 7 TeV per beam with a Phase 2 geometry model for different muon station in central and forward part of CMS detector. Results are normalized for an instantaneous luminosity of $5 \times 10^{34}\ cm^{-2}s^{-1}$ assuming an inelastic scattering cross section of 80 mb [25].

the deposition of hydrocarbon polymers on the electrodes.

Also, during the development of the Multi Wire Proportional Chamber (MWPC) a progressive degradation of performance was observed. In the de-

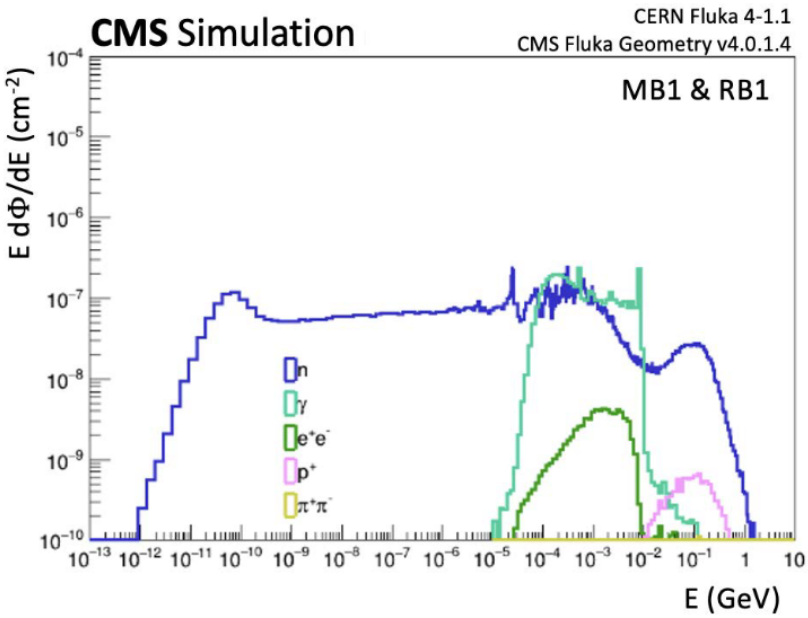

Figure 2.5: Simulation (CERN fluka 4-1.1) of the energy spectra of the particles in the volumes covered by the MB1 chambers of Wheel-2 for the CMS Phase 2 detectors during HL-LHC. Fluxes are normalized to a single pp-collision [26].

tectors secondary discharges occurred after irradiation due to polymerization of the electrodes or molecular dissociations. A degraded detector showed increases in the background rate (dark current) even when exposed for a short time to high radiation and the effect persisted after removal of the source.

These effects are referred to as classical aging and are related to the formation of deposits, which can be conductive or insulating, but either case, they end up fully covering the electrodes with a coating. This coating inevitably degrades the detector performance. The deposits generally are the products of chemical reactions that occur in the avalanche plasma close to the anodes of the detector, schematically illustrated in Figure 2.8. This polymerization process, well-known in plasma chemistry, is thus the process by which some monomer radicals associate in subsequent chain reactions to form a very large molecule, frequently of high molecular weight. During operation of a gaseous detector, formed molecules will be removed by the gas flow if they are light enough, or be deposited or react with electrode materials inducing typical aging processes.

Inside a gaseous detector, during the stages of gas amplification, many

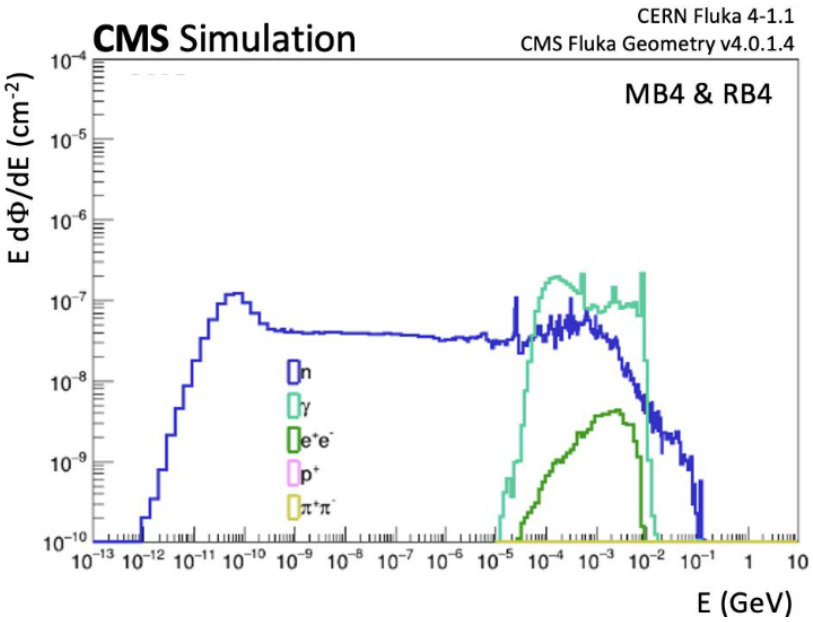

Figure 2.6: Simulation (CERN fluka 4-1.1) of the energy spectra of the particles in the volumes covered by the MB4 chambers of Wheel-2 for the CMS Phase 2 detectors during HL-LHC. Fluxes are normalized to a single pp-collision [26].

molecules break up in collisions with electrons, due to de-excitations of atoms and in UV photon absorption processes. Whereas most ionization processes require electron energies greater than 10 eV, the breaking of covalent molecular bonds and formation of free radicals requires only 3-4 eV. This can lead to a higher concentration of free radicals than that of ions in the gaseous discharges.

Since free radicals are chemically very active, they will either recombine to form the original molecules or other volatile species, or may start to form new cross-linked molecular structures of increasing molecular weight. When the polymerized chain becomes large enough for condensation to occur, it can diffuse to an electrode surface. This has far-reaching consequences for chamber operation since these polymers exhibit excellent adhesion properties to surfaces, are resistant to most chemicals and are insoluble in most solvents.

Deposits on the wires can take any form from smooth layers to long thin whiskers. On the cathodes, deposits usually consist of spots of thin insulator. Defects of this latter kind can often be correlated with a discharge pattern, which may be interpreted as Malter effect which is particularly disastrous.

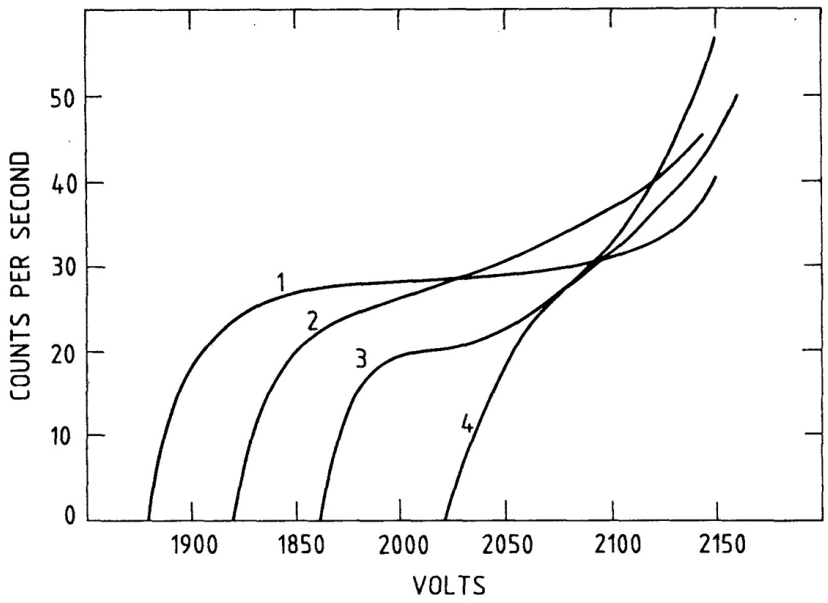

Figure 2.7: Progressive degradation of a Geiger Counter while being exposed to radiation. Curve 4 is the singles counting rate vs voltage measured after 10^8 counts.

Malter effect can occur if the conducting cathode is covered with a thin insulating layer by polymerisation. Charges build up on this insulator layer until the electric field is strong enough to extract electrons from the cathode through the layer into the gas where they initiate new avalanches.

A positive feedback between electron emission at the cathode and amplification at the anode can thus develop and will cause high ionization densities in the chamber, which can eventually lead to the classical self-sustained Malter discharge. Several factors may facilitate its ignition, such as insufficient conductivity of the cathode, highly ionizing particles, sparks, sharp points on electrodes causing corona discharges, or thin anode wires. The fact that the build-up time decreases with higher ionization rate and that the discharges take some time to decay after irradiation is timed off, give support to this explanation, as does the observation that addition of water vapor is reducing the discharges, probably introducing some conductivity. If the Malter effect remains undetected for a sufficiently long period of operation, it can spread over a large area, thus causing irreparable damage to the chamber.

One of the aspects to be particularly cautious is the materials used during the detector construction. Extensive laboratory tests are crucial to evaluate the aging properties of gasses and materials. These tests include out-gassing

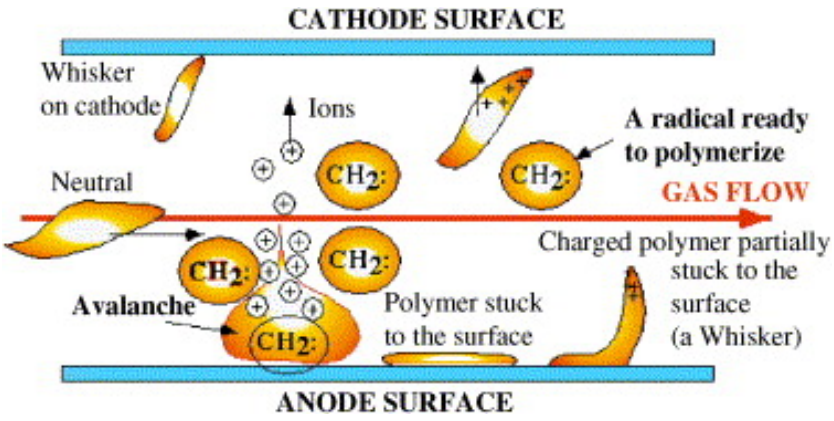

Figure 2.8: Chemical reaction occurring in the anodes of a gaseous detector that leads to radiation aging.

tests, accelerated aging tests, and prototype detector evaluations under realistic conditions. Factors such as irradiation rate, ionization density, particle type, and gas flow significantly influence aging rates. It is to be noted that materials might undergo structural changes induced by the effect of ionizing radiation, liberating new out-gassed pollutants that can promote polymerization. Silicon contamination, known for its rapid polymerization rate, is particularly detrimental, emphasizing the need for careful material selection.

NASA's database of low out-gassing materials serves as a useful reference for selecting suitable materials for gas detectors.

In addition, the gas distribution system needs to be maintained particularly clean, since impurities in the gas, which are transported with the gas flow may also directly deposit on the surface of electrodes and insulators due to electrostatic forces. Organic materials can out-gas or some reactive gasses (such as dimethyl ether, DME) can attack chamber materials and plumbing.

Furthermore, initially neutral gasses sometimes become reactive because of the species created in the avalanche process close to the wire. The created species are reactive enough to remove layers of some materials, mechanically damaging the detectors and polluting the chamber gas. For example, tetra fluoride radicals can remove thin layers of material on coated wires. While this capability might help to remove deposits from polymerization, it may on the other hand turn into a serious problem when the reactive species attack assembly materials. The probability of all these mechanisms to occur depends on a large number of factors: gas flow, gas gain, geometry and electric field configuration as well as the presence of additives have, amongst others, been demonstrated to play an important role. Moreover, the choice

of the gas mixture needs to be selected taking aging effects into account. For instance, the addition of oxygenated or hydrogenated species can shift the chemical balance towards etching or polymerization, respectively. Gas mixtures for detectors, typically noble gasses combined with hydrocarbons, must be chosen carefully to mitigate aging effects. While hydrocarbons tend to polymerize over time, additives like oxygen or water can improve detector lifetimes by reacting with polymer precursors to form volatile species. As mentioned, CF4-containing mixtures are promising due to their balanced polymerization-etching properties but require stringent control of pollutants to maintain performance. Experience has shown that the purity of the gasses used is also of highest importance and that it must be maintained over the whole lifetime of the experiment: examples have been reported where a temporary use of polluted components led to a degradation of detector performance which persisted even after the pollution was removed from the system again.

Comparisons with results obtained in plasma chemistry have led to an improved understanding of aging phenomena, but due to the large complexity of the processes involved it has until now not been possible to derive recipes which can be generally applied to all high rate applications. The demand for radiation hardness, especially in high-rate experiments like those at the LHC, has necessitated systematic studies to identify materials and gasses with acceptable aging properties. This need is again critical in view of HL-LHC. Extensive laboratory tests are crucial to evaluate the aging properties of gasses and materials. These tests include out-gassing tests, accelerated aging tests, and prototype detector evaluations under realistic conditions. Factors such as irradiation rate, ionization density, particle type, and gas flow significantly influence aging rates.

As already mentioned, the symptoms that become visible in the detectors when aging occurs are gain loss (reduction of pulse heights), worsening of the energy resolution, excessive chamber currents (dark currents), and potential self-sustained discharges. In extreme situations, also electrical breakdown or broken wires can be spotted. An enormous number of studies have been carried out and they are documented in [28], [29], [30], [31] and [32] , for example.

2.4 Radiation damage on electronics

Electronics can be vulnerable to the effects of radiation, causing malfunction or decreased performance. The same process by which silicon sensors are excellent radiation detectors, makes our electronics sensitive to the accumu-

lation of charge generated by the interaction with the radiation field. The electronics present in the CMS detector are usually inaccessible so quantifying the expected damages during operation is critical to avoid disastrous consequences in the experiment's performance.

As energetic particles pass through an electronic device (we will address only silicon based devices here), a number of ionic interactions occur. Some radiation particles (such as heavy ions) are directly ionizing, while others (such as protons) cause secondary radiation ionization through nuclear reactions. For directly ionizing particles, the passing ion loses energy and this energy is transferred to bound electrons, which are ionized into the conduction band. This leaves a trail of electron-hole pairs in the wake of the ion's path. The rate of charge deposition per unit length of an ion is known as its Linear Energy Transfer (LET). This value not only depends on the type and speed of an ion, but also on the material through which it passes. If there is no electric field at the point where an electron-hole pair is created, the electron and the hole will usually just recombine without any serious effects to the device. If, however, there is an electric field at the point where the electron is ionized into the conduction band, the electrons and holes will quickly separate. This latter situation is encountered often in Complementary Metal Oxide-Semiconductor (CMOS) devices in the depletion region of reverse bias pn-junctions. This separation or drift of electrons and holes is best modeled by a small instantaneous current pulse.

The effects of the radiation in electronics can be classified in different categories, being one starting point criteria whether the effect is the result of the accumulation of damage from multiple particles or just one single particle. Examples of cumulative damage include Total Ionizing Dose (TID) and Displacement Damage Dose (DDD). Failures resulting from a single particle can be destructive or non-destructive to the device and may include memory upsets, latchup, gate rupture, burnout and other phenomena that are generally described as Single Event Effects (SEE).

2.4.1 Total Ionizing Dose

In semiconducting materials the passage of ionizing radiation can create the accumulation of charge. The incident radiation can ionize the material but the electron-hole pairs formed may not recombine entirely. Electrons have much higher mobility, so they can exit the material, leaving holes trapped inside.

Here are a few examples of TID Effects on electronic devices:

- Threshold Voltage Shifts: The trapping of holes in the oxide causes

charge build-up in the bulk of the oxide. These charges will screen or increase the gate oxide of MOS transistors' electric fields, leading to a change in its I-V characteristic. The most prominent change is the shift of the threshold voltage which is negative for NMOS and positive for PMOS. As a result, a device might become unresponsive to some commands as it might be "stuck" in a specific state.

- Increased Leakage Current: In the Field-Isolation oxides such as Shallow Trench Isolation oxide, charges might draw an image charge in the semiconductor which can reverse the interface and free leakage paths. This can only occur in NMOS transistors. These parasitic leakage currents have degraded timings and increased power consumption.

- Amplifier Gain Degradation: TID-induced damage in bipolar transistors usually manifests as a reduction in bipolar gain with increasing total dose exposure. To compensate for it, more power needs to be supplied to the device.

2.4.2 Displacement Damage Dose

This type of cumulative damage is caused from the rearrangement of the atoms in the crystal lattice of the semiconducting material, usually caused by the impact of a high energy proton or neutron. These impacts can create microscopic defects that turn into recombination centers or traps that alter the electronic bands and, therefore, affect the functionality of the components.

2.4.3 Single Event Effects

This type of errors are non cumulative but they happen instantaneously in reaction to the passage of a particle through the electronics component. Still, they can be classified in non-destructive errors or more dangerous destructive errors.

2.4.4 SOFT ERRORS (Non-Destructive)

- SEU - Single Event Upset: SEU is a change of state of an electronic device storage element caused by a single ionizing particle. These events usually do not affect the reliability and function of a system over time and are easier to fix than hard errors. SEEs that result in one upset are called Single Bit Upsets (SBU), whilst those resulting in multiple

upsets are named Multiple Cell Upsets (MCU). Several upset cells that are part of the same logic word are referred to as Multiple Bit Upsets (MBU). MBU causes multiple bit errors during one measurement. The SEUs usually affect latches, memory devices, and sequential logic.

- SET - Single Event Transient: SET occurs when the motion of charges by a single particle, causes a temporary (transient) voltage glitch. This transient can recover quickly without other actions needed to clear the error condition. Nevertheless, the danger of it being latched at a wrong logic level is present and higher in faster devices. SETs affect mostly analog and mixed-signal circuits.

- SEFI - Single Event Functional Interrupt: SEFI occurs when a disturbance of state registers interrupts the normal operation of circuits and the affected device enters a different operation mode or locks-up. In essence, SEFIs are SEUs taking place at the control sections of the circuit. These are more difficult to restore than other SEUs and usually, a software reset or a power-cycling is required. SEFIs are SEUs that occur in critical circuit components, such as the power-on/reset circuitry. When one of these bits is upset it often takes the entire device off-line.

2.4.5 HARD ERRORS (Destructive)

- SEL - Single Event Latch-up: SEL is a type of hard fault which is usually catastrophic to the system. The passage of a single energetic particle can trigger a parasitic PNPN structure drawing an abnormally high operating current. If the power input is not reset in time the device is at risk of suffering from a potentially disastrous overcurrent episode that can result in structure overheating and melting. The SEL can occur with Complementary Metal-Oxide-Silicon CMOS and BiCMOS devices in structures such as the electrostatic discharge (ESD) or overvoltage protection circuits. SELs do not take place in Silicon-on-Insulator (SOI) devices, which suppress any parasitic PNPN structures (thyristor).

- SESB - Single Event Snapback: SESB is another self-sustained high-current state caused by radiation. Its effect resembles an SEL but the mechanism differs entirely. A snapback takes place within a single NMOS structure when the electric field between Source and Drain is high. During a radiation event, the ionization charge can trigger avalanche multiplication conditions and activate a parasitic NPN bipolar transistor between Drain and Source. The amount of current drawn

is much smaller compared to a latch-up but it can still result in local overheating of that structure. SESB has been observed in NMOs structures and SOI devices and can be removed with lowering the drain bias below the avalanche multiplication region.

- SEHE - Single-Event Hard Errors: Single-Event Hard Errors, also referred to as "stuck" bits, are memory bits that are unable to be changed by a write-process, therefore rendered non-functional. The mechanism behind this is attributed to microdose effects induced by single ions. As with general TID accumulation, heavy ions themselves too create hole traps in the SiO_2/Si interfaces. However, the density of these traps is highly peaked around the ion track in contrast to the roughly isotropic profiles induced by protons, electrons or gamma radiation. This streak of traps is able to establish leakage paths and "pin" the affected transistor to either a closed or open state. As a result, the memory cell gets "pinned" to either a "1" or "0" state.

- SEDR - Single-Event Dielectric Rupture: SEDR is caused by an ionized particle inside the high-field region of a dielectric which creates a conductive path, resulting in a current-jump phenomenon (jump in the core power supply). However, SEDR is rather considered an academic interest, as it is mostly observed in testing and not in space.

- SEGR - Single Event Gate Rupture: SEGR is caused by the passage of a heavy ion through the neck area of a Double Diffused Metal Oxide Semiconductor (DMOS) power transistor when in the OFF state; the generated holes drift towards the gate and accumulate at the silicon-gate oxide interface. If not diffused or recombined at the lateral p-regions in time, they develop a local electric field exceeding the intrinsic breakdown dielectric potential. This results in the dielectric breaking down and short-circuiting the gate with the substrate. The SEGR affects mainly the power MOSFET and recently has been observed in MOS-based digital and linear integrated circuits resulting in destructive consequences. It is also often observed simultaneously with Single Event Burnout (SEB) in power MOSFETs.

- SEB - Single Event Burnout: SEB is caused by a single energetic particle charge (primarily heavy ions) that results in localized high-current state in the body of the device. This type of hard error often results in catastrophic failure. The SEB affects primarily bipolar transistors and N-channel power MOSFET in space, but has also been observed in high voltage diodes in terrestrial applications.

2.4.6 Radiation effects in FPGAs

An FPGA (Field-Programmable Gate Array) is a semiconductor device that allows users to configure its internal hardware logic after manufacturing, making it a flexible solution for a wide range of applications. Unlike traditional fixed-function ASICs (Application-Specific Integrated Circuits), FPGAs consist of an array of programmable logic blocks interconnected through reconfigurable routing resources. The code that describes the specific architecture implemented is called firmware. This architecture enables the creation of custom digital circuits tailored to specific tasks, such as signal processing, data encryption, or real-time control, without the need for expensive fabrication. FPGAs are particularly valuable in fields requiring rapid prototyping, hardware acceleration, and adaptability, including telecommunications, aerospace, and embedded systems.

FPGAs are electronic devices based on CMOS technology, as are most of the digital electronics. Particles traveling through silicon layers of a digital electronics device can cause both transient and permanent flipping of the bit held by the Complementary metal oxide-semiconductor (CMOS) element. The type of errors that we are generally concerned about are SEU, SET, SEL, SEFI and SEGR. For the radiation doses and energies that are to be expected for DTs in HL-LHC, the effects are expected to be relatively mild.

During operation under radiation, there exist mitigation techniques to deal with the effect of SEUs in the behavior of the programmed logic. The most common is the use of TMR (Triple Module Redundancy) technique, in which each flip-flop is tripled and sent to a majority voter which is where the output is extracted. Accordingly, two SEUs are required in the same part of the logic to actually have an effect in the behavior of the circuit.

However, protecting against SEU in the firmware design is not enough to operate safely an FPGA and SEFIs can become an increasingly concern. When a design is uploaded to an FPGA, a configuration bitstream is sent to the device and stored in some sort of memory (usually SRAM). This bitstream defines the operation of the components inside the FPGA. Changes to this bitstream stored in memory as a result of radiation effects, correspond to changes in circuit operation which may or may not cause the overall circuit to malfunction. FPGAs are primarily vulnerable to radiation because the radiation is able to upset the configuration memory of the FPGA and thereby change the operation of the circuit. However, upsets are not limited to the logic configuration bits, they can also affect the routing bits, the control logic bits, or any other configurable bit in an FPGA.

As will be described later, in the DT electronics we plan on using a different type of FPGAs, not SRAM based but FLASH based, which are

much less sensitive to radiation.

2.4.6.1 Cross section as measurement of radiation damage

For the estimation of irradiation resistivity of a digital electronics device, its cross section σ is used as a crucial parameter, giving the error probability as a function of particle fluency and measured in units of cm^2. It is given by

$$\sigma = ne/F = ne/(np/A) \tag{2.1}$$

where:

- $\sigma[cm^2]$: Device cross section
- ne: Number of errors
- $F[cm^{-2}]$: Particle fluency
- np: Number of particles
- $A[cm^2]$: Area through which the particles pass

Device Cross Section is used to estimate the number of errors that can be expected during the operation of the whole device (for instance, the FPGA). But, of course, the cross section - or error probability - also can be determined for a single bit within a device. The outcome of the radiation tests that we will perform, will be the cross section expected in the FPGA under test, and it will be possible to calculate out of it the number of expected SEUs during operation at HL-LHC.

2.5 Drift Tubes at HL-LHC

2.5.1 Estimation of the particle fluxes of DT at HL-LHC

An important input to characterize the HL-LHC electronics under radiation is the knowledge of the radiation fluxes that could be expected at HL-LHC. In order to get an estimation of those, a study of extrapolating the present LHC occupancies in the DT detector has been made.

The occupancies in the DT detector have several components:

- Muon tracks: each muon traversing a DT chamber will leave a track of hits on each DT cell. Except in the I-beams, where the detector is blind, at least one signal is expected from each single cell. In general this muon track will translate into 8 hits in the phi view, one from each layer and 4 hits in the theta view. During the ionization process, sometimes the ejected electrons possess sufficient energy to produce further ionizations in the cell which are called secondary ionizations. The electrons generated in those are called delta rays and are an important contribution to having more than one hit per cell when a muon crosses by. Its contribution is expected to be in the few percent [33].

- Punch through: Even if the HCAL detector has been made dense enough and up to 10 radiation lengths are transversed before reaching the DT chambers, sometimes the hadronic showers extend into the first DT stations. This is particularly frequent in the MB1s of the external wheels because the junction between the Barrel HCAL and the Endcap HCAL is far from perfect. The resulting radiation is made of protons, pions and other hadronic components and can generate track-like signals that can be reconstructed out of the hits of several consecutive layers.

- Single hit background: The activation of all the materials in the detector and in the cavern end up creating a flux of particles that permeate the cavern. An important contribution comes from the neutrons that have a long lifetime and can scatter elastically in the cavern for quite some time, producing effects uncorrelated with the beam structure. The resulting effects, visibles in the DT detector, are single cell signals which are correlated with the LHC beam structure and follow the luminosity profile.

- Electronic noise: the distribution of the high voltage inside the chamber is usually responsible for injecting a certain amount of noise in the electronic circuit. Spikes due to not perfectly terminated distributions or isolations breaking up, can generate single cell electrons that end up generating a hit. This noise is independent from the LHC operation and does not grow in principle with the luminosity.

During LHC operation we have focused on the study of distribution of the background inside the detector versus luminosity, since its correlation follows very well the LHC luminosity. The method for obtaining a quantitative estimation of the background profits from the large time window that the DT system has. Accordingly, for each event readout in CMS, we get a snapshot

of the signals present in the system for a period of 1 μs. Therefore, we can measure the accumulated amount of signals averaging over all the different particles contribution. With this method, we obtain a value of the hit rate per channel in the different chambers. The obtained distribution is very inhomogeneous in the different regions of CMS, with some chambers very affected (MB4s in all wheels for single hits mainly and MB1s of external wheels, YB-/+2, for punch through tracks). The per channel distribution obtained at a particular luminosity for each of the chambers can be seen in Figure 2.9.

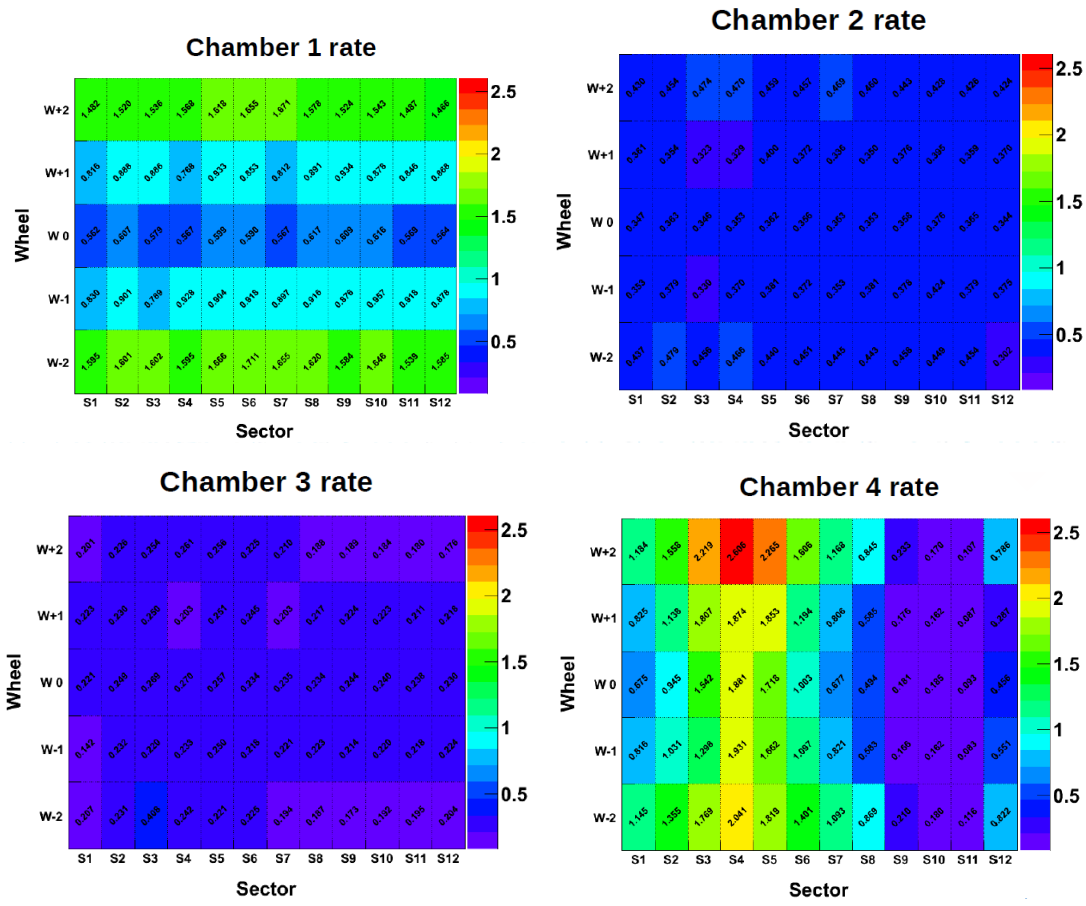

Figure 2.9: Rate per DT chamber channel in Hz/cm^2 for each of the DT chambers in the CMS detector calculated at an average luminosity of $4.645 \cdot 10^{33} cm^{-2} s^{-1}$

As can be seen, the worst case is the MB4 chambers, which suffer from the radiation field that permeates the cavern. Still, we can appreciate that

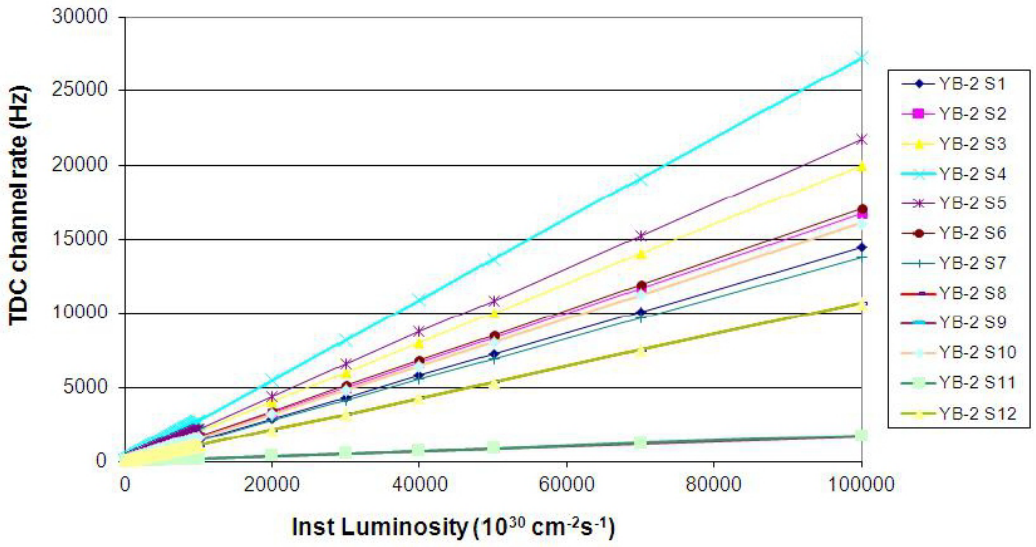

Figure 2.10: Extrapolation of the background rates measured in MB4 chambers for luminosities up to 10^{35} $cm^{-2}s^{-1}$.

the correlation of these measurements with luminosity is very linear, as can be seen in Figure 2.10. Extrapolating linearly these measurements to 10^{35} $cm^{-2}s^{-1}$ of instantaneous luminosity, we obtain maximum rates of 27 Hz/cm^2 which correspond to 27 kHz/TDC channel for the worst MB4.

Several contributions need to be added to this number to account for increases of energy or even electronic noise in the detector. The contribution from muon like signals is relatively low, since we have measured that it is in the order of 3.6 kHz/channel for MB1 and 0.3 kHz/channel for MB4.

Accordingly, and including some safety margin, a takeaway number that we will use for the design of the new system is a maximum expected hit rate of 50 kHZ/channel or 50 Hz/cm^2.

2.5.2 Study on the longevity of ROB electronics

In order to study if the legacy electronics, that is, the ROB board can withstand the expected conditions at HL-LHC, a setup was prepared with some boards for hit injection and one board to control the L1A generation, clock distribution and L1A latency control. With this setup the L1A rate can be controlled and also, the L1A latency, which is expected to be increased to 12.5 μs (from 4 μs) for HL-LHC to allow injecting the outer tracker layer into

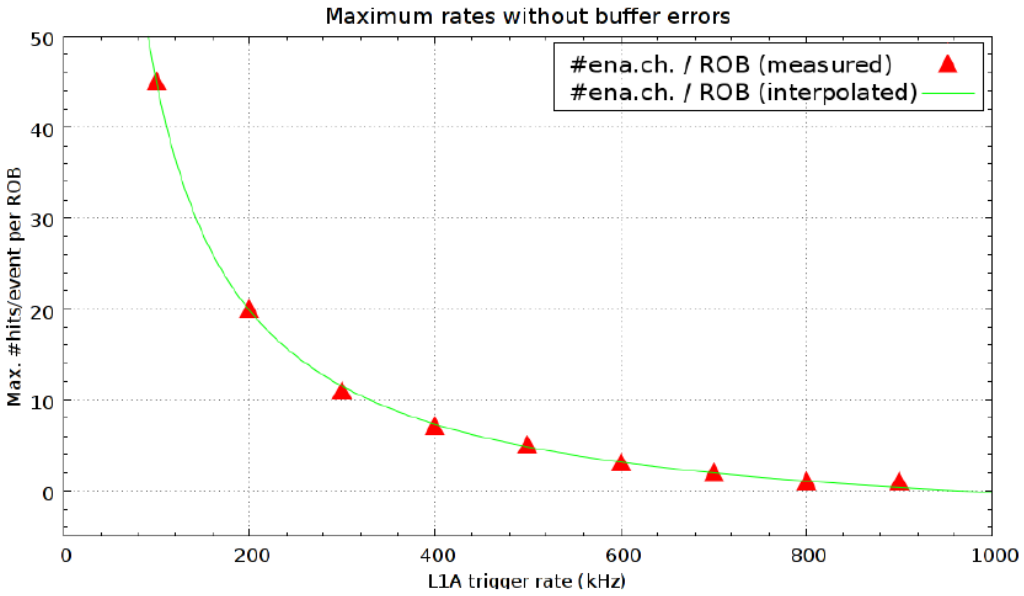

Figure 2.11: Relationship between L1A rate and the number of hit's processed without error.

the Level 1 Trigger decision. Some measurements were performed to find out the point at which the ROB memories saturate can be studied. Results can be seen in Figure 2.11.

The graphic shows that there is a monotonically decreasing dependency between the maximum read-out capability of a ROB and the L1A trigger and hit rates.

Throughput is limited mainly because of the round-robin method which is used to coordinate different ASICs HPTDCs (High Performance Time to Digital Converter) which are used inside the ROB boards. They share the same bus for sending data through the 240 Mbps readout link to the ROS board. This serial link is clearly the major barrier to achieve higher read-out data rates.

As mentioned before, the maximum expected background rate is 50 kHz/channel (once every 20 μs), while the readout window is 1.25 μs. With 128 channels/ROB, this means that if the hits were perfectly distributed, we will still have a minimum of 8 hits/event in each time window. And this is without the contribution of real muons, which will insert additionally another 8 hits/ROB.

As can be seen in Figure 2.11, the maximum L1A rate that we could stand with 8 hits/ROB is approximately 300-350 kHz. However, for HL-LHC, CMS

is planning to run between 500 kHz and 750 kHz of L1A. So it is clear that present ROBs will not be able to stand such a L1A rate with the expected background, and therefore, need to be replaced.

2.5.3 DT upgrade for HL-LHC

The existing DT detector is essential for identifying and measuring muons at the required precision and accuracy needed to fulfill the CMS physics program. Therefore, it must be guaranteed that its performance will be sustained at high luminosity. It should be noted that even if there is some redundancy between the DT and RPC detectors, there are various factors that make DT indispensable. On the one hand, the position resolution that DT offers (100 μm) is much better than RPC one (1 cm) and this position resolution is important for measuring the transverse momentum of the highest energetic muons, where the DT detector resolution is better than the tracker one. On the other hand, the RPC detector is suffering from important gas leaks and almost 30% of the barrel detector is switched off as of today. Having the RPC gas mixture ($95.2\%C_2H_2F_4 + 4.5\%C_2H_{10} + 0.3\%SF_6$) a very high GWP (Global Warming Potential), its operation under these conditions is at stake.

From studies performed during its early design [25], the DT chambers and internal FEB electronics should continue to work at the HL-LHC, but the electronics attached to the DT chambers in the so-called Minicrates, will not stand the HL-LHC conditions. Before we have described the problematic with the ROB boards, but other boards in the Minicrates will also suffer. For instance, CCBs (Chamber Control Board, a board that controls ROBs and TRBs in the Minicrate) will not withstand the radiation fluxes and the TRBs, which already showed a large mortality rate at the beginning of the operation back in 2003 due to the wire bondings in their custom modules, are unlikely to safely operate for another 10 years.

During Long Shutdown 3 (LS3) the Minicrates must be replaced by new Minicrates (MiC2), which will be able to cope with the Phase 2 conditions in terms of readout rate (L1A of 750 kHz). The plan is to simplify enormously the new Minicrates and use only one type of board which performs the streaming of all the DT chamber incoming hits, without any filtering. This new board is called OBDT (On-Board electronics for Drift Tubes). Increased data bandwidth will be required to cope with this full streaming mode. The Minicrate functionality will be reduced; the trigger and event building logic will be transferred to the back-end electronics outside of the experimental area in the counting room, becoming accessible at all times and

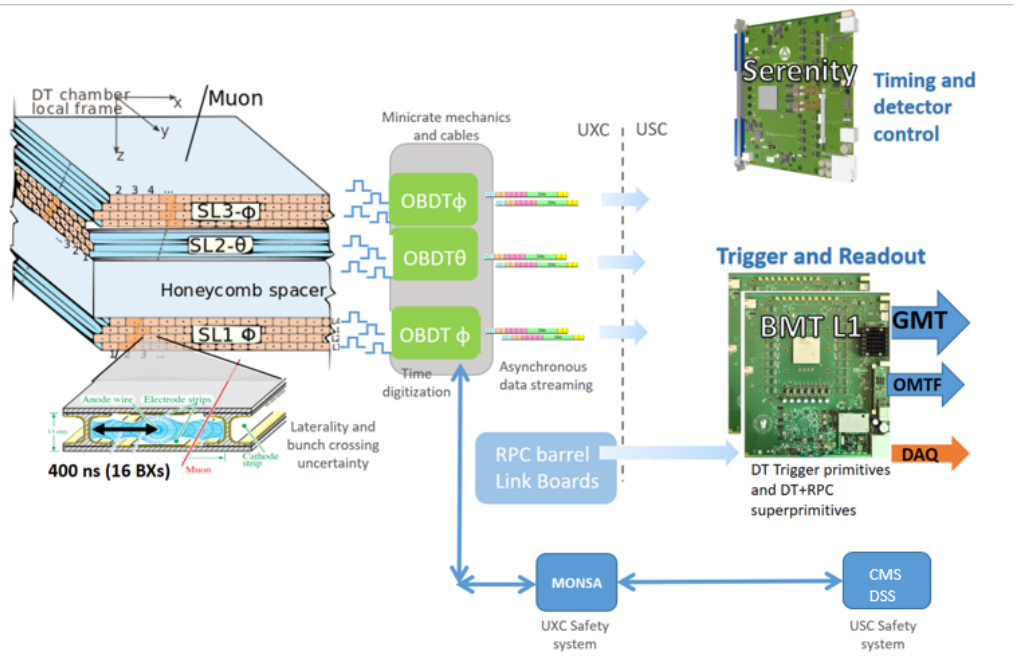

Figure 2.12: Diagram of the new architecture for the CMS Phase 2 DT systems that will be installed for operation during HL-LHC. GMT is the Global Muon Trigger system that receives the DT Trigger Primitives. DAQ refers to the Data Acquisition system that receives the readout data. DSS is the CMS Detector Safety System. UXC is the CMS experimental cavern and USC is the CMS Service cavern. BX refers to LHC bunch crossing which represents a unit of time of 25 ns.

allowing the implementation of a more powerful trigger system.

The backend electronics will have to be replaced to operate under this new data acquisition scheme and we expect to have two independent systems, one for the configuration and monitoring of the new OBDT boards implemented in the Serenity board [34] and another one to perform the readout and trigger of the DT chambers, implemented in the BMTL1 board [35]. A scheme can be seen in Figure 2.12.

The new MiC2 design brings several advantages such as reducing complexity, removing bandwidth constraints and very importantly, reducing the power consumption by a factor 2, which also has important implications in terms of reducing the cooling system needs. The MiC2 will be located inside the CMS wheels, in a very inaccessible place that does not allow the air to flow and where the magnetic field prevents from using active cooling through

ventilators. Cooling will be performed through conduction to a water circulation system at 17°C. Therefore, it is important that the system can operate safely and dissipate as little heat as possible.

The OBDTs are the heart of the new MiC2. They receive signals from the FEBs for each anode wire and assign a digital timestamp. They host a multi-channel TDC implemented in radiation tolerant FPGAs and the data are transferred out of the experimental cavern using CERN developed high bandwidth optical link technology.

The OBDT system will be made of 830 boards to readout 172,200 channels from the DT chambers. It will be made of two type of boards: OBDT-phi (designed at INFN Legnaro), in charge of digitizing the signals coming from the DT wires that measure the azimuthal phi coordinate in CMS, and the OBDT-theta (designed at CIEMAT), which will digitize the signals from the wires that measure the polar angle theta coordinate. The two boards have similar functionality but slightly different requirements. The most critical is because of the impossibility to extract all DT chambers. Therefore, OBDT-theta needs to maintain the legacy cables and connectors. In the phi view, however, the legacy cables that interconnect the DT chambers and the Minicrates will be replaced with new cables that shield each differential pair to minimize noise.

The OBDT-theta board has been built around a Microsemi Polarfire FPGA, responsible for the time digitization of up to 228 input signals. This time digitization of the input signals will be performed inside the FPGA, providing a coarse time measurement and a fine time measurement. The coarse measurement is performed through a counter which is incremented with a 40 MHz clock, that is, its time bin is 25 ns and consists in 12 bits, allowing to measure a range of up to 4096, though this range will be reduced to 3564 to be synchronized with the LHC orbit.

The fine measurement is performed using the deserialization method inside the FPGA. A deserializer module is implemented on each of the 228 differential input channels and it is operated at 640 MHz in DDR (Double Data Rate) mode, that is, effectively 1.2 GHz, which provides a time bin of 0.78 ns. Therefore, up to 5 bits are used to code the fine time measurement.

Both the coarse and the fine time measurement of each signal are combined with the information of the channel number to provide a 25 bits digital word. All the time measurements are referred to a periodic signal called BC0 (Bunch Crossing 0), which can be received externally or generated internally. For operation under LHC, this signal is expected to arrive synchronously through the TCDS (Timing and Control Detector System) [36] and mark the start of a new LHC orbit, which is repeated after 3564 clock cycles of 25

ns (i.e., bunch crossings).

In the foreseen operation mode, each time measurement is expected to be made of the time at which the collision took place (certain number of 25 ns clock cycles after the BC0), the time of flight of the muon to the actual DT cell and the drift time of the electron to the anode. This last contribution is the one that is expected to be proportional to the position of the muon inside the cell due to a constant drift velocity which is set to be $\sim$54.5 μm/ns by carefully controlling the gas mixture. Additional contributions to the time measurement are expected from the delay introduced by the cables or the anode wire itself. These contributions need to be corrected during the DT system calibration procedure. The bunch crossing at which the muon was generated should be marked by the L1A generated at the CMS Trigger system.

Communication to this board is based on two VTRx+ (Versatile Link Transceivers Plus) [37] that provide two bidirectional links for slow-control and six transmitter links, capable of output data up to 10.24 Gbps each to the backend system, achieving up to 60 Gpbs. One of the bi-directional links goes to the lpGBT (Low Power Gigabit Transceiver) ASIC (Application Specific Circuit) [38] in the OBDT board, which provides the main slow-control functions and reception of the LHC clock and some TTC signals. The other one is directly connected to the FPGA serving as a secondary slow-control to recover OBDT-theta in case of loss of main slow-control. The protocol implemented so far follows the lpGBT protocol for all links.

The lpGBT chip plus a SCA (Slow Control Adapter ASIC) chip [39] in the board allow clock and synchronization reception as well as the configuration and monitoring of the Microsemi FPGA. Through this link it is also possible to implement the different slow-control functionality of the barrel system, such as setting the FEBs discriminators thresholds and bias values, implementation of the I^2C links for temperature monitoring and channel masking, communication to the PADC, RPC and Alignment slow control chains and finally, control of the test pulse generation mechanisms that allows to perform the DT chamber time measurements calibration for the theta view superlayers.

The OBDT-theta board contains two power rails, one for 3 Volts which is the rail used for the FPGA and most of the logic. And another rail at 5 Volts to operate the testpulse calibration electronics and other external services such as the PADC, RPC and Alignment I^2C systems. Several power supplies are needed (2.5 V, 1.8V, 1.5 V, 1.2 V and 1.05 V) by the different components, and they are generated by low drop linear regulators, which provide very low noise.

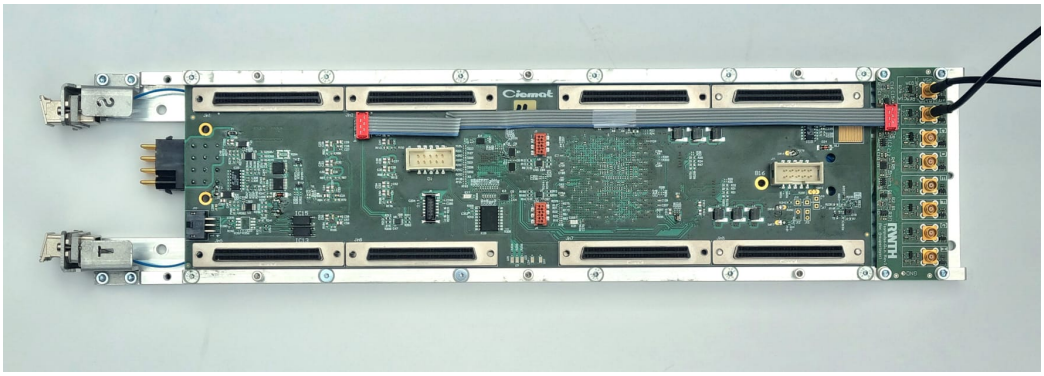

Figure 2.13: Image of an OBDT-theta and Testpulse-theta boards fixed to the mechanical frame that connects them to the Minicrate.

A custom safety system has also been designed in the OBDT-theta to protect the electronics in case of malfunction. This system protects against overcurrents in both rails, overvoltages (linear regulators maximum voltage is 6 Volts) and over temperatures. If any of these alarms are generated, the system flags it to an external system (so called, MONSA [40]) and also, it powers off the rest of the OBDT-theta electronic's chain.

An image of the OBDT-theta board can be seen in Figure 2.13.

A first prototype of the OBDT board (OBDTv1) was designed and built with the same functionality but without using the latests ASICs from CERN, since they were not available. Therefore, a previous version of the transceiver ASIC was used (GBTX [41]) as well as commercial optical components. This board is the one that we used for the radiation characterization at CHARM described in Chapter 6.

2.6 Summary and Conclusions

In this chapter the expected plans at the LHC collider to increase its luminosity in the HL-LHC phase have been revisited as well as the overall expected impact in the CMS experiment.

In further detail, the implications for gaseous detectors is studied together with the literature of the major phenomena that arise when exposing gaseous detectors to a long duration radiation field. The aging effects which depend on the accumulated charge as a consequence of this radiation field have been revisited. Similarly, the effects from this radiation in electronics are detailed in order to be able to design a new system capable of surviving the HL-LHC

environmental conditions.

The detail of how this HL-LHC radiation field will be in the location of the DT detector is studied and data from the CMS operation is used to obtain the present radiation background. With this information, extrapolations to the HL-LHC conditions are performed, showing that a very good linear relationship can be obtained that allows to get reliable estimations of the future background environment.

Having this information, which is complementary to the simulations of the CMS radiation field, is critical to allow evaluating the capability of the present electronics to survive the CMS Phase 2, and the tests performed at laboratory to evaluate this capability are presented. This tests showed that these electronics needs to be replaced and the plan for the new system is outlined.

Chapter 3

Studies of the Longevity of DT Chambers at GIF++

By the time HL-LHC is expected to start, the DT system will be more than 20 years old and it will be required to operate another 10 years integrating around 10 times more luminosity than it was designed for. The impact on the performance of the detector under the new radiation conditions has to be evaluated. The objective of the next phase of operation is to maintain detector performance under the new HL-LHC background conditions, specifically in:

- muon track resolution, particularly relevant for high p_T muons
- barrel muon trigger and its matching with the tracking trigger
- standalone muon trigger (independent from the tracker)

Even in the event of a perfectly non-degraded detector, the increase of pile-up and occupancy due to higher instantaneous luminosities could compromise system performance. At present, the background and the muon rates have been extrapolated to HL-LHC luminosities; with maximum hit rates expected in the order of 50 kHz/cell. Single cell inefficiencies due to any type of signal or background hit masking a valid signal hit as a consequence of the system dead time represents a single cell inefficiency close to 1% and is not expected to degrade significantly muon reconstruction overall. For the chambers with the higher segment rates background (mainly punch-through in the inner forward chambers) there are indications that the readout buffering capability could be close to the limit in HL-LHC, having a larger impact O(5%), but the new TDC has been designed to make this effect negligible. The impact on the trigger would be higher in the legacy architecture since at

present, it has 400 ns dead time after each signal instead of 100 ns in the TDC (readout), which turns into 0.3% trigger segment inefficiency (probability of not having any type of trigger primitive in a chamber as a consequence of hits being lost) and almost 8 % inefficiency for high quality triggers (probability inside a chamber of a High quality trigger primitive becoming a Low quality one). This inefficiency has been removed with future design.

3.1 Baseline considerations about aging of DT chambers at construction

Tests involving insulation breakdown have been performed in [23]. They suggest that, at the typical field of 2 kV/mm, the system lifetime is in the order of 108 years, which translates into a 4% probability of failure on one out of the 172200 tubes of the full Drift Tube system in 20 years [9]. This probability can be reduced by one order of magnitude reducing the strips voltage by 300-400 V while keeping the wire gain constant. The High Voltage Boards (HVB) consist of a multilayer FR4 structure and host passive components only. Failures are highly improbable and not expected if safely operated. Only one HVB out of $\sim$ 11 000 has been substituted (in LS1) and it was due to a problem that appeared during an intervention in that chamber.

A lower chamber operating voltage would certainly improve their lifetime. FEBs were tested up to a radiation dose and a neutron flux almost one order of magnitude larger than the expected at HL-LHC and no damage was detected. Extensive accelerated aging tests were also performed on 20 FEBs at high temperature (125°C) for 3200 h and no degradation was observed, which corresponds to a MTBF (mean time between failures) better than one board per LHC year, limited by statistics. This is less stringent than what has been observed so far, namely 4 failures in 10 years, and implies a negligible contribution by the end of HL-LHC. However, interventions to cope with a possible failure of one of the above items require opening the front or the back cover of a SL. This is a risky and time consuming intervention which is only possible during long shutdowns. Indeed, since the FEBs are inside the chamber gas volume, if a massive FEB replacement is needed, it would be considered preferable to replace a full chamber.

The DT chamber gas mixture is a safe Ar/CO_2 (85%/15%). Gas leaks, changes in the gas mixture, gas contamination with oxygen, water or even pollutants from outgassing of chamber material will degrade system behavior. All these aspects are important for the optimal performance of the chambers and are carefully monitored to minimize contaminations that can degrade

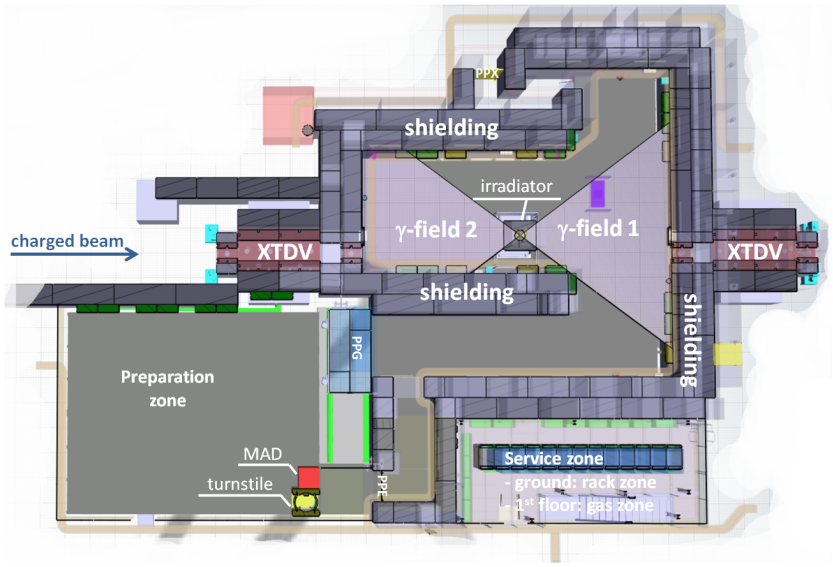

Figure 3.1: Layout of the Gamma Irradiation Facility ++

chamber operation.

Wire aging induced by all the components present inside a tube (glues, O-Rings, plastic parts) has been studied at construction time for LHC conditions [42] and is being studied at the GIF++ (Gamma Irradiation Facility) facility for HL-LHC conditions.

3.2 DT aging campaigns at GIF++

3.2.1 The GIF++ Facility at CERN

GIF++ [43] at CERN was the facility used to irradiate the DT chambers, as well as other muon detectors, and assess the effects of the ionizing radiation on the performance of the detector. The facility provides a high activity ^{137}Cs source emitting 662 keV photons and a high energy muon beam coming from the SPS, one of the accelerators in the CERN complex.

The high activity of the source allows the integration of dose at the level of the HL-LHC in a reasonable amount of time. In the case of the DT chambers, that are located in a relatively low occupancy region inside the CMS yoke, the irradiation requirements are smaller than other muon detectors and the DT setup is located in the further side of the source in the γ-field 1 downstream as seen in Figure 3.1.

The dose rate present in the bunker where the chambers are placed is regulated by a series of attenuation filters that can be controlled remotely. The configuration of the filters must be agreed upon by all the GIF++ users and, since the drift chamber cannot surpass a certain dose rate threshold (because of the safety mechanism that shuts down the chamber when the current in the wires is too high), it is very important to try to maximize the low-intensity irradiation time in stable conditions. The study regarding the installation of an additional filter to try to further reduce the amount of dose received in our setup while not modifying other users conditions can be seen in Appendix A.

The muon beam provided by the SPS is very clean and can be centered in the chamber comfortably. It allows the characterization of the detection efficiency with and without the background irradiation provided by the source, being a quite good model of HL-LHC conditions. Coincidence of beam scintillators upstream and downstream provides a pure muon beam trigger. The chamber has also auto-trigger capability, which is used for cosmic muon data-taking. Beam data is discussed elsewhere and can be used to characterize the detection efficiency with and without background irradiation. The bunker where the detectors are placed for irradiation is divided in two regions (upstream and downstream), each region has a different set of attenuation filters that can be set independently. To install the DT chamber in the bunker the roof needed to be opened which is a labour-intensive operation, the detector was placed in the downstream side on top of two rails to enable displacement during the different periods of data taking.

The data taking setup is installed in the Service zone and is connected to the chamber through long cables passed below the floor of the bunker. The setup consists of two computers: one with Linux in charge of the run control and data taking and other with Windows that runs the software needed for configuration and event display. Multiple irradiation campaigns have been performed at GIF++, 2015 and 2016 with a MB1 chamber and 2017 with a MB2. The results presented here correspond to the MB1 chamber irradiated during 2016.

The first tests began in 2015 with a MB1 spare chamber, seen in Figure 3.2, identical to the ones operated in the CMS detector, that had not been irradiated before. During the 2015 campaign, there were many instabilities in the test stand and obtaining quantitative results was very complicated. However, we could clearly observe a degradation of the chamber performance after an integrated dose close to HL-LHC. The effect seems to be concentrated on the wires and we exchanged some of them and repeated the irradiation exercise in 2016. The results presented here correspond to an analysis of the

Figure 3.2: MB1 chamber installed at GIF++ seen from the position of the source

wire currents during the irradiation period and a conversion of the measured dose to the expected accumulated dose in the CMS chambers during HL-LHC.

3.2.2 Dosimetry at GIF++

One of the critical parameters to obtain during an irradiation campaign is a precise measurement of the integrated dose. Measuring the effects of the aging at different values of integrated dose will allow for the comparison with expected values for the HL-LHC. The integrated dose will be the abscissa axis for all the plots that describe the evolution of the different parameters under study. It is, therefore, crucial to measure it with precision in order to extrapolate the behavior during HL-LHC conditions.

Some simulations [44] exist on the expected dose received at each location but the actual values are very dependent on the detectors and other material located between the source and your particular chamber. Accordingly, to have reliable integrated dose values, it is necessary to perform on site measurements.

3.2.2.1 Dose measurement devices

In order to characterize the dose deposited on the chamber different hardware has been tested to choose which device can provide the best solution, taking into account the need for precision, repeatability and frequency of measuring. The following instruments have been used:

- RADMON

  The RADMON [45] sensor contains a radiation sensing field effect transistor (RADFET) used to measure the integrated dose and a thermistor that gives a value of the temperature.

  When exposed to ionizing radiation, positive charge builds up and the threshold voltage increases. The setup used at GIF++ consists of two Keithley 2410 sourcemeters that inject a constant current in the RADFET and the thermistor, and measure the voltage drop. With these voltage values the total integrated dose can be calculated while taking into account the effect of the temperature in the measurements.

- RAMSES

  RAMSES [46] uses an ionization chamber and a data acquisition system to provide the equivalent dose rate measurements every hour. The monitoring data can be accessed by requesting the data to the working group responsible for the measurement.

- Portable dosimeter

  A commercial calibrated portable dosimeter with a Geiger-Müller tube (Automess 6150 AD) was used. This device measures equivalent dose rate in real time as well as integrated equivalent dose.

The method used in GIF++ was to set the source filter configuration, place the dosimeter in the desired position, reset the integrated dose counter and start the irradiation. With this measurement an equivalent dose value can be associated to the attenuation used at any given time.

At first the dose was measured using the RAMSES detector installed in the GIF++ bunker. This method had the disadvantage of requiring the request of the data to the group responsible for the measurement, having a measurement that was not taken in the position of the DT chamber and a measuring frequency of 1 hour which led to lack of synchronization with the dose and High Voltage current monitoring. In order to achieve better time granularity and faster availability of the measurements a different approach was taken for the dose monitoring. The dose was measured using a

Figure 3.3: Portable dosimeter Automess 6150 AD

portable dosimeter that was positioned in both the chamber position and on the RAMSES, consecutively. The process consisted in placing the dosimeter in the position under study, exiting the bunker, switching ON the source for 3 minutes and entering the bunker to retrieve the measurement. This process was repeated many times to get values for different attenuation filters. The results obtained with the RADMON were not conclusive, so they were not used for calibration. To validate the results the dose rate for the measurements in the RAMSES position was calculated and compared with the measurement from the RAMSES sensor itself, both devices measured the same dose rate. A value of the dose rate was associated to each attenuation filter using the data from the portable dosimeter. Every 30 seconds a computer program collected the values of the currents from the power supply and the parameters in the bunker (pressure, temperature, filter configuration and source status) and stored them in ASCII files. These ASCII files could be read via software and associate a value of the dose rate to each timestamp according to the filter configuration in that moment and calculate how the integrated dose was increasing in the chamber. In later stages of the irradiation the RAMSES system could be accessed in real time under the name REMUS [47], which made dose measurements easier and more precise.

During the irradiation campaign the layout of the detectors placed in the bunker changed a few times, altering the irradiation that was received by the chamber. To keep the conversion factors as reliable as possible, the dose measurements were repeated using the portable dosimeter, and the conversion values recalculated for the different periods with altered conditions. So for each bunker layout there was a proportionality factor that converted the dose measured by the bunker's sensors to dose reaching the chamber.

	Energy bins (keV)											
Position	0-20	20-40	40-60	60-80	80-100	100-200	200-300	300-400	400-500	500-600	600-662	total
D1	9.9E+03	1.7E+04	2.9E+04	2.2E+05	3.3E+05	4.7E+06	3.9E+06	5.2E+06	7.4E+06	8.3E+06	3.3E+07	6.4E+07
D2	0.0E+00	3.9E+02	1.2E+04	6.4E+04	8.4E+04	1.0E+06	5.9E+06	3.6E+05	6.6E+05	8.3E+05	3.3E+06	6.9E+06
D3	0.0E+00	1.2E+03	1.1E+04	4.2E+04	6.2E+04	6.5E+05	3.4E+05	2.2E+05	2.4E+05	2.9E+05	1.1E+06	3.1E+06
D4	0.0E+00	2.4E+03	1.4E+04	4.1E+04	5.8E+04	5.5E+05	2.9E+05	1.7E+05	1.6E+05	1.7E+05	1.4E+06	2.7E+06
D5	0.0E+00	0.0E+00	1.1E+04	3.6E+04	4.9E+04	4.5E+05	2.5E+05	1.6E+05	1.6E+05	1.6E+05	1.4E+06	2.7E+06
U1	8.6E+03	1.5E+04	3.1E+04	1.8E+05	3.0E+05	4.7E+06	4.0E+06	5.2E+06	7.5E+06	8.2E+06	3.3E+07	6.4E+07
U2	0.0E+00	7.9E+02	1.2E+04	7.0E+04	9.8E+04	1.3E+06	6.5E+05	3.5E+05	6.9E+05	8.1E+05	3.3E+06	7.5E+06
U3	0.0E+00	1.2E+03	1.6E+04	6.8E+04	7.4E+04	8.6E+05	4.7E+05	2.3E+05	2.4E+05	2.8E+05	1.1E+06	3.6E+06
U4	1.3E+03	1.2E+03	2.7E+04	1.0E+05	1.5E+05	1.6E+06	9.6E+05	3.8E+05	3.7E+05	3.7E+05	4.1E+06	8.3E+06
U5	2.2E+03	2.0E+03	3.1E+04	1.2E+05	1.7E+05	1.3E+06	7.5E+05	3.9E+05	3.3E+05	2.6E+05	1.7E+06	5.4E+06
U6	0.0E+00	0.0E+00	1.2E+04	4.8E+04	5.9E+04	5.1E+05	1.3E+05	4.5E+04	2.2E+04	7.9E+02	0.0E+00	9.2E+05
U7	4.3E+02	7.9E+02	1.9E+04	8.1E+04	9.9E+04	8.8E+05	4.9E+05	2.5E+05	1.6E+05	1.6E+05	1.4E+06	3.7+06

Table 3.1: Simulated flux $[\frac{counts}{s \cdot cm^2}]$ downstream and upstream attenuators open (from [44]).

3.2.2.2 Dose measurements

Using the setup mentioned in the previous section a measurement of the dose during the 2016 irradiation campaign was made, as shown in Figure 3.18. During most of the irradiation it was possible to keep a very controlled low dose rate so the chamber's safety system will not shut it down due to overcurrent in the wires.

3.2.2.3 Dose conversion factors

The dose measuring devices available for the irradiation campaigns are designed with radiological protection in mind and, therefore, measure equivalent dose (Sv), which quantifies the health effects on the human body. The system under study is not biological in nature so, in order to correlate with other studies and measurements, a conversion to absorbed dose (Gy) is needed. We will use the values proposed by the International Commission on Radiological Protection (ICRP) in 3.4.

To make a correct conversion from equivalent dose to absorbed dose the incident photon energy is needed. Using the simulation from [49] a conversion factor is calculated.

The MB1 was placed in the D4 position depicted in the Figure 3.5. With the data from Table 3.1 we can calculate the percentage of total flux distribution for every energy bin. Multiplying the conversion factors issued by the ICRP for each energy bin with the percentage of photon flux irradiating the D4 position in the bunker, a conversion factor can be estimated for the total of the irradiation spectra as shown in 3.2.

Further corrections need to be applied in order to get a precise measurement of the dose. There are two factors that affect the dose characterization, the distance between the sensor and the chamber and the inhomogeneous

CONVERSION COEFFICIENTS FOR USE IN RADIOLOGICAL PROTECTION

Table A.21. Conversion coefficients[a] for the ambient dose equivalent, $H^*(10)$, and directional dose equivalent, $H'(0.07,0°)$, from photon fluence and air kerma free-in-air

Photon energy (MeV)	$H^*(10)/K_a$ (Sv/Gy)	$H'(0.07,0°)/K_a$ (Sv/Gy)	K_a/Φ (pGy cm^2)	$H^*(10)/\Phi$ (pSv cm^2)	$H'(0.07,0°)/\Phi$ (pSv cm^2)
0.010	0.008	0.95	7.60	0.061	7.20
0.015	0.26	0.99	3.21	0.83	3.19
0.020	0.61	1.05	1.73	1.05	1.81
0.030	1.10	1.22	0.739	0.81	0.90
0.040	1.47	1.41	0.438	0.64	0.62
0.050	1.67	1.53	0.328	0.55	0.50
0.060	1.74	1.59	0.292	0.51	0.47
0.080	1.72	1.61	0.308	0.53	0.49
0.100	1.65	1.55	0.372	0.61	0.58
0.150	1.49	1.42	0.600	0.89	0.85
0.200	1.40	1.34	0.856	1.20	1.15
0.300	1.31	1.31	1.38	1.80	1.80
0.400	1.26	1.26	1.89	2.38	2.38
0.500	1.23	1.23	2.38	2.93	2.93
0.600	1.21	1.21	2.84	3.44	3.44
0.800	1.19	1.19	3.69	4.38	4.38
1	1.17	1.17	4.47	5.20	5.20
1.5	1.15	1.15	6.12	6.90	6.90
2	1.14	1.14	7.51	8.60	8.60
3	1.13	1.13	9.89	11.1	11.1
4	1.12	1.12	12.0	13.4	13.4
5	1.11	1.11	13.9	15.5	15.5
6	1.11	1.11	15.8	17.6	17.6
8	1.11	1.11	19.5	21.6	21.6
10	1.10	1.10	23.2	25.6	25.6

[a]Data compiled from *ICRU Report 47* (1992a) using Hubbell and Seltzer (1995). The K_a/Φ data are slightly different from those used for the protection quantities (see Table A.1) which used earlier data from Hubbell (1982).

Figure 3.4: Conversion factors [48] between dose units

irradiation field due to other detectors placed between the source and the chamber.

The sensor used for recording the dose as function of time for the whole irradiation was not in the same position as the chamber. Using a portable dosimeter, a correction factor was calculated to extrapolate the values from the sensor to the position of the chamber.

In addition to previous calculations, an exercise was made to calculate in detail the inhomogeneities of the dose along the DT chamber surface. A set of measurements were made using a dosimeter placed on an automated platform to get a two-dimensional distribution of the dose rate in the chamber. The results are shown in Figure 3.6.

The areas with low dose rate correspond to two trapezoidal detectors installed by other users of the facility between the radiation source and the DT chamber, as can be seen in Figure 3.7.

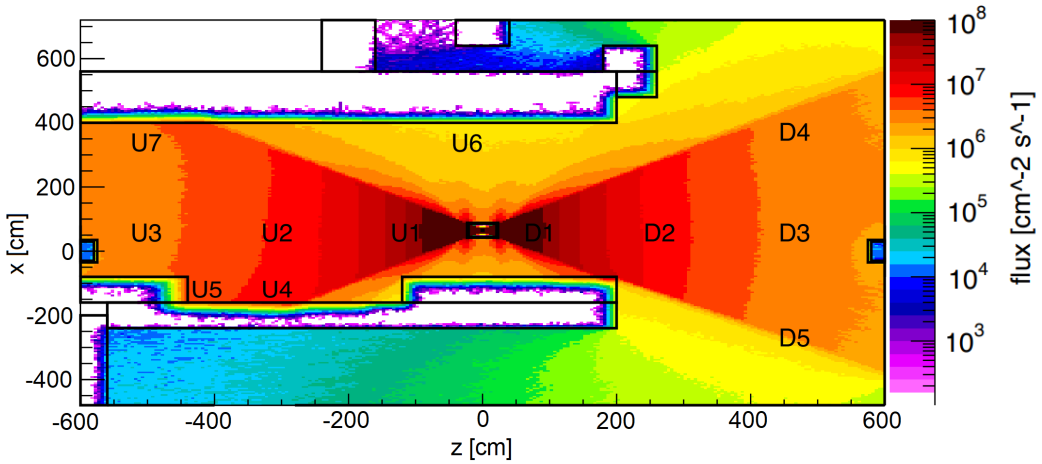

Figure 3.5: Irradiation flux simulation inside the GIF++ bunker [44].

3.3 Current and gain measurements

One of the main observables in a detector that show a decrease when exposed to irradiation is the gain. The front-end electronics of the DT chamber are made by the FEB boards which allocate MAD ASICs responsible for pre-amplifying the wire's signal and discriminate them versus a programmable threshold. These boards are located inside the gas volume, therefore we can only measure the discriminated signal and we have no direct access to the integrated charge and thus, to a direct measurement of the cell's gain. Since is not possible to measure the gain on the chamber per interaction (by a muon or photon), the analysis we are performing here will be focused on estimating gain variations using an observable that is measured comparing the current in the HV wires, generated by the superposition of multiple hits, and the dose measured independently.

3.3.1 2015 MB1 Irradiation

The first tests began in 2015 with a MB1 spare chamber, identical to the ones operated in the CMS detector, that had not been irradiated before. The DT chamber was placed vertically in a rail parallel to the wall on the downstream side of the irradiation field and its correct position was verified before irradiation. Since the dose rate was to be minimized, the irradiation was performed on the edge of the GIF++ irradiation cone, i.e. with a rather inhomogeneous field. This is the reason of the large difference between Wire

Energy bins (keV)	Percentage of total flux	H*(10)/Ka (Sv/Gy)	Conversion factor
0-20	0	0	0
20-40	0.0841	0.61	0.0005
40-60	0.4903	1.47	0.0072
60-80	1.4359	1.74	0.0250
80-100	2.0312	1.72	0.0349
100-200	19.2617	1.65	0.3178
200-300	10.1562	1.4	0.1422
300-400	5.9536	1.31	0.0780
400-500	5.6034	1.26	0.0706
500-600	5.9536	1.23	0.0732
600-662	49.0299	1.21	0.5933
		total	1.3427

Table 3.2: Percentage of total flux in D4 position (from [44]), conversion coefficients according to energy range from [48] and conversion factor normalized to the percentage of total flux.

0 and Wire 1 in Figure 3.8b.

For three months the detector was irradiated with different dose rates using the gamma source at GIF++ and a muon beam coming from the SPS. The muon beam was used to determine the performance of the chamber before and after irradiation. The values of the currents were recorded every time they changed, and the RAMSES system was used to measure the dose integrated every hour, both measurements were synchronized via software.

In Figure 3.8a the current is shown for each layer inside the SL Phi 1. During the first weeks the setup was tested with different configurations, ensuring that the trigger and readout were operational.

At the beginning of September, a stable irradiation period started. During the first two weeks only half of the layers were powered (wire 0) and a steady drop of current can be observed, later the rest of the layers were powered (wire 1). The wire 1 channels have a more pronounced decrease due to a higher exposure to radiation than the wire 0 ones. It can be observed that the decrease in current slows over time, tending to a plateau in the final stages of the testing period.

SL Theta 3.8b is located between SL Phi 1 and Phi 2 but with perpendicular orientation, so the irradiation profile among the wires 0 and 1 is very similar, unlike the Phi SLs. This translates in a closer value for the currents

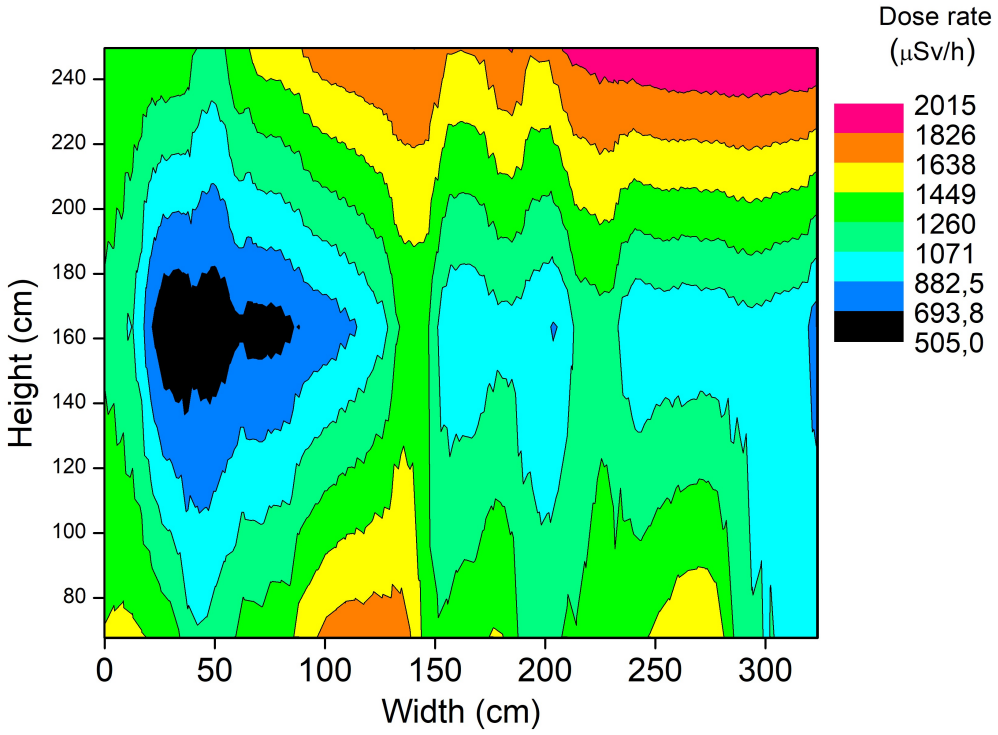

Figure 3.6: Two-dimensional dose rate distribution on the DT chamber installed at GIF++.

of both wires. There is a peak due to an increase in the high voltage of the chamber during the second week of September that results in an increase in current not related to an increase in the dose rate, but to a change in the operational conditions during the irradiation.

The SL Phi 2 is represented in Figure 3.8c. This SL is positioned behind Phi 1 and Theta, so the dose rate that is integrated there is lower than the one in Phi 1. Therefore the values of the current are lower while keeping a similar behavior.

The analysis of the currents and of the TDC data of the MB1 chamber placed inside GIF++ from August 2015 till end 2015 showed a relevant decrease of the current at fix GIF++ flux rate (as function of the integrated dose) and a visible (but less prominent) degradation of the efficiency of the layers of the chamber (varying in the 12 layers according to gamma absorption). Once the chamber was placed outside the GIF++ area, cosmic ray data were collected with auto-trigger; and the analysis of such data confirmed a degradation of the efficiency.

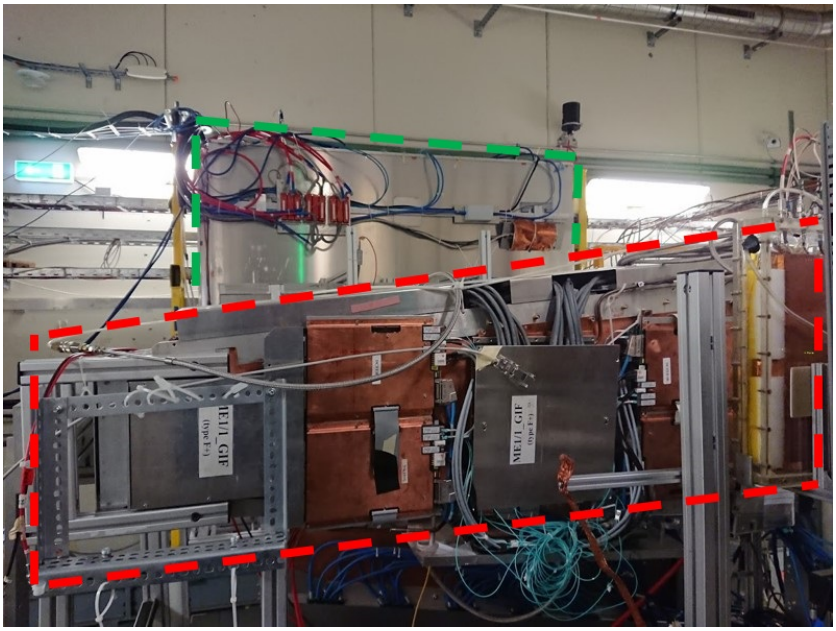

Figure 3.7: CMS DT spare chamber (rectangular detector with green outline) placement in the GIF++ bunker, shadowed by a CSC chamber (red outline).

3.4 Investigation Plan at GIF++

Since the operating conditions in 2015 were unstable and did not allow to obtain quantitative results, a more detailed plan was developed. Three main investigation lines were set in order to understand and quantify the aging effect seen at GIF++ and a further line of activity was developed at INFN Legnaro (LNL) :

1. Evaluating/excluding if the deposit of material on the wires which caused the degradation of the performances of the cells was caused by gas tube connections used in the external gas circuit (Rilsan), which is known to be very porous to water.

2. Identifying which parts inside the gas volume could be the origin of the material deposited on the wires.

3. Quantifying the rate of the degradation (and its dependence on the integrated dose) to evaluate its impact for HL-LHC operation, performing aging tests at a much lower acceleration factor approximately 10 times that expected in HL-LHC.

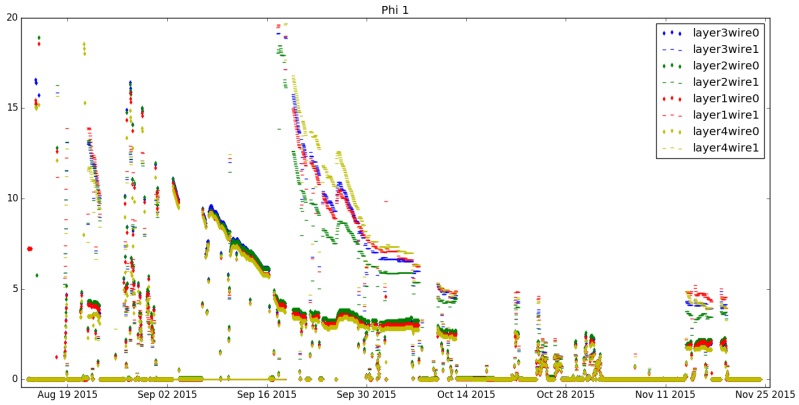

(a) Current as a function of time for SL Phi 1

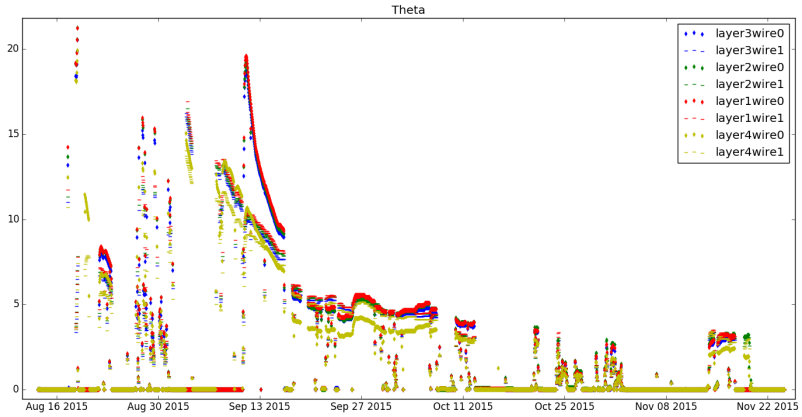

(b) Current as a function of time for SL Theta

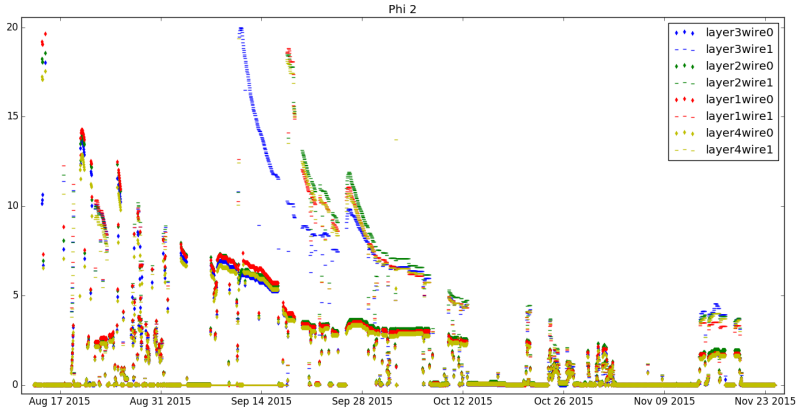

(c) Current as a function of time for SL Phi 2

Figure 3.8: Currents as a function of time for the three Superlayers during the 2015 irradiation of an MB1 chamber.

4. Analysis of the coating on the wire.

To address point 1, the study of the effect of the Rilsan tube used for the DT in 2015 at GIF++, it was decided to build simple cylindrical tubes, so called monotubes, of 5 cm in diameter and 80 cm long, Al made and with a 50 μm golden plated wire in its center. The tubes performances were studied at the LNL MB3 telescope and then installed in the GIF++ area. Two monotubes (reference monotubes, one placed outside the GIF++ area and one inside) were fluxed with gas throughout steel and copper pipes and one was fluxed with the used (20 m) Rilsan tube and placed inside the radiation area. The current of the Rilsan gas tube indeed presented a lower value with respect to the reference monotube inside the GIF++ with gas metallic piping, but the decrease was verified to be not permanent: by exchanging the gas lines the current was recovered. Reducing the Rilsan gas tube length, the decrease of current was verified to be proportional to the Rilsan length.

On point 2, i.e. to identify the origin of the deposits it was decided to build a small prototype of DT chamber cells consisting of two DT cells only (bicells) [50], using the same materials as the DT chambers. Several were built in order to be able to experiment easily the effect of specific factors on the aging process such as HV setting, gas flow or the concentration of standard contaminants in the system like H_2O or O_2 . The bicells are divided into three different zones: the main central one with the gas active volume, and two smaller ones at its sides, in which all the electronics for high voltage (HV) and signal processing are placed. Such a configuration allows to have the HV and the FE electronics not in contact with the gas fluxing inside the cells. Aluminium slabs (1 m, 2 m, 12 cm, 2.5 mm) are used to delimit the entire volume on bottom and top. The top slab is divided into three parts (HV region, FE electronics region and sensitive wire region) which are fixed to the rest of the structure using screws in order to be removable independently. The removable covers allow to inspect the interior of the cells and to change the wires when needed. The central zone is separated from the two ancillary parts by two aluminium blocks with several holes for gas pipes and for HV cables. These two blocks and the walls of the bicells are glued to the basis as well. In the active parts the aluminium I-beams (85 cm long) are glued to the bottom slab, the gold coated steel anode wires (50 μm in diameter) will be in the center, and the aluminium strips sticked to the upper and the lower slabs in the middle of each cell. The I-beams are partially covered with Mylar tape for isolating the aluminium strips which serve as cathode.

3.4.0.1 Wire replacement in the MB1 chamber

To address point 4 after the irradiation campaign from 2015 3.3.1, 8 wires from SL Phi 1 were extracted for analysis and replaced with new ones with the same original materials. The operation took place in two different occasions, one in February and other in August 2016. The wires changed in February were C11L3, C49L2 and C48L3, where C11, C49 and C48 correspond to the cell number; all taken from SL Phi 1. The wires were divided and the samples sent to CIEMAT, INFN Padova and CERN for analysis.

The results from the microscopy analysis indicate that a coating is being formed on the wires and it could be the responsible of the loss of gain observed in the detector. As can be seen, the wire diameter had changed from 56 μm to 65 μm. The spectral analysis indicates that material present is probably a hydrocarbon polymer with some silicon that is presumably produced from the outgassing of the internal materials present inside the chamber.

The spectra in Figure 3.9b shows the following proportions: Carbon 48.59%, Oxygen 29.19%, Gold 20.42%, Silicon 1.79%. These results point towards a deposit of a hydrocarbon polymer with some Oxygen and Silicon.

The wires that were changed in August were C21L1, C21L3, C22L2, C22L3 and C22L4. The high voltage connections of these wires, together with the ones changed in February, were re-cabled and connected to the same high voltage board in order to isolate the monitoring of the current of the replaced wires in a single layer (Phi 1 Layer 2 wire 0).

3.4.1 2016 MB1 Irradiation

To address point 3, a spare chamber was placed vertically at around 3 m from the source and with SL1 facing the source, it was irradiated at a low accelerating factor ($\sim$10 times the expected dose rate at HL-LHC) in two campaigns that finished in February 2019. This to be compared with high acceleration factor ($\sim$100) used in the 2015 irradiation campaign. The chamber went through several tests in order to understand its response under irradiation and after a full irradiation period of few months. Weekly scans were performed varying the detector operational parameters (high voltage and front-end threshold) and the attenuation filters of the source (i.e. the background dose rate on the detector). Data from two test beams with muons from the SPS were recorded to characterize the chamber before and after the full irradiation period. The HV scan were taken with anode voltages ranging from 3200 to 3700 V in 50 and 100 V steps. The front-end threshold was also probed for values from 10 to 40 mV in 10 mV steps. We note that, however, most of the data recorded was taken for front-end threshold values of 20 and

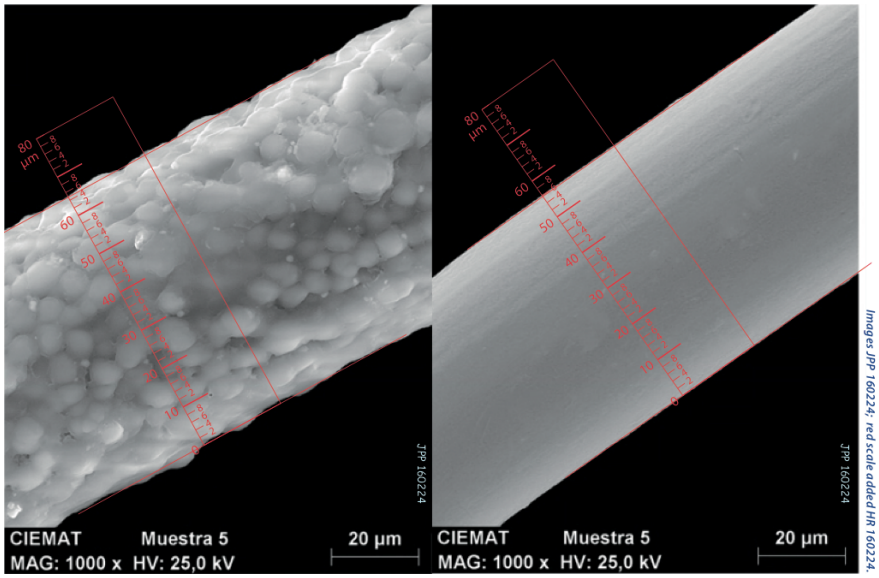

(a) Wire with deposit (left): $65\mu m$ diameter; clean wire (right) $56\mu m$ diameter. The deposit layer is thus about $4.5\mu m$ thick.

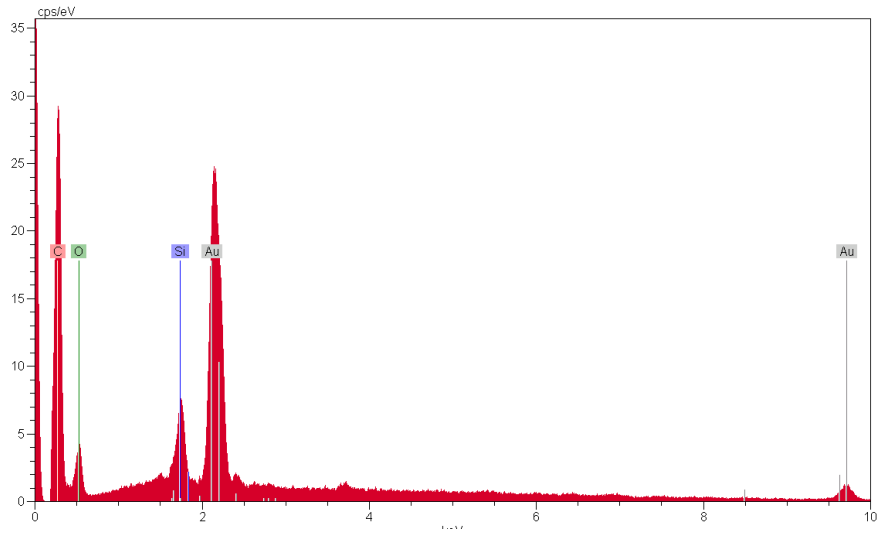

(b) Spectral analysis of a wire extracted from the MB1

Figure 3.9: Analysis of a DT wire.

30 mV. The chamber was operated with a gas mixture of Ar/CO_2 85%/15% and a gas flow 40 l/h, as it is done with the DT chambers operating at the CMS detector.

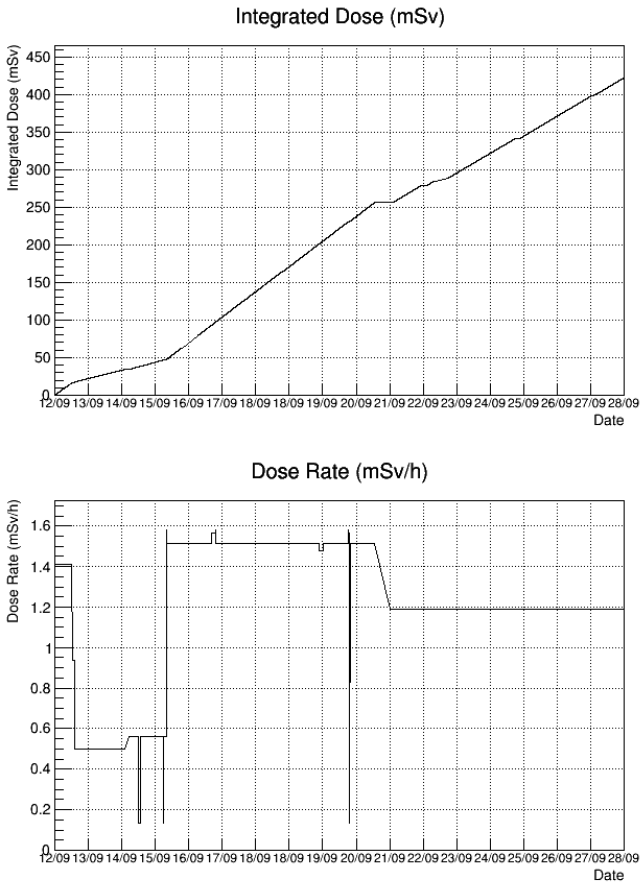

Figure 3.10: Integrated dose and dose rate as a function of time for the 2016 irradiation.

3.4.1.1 Dose measurements

After replacing the wires we managed to get a period of irradiation with minimal deviations from the desired configuration. In Figure 3.10 the integrated dose and the dose rate for such period is shown. Initiating a new irradiation with a subset of wires without any accumulated dose allowed for a great opportunity to study the evolution of the loss of performance under irradiation.

3.4.1.2 MB1 currents after wire exchange

We presented some currents measured in Section 3.3.1 but the full gain analysis has been performed after exchanging the wires. The wire exchange allowed

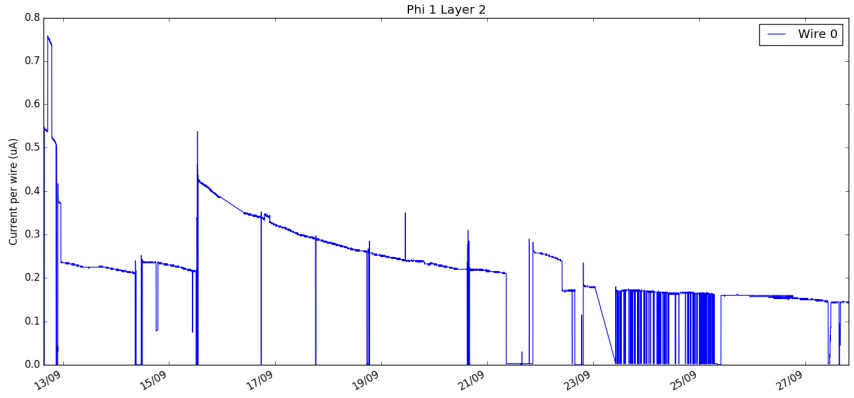

Figure 3.11: Current as a function of time for 2016 data taken with the newly installed wires on the MB1 chamber

to reconnect the high voltage supply in such a way that the monitoring of the current for the new wires was isolated from the rest. In Figure 3.11 the current normalized to each of the 8 new wires can be observed.

It can be observed in Figure 3.11 that when the voltage increases at the beginning of the plot (indicated by the sharp increase of the current) the current decreases faster than during the rest of the irradiation. Some steps in the plot are due to changes in the operating voltage but others appear when changing the attenuation filters in the bunker. Since the gain of the detector cannot be measured directly a new observable was considered that is proportional to the gain of the detector.

$$A = \frac{Current(\mu A)}{Doserate(\frac{mGy}{h})} \tag{3.1}$$

This variable is represented in Figure 3.12. It can be observed that there are increases that are tied to setting higher attenuation filters, which correspond to lower dose rates. This behavior suggests that the response of the current is not linear with the amount of incident dose. The irradiation has been most of the time at a constant dose rate so a correction is proposed in Figure 3.13.

In Figure 3.13 there is a representation of the current per dose rate as a function of the integrated dose with some corrections offsetting the lack of continuity during different configuration periods to smooth the curve and

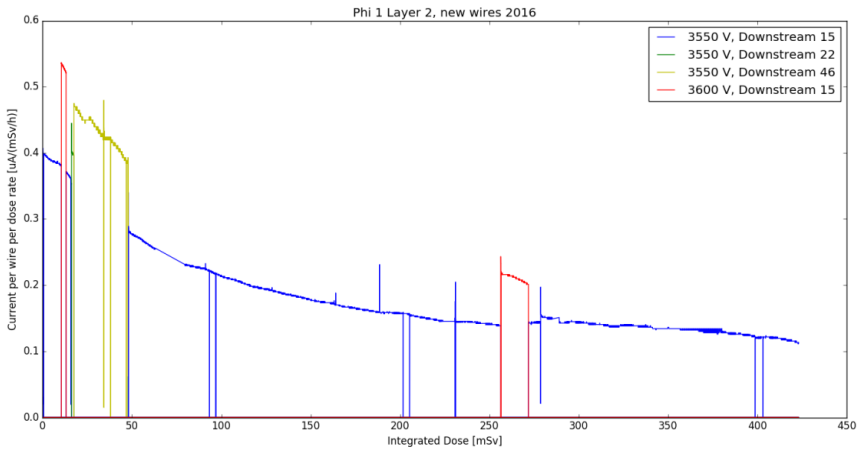

Figure 3.12: Current per dose rate per wire as a function of integrated dose in the replaced wires of the MB1

enable the fitting with a mathematical function to get an estimation of the gain of the chamber after the integration of the full dose expected during the High Luminosity LHC. During the 400 mGy represented in the plot, the gain has decreased to one third the initial value, although some tendency towards stabilization can be seen.

3.4.1.3 Extrapolation to the integrated luminosity at HL-LHC

The variable that will be used to compare with the expectations of the DT chambers at CMS is not the integrated dose, but the equivalent integrated luminosity. To get it, a conversion factor of $0.42 \frac{fb^{-1}}{mGy}$ is applied to the integrated dose to get the equivalent integrated luminosity. This conversion factor calculated from simulation [49] was found to be consistent with the one measured from the gain at GIF++ and CMS comparing the current/dose rate before aging and the slopes of HV current vs instantaneous luminosity shown in Table 3.3.

The gain, estimated as current per wire and dose rate unit, of the replaced wires before the aging process was measured to be 0.4 μ A/wire per $\mu Sv/h$ in GIF++. This can be seen in Figure 3.13 where the source was attenuated using the filter that provides a nominal attenuation of 15. Accordingly, one can derive the foreseen correlations between the current on the wires and the dose rate:

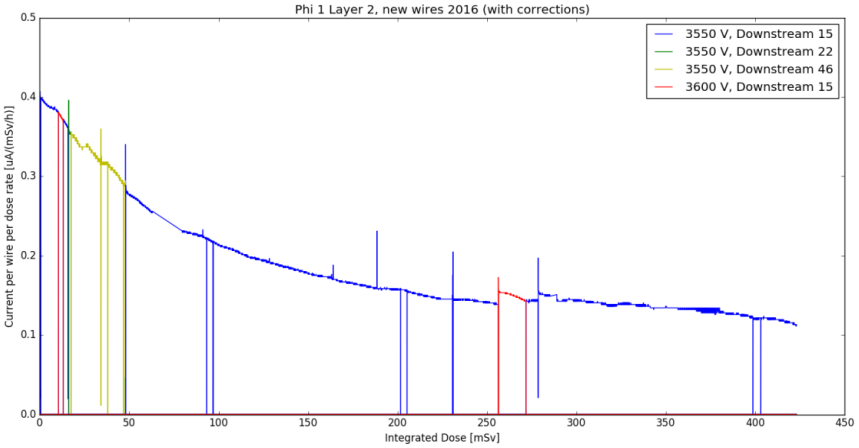

Figure 3.13: Corrected current per dose rate as a function of integrated dose in the replaced wires of the MB1

$$1\ \mu Sv/h = 0.4\ \mu A/wire$$
$$1\ \mu Sv/s = 1440\ \mu A/wire$$
$$1\ \mu Gy/s = 1.3\ \mu Sv/s = 1.872\ mA/wire$$
$$1\ mA/wire = 0.5341\ \mu Gy/s$$

On the other hand, the current dependance in the DT chambers in the CMS detector with the instantaneous luminosity was found to be linear and, in the most exposed chambers, the MB1 chambers of the external wheels,

	Wheel -2	Wheel -1	Wheel 0	Wheel +1	Wheel +2
MB4 S4	3.7 ± 0.3	3.7 ± 0.3	3.1 ± 0.2	3.4 ± 0.2	4.3 ± 0.4
MB4 S3-S5	3.4 ± 0.4	2.1 ± 0.2	2.7 ± 0.2	3.0 ± 0.2	2.3 ± 0.3
MB4 S1-S7	7.0 ± 0.4	5.0 ± 0.3	3.8 ± 0.2	4.6 ±0.3	6 ±0.2
MB4 S12-S8	4.8 ± 0.3	3.0 ± 0.2	2.2 ± 0.2	2.6 ± 0.2	3.7 ± 0.2
MB1	9.9 ± 0.6	4.4 ± 0.3	1.6 ± 0.2	4.2 ± 0.3	10.0 ± 0.6
MB2	2.1 ± 0.2	0.90 ± 0.05	0.50 ± 0.03	0.80 ± 0.05	2.0 ± 0.2
MB3	0.4 ± 0.1	0.4 ± 0.1	0.4 ± 0.1	0.4 ± 0.1	0.4 ± 0.1

Table 3.3: Estimated integrated charge in mC/cm up to the end of HL-LHC operations (3000 fb^{-1}) based on measured currents as a function of instantaneous luminosity.

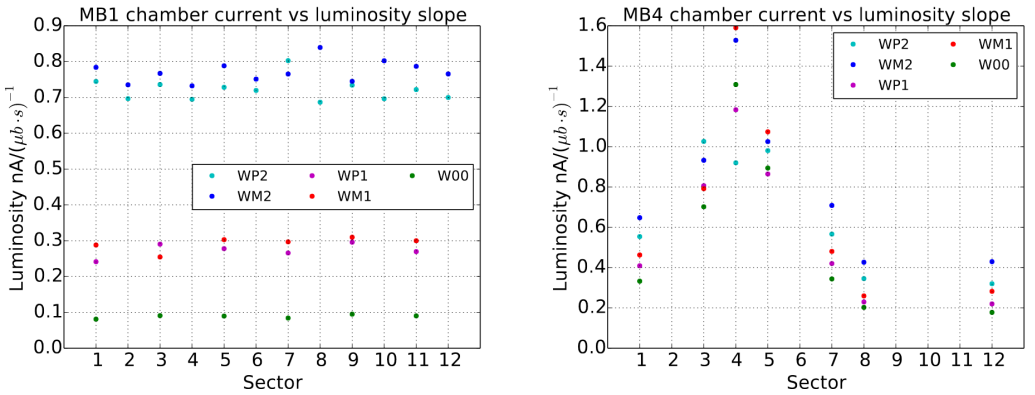

Figure 3.14: HV current dependence on instantaneous luminosity in MB1 (left) and MB4 (right) as a function of the sector number, i.e. azimuthal angle, where 4 and 10 correspond to the top and bottom sectors, respectively, from [23]

have a slope of ~ 0.75 nA/wire per $\mu b^{-1}s^{-1}$ at Point 5, see Figure 3.14:

$$\mu b^{-1}s^{-1} = 0.75\ nA/wire$$

Making the generally accepted assumption of accelerated irradiation that aging is proportional to charge integrated by the wire and that integrated current in CMS and GIF++ have the same impact in aging we can get the same conversion factor changing to the same units:

$$\mu b^{-1} = 0.5341 \times 0.75/10^6\ \mu Gy fb^{-1} = 0.401\ mGy$$

which compares well with the simulation prediction of 0.42 mGy/fb^{-1}.

The conversion to integrated luminosity at HL-LHC enables the comparison with the expected values during HL-LHC and the previous irradiation from 2015. The current per wire for both irradiation periods has been represented in Figure 3.15, normalized to the luminosity rate and as a function of the integrated luminosity.

It can be observed that both wires 0, before and after the exchange, have similar current values at the same integrated luminosity level. Wire 1 presents lower values of current per luminosity rate, this can be due to a non-linear response of the wire current to the incident dose or a different

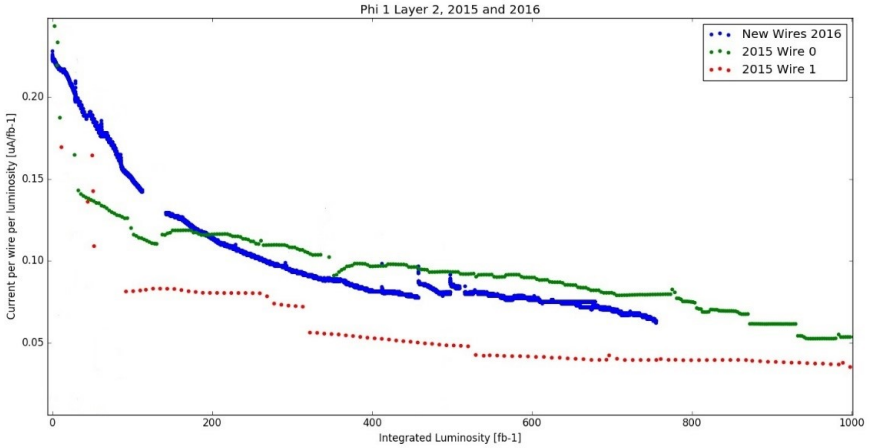

Figure 3.15: Current per instantaneous luminosity as a function of the integrated luminosity of the replaced and old wires

dose distribution in the chamber since the wires are in a different position. Also, the plot shows the tendency for the values of the current to stabilize at higher integrated luminosity. The irradiation during 2015 had frequent changes in the operating conditions and the acceleration factor was one order of magnitude higher as can be seen in 3.3.1.

3.4.1.4 Conversion of the current reduction of the DT chamber to gain

One parameter of great interest for the study is the gain of the detector, in the case of the DT chambers it cannot be measured directly so an estimation was made using a previous study in one of the prototypes [51].

$$ln(Gain) = -16.6 + 8.24 \cdot 10^{-3} \cdot V \tag{3.2}$$

Where V is the operating voltage of the wires. The initial value of the gain was normalized to the value from the fourth Quadruplet prototype (Q4) [52]. The Q4 was fabricated to validate the design of the DT chamber and consists of 4 layers with 16 wires per layer with the same functionality as one DT SL. For the value of 3550 V used during GIF++ irradiation, the resulting gain is 312387.6.

In Figure 3.16 the evolution of the gain as a function of the integrated luminosity is shown. During the first 750 fb^{-1} the gain was reduced to a third

of its initial value and a tendency towards a stable value can be appreciated. 30% of the loss of gain can be observed in the first 100 fb^{-1}, this suggest that the polymerization process responsible for the loss of gain happens faster when the wire has less coating and it saturates at higher values of integrated dose. This saturation in the aging suggests a geometrical hypothesis, namely that when the full wire is covered with coating the deposition slows down. However, the drop of gain itself slows down the generation of radicals to be deposited. The relation between the gain and aging speed is, a priori, not known.

The gain was fitted to a function in order to be able to extrapolate later on to the expected gain values for the HL-LHC:

$$Gain = \frac{1}{a + bL^C} \tag{3.3}$$

$$a = 3.010 \times 10^{-6} \quad b = 7.714 \times 10^{-8} \quad c = 0.739 \tag{3.4}$$

Through this formula, we can calculate for the expected 3000 fb^{-1} of the 10 years of operation of the HL-LHC, the gain is estimated to be 10% its original value if operating with the same conditions. Figure 3.16 was published as Figure 3.8 in The Phase-2 Upgrade of the CMS Muon Detectors Technical Design Report [23].

3.4.1.5 VDC chambers

In order to crosscheck our results an exercise to compare them with other system in CMS has been attempted. The Velocity Drift Chamber (VDC) [53] is a small gas detector installed in the output of the gas line of the CMS DT chambers, with the purpose of measuring the drift velocity. Inside the gas volume a homogeneous electric field is generated by a cathode while two electron beams coming from ^{90}Sr sources cross the volume and move towards scintillators on the opposing side, ionizing the gas along the way. The electrons produced by the ionization drift towards the anode and produce a signal that is compared with the trigger from the scintillators to get a measurement of the drift time. The VDC chambers have a similar working principle to the DT ones, so it is interesting to analyze their behavior in order to better understand the aging process. A similar decay of the current was observed in the VDC chambers installed in Point 5, compared to the MB1 at GIF++. On Figure 3.17 can be observed that the values of the current decay at a steady rate and tend to a constant value. External measurements requested by the RWTH group from Aachen show a Silicon based coating on the wires extracted from the VDC.

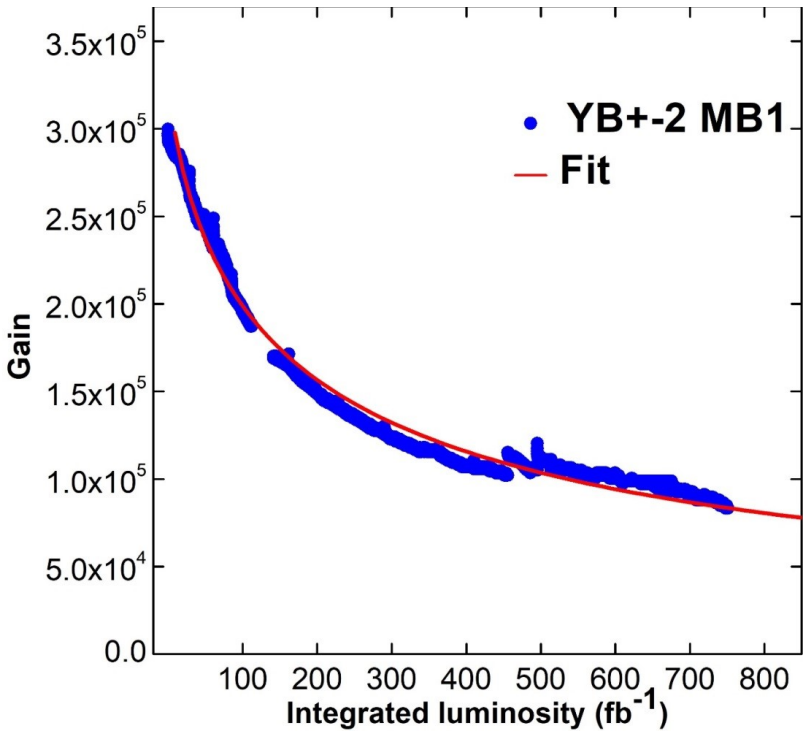

Figure 3.16: Estimated gain as a function of the integrated luminosity for the MB1 YB ±2 chamber at HL-LHC

The aging observed in the VDC and GIF++ chambers suggests the same aging phenomena independently of the spectra of the incident particles (photons from ^{137}Cs and electrons from ^{90}Sr). The differences observed for the different VDCs are due to a normalization in the starting point, each chamber has a different starting value of the current, but it converges to a similar final value.

3.5 2017-2019 Irradiation Campaign

The DT MB2 spare chamber under study was moved inside the bunker in October 2017. Placed vertically in a rail parallel to the wall on the downstream side of the irradiation field at around 3 m from the source and with SL1 facing the source, it was irradiated at a low accelerating factor ($\sim$ 10 times the expected dose rate at HL-LHC) in two campaigns that finished in February 2019. The chamber went through several tests in order to understand its response under irradiation and after a full irradiation period of

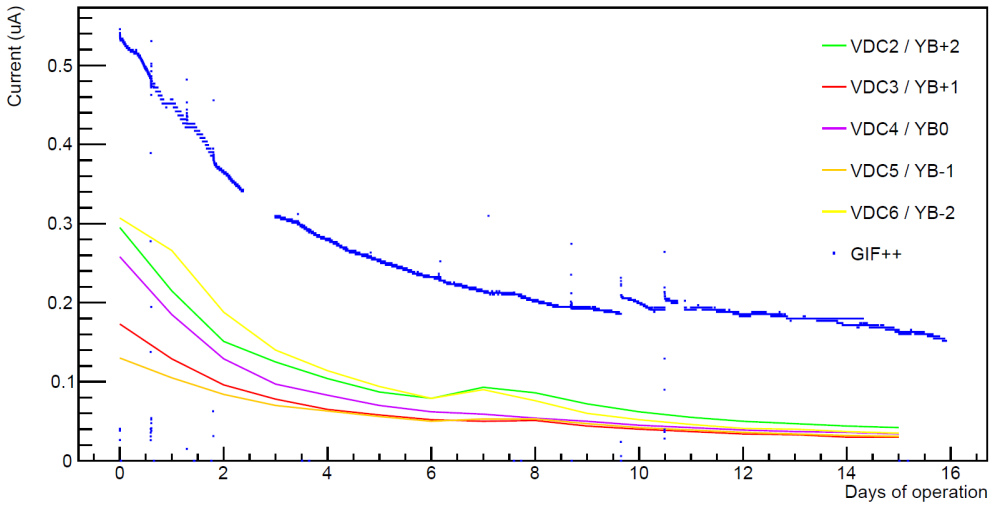

Figure 3.17: Current as a function of time for the VDC and MB1 chamber at GIF++

few months. Weekly scans were performed varying the detector operational parameters (high voltage and front-end threshold) and the attenuation filters of the source (i.e. the background dose rate on the detector). Data from two test beams with muons from the SPS were recorded to characterize the chamber before and after the full irradiation period. The HV scan were taken with anode voltages ranging from 3200 to 3700 V in 50 and 100 V steps. The front-end threshold was also probed for values from 10 to 40 mV in 10 mV steps. We note that, however, most of the data recorded was taken for front-end threshold values of 20 and 30 mV. The chamber was operated with a gas mixture of Ar/CO_2 85%/15% and a gas flow 40 l/h, as it is done with the DT chambers operating at the CMS detector.

3.5.1 Integrated Dose

From October 2017 to February 2019 the DT chamber was irradiated with a constant dose rate of $\sim 0.7\ mGy/h$; the irradiation dose has been measured during this period, as explained in Section 3.2.2. Figure 3.18 shows the total integrated dose as a function of time reaching a total integrated dose of about 2600 mGy. The flat areas in the figure corresponds to periods when the chamber or the source have been kept off, like the Christmas break.

The layers 1 and 4 from SL Phi 1 were irradiated with HV on (3550 V).

The rest of the chamber was irradiated with HV in standby (1900 V) and used as reference.

The vertical grey lines correspond to the 2017 and 2018 winter breaks when the chamber is kept off and the vertical orange lines mark the two irradiation and data-taking periods (eras). During summer 2018, 8 wires were extracted for later inspection and replaced with new non-aged wires.

The dose rate and integrated dose are converted to expected instantaneous and integrated luminosities, respectively, for the MB1 chambers on the external wheels ($YB \pm 2$) expected at the HL-LHC from extrapolation of Run2 measurements as explained in Section 3.4.1.3. The total integrated dose of about 2600 mGy corresponds to about 4800 fb^{-1} of HL-LHC data, which represents 1.6 times the expected integrated luminosity at the end of the HL-LHC. This value is also confirmed from an alternative method using the total integrated charge of a non-aged layer and the integrated charge expected at the HL-LHC.

The irradiation period started in October 2017 with the chamber at the same conditions for all layers. All layers have been irradiated, given that they were placed inside the GIF++ bunker, but only the layers SL1L1 and SL1L4, L1 and L4 from the first SL, were aged by keeping the voltage at 3550 V under the exposure of the radiation source. In this section the results of the hit detection efficiency as a function of the high voltage applied to the anode wires of the chamber are presented as well as the hit efficiency as a function of the integrated and the instantaneous luminosity for cosmic rays and for muons from the CERN SPS beam. The currents as a function of the integrated luminosity are also shown in this section, corresponding to the current on the anode wires when the source is switched on.

3.5.2 Hit Efficiency analysis

The hit efficiency is a relevant figure of merit for the performance of the detector. The efficiency to detect a single hit in a cell of a layer was defined and measured as the ratio between the number of detected and expected hits. The position of expected hits was determined using as probes sets of well reconstructed track segments with associated hits in at least 4 layers in SL3 and at least 1 layer in SL1. For a given segment, the intersection of this track segment with the layer under study determined the position, therefore the cell, where a hit was expected: the cell was considered efficient if a hit was found within it.

$$\epsilon = \frac{Found\ \ hits}{Expected\ \ hits} \tag{3.5}$$

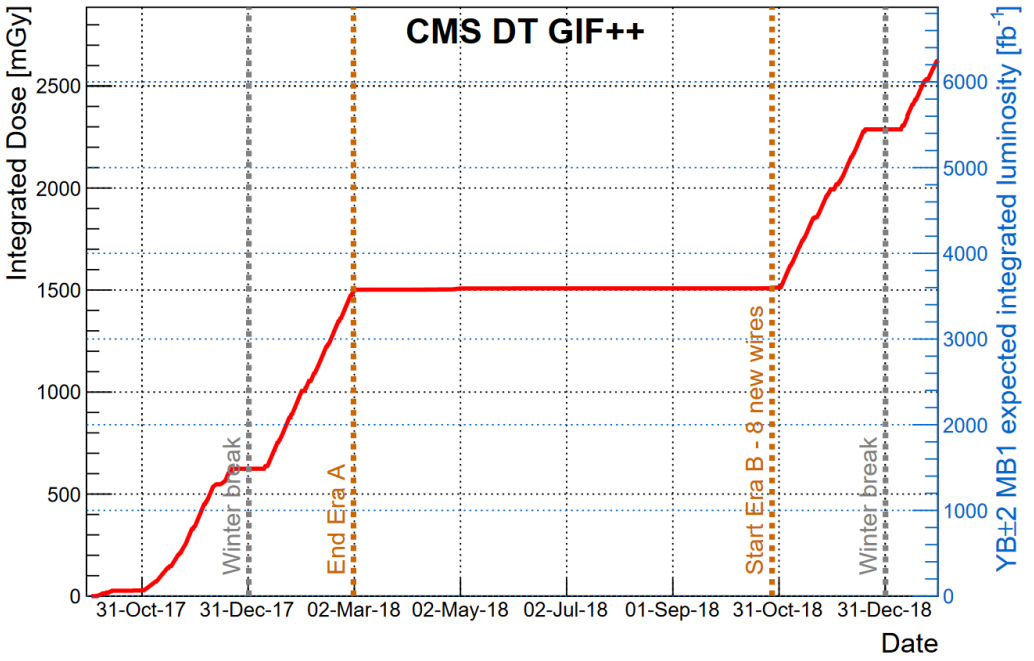

Figure 3.18: Integrated dose [mGy] as a function of time for the 2017-2019 irradiation at GIF++. The axis on the right shows the equivalent expected luminosity for MB1 chambers in the external wheels for the HL-LHC as discussed in 3.4.1.3

During the irradiation period measurements are carried out approximately once a week in order to assess the performance of the detector after a week under irradiation, in particular for the aged layers SL1L1 and SL1L4, which were the ones with the High Voltage ON, while the rest of the layers were in standby. These measurements are performed with the source switched off and cosmic muons. The DT auto trigger was used for cosmic muon tracks, identifying a track in both projections on SL2 and SL3 of the DT chamber, avoiding any bias on the layers irradiated with HV on. Source Off Figure 3.20 shows the hit efficiency as a function of the integrated luminosity for SL1L1 and SL1L4 for a HV value set to 3550 V and a front-end threshold of 30 mV, each of the points in this plot corresponds to the data-taking during HV scans (with the source off) that were collected every week. The total data collected corresponds to twice the expected integrated luminosity of one HL-LHC run. The vertical grey lines correspond to the 2017 and 2018 winter breaks when the chamber is kept off, the vertical blue lines represent the expected integrated luminosity for the HL-LHC run and the

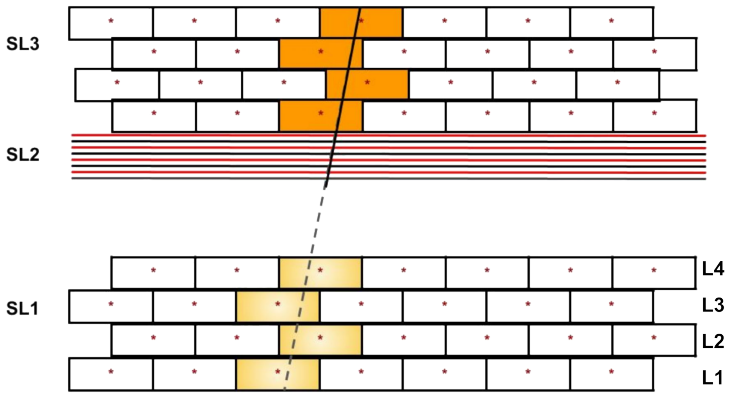

Figure 3.19: Illustration of a DT chamber and a reconstructed track segment with 4 associated hits in SL3 extrapolated to SL1

orange lines mark the two irradiation and data-taking periods between 2017 and 2019. A degradation of the efficiency of about 10% is observed at the accumulated integrated luminosity expected for a full HL-LHC run (with a safety factor 1.6). These results are for the most exposed chambers but can be scaled down according to the expected dose in the different regions of the detector as shown in [54]

3.5.3 High Voltage Scans

Measurements varying the high voltage of the anode wires of the chamber cells are performed systematically since this is a very useful method to evaluate the performance of the chamber.

In Figure 3.21 the efficiency for three different integrated luminosity datasets is presented. In the plot the open circles represent the HV scans for L1 while the full circles represent L4 in order to show the efficiency drop due to the irradiation exposure. After the full irradiation it can be observed that the plateau is shifted to higher High Voltage values, and not being reached at 3550 V any longer. Figure 3.22 shows the comparison of the hit efficiency for the front-end threshold values of 20 mV and 30 mV at the end of the irradiation period, corresponding to an integrated luminosity of 4400 fb^{-1}. As expected, the hit efficiency for the front-end threshold value of 20 mV is higher than for 30 mV, this difference increases in the area below the plateau region.

Scans varying the strip and cathode voltages were performed as well. As conclusion from these studies, the hit efficiency is higher for a lower voltage

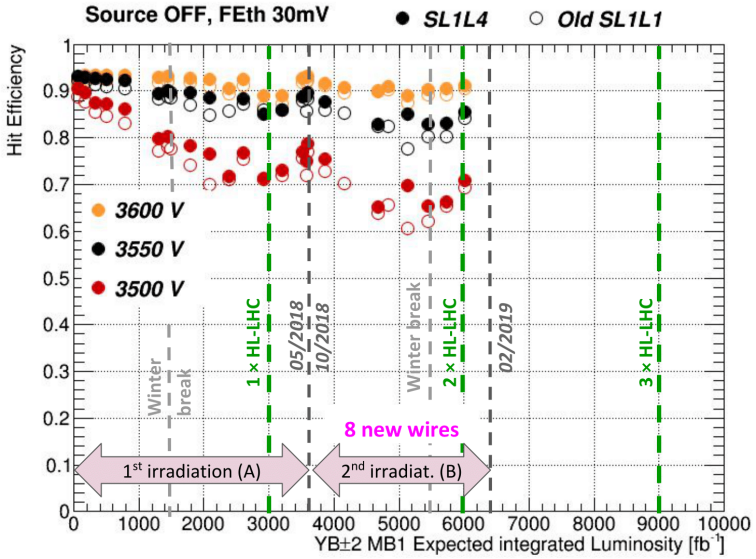

Figure 3.20: Hit efficiency for cosmic muons as a function of integrated luminosity for the aged layers (SL1L1 and SL1L4) at 3550 V with a front-end threshold of 30 mV during the 2017-2018 campaign on an MB2 chamber.

in the strips and whereas does not vary for different values of the cathode voltage. This last point is predicted given that the gas amplification of the cell does not change when changing the cathode voltage.

3.5.4 Results from operation in a Muon Test Beam

As discussed previously, one of the advantages of the GIF++ facility is the combination of a high flux of photons from the radiation source with a high momentum muon beam from the CERN SPS. The external trigger scintillators were used for muon tracks, identifying a track in both projections on SL2 and SL3 of the DT chamber in coincidence with the scintillators, avoiding any bias on the layers irradiated with HV on. Figure 3.23 shows the hit efficiency for the muon beam as a function of dose rate for the aged layers (SL1L1 and SL1L4) at 3550 V and for SL1L3 (non-aged) at 3600 V. The test beam was performed after an irradiation integrated dose equivalent to an HL-LHC integrated luminosity of 2800 fb^{-1}. It is observed that the hit efficiency of the reference non-aged layer does not depend on the background rate. However the efficiency for the aged layers drops due to the irradiation exposure after the given integrated luminosity and in addition the efficiency also depends

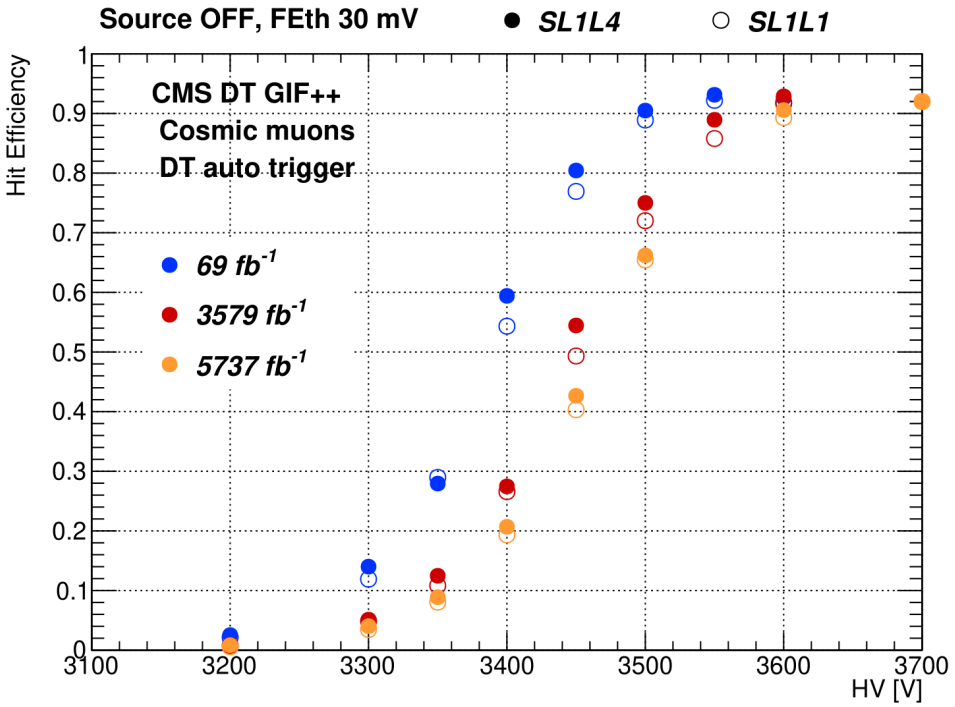

Figure 3.21: Hit efficiency for cosmic muons as a function of HV for the aged layers (SL1L1 and SL1L4) when the source is off and the front-end threshold 30 mV for different values of the integrated luminosity

on the background rate. An inefficiency of around 25% is observed at the expected HL-LHC.

3.6 Summary and Conclusions

In this chapter I have described the work performed during the irradiation of the DT chambers at the GIF++ facility at CERN. Construct and execute on the field tests with the real DT detectors was crucial to evaluate its aging after the expected radiation accumulated during its operation under HL-LHC.

At GIF++, large area detectors can be placed and irradiated during months with a very intense gamma source. This facility allowed us to perform accelerated tests that accumulate all of the dose expected at HL-LHC but integrated over the course of weeks or months.

My contribution to the realization of these tests was crucial and span

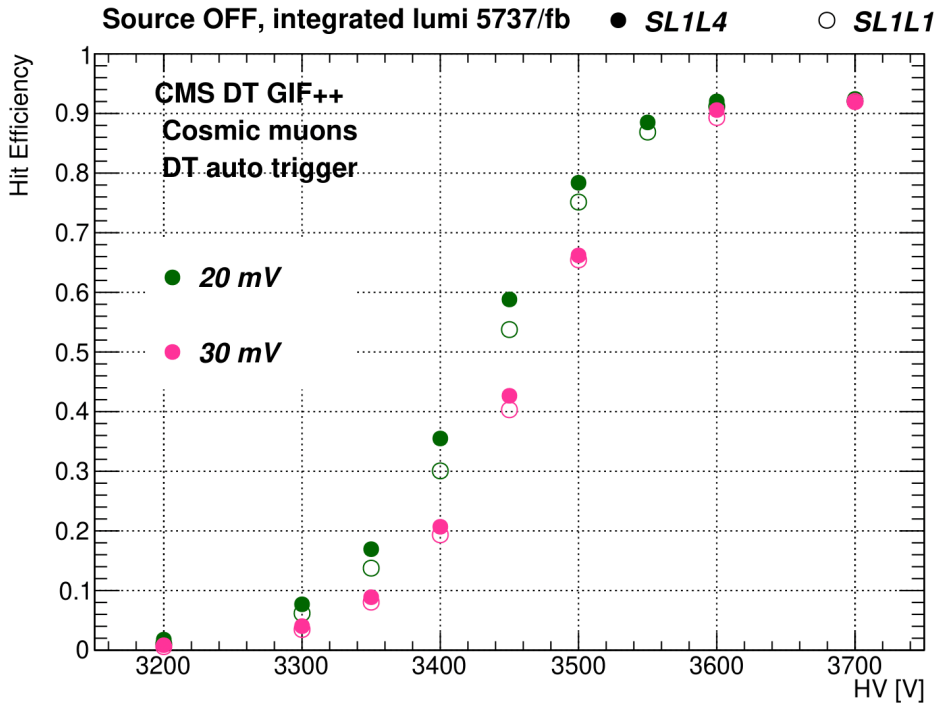

Figure 3.22: Hit efficiency for cosmic muons as a function of HV for the aged layers (SL1L1 and SL1L4) when the source is off and the front-end threshold values of 20 and 30 mV

from the installation and commissioning of the system, data taking, measurements of the radiation dose, analysis of the data and detailed study of the currents and the gain of the DT detector. These studies are the core of the estimation of the loss of gain and of the measurements that allow to extrapolate the obtained data of hit efficiency to the corresponding expected integrated luminosity.

The tests performed at GIF++ have covered many years of different conditions operations, and obtaining coherent results, where the different variables are under control, has been challenging.

After extensive irradiation campaigns the results confirm that a coating forms surrounding the wire, and creates a reduction of the hit efficiency of the detector. The deposit is confirmed to be made of carbon and silicon. Carbon can be found in the gas mixture and silicon on the glues present inside the cell. The glues present inside the cell can produce outgassing, releasing products that can react with other substances present in the gas

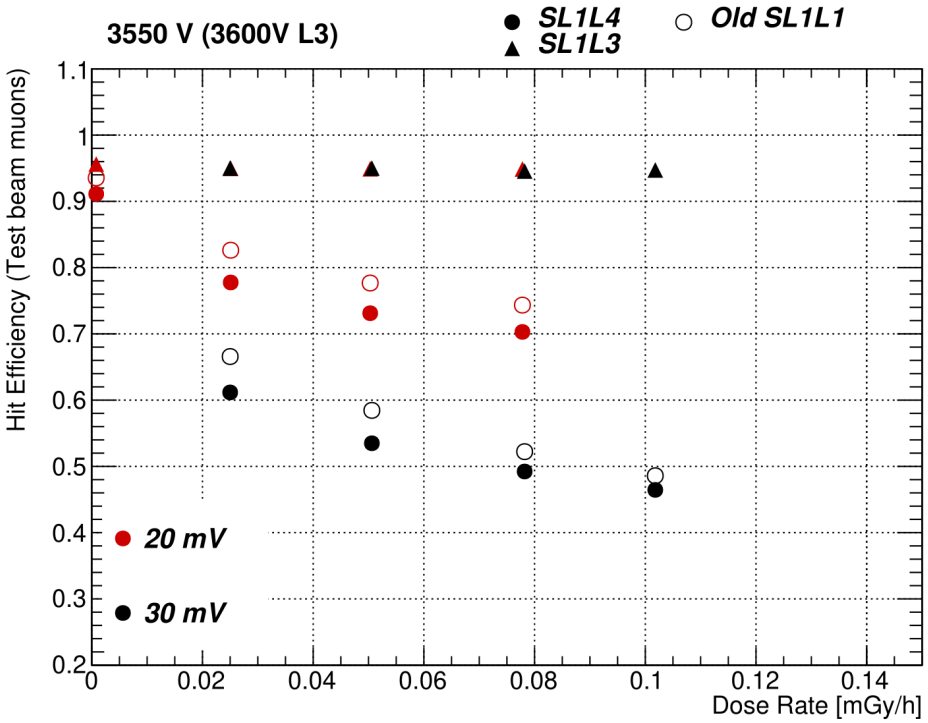

Figure 3.23: Hit efficiency for test-beam muons as a function of dose rate for the aged layers (SL1L1 and SL1L4) and the non-irradiated layer SL1L3

volume.

Still, the confirmation that the observed hit efficiency loss is relatively mild for the majority of the DT detector remains. The results obtained here have been critical to be able to perform estimations of the expected DT detector degradation during its operation at HL-LHC and use this information to create the aged samples to study the performance of improved trigger algorithms for the future operation of CMS.

Chapter 4

Interpretation and modelling of GIF++ results

In this chapter, I focus into the interpretation and modeling of experimental results obtained from the GIF++ facility at CERN, to better understand the aging phenomena observed in the DT chambers. The primary objective is to construct a mathematical model that accurately represents the degradation processes observed.

The approach presented is rooted in classical aging theories for gaseous detectors, which emphasize changes in the detector's electrical properties over time, being its more sensitive part, its wire, and thus, the model focuses on it.

With the help of some simulations performed in the GARFIELD++ [55] software, several hypothesis have been performed about the behaviour of the wire in the different conditions and the parts that are affecting to a higher extend the degradation of its behaviour under the received dose.

Through this model, we aim to capture and quantify the impact of prolonged irradiation exposure on the detector's performance, providing insights into both the mechanisms of aging and the resulting performance degradation. Comparing the model results to the data obtained at GIF++, a better understanding of the process involved is achieved. One of the highlights from this model as will be seen, is that it also allows explaining the behaviour of the loss of hit efficiency with high dose rates.

4.1 Baseline hypothesis for aging

As can be found in the literature [56], the classical aging scenario is based on pollutants being developed in the gas volume of the chamber and then, assuming they are ionized, or eventually get ionized due to the incident radiation, they drift towards one of the electrodes, where they polymerize growing a deposit.

For the DT chamber, the results from previous chapter show a decrease of gain which seems to follow quite well the expectations from a classical aging. No hints of Malter effects have been spotted on the cathodes (no self sustained currents increase) nor other relevant and outstanding effects, apart from a monotonous loss of gain with irradiation, which translates into a loss of hit efficiency.

The SEM images also show an increased wire diameter, which goes from 56 μm in diameter up to 65 μm when the wire is aged. The installed wires are 50 μm in diameter, so it can be assumed that the wire diameter has increased by 6 μm due to the removal of the tension of the wire. Making the addtional hypothesis that this reduction in the wire diameter due to the tension is independent of the coating, we conclude that the coating covered the surface to become a wire of 59 μm by the time of the image. That is, the radius did increase from 25 μm to 29.5 μm. These wires were extracted after a very long radiation period in the MB1, where the major loss of gain had already happened and a plateau had been reached. In what follows, we will assume that this is the estimated diameter for a deeply aged wire.

From the SEM images, the outside cover of the wire has lost its smooth surface and its clearly made out of rounded deposits. The analysis of those deposits seems to show a very large component of Carbon, Oxygen and Silicon, although the relative amounts vary, with Carbon being associated to a faster drop in gain. As mentioned in previous chapter, the origin of Silicon comes from the glue used in the cathodes.

The principal hypothesis is that gamma photons from the GIF++ source, which have a large energy (662 keV), can break the different molecules in the gas. Even without external pollutants, the dissociation energy of CO_2 into CO and oxygen is 2.94 eV and the consequent dissociation energy of CO is 11 eV. Also a certain fraction of water vapor is present in the gas, being the energy of breaking apart an H_2O molecule of 9.54 eV. The ionization energy of Hydrogen is 13.6 eV, from Carbon is 11.26 eV, etc. Apart from other components outgassing such as the cables plastic covers, electronic boards, etc., there is plenty of opportunities to generate in the gas itself CH_4, which tends to create chains of hydrocarbon polymers.

Let's assume then that the main aging effect is a result of the wire getting covered with a deposit layer which composition is based on hydrocarbon polymers. The impact of this deposit on the cell performance depends somehow on the electrical performance of this deposit which has a resistivity and dielectric constant which in principle, are not known.

4.2 Modeling of the voltage in an aged wire

We are going to assume that the electrical performance of a wire covered by a deposit can be modeled by a wire covered by a deposit cylinder with a given resistivity and electrical permittivity and surrounded by another cylinder that acts as cathode. The assembly is very similar to a coaxial wire with two different materials surrounding the wire cylindrically.

The DT cell has rectangular shape as can be seen in Figure 4.1, however, in the following, we are going to use the approximation that the symmetry is cylindrical. In Chapter 3 we verified experimentally that the gain in the chamber depends on the strip voltage, with very little dependence in comparison with the cathode voltage. Accordingly, we are going to consider the radius of the outer cylinder is the distance to the strip, which is at 6.5 mm from the wire and connected to 1800 V.

The goal is to calculate the effective voltage and electric field at the border of the external coating, since this will be the actual voltage that the electrons from the muon tracks will see for drifting and during the avalanche process.

Let's start with the description of the electrical field of a wire inside a cylinder. Considering a geometry as in Figure 4.2, the electrical field surrounding the wire and within the cathode is described by equation 4.1 and is proportional to the inverse of the radius to the wire.

$$\vec{E}(r) = \frac{\lambda}{2\pi\varepsilon_0\varepsilon_r r} \tag{4.1}$$

where:

- λ is the linear charge density.
- ε_0 is the permittivity of free space.
- ε_r is the permittivity of the medium between the wire and the cathode.
- r is the radial distance from the wire.

The corresponding voltage that can be found at each point inside the cylinder can be found by integrating the electric field.

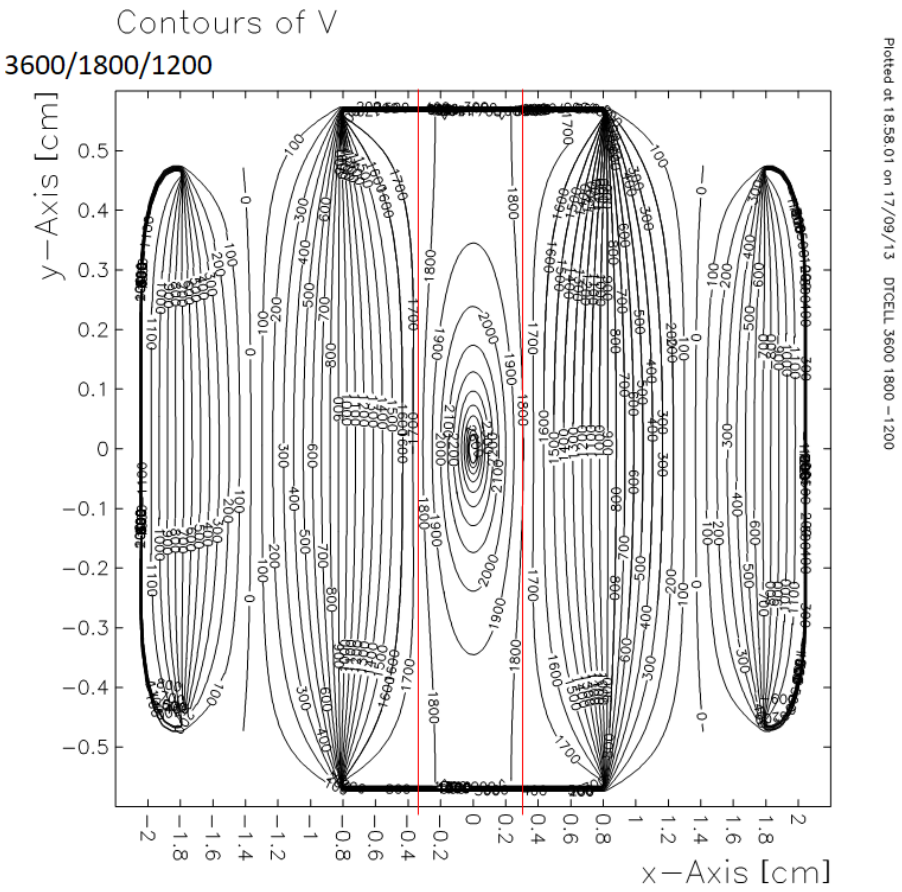

Figure 4.1: Representation of the equipotential lines inside the drift cell with the anode at 3600 V, the strips at 1800 V and the cathode at -1200 V.

$$V(r) = -\int_a^r \vec{E}(r)\, dr \tag{4.2}$$

The resulting voltage is described by equation 4.3. As can be seen, the voltage at each point decreases logarithmically with distance from the wire.

$$V(r) = V_a - \frac{\lambda}{2\pi\epsilon_0\epsilon_r} \ln\left(\frac{r}{a}\right) \tag{4.3}$$

And the capacity of the wire per unit length can be expressed as in equation 4.4:

$$C = \frac{2\pi\epsilon_0\epsilon_r}{\ln\left(\frac{b}{a}\right)} \tag{4.4}$$

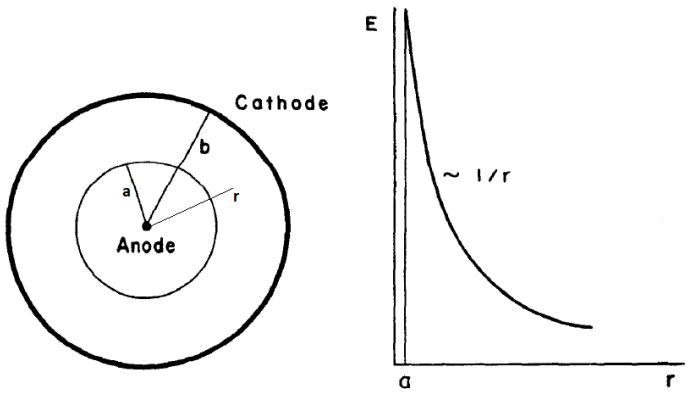

Figure 4.2: Diagram of a wire of radius a inside a cylinder of radius b (left) and representation of the electrical field between the anode and the cathode. This is the typical construction of a drift tube.

For the case of a clean wire, the relative electrical permittivity can be considered that of the air, thus, $\epsilon_r = 1$. Let's now consider the situation in which we also have a coating covering the wire. This coating will have a given electrical permittivity ϵ, which can be reference to the vacuum permittivity through ϵ_r. In addition, this coating will have a given resistivity, different from that of the gas. The assembly, together with the nominal voltages at each point and the radius of each cylinder can be seen in Figure 4.3.

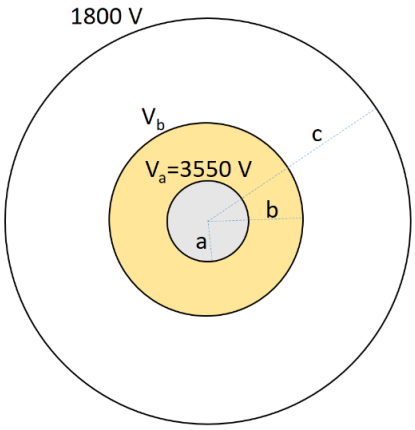

Figure 4.3: Representation of the assembly of cylindrical wires through which we model the inner of the DT cell when coating has been attached to the wire.

This assembly can be modeled through the assumption that they repre-

sent two capacitors in series as in Figure 4.4 with their corresponding resistance in parallel. Capacitor 1 is the capacitor formed by the inner wire and the coating, and capacitor 2 the one formed by the coating and the external strip (which has been modeled as a cylinder).

On top of this, we have a resistance in parallel with each capacitor. The one of the gas is very large ($\sim 10^{16}$ $\Omega \cdot$m) and can basically be ignored. Instead, the one of the coating has an important impact in the presence of large ionization currents, as will be shown below.

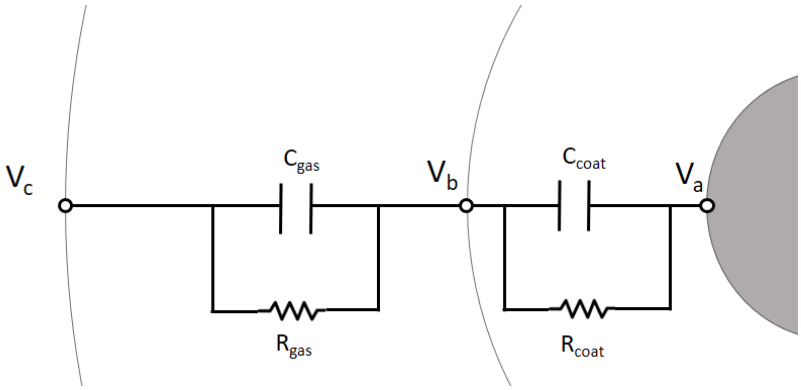

Figure 4.4: Representation of the two capacitors in series through which the DT cell with its wire and its coating are modeled.

The capacitance of each of the capacitors is given at equation 4.5 and equation 4.6:

$$C_1 = \frac{2\pi\epsilon_0\epsilon_r}{\ln\left(\frac{b}{a}\right)} \tag{4.5}$$

$$C_2 = \frac{2\pi\epsilon_0}{\ln\left(\frac{c}{b}\right)} \tag{4.6}$$

The performance of this equivalent circuit models the signal generation in the cell. However, neither the resistor nor the capacitance can explain the observed loss of gain nor loss of hit efficiency when the current flowing in the cell is small (cosmic data). We have to look at the intrinsic amplification capability of the wire detector, the avalanche close to the wire, to explain what we observe.

4.2.1 Voltage versus the distance to the wire's center

If we assume that no current is being injected into the system, we can obtain the voltage at each point in space "r" from equations 4.1 and 4.3. This can

be done for each of the three different regions:

- $r < a$: This is the metal of the wire and therefore, its permittivity is infinite. Its voltage is fixed for all points in space and equal to V_a, that is, 3550 V. The electrical field inside the wire is 0.

- $a < r < b$: This is the coating region. The voltage is expressed as:

$$V(r) = V_a - \frac{\lambda}{2\pi\epsilon_0\epsilon_r} \ln\left(\frac{r}{a}\right) \tag{4.7}$$

  For r=b:

$$V_b = V_a - \frac{\lambda}{2\pi\epsilon_0\epsilon_r} \ln\left(\frac{b}{a}\right) \tag{4.8}$$

- $b < r < c$: This is the region of gas, where we assume a resistivity and permittivity like air. It ends on the cathode (r=c) and the voltage can be expressed as:

$$V(r) = V_b - \frac{\lambda}{2\pi\epsilon_0} \ln\left(\frac{r}{b}\right) \tag{4.9}$$

  For r=c:

$$V_c = V_b - \frac{\lambda}{2\pi\epsilon_0} \ln\left(\frac{c}{b}\right) \tag{4.10}$$

From 4.8 and 4.10 we can resolve the two incognitas (λ and V_b) and calculate the voltage at any point r.

Explicitly:

$$\frac{\lambda}{2\pi\epsilon_0} = \frac{V_b - V_c}{\ln\left(\frac{c}{b}\right)} \tag{4.11}$$

and

$$V_b = \left[\frac{V_a\epsilon_r}{\ln\left(\frac{b}{a}\right)} + \frac{V_c}{\ln\left(\frac{c}{b}\right)}\right] \left[\frac{1}{\frac{\epsilon_r}{\ln\left(\frac{b}{a}\right)} + \frac{1}{\ln\left(\frac{c}{b}\right)}}\right] \tag{4.12}$$

The results can be seen in Figure 4.5 where the voltages at each point inside the cylinder have been calculated for different wire diameters. As can

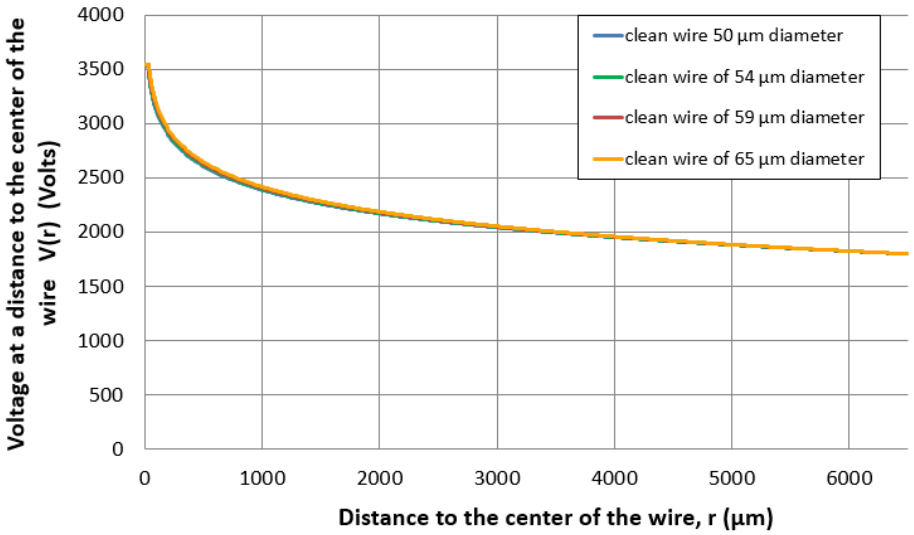

Figure 4.5: Voltage at each position inside the simulated DT cell versus the distance to the center of the wire. Four different configurations of wire diameter are represented, having all of them a similar behaviour.

be seen, all of them start at 3550 V, voltage at the inner wire, and drop to 1800 V at 6.5 mm, which is the voltage at the strip location.

All of the cases behave pretty much the same, except in the region close to the wire, where larger differences can be seen. This region in the vicinity to the wire has been enlarged in Figure 4.6. As can be seen, the voltage drops at the same slope for each wire diameter but the point where they start to drop changes because of the actual diameter.

4.2.2 Electric field versus the distance to the wire's center

The electric field for different radius of the coating is represented in Figure 4.7. There we can see very clearly how the maximum electric field drops depending on where the coating ends. This position where the coating ends is important because this gradient of electric field has a strong impact on the actual avalanche that can be created. For a clean wire of 50 μm, the maximum electric field of 125 kV/cm but it will reduce to 107 kV/cm for an aged wire of 59 μm. This reduction of the maximum electrical field will reduce the gain accordingly.

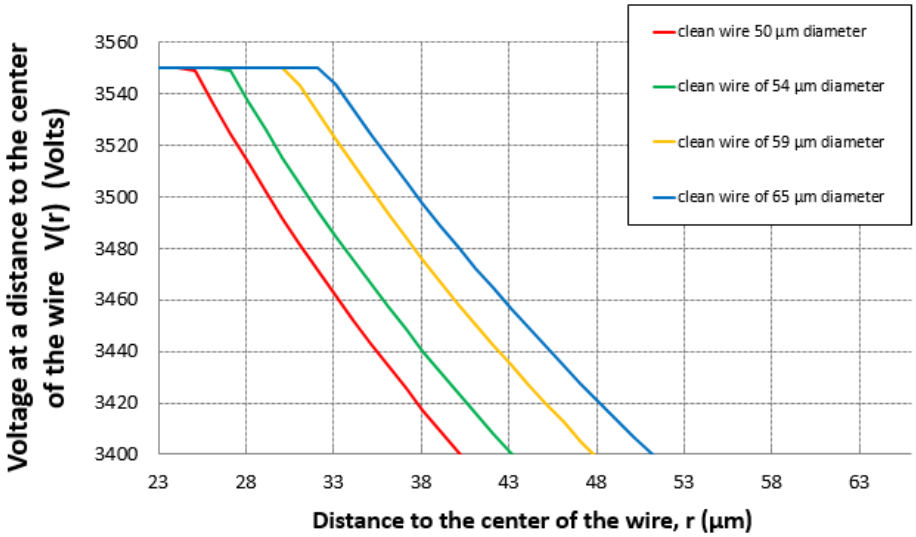

Figure 4.6: Voltage at each position inside the simulated DT cell versus the distance to the center of the wire. Region close to the wire has been enlarged for easier visualization. Different configurations of wire diameter are represented.

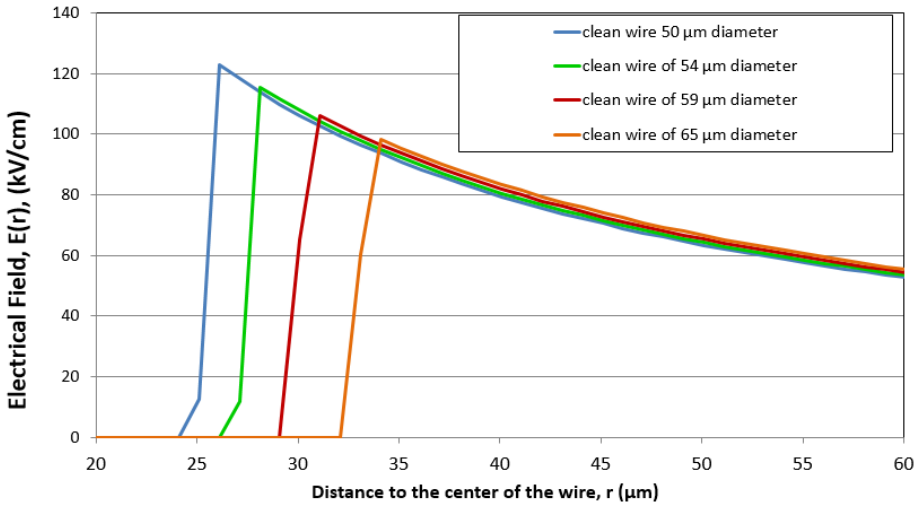

Figure 4.7: Electric field for different configurations of the wire diameter as a function of the position versus the wire center. As can be seen the maximum electric field gets very much reduced as one moves away from the wire's center.

4.2.3 Effect of the dimensions of the outer cylinder

Let's represent the voltage at each point depending on the selection for the outer cylinder radius and voltage. As can be seen in Figure 4.8, having the

strips at 6.5 mm connected to 1800 V, maintains a higher voltage within the cell, and does not allow such a drastic voltage drop that would happen if we only had as second electrode the cathodes at -1200 V. This means, that the strip allows to have a smoother potential as a function of the distance to the cathode, which will translate in a more uniform drift velocity and more square time box.

At the beginning of the chapter in Figure 4.1 we could also see the simulation of the drift lines within the cell, and we could see that, horizontally, we were reaching 1800 V at 3.1 mm, instead of at 6.5 mm.

As can be seen in Figure 4.8 when we set 1800 V at 3.1 mm, the curve is pretty much the same as with the 6.5 mm one. This means that the vertical/horizontal asymmetry that we have inside the cell is small and that the behaviour is very similar in the regions of the wire facing the strips, versus the regions of the wire that face the cathodes.

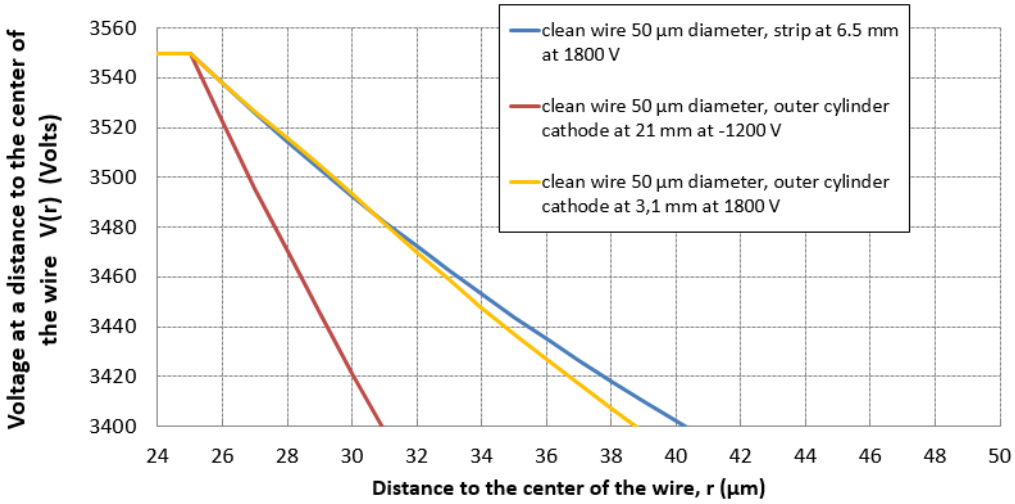

Figure 4.8: Voltage as a function of the distance to the center of the anode wire for different diameters and voltages of the outer cylinder. As can be seen the effect of the strip is to smooth the voltage drop inside the DT cell.

4.2.4 Gain as a function of the electric field

In what follows, we will perform some calculations to obtain approximate values of the expected gains for different wire diameters.

Gaseous detectors rely on the avalanche process to achieve high gains [57]. An avalanche process gets originated in the vicinity's of the wire due

to the intense electrical field. When the strength of the field is above about 10^4 V/cm, an electron can gain enough energy between collisions to cause secondary ionization in the gas. After such an ionizing collision, two free electrons exist in place of the original one. In an uniform electric field under these conditions, the number of electrons will grow exponentially as they are drawn in a direction opposite to that of the applied electric field. The production of such a shower of electrons is called a Townsend avalanche and is triggered by a single free electron.

The growth of the population of electrons is terminated only when they reach the anode. The total number of electrons produced in the avalanche can easily reach 1,000 or more, and the amount of charge generated in the gas is also multiplied by the same factor. This process is the basis for obtaining gaseous detectors with high sensitivity and therefore, it is important to maintain a relatively high gain in the detector to maximize the signal to noise ratio. Noble gases are used because, contrary to other gases such as oxygen, they don't tend to collect the free electrons in the gas and therefore, the avalanche can be formed.

However, in a Townsend avalanche there are many excited molecules formed and when these excited molecules return to their ground state, they emit an ultraviolet photon. This light may travel centimeters through the gas before being reabsorbed, either in a photoelectric interaction involving a less tightly bound shell of a gas atom or at a solid surface. If a free electron is liberated in this absorption process, it will begin to drift toward the anode wire and can produce its own avalanche. By this mechanism, one avalanche can breed another, spreading throughout the entire volume of the gas-multiplication region around the anode wire. This uncontrolled spread of avalanches throughout the entire detector is known as a Geiger discharge. At some point there is the need to finish the avalanche so not to reach the Geiger-Müller state. A quencher gas needs to be added that can absorb some of the electrons.

In our case, the spread of avalanches is inhibited through the addition of a small amount of a second gas (for example, CO_2) that absorbs the ultraviolet photons without producing free electrons.

The Townsend avalanche takes place in a time span of less than one microsecond under the typical conditions present in a proportional counter. Therefore, this charge normally contributes to the pulse that is observed from the interaction of a single incident quantum.

The avalanche process in a DT cell is characterized by the Townsend coefficient α, which represents the number of ionizing collisions per unit length. The gain G (also called the gas gain) is defined as the total number of elec-

trons collected by the anode per initial electron. It characterizes how much the initial ionization caused by a passing particle is amplified through secondary ionization processes. The gas gain is calculated by integrating the Townsend coefficient over the distance from the wire to the cathode. The gas gain G can be expressed as in equation 4.13:

$$G = \exp\left(\int_{r_0}^{r_c} \alpha(r)dr\right) \tag{4.13}$$

where:

- α(r) is the Townsend coefficient, which depends on the electric field E(r).
- r_0 is the radius of the anode.
- r_c is the radius at which the avalanche starts.

The Townsend coefficient α(r) (equation 4.14) is typically an exponential function of the electric field E(r):

$$\alpha(r) = A\exp\left(-\frac{B}{E(r)}\right) \tag{4.14}$$

where A and B are constants that depend on the gas type and pressure.

It is clear that the larger the electric field, the larger the gain through a double exponential, which is what characterizes the explosive nature of this avalanche formation or secondary ionization.

The avalanche multiplication factor is a function of the applied voltage, gas type, pressure, and the geometry of the detector.

Small size electrodes, create large gradients of electric field. Thus, the smaller the wire, the higher the electric field in its surroundings and thus, the larger the acceleration of the electrons and the larger the avalanche process, and consequently, the larger the gain.

4.2.4.1 Estimation of the Townsend coefficient

Obtaining reliable values of the Townsend coefficients is relatively challenging because of the exponential dependence of α on the field which may induce large errors in the estimate even for small differences in the value of the parameters used.

Very often, they are obtained experimentally but also the dependence on the exact electrical field gradient induces large errors. The general practice is using simulation programs such as MAGBOLTZ [58] to perform this computations.

In what follows we will perform a simulation with the program GARFIELD++, which is a toolkit for the detailed simulation of particle detectors based on ionisation measurement in gases or semiconductors. The main area of application is currently in micropattern gaseous detectors.

An interface to the MAGBOLTZ program is provided for the computation of electron transport properties in nearly arbitrary gas mixtures. MAGBOLTZ solves the Boltzmann transport equations for electrons in gas mixtures under the influence of electric and magnetic fields.

4.2.4.2 Results from GARFIELD++ simulations

A simulation of the DT cell in GARFIELD++ with the different electrodes can be seen in Figure 4.9. In GARFIELD++ it is not possible to simulate crossing nor finite planes, accordingly, the strips and cathodes have been emulated by a consecutive set of wires at the same voltage.

The medium has been selected as Ar/CO_2 85%15% and in Figure 4.10 we can see the drift velocity for the gas mixture selected which matches well the plateau of expected 54.5 μm/ns.

The electric field on each point can be seen in Figure 4.11.

From this simulation, we can obtain the Townsend coefficients for each value of the electric field. The results obtained are presented in 4.12.

Using this calculated Townsend coefficient and the electrical field on each point, which we have obtained in Figure 4.7, and integrating as per equation 4.13, we can obtain the actual gain for each wire diameter.

It is worth mentioning that this calculation is very sensitive to errors in the α parameter and in quantization errors due to the double exponential. Careful parametrization of α has been done based on the results of 4.12. In addition, it was clear that a contribution coming from the cathode needed to be added, since even if smaller effect than the strip, it does play a role in the gain of the DT cell. Accordingly, the electric field gradient has been estimated for the region up to the cathode, and the corresponding Townsend coefficients have been obtained and taken into account for obtaining the final gains.

Through the integration of the Townsend coefficients for all the radius, the gas gain has been obtained. The gains in logarithmic scale achieved by wires of different radius can be seen in Figure 4.13. The values are also

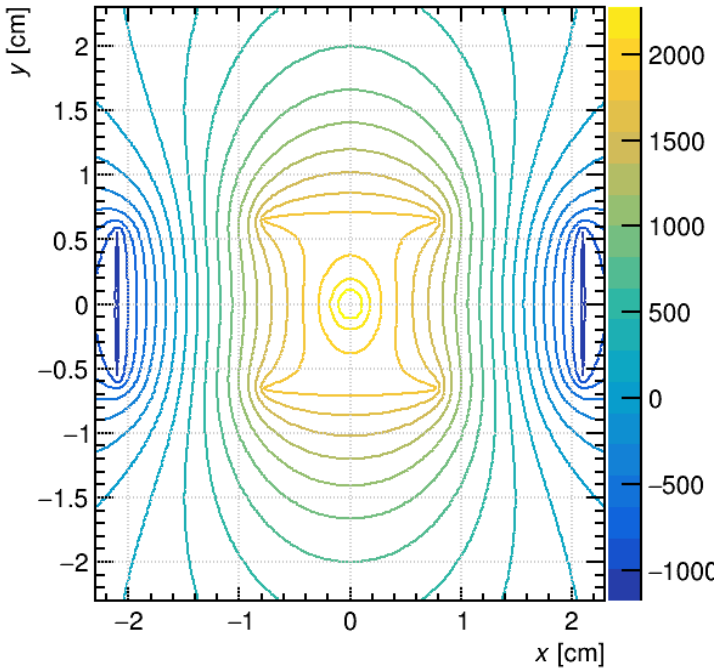

Figure 4.9: Equipotential lines inside a simulated Drift Cell in Garfield with the wire at 3550 V (50 μm diameter), the cathodes at -1200 V (11.5 mm wide) and the strips at 1800 V (16 mm wide).

represented in Table 4.2.

As can be seen, at the nominal voltage of 3550 V, the drop of gain goes from 3.23 10^5 to 1.12 10^5 for an increase in radius of 4.5 μm.

Voltage	**25 μm**	**27 μm**	**28 μm**	**29 μm**	**29.5 μm**	**32.5 μm**
3500	2.16	1.35	1.08	0.88	0.79	0.46
3550	3.23	1.96	1.54	1.24	1.12	0.63
3600	4.91	2.87	2.24	1.77	1.59	0.88
3700	11.76	6.42	4.85	3.74	3.31	1.71

Table 4.1: Gain (to be multiplied by 10^5) calculated from the Garfield++'s Townsend coefficients for different voltages and different values of the wire radius.

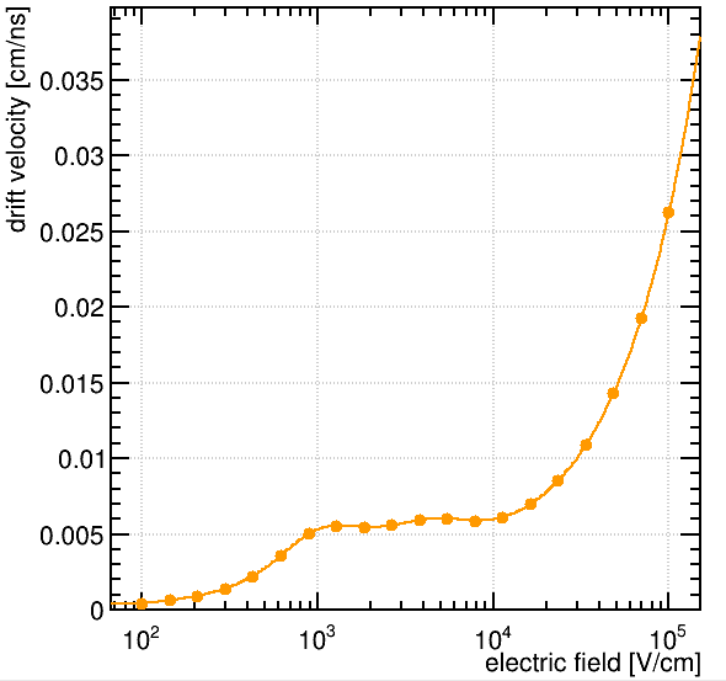

Figure 4.10: Drift velocity in a simulated DT cell in GARFIELD++ as a function of the electric field. As can be seen, for the region of 1 kV/cm to 10 kV/cm, the drift velocity is constant, as expected in our cells.

4.2.5 Comparison of the gain model with GIF++ data

Let's come back to the results obtained at GIF++ that have been presented in Chapter 3. First we compare the model results of the gain versus the wire radius from previous section with the gain observed in Figure 3.16 for the MB1 before aging and see that overall the values are similar and appear to match well. After integrating 750 fb^{-1}, we can see in Figure 3.16 that the drop of gain in the MB1s cells goes from 3.2×10^5 to 7.5×10^4. Unfortunately we do not have coating measurements for all irradiations, but we can take the increase of radius that we see with the SEM from 50 μm to 59 μm as an asymptotic upper value to what the coating can grow for very large integrated doses since this picture was obtained after a very large irradiation at large irradiations factors, O(100). After aging, the gain loss is larger in the MB1 case than in our model by almost a factor 2.

Now we will crosscheck if similar results can be obtained from the data of the MB2 chamber irradiation. Let's try to calculate the gain drop between the curves seen in Figure 4.14. There we can see that the DT cell behaves as if the total shift of voltage between the smallest accumulated dose and the

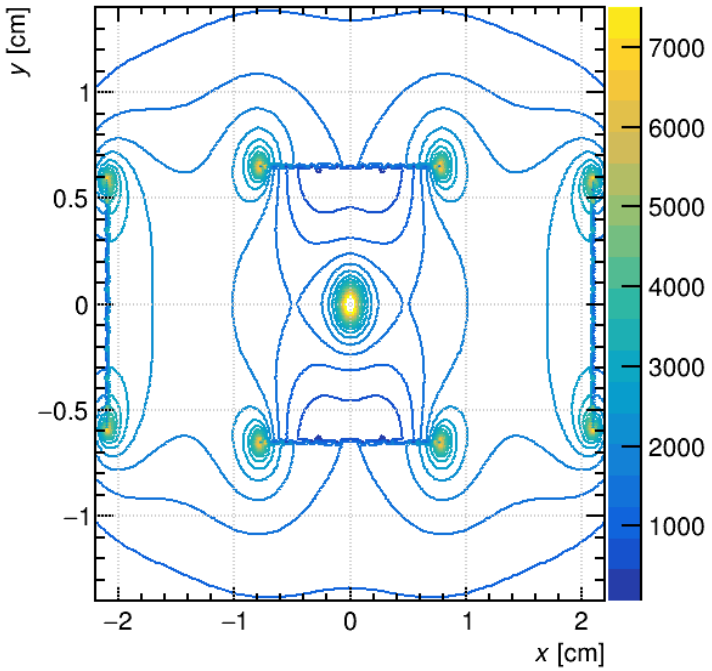

Figure 4.11: Electrical field in a simulated DT cell in GARFIELD++.

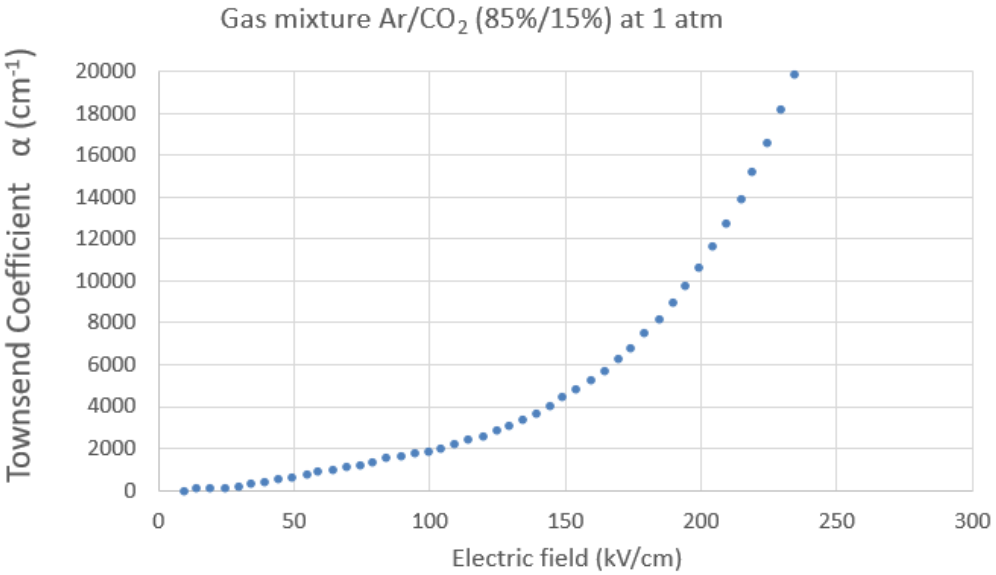

Figure 4.12: Townsend coefficient as a function of the electric field for the DT gas mixture.

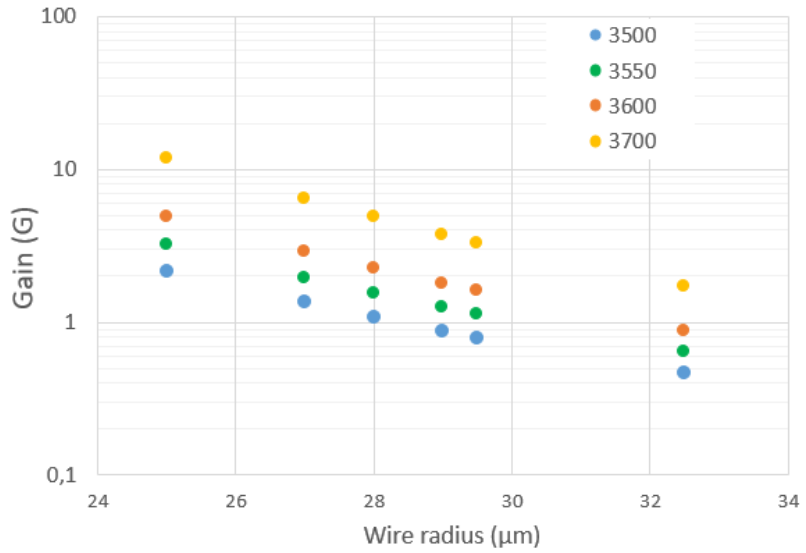

Figure 4.13: Values obtained for the gain of a DT cell (to be multiplied by 10^5) as a function of the radius using the Townsend coefficients obtained from Garfield++.

largest, would have been approximately 80 V, that is, from 3550 V to 3470 V. The voltage shift at half efficiency is marked in Figure 4.14.

Let's assume that the nominal gain of 3.2 10^5 is correct, since it has also been measured at the laboratory several times, and let's cross check which is the gain for the aged scenario of the MB2 chamber.

The question is if we can measure the gain from the hit efficiency data in Figure 4.14.

The average pulse height is directly proportional to the gain, because it is due to the number of electrons that have been created in the Townsend avalanche.

The assumption is that the quasi-linear transition in wire HV corresponds to the gains that are gradually crossing the FEB threshold, the distribution not being a step function from the spread in signals for a give gain.

Regardless of the pulses spread, when the hit efficiency drops to half, half of the hits have a height enough to pass the FEB threshold and half are incapable of doing so.

This means that the average pulse height when efficiency is halved corresponds to the FEB threshold.

The method relies on Figure 4.15, which is obtained experimentally with the DT chambers as in publication [51]. Thus, inverting the known relation

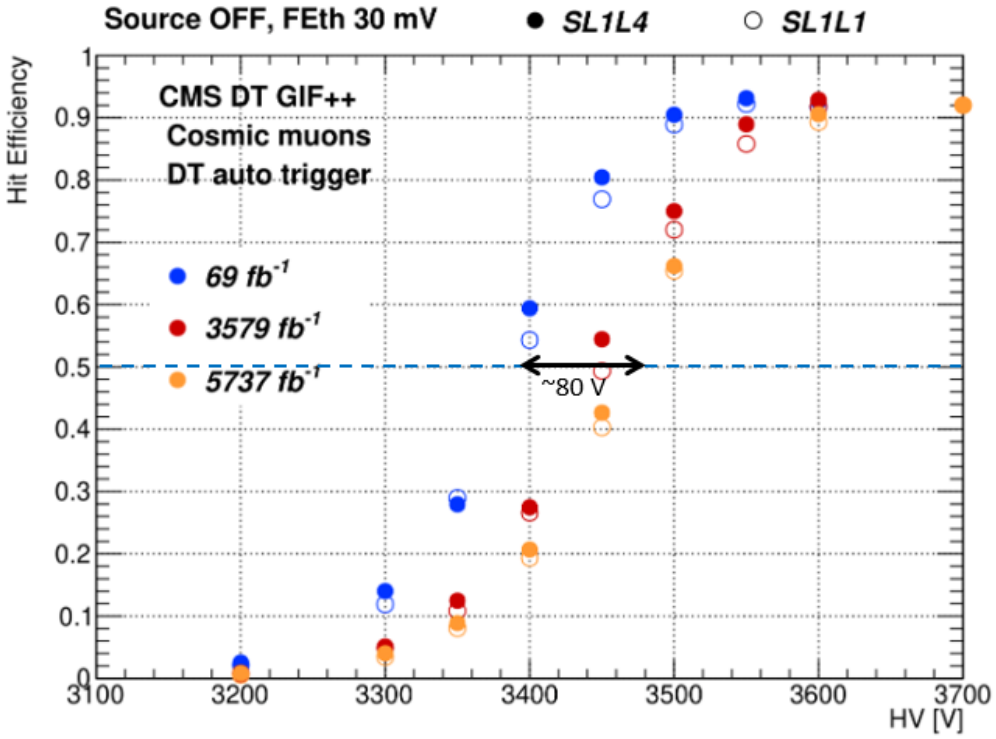

Figure 4.14: Hit efficiency for cosmic muons as a function of HV for the aged layers (SL1L1 and SL1L4) when the source is off and the front-end threshold 30 mV for different values of the integrated luminosity. The separation in voltage between the curves of different accumulated dose is overlaid.

G(HV), the effective HV for a given gain can be extracted. The hypothesis is that at the 50% hit efficiency point, the gain is exactly the same for all the hit efficiency curves. Knowing this, we can go back and calculate the gain at the nominal voltage of the aged MB2 detector which is approximately 1.3 10^5.

The comparison between the gains obtained in the model developed and in the two sets of measurements performed at GIF++ is summarized in Table 4.2. As can be seen, the results of the model and of the MB2 measurements are very similar. This good agreement between the measurement and the calculation gives confidence that the model developed works well and the effect we are seeing is to a large extent due to this increase of radius, which has an important effect in the reduction of the Townsend coefficient and thus, on the avalanches.

Another conclusion that can be extracted, is that in the MB1 we were reaching a gain of $\sim 7.5 \cdot 10^4$ with only 750 fb^{-1} accumulated, while in the

MB2 it took 5737 fb^{-1} to reach a gain of 1.3 10^5.

The different behaviour of the MB1 and the presented MB2 data are not well understood to date, underlying the difficult experimental exercise that represent these multi-year irradiations of gas detectors [59]. The acceleration factors for the irradiations in Table 4.2 were the same.

Moreover, in an earlier MB2 irradiation, not shown in this thesis, the gain drops as fast as the MB1.

Analysis of the coating of the wires extracted after the slower MB2 irradiation contained much less Carbon, which sheds some doubts on the universality of the process generating the coating we are studying. It cannot be excluded, for instance, that some contamination from the gas source accelerated the aging of the MB1. Or that the materials in the chamber stop out-gassing after several years inside the GIF++ photon field.

With these uncertainties in mind, and with the considerations that will be made in the last section of this chapter about the effect of the dose rate, it can be concluded that the observed drop of gain is within a factor of 2 of the values calculated in the model assuming all the gain loss is due to the increase of diameter, which is satisfactory level of agreement.

Case	**Thesis Model**	**MB1 750 fb^{-1}**	**MB2 5737 fb^{-1}**
Clean wire 50 μm	$3.23{\cdot}10^5$	$3.2{\cdot}10^5$	$3.1{\cdot}10^5$
Aged wire 59 μm	$1.12{\cdot}10^5$	$7.5{\cdot}10^4$	$1.3{\cdot}10^5$

Table 4.2: Gain comparison between the model presented in the thesis and the data measured at GIF++ for the MB1 and MB2 chamber.

4.2.6 Hypothesis for the dynamic variation of the gain with the dose rate

From all the effects that we have observed during these longevity studies, there is one that is particularly puzzling. In particular, the effect observed in Figure 3.23, in which the hit efficiency is significantly reduced as the dose rate increases. This means that there is a drop of gain related with the dose rate, beyond the expected drop of gain that only depends on the wire diameter. On top of that, this effect only seems visible in the case of an aged wire, that is, the hit efficiency does not seem to drop with increased gamma flux if the wire is clean.

The fact that it is a recoverable effect that disappears (modulo the accumulated dose) when the gamma flux is reduced or eliminated is particualarly intriguing. Also, the effect is larger when the threshold is increased, which

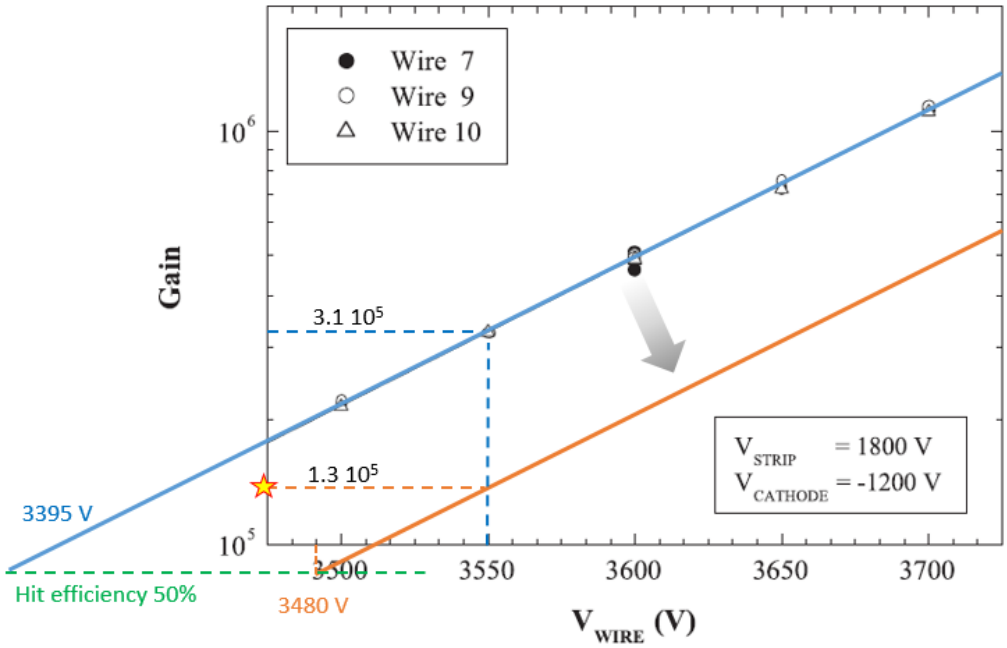

Figure 4.15: In light blue, it is represented the dependence of the wire gain on the wire's voltage for a fixed value of strips 1800 V and cathodes at -1200 V as obtained experimentally at CERN ([51]). Overlaid are the values of the gain at 50% hit efficiency (green) which is a common gain for any aged scenario. In orange, the line for the aged chamber that reaches 50% hit efficiency at 3480 V which means that its gain at 3550 V corresponds to approximately 1.3 10^5.

points to a lower charge being collected. Collecting a lower charge is reasonable as the wire ages due to the reduced gain, but one would expect that the reduced charge depends only on the amount of aging of the wire, and not on the incident flux.

We can consider the hypothesis that we are just seeing the effect of space charge being generated inside the gas volume of the drift cell, and that when this extra space charge is removed, the efficiency is recovered.

However, this is not what happens because it does not happen for a clean wire. As can be seen in Figure 3.23, the hit efficiency does not drop if the wire has not aged, and then, it drops differently depending on how much aged it is. That is, there is a dependency on the hit efficiency with the instantaneous dose rate that depends both on the gamma flux (space charge in the cell) and on how aged the wire is.

The model explains this effect via the growing resistance of the coating

R_{coat}. When the chamber is being irradiated with gammas, what we are seeing is a current source being injected at the coating edge. The equivalent circuit is presented in Figure 4.16.

In cosmic data taking, this current is basically ~ 0 and the effect of the coating comes through the gain modifications modeled above.

In contrast, if a high dose rate is present, and after a certain amount of time (which depends on the time constant τ = R x C), the actual value of the voltage at the coating edge V_b corresponds to equation 4.15 where the current represents the actual current due to the gamma flux and includes the effect of the avalanches:

$$V_a - V_b = I \cdot R_{coat} \tag{4.15}$$

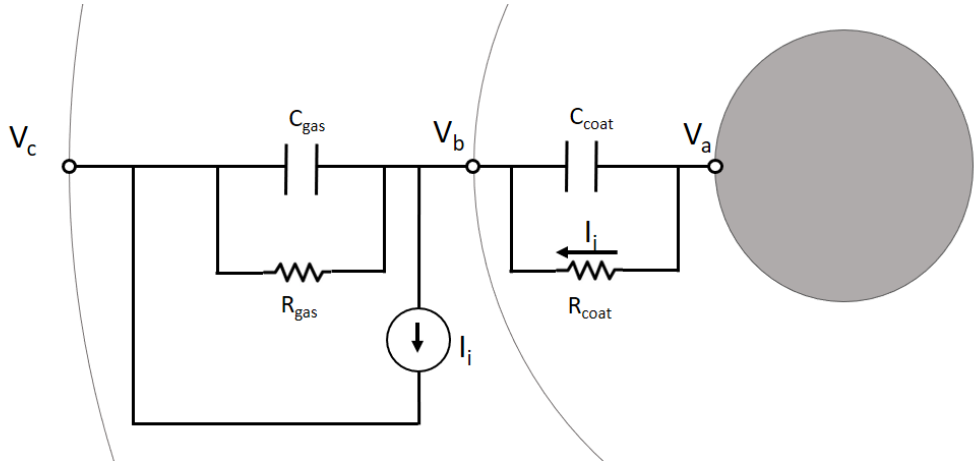

Figure 4.16: Equivalent circuit of the DT cell under gamma flux irradiation. The current I_i represents the current due to the gamma flux for different dose rates "i" and assumed to be after the avalanche.

This voltage V_b will be smaller, the higher the coating resistance. It is clear that the larger the coating, the larger its resistance.

Let's try to see if we can quantify this effect. To do that we will be using the results from Figure 4.17. In this Figure we can see the currents versus increasing gamma fluxes (dose rates) for different situations. Layers 2 and 3 have not been aged, and thus, behave like the ideal detector. There is a certain hint of saturation as the flux increases to the maximum values, which means that even the clean wires suffer from some effect of a resistance. This resistance is compatible with the one of the clean wire as we will see later.

The situation is different for the wires in Layer 1 and Layer 4. Both of them are being aged and the plot represents two different points of aging in

those wires. As can be seen, the larger the aging, the less current they are capable of sustaining.

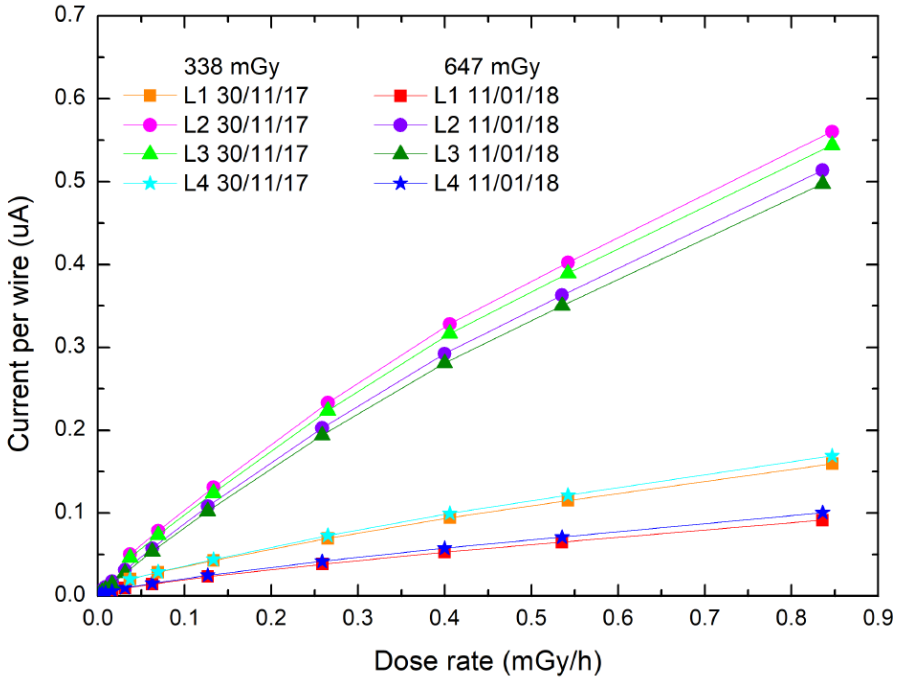

Figure 4.17: Currents per wire versus de dose rate of the gamma flux at GIF++ for different wires and with different levels of aging.

In those aged wires, we can see that the slope of the current vs dose rate decreases with increasing aging. This is expected, because the dose rate is proportional to the rate of ionization in the chamber (thus, to the primary electrons) and the measured wire current is the result of applying the multiplication gain, so the slope of these curves is proportional to the avalanche multiplication gain G. Let's call this quotient "dose-rate Gain" G', and let's call p the proportionality constant to the wire multiplication gain G, where p is strongly related to the number of primary electrons generated by each irradiation gamma photon.

$$G' \equiv \frac{wire\ current}{dose\ rate} = p \cdot G \tag{4.16}$$

As it can be seen in Figure 4.17, each curve is slightly concave, that is, the dose rate gain is not constant with increasing values of the dose rate. This effect can be better seen in 4.18, in which the dose-rate Gain G' has been represented versus wire current, for the clean wire and the two aged samples.

If the drop of gain was independent of the dose rate, these curves should be horizontal. However we see an exponential dependence of the dose-rate Gain G' with the wire current. The point in which these curves cross the wire current $= 0\ \mu m$ axis, should correspond to a loss of gain that is only related to the wire diameter increase, let's call this gain G'_0. Then, as the dose rate increases, we see that the gain keeps dropping continuously with the dose rate.

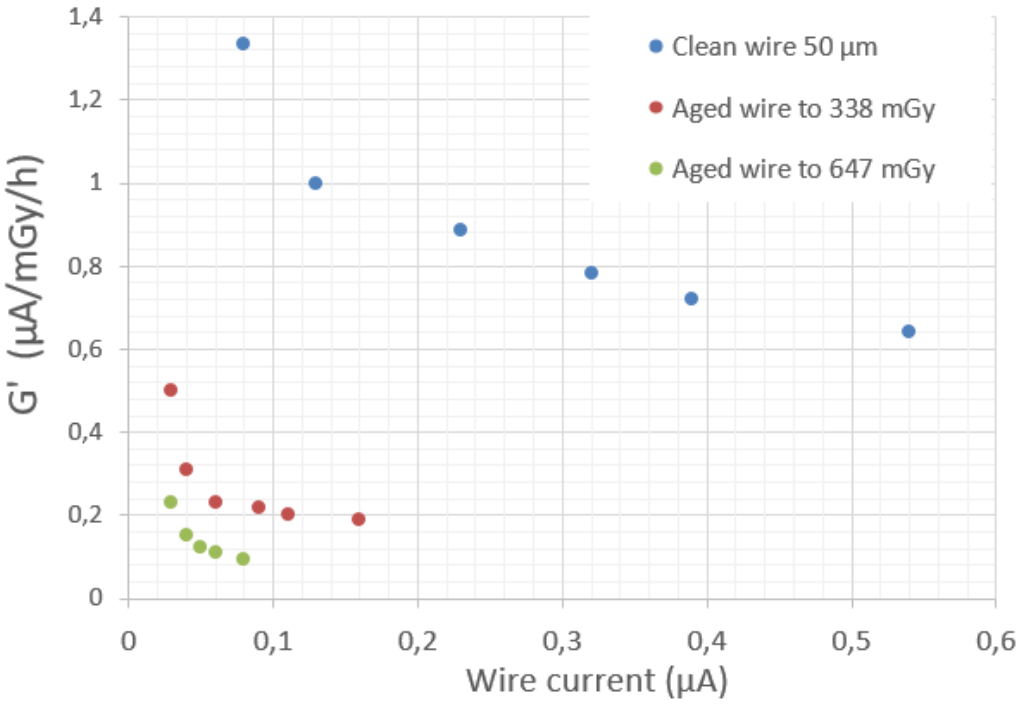

Figure 4.18: Ratio of the current per wire versus the dose rate for different intensities of the gamma flux at GIF++ as a function of the current in the wire. This ratio is proportional to the gain of the DT cell, since it relates the number of electrons collected for a given number of gammas. Different levels of aging in the wire are represented. It can be seen that the larger the aging, the lower the gain. It can also be seen that this drop of gain is not flat versus the wire current.

Let's now plot the natural logarithm of this curve in 4.19. We have removed the first points that correspond to a very low currents, because clearly they had a very large quantization error. In this curve we can see that the decrease of $ln(G')$ with wire current is linear (equation 4.17).

$$ln(G') = ln(G'_0) - m \cdot I \tag{4.17}$$

If we substitute G' definition from equation 4.16, we obtain:

$$ln(G) = ln\frac{G'_0}{p} - m \cdot I \tag{4.18}$$

The result of the linear regression of these data points corresponds to the first two rows of Table 4.3.

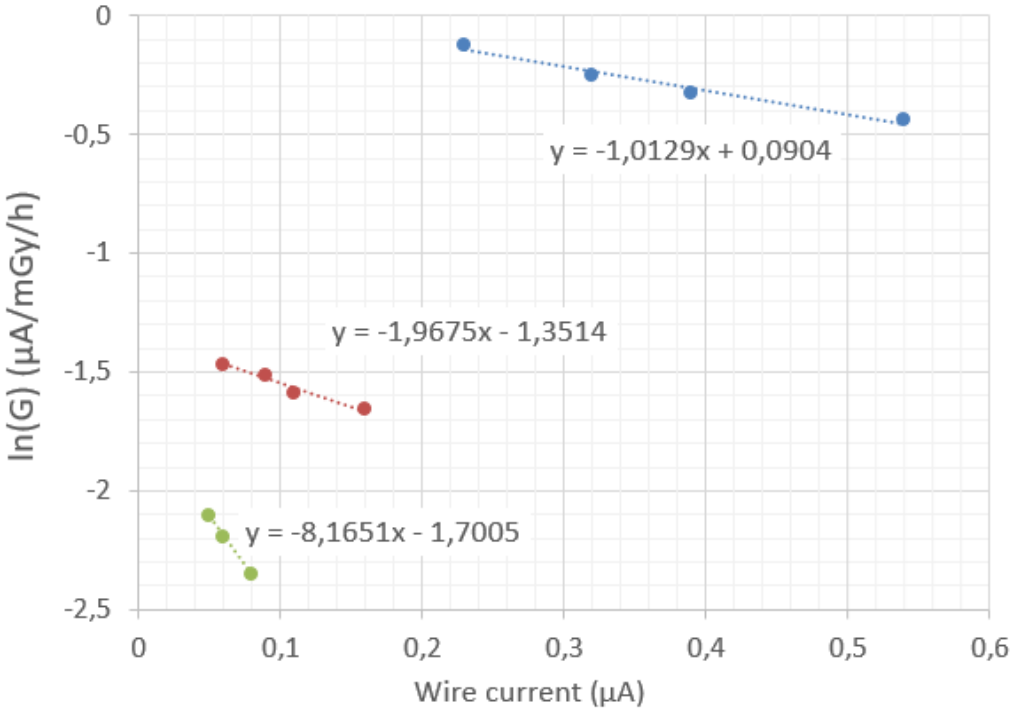

Figure 4.19: Calculated gain (natural log) as a function of its wire current for each of the three cases. In blue is the wires that have not aged, in red the wire that has aged 338 mGy and in green the wire that has aged 845 mG.

As we saw in Figure 4.16, we can model the electrical behavior of the coating as a series impedance to the anode. Under this model, we can write the voltage at the surface of the coating under high dose-rate conditions as a function of this series resistance and the wire current I:

$$V_b = V_a - I \cdot R_{tot} \tag{4.19}$$

Where we have named the series resistance R_{tot} instead of R_{coat} because, as we will later see, there are other contributions to the total series resistance.

In Chapter 3, we established that there is an exponential relationship between the wire multiplication gain G and the wire voltage V for a clean wire given by:

$$lnG = -16.6 + 8.24 \cdot 10^{-3} \cdot V \tag{4.20}$$

This relationship has been obtained for a non-aged wire, and the parameters for this equation under aging have not been experimentally determined. In the following analysis we have assumed that the slope of this relationship applies to the aged wire, which is not necessarily true, and thus the values obtained should be taken as a qualitative validation more than actual predictions.

Substituting I from equation 4.19 into equation 4.20 we obtain:

$$ln(G) = -16.6 + 8.24 \cdot 10^{-3} \cdot (V_a - I \cdot R_{tot}) \tag{4.21}$$

Which can be rewritten as:

$$ln(G) = (-16.6 + 8.24 \cdot 10^{-3} \cdot V_a) - (8.24 \cdot 10^{-3} \cdot R_{tot}) \cdot I \tag{4.22}$$

No information can be obtained from the comparison of the current independent terms of equations 4.18 and 4.22, because the p proportionality constant that relates G' and G is unknown. However, if we equate the current-dependent terms, we obtain the following relationship that allows us to quantify the value of R_{tot} from the value of slope from the linear regression of $ln(G')$ vs I.

$$R_{tot} = \frac{m}{8.24 \cdot 10^{-3}} \tag{4.23}$$

The results of the R_{tot} obtained are shown in Table 4.3. In addition, the resistance of the wire coating can be calculated by subtracting to the resistance of an aged wire, the total resistance seen by a not aged wire.

It is worth noting that the not-aged wires, free of coating, should not have a series resistance due to the coating. As can be seen in Figures 4.18 and 4.19, clean wires too show a dose-rate-related gain loss, although of much lower magnitude. The origin of this resistance is well known and it is due to protection resistors present in the HV distribution boards inside the chamber volume between each of the three electrodes of the cell and the external power source. The resistance of the wire coating can be calculated by subtracting

	Not aged wires	**338 mGy (845 fb^{-1})**	**647 mGy (1617.5 fb^{-1})**
m (slope)	1.0129	1.9675	8.1651
$ln(G_0')$	0.0904	-1.3514	-1.7005
$\mathbf{R}_{tot}(M\Omega)$	123	239	991
$\mathbf{R}_{coat}(M\Omega)$	0.00	116	868
Resistivity ($\Omega \times cm$)	0.00	-	> 8 x 10^{12}

Table 4.3: Calculation of the resistivity of the wires and its coating

to the resistance of an aged wire, the total resistance seen by a not aged wire (123 MΩ).

Thus, the remaining resistance can be attributed to the coating, which increases as the coating diameter increases, as expected. The actual resistivity from the material depends on the wire diameter on each case, which is not known. Still, taking 4.5 μm as an upper limit of the radius increase, given it was measured after very large integrated dose, one can derive a lower limit to the resistivity of the coating. The resistivity of a cylindrical shell is:

$$R = \frac{\rho}{2\pi L} \ln(b/a) \tag{4.24}$$

Using b=29.5 μm and a=25 μm as the outer and inner radius of the shell, and L= 250 cm the wire lenght, the derived lower limit to the resistivity is 8 10^{12} Ω x cm, which is compatible with good insulating materials as plastics or ceramics.

4.3 Summary and conclusions

In this chapter, I have focused on obtaining a model for the aging phenomena that the DT chamber have suffered during its irradiation at the GIF++ facility at CERN.

This model follows the classical expectations for aging in gaseous detectors and is centered on the impact on the most sensitive part of the detector, its wire.

By modeling the DT cell as two concentric cylindrical capacitors, the voltage and electrical field in the DT cell can be obtained and results about its expected performance can be obtained, particularly, the gain reduction as a consequence of the wire diameter increase and its effects on the avalanche formation. Quantitative results have been obtained using GARFIELD++ and MAGBOLTZ numerical simulations

I have compared this simulations with the experimental data acquired during the irradiation at GIF++ of the DT chamber, in order to evaluate if this model can represent the aging effects that we have observed.

The conclusion obtained is that the effects observed at GIF++ on a DT chamber seem to follow well the classical aging phenomena on gaseous detectors with a loss of gain and hit efficiency which is compatible with a coating surrounding the wire and increasing its diameter.

In addition, an effort has been made to explain the effect of the loss of gain versus the dose rate, which was not straight forward. A model where the coating surrounding the wire represents two capacitors acting in series plus the corresponding resistors in parallel is used.

A value for the resistance of the coating can be obtained from the measurements performed.

Therefore, the explanation of the detector behavior under high instantaneous radiation field appears also to satisfy the observations.

Chapter 5

Mitigation of the DT Chambers aging

As has been discussed above, there are multiple negative effects that can affect particle detectors under radiation. In order to reduce its impact and maximize detector lifetime, appropriate mitigation strategies have been envisaged. Three mitigation strategies that have been implemented in the DT chambers will be discussed in this chapter:

1. Adjust chamber and electronics working point.
2. Modify the gas flow.
3. Shield the DT chambers.

5.1 Operational adjustments

One of the least invasive methods for mitigating the damage of radiation on the DT chambers is to change the operational parameters along the life of the detector. If, by the end of the detector lifetime, the hit efficiency starts to decrease due to aging, there is margin to recover gain simply by increasing the HV. Several HV set values have been evaluated on aged spare chambers after having received an integrated dose of the order of that expected at HL-LHC at GIF++ Muon test beams. Appropriate safety factors have always been considered, as discussed in Chapter 3. Full recovery of hit efficiency was achieved by increasing 100 V the wire's HV, keeping the strip voltage constant, or by reducing the strip voltage by a similar amount at constant wire voltage, as expected from the Drift Tube characteristics [33]. This recovery method is only limited by the system capability to increase the wire HV. The

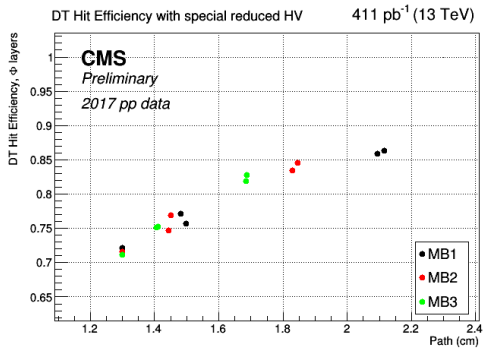

(a) Hit Efficiency below plateau vs. path length in the drift tube.

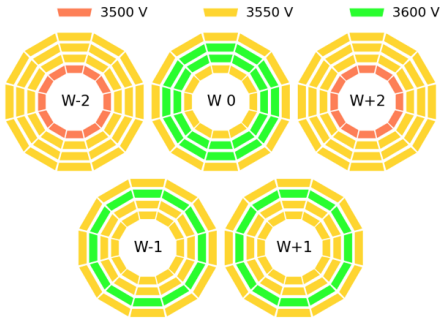

(b) High Voltage values after optimizing for longevity.

Figure 5.1: In the left plot the hit efficiency of each station in each wheel is plotted as the average path a high energy particle coming from the interaction point. The right plot depicts the HV values after final optimization in 2018.

present CAEN A877 HV PS supplies, which are located in the experimental cavern, have a protection that limits this increase to 150 V, i.e. 1950 maximum difference between strip and wire electrodes. Nevertheless, a new board model is being prepared in collaboration with CAEN that allows to program this protection value between the wire and strip electrodes. Thus the PS system will be able to provide to the wire the maximum value distributed from the service cavern, 4000 V, and even further lower the strip.

On the other hand, a decrease of the gain at an early stage in the detector lifetime can slow down the aging process. As discussed in chapter 3 the gain loss per unit of integrated luminosity is dependent on the voltage at which the detector operates. Thus by reducing the wire voltage from the initial operating point of 3600 V, the rate of performance decay will slow down at the cost of a lower amplification of the signal pulses. Lowering the operational HV has the undesired side-effect of a lower hit efficiency. With lower gain the avalanche produced near the anode will be smaller and, therefore, the total accumulated charge is also lower. As a result, the pulse of the collected signal will have a smaller height and it may not pass above the threshold of the FEB comparator. Hit efficiency can nevertheless be recovered lowering the FEB threshold voltage. The counterpart effect of a lower threshold is that it introduces a certain amount of noise in the system because some electronic noise signals may promote to real hits while before they were being filtered.

To keep the impact on the hit reconstruction efficiency negligible, the FEB threshold acting on the pulses coming from the wires was lowered to 20 mV from the conservative value of 30 mV that was used previously. This was done

after checking that the additional noise injected in the 250 DT chambers installed in CMS was acceptable. The reduction in threshold allowed to decrease HV from 3600 V to 3500 or 3550 V depending on the location in the detector since the amount of signal generated by a muon in each drift tube depends linearly with the length of the path in the tube. This can be very well be observed in Figure 5.1a by reducing the HV below the plateau to the linear part of the Hit efficiency vs HV curve. The Figure shows that the efficiency below plateau is proportional to path traveled within the drift tube by the muons, being lowest for tracks that are normal to the chambers, which can be easily understood as a lower path results in a lower ionization.

Figure 5.1b depicts the HV values after final optimization in 2018. To give a reference of the impact of this optimization, each 50 V decrease results roughly in an extension of the chamber lifetime of a factor of roughly 1.5.

In summary, the logic is to decrease the gain during the majority of its lifetime, which in turn will reduce the rate of depositions in the wires. To compensate for the loss of gain, the sensitivity of the FEBs is increased, by lowering its detection threshold. And then, at the final stages of operation, the HV can be increased again to recover for the loss of efficiency, extending the detector lifetime.

All HV set-point modifications need to be evaluated and monitored periodically with collision muon data in order to track the impact on the efficiency and adjust if needed. On top of the direct hit efficiency effect discussed above, the reduction of the pulse height also involves a small shift of a few nanoseconds in the time of arrival of the pulses due to their finite rise time that requires to be corrected to achieve the optimal performance of the detector. After changing the HV and FEB thresholds set point, this small shift was measured and corrected in the Trigger Boards located in the Minicrates using cosmics and collision data [60]. To give an order of magnitude, a 50 V change results in a shift of 2-4 ns.

Motivated by effects discussed above limiting the detector lifetime, efforts have been put during the design of the DT Phase 2 upgrade to minimize the amount of noise in the system, allowing it to operate at a lower FEB threshold value. One of the items that was identified as having a large impact is the long path of signal cables that runs between the DT chamber (from the FEB) and the Minicrate electronics (future OBDTs). These cables (more than 2 meters long in general) are flat parallel 68 wires unshielded cable and pick up a significant amount of environmental electromagnetic noise. As a consequence, these cables will be replaced with a shielded and shorter version which has proven to reduce the amount of noise and will allow programming a lower threshold. In the theta view, these cables are buried in the detector

and cannot be exchanged without the extraction of the chamber which is impossible in LS3. However the theta FE cables run along the iron yoke depth which is nearly void of active electronics, and thus are less exposed to electronic noise that the phi cables that run over the wheel surface.

5.2 Gas system modifications

Since in Chapters 3 and 4 we have concluded that the aging that we observe is due to deposits in the anode wires, it is clear that maintaining a clean gas distribution with few impurities is critical to minimize aging. This was taken into consideration during the chamber and gas system design, trying to avoid out-gassing materials. During early aging tests of the DT chambers, only Si deposits were observed, traced back to glue of the strip and cathodes, but at a very slow rate that did not significantly limit the chamber's lifetime [42]. However, this did not took into account that the ionization during the avalanche creates organic ionized molecules that tend to polymerize and pollute the gas, acting, in fact, as if the irradiated chambers were out-gassing.

From LHC start-up the DT gas circuit has been operated in re-circulation mode, injecting only 15 % fresh gas to the DT chamber circuit, which resulted in a constant level of air and water vapor (from leaks) in the system. Keeping some water concentration is considered desirable to avoid discharges. The air concentration needs to be kept constant because it affects a crucial operation parameter of the DT chambers: the drift velocity. However, as a consequence of the re-circulation, any out-gassing inside the chamber generating impurities would be circulated over and over within the gas system. Even worse, out-gassing from chambers receiving large irradiation would pollute the full system.

To minimize the impact of pollutants, a strategy was put in place to avoid gas re-circulation during the operation of LHC. The gas circuit operation was changed to open loop with 100 % fresh gas injected, i.e. the gas was not recirculated. However this change of operation modified the concentration of air and H_20 in the gas, as shown in 5.2a. To avoid discharges due to drier gas in open loop operation, an humidifier was introduced upstream with feedback from the humidity measurement such that the concentration of water vapor remains at the same value as in closed loop operation. As mentioned, the air concentration needs to remain constant to avoid changes in the drift velocity. This is illustraded by the change in drift velocity measured by the VDC in the CMS DT exhaust during a change from open to closed loop in 5.2a and by the parameterized dependence of the drift velocity with N_2 concentration in 5.2b. Moreover Oxygen is found in the literature as a protective gas against

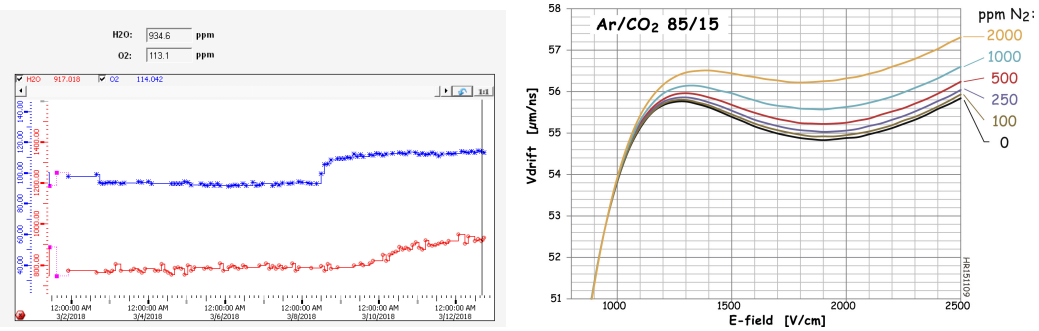

(a) O_2 and H_20 concentration.

(b) Simulation Drift velocity values from [53].

Figure 5.2: In the left plot the concentration of O_2 and H_20 is shown during a change from closed to open loop. The right plot shows the impact of air leaks on the drift velocity.

polymers [61]. To control the level of air in the system during open loop, the mixer was upgraded to be able to mix three gasses (Ar,CO_2 and air). This allowed to control the concentration of air in the system independently on the leaks. During winter technical stops and long shutdowns, where no radiation is expected to increase out-gassing, the DT system is brought back to closed loop operation, reducing in this way the amount of gas required and thus the cost.

The mentioned changes in the operational parameters will clearly minimize the performance losses due to radiation. However it is clear that minimizing the total dose collected is the primary way of minimizing aging. Accordingly, a radiation shielding strategy has been studied and executed to reduce the amount of radiation that reaches the DT chambers.

5.3 Drift Tubes Radiation Shielding

5.3.1 Shielding Installation

As already discussed, background radiation affects the DT chambers in several ways: not only it increases the amount of noise to be readout, but it also increases the collected charge at the wires, and thus, increases the aging of the DT chambers. As shown in Section 2.2 (Expected background radiation at CMS), both the flux of neutrons and photons is very high. To mitigate the negative effects on the chambers a shielding system was installed surrounding the external MB4 chambers on the top half of CMS, which are the chambers

that suffer more the effects of the external background, as can be seen in Figure 5.4a. Therefore, an ideal shielding will protect both from neutrons and from photons, being the protection from neutrons more complicated. Neutrons have a somewhat long decay time and big elastic cross-section so they permeate the experimental cavern and generate signals that are collected by the DTs. These neutrons come mainly from back-scattering produced by particles that escape the inner layers of the detector through the forward shielding. CMS reinforced this forward shielding during the Long Shutdown 2 (LS2) to minimize the flux of neutrons in the cavern.

There is an additional difficulty when trying to shield neutrons, in that the cross-section is highly dependent on energy, which entails that a good absorber for fast neutrons will not be optimized for thermal neutrons. The most common method for protection against neutrons, that usually are a mixture of thermal and fast neutrons, is to assume that all of them are fast and use a material with high hydrogen concentration to moderate them down to thermal neutrons with a material with good capture cross-section for thermal neutrons. Finally a layer of a material with high atomic number to attenuate the gamma radiation produced during the neutron capture is required.

With this in mind one of the chosen materials for the shielding has been borated polyethylene. The polyethylene back-scatters and thermalizes the neutrons due to its high presence of hydrogen atoms, lowering their energy so the Boron can absorb them, emitting gammas. An additional layer of lead behind the borated polyethylene shields from the resulting gamma radiation produced by the boron neutron capture, as well as background photons present in the CMS cavern.

Multiple particle types can produce ionization in the DT chambers, but the main interest of the sub-detector is the detection of muons. Under these conditions the purpose of the radiation shielding is twofold: reduce the amount of radiation that can degrade the detector, both the electronics and the wires, as well as reducing the occupancy by blocking particles that could degrade muon detection.

The radiation shielding structure [62] is composed of two major parts. The supporting structure and the actual shield, organized in cassettes. There are 6 cassettes per chamber, each of them built as a rectangular aluminum cassette that stores a 7 mm thick lead sheet plus a 3 cm thick 5% borated polyethylene sheet (except in the sector 4 chambers where the borated polyethylene is 9 cm thick due to the need of a higher shielding factor). There are two dimensions for the cassettes, the standard 1756 x 827 mm (161 units) and the reduced 1456 x 827 mm (20 units) that is needed for the sector 4

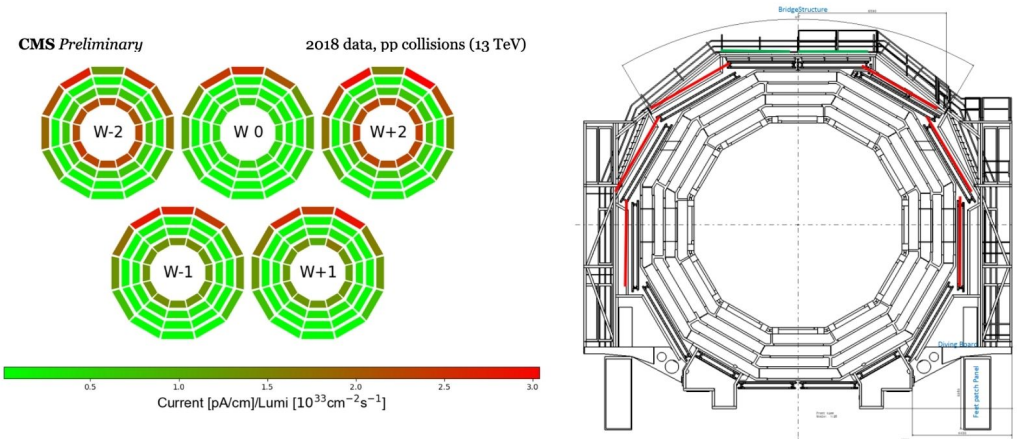

Figure 5.3: Integral of the signals generated in the chamber during collisions as measured by the High Voltage current per instantaneous luminosity unit (left). The top chambers of the outer wheels (W±2) were covered with prototype shields. Sectors covered in LS2 installation (right)

chambers. These cassettes weight 256 Kg and are completely encapsulated in a 1.5 mm AW5754 aluminum box to mitigate the fire hazard related to polyethylene. The design and construction of this system was carried out at CIEMAT, including the tool for installation on the CMS wheels with its associated motor's control. The installation in the detector was performed also with the help of CIEMAT's personnel and was finished in October 2020.

5.4 Shielding Performance Evaluation

In this section a comparison between data before and after the shielding installation will be presented. The data used to evaluate the shielding performance is the occupancy of the detector. Hit rate variations are a measure of how much of the background radiation generating background hits has been attenuated. This approach tackles phenomena related to the presence of background radiation but not directly related to the aging of the detector due to the formation of deposits on the anode.

In Figure 5.4a the occupancy for all the chambers of the MB4 station is shown as a function of wheel and sector. As described in Chapter 1.3.2 the

DT chambers are divided into 5 Wheels, which in turn have 12 sectors and each of these sectors has 4 MB stations. The 2d plot is organized horizontally by sectors and vertically by wheels. Some channels (each one representing a singular wire in a cell from a DT chamber) can be faulty and have an extremely high hit-rate that distorts the analysis, so they have been removed from the analysis.

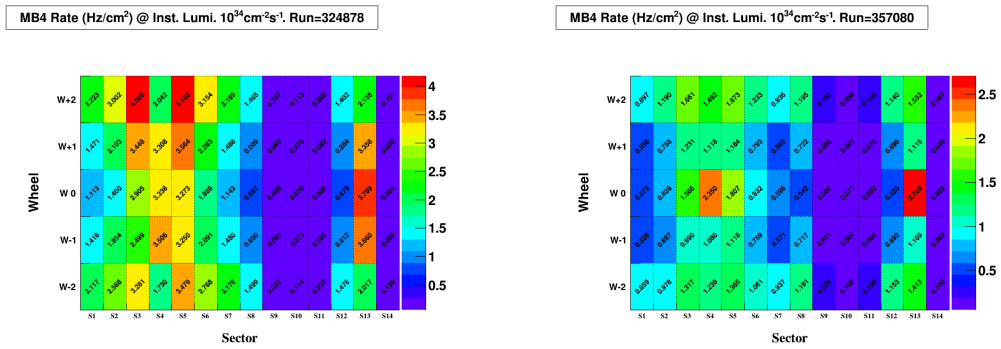

(a) Occupancy for a MB4 chamber before the installation of the shielding .

(b) Occupancy for a MB4 chamber after the installation of the shielding.

Figure 5.4: Occupancy of the MB4 chambers displayed as a function of the sector and wheel extrapolated to a luminosity of 10^{34} cm^{-2} s^{-1}. The lower values around sector 10 correspond to chambers close to the floor of the cavern.

After installing the shielding new data was recorded and represented in Figure 5.4b. The heat-map shows a decrease in occupancy for most of the chambers with a lesser impact on the lower sectors (from 8 to 12), expected since they are not shielded, as can be seen in 5.3 but confirms that the shielding has reduced the occupancy on the top sectors substantially. The top horizontal sector, S4, does not show an improvement because it was already covered with shielding prototypes before LS2. The ratio of the occupancy before and after shielding installation can be seen displayed in Figure 5.5: the improvement represents an increase of the chamber lifetime in the range 2.5-3 for fully shielded chambers.

5.4.1 GAMOS Simulations

GAMOS (Geant4-based Architecture for Medicine-Oriented Simulations) [63] is an open-source software toolkit developed for simulating particle interactions and transport in various applications, particularly in the field of medical

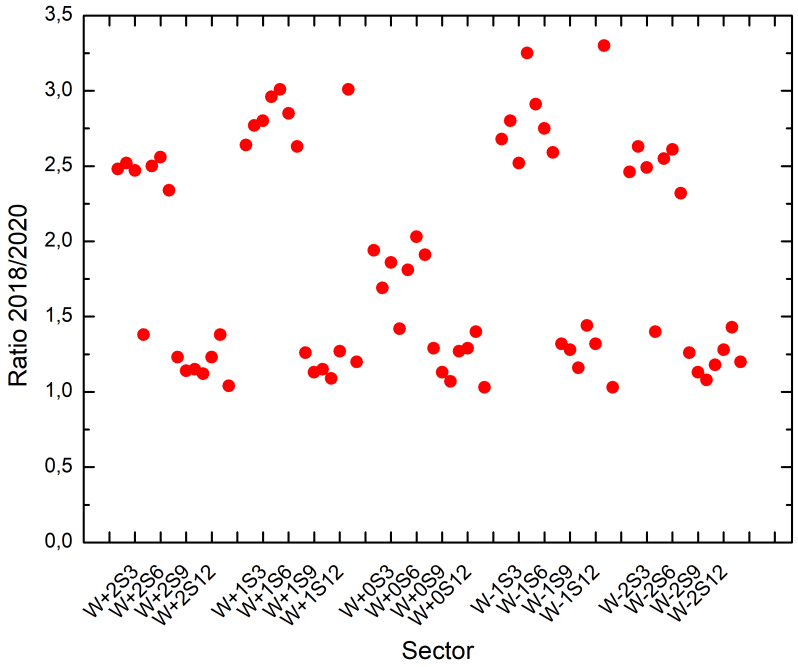

Figure 5.5: Ratio between occupancy for the MB4 chambers before and after shielding installation. Wheel 0 chambers were only shielded in a fraction of their surface due to mechanical integration problems.

physics and radiation therapy. GAMOS builds upon the Geant4 toolkit [64], which is a widely used Monte Carlo simulation toolkit for particle interactions with matter implemented in the C++ programming language. Geant4 is an extremely versatile framework, but that versatility comes with requiring expertise in C++ and object-oriented programming. It provides a user-friendly interface and extends Geant4's capabilities to originally cater to medical simulations, but has since developed to serve a wider range of use cases. The framework offers a range of features, including geometry modeling, visualization tools, physics processes, and scoring mechanisms. It provides flexibility in designing complex geometries, defining radiation sources, and incorporating various physics models for simulating particle interactions. GAMOS also offers advanced visualization capabilities to aid in the analysis and interpretation of simulation results.

GAMOS will be used to simulate how the radiation environment present at the CMS cavern will interact with the shielding.

Table 5.1: GAMOS simulation results in % for the listed configurations launching 1000 neutrons or photons perpendicular to the shield.

Shielding	Emerging Neutrons	Emerging Gammas
30 mm borated PE	44.8	51.7
30 mm borated PE + 7 mm Lead	30.3	3.7
15 mm borated PE + 7 mm Lead	55.3	5.5
30 mm borated PE + 14 mm Lead	28.3	3.6
30 mm borated PE + 7 mm Lead + 100 mm Iron	2.1	0

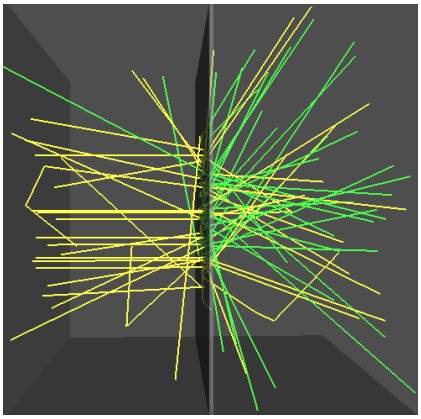

Figure 5.6: 3D representation of the simulation of 100 neutrons (in yellow) reaching the shielding from the left, with secondary photons are represented in green.

5.4.2 Shielding Configurations

Different layouts have been simulated, varying the thickness of the different materials of the shielding. All MB4 shielding simulations will begin with 1000 neutrons incident in the shielding with energies from 0.025 eV to 100 MeV distributed with equal probability in $\log_{10}(E)$ and we will focus on the amount and nature of particles after all the layers, thus giving us a sense of the effectiveness and estimating the attenuation of the configuration under study.

We will begin with 30 mm of borated polyethylene as the only layer of shielding, as shown in the first raw of Table 5.1. We are off to a good start with only 44.8% of the neutrons managing to cross the shielding, but the gamma radiation generated during the neutron capture by the Boron is very

high at 517 particles. In this configuration the source of neutrons is adjacent to the borated polyethylene and will be the starting point of the simulations as we add different constraints to better characterize the options available for installation. We will further modify the simulation to include a layer of lead between the polyethylene and the chambers that we want to protect.

After 30 mm of borated polyethylene and 7 mm of lead, 30.3 % of neutrons manage to reach the other side, reducing the incident flux by a factor of 3.3. This value can be compared with the measured attenuation factors in Figure 5.5 in the range 2.5-3 for fully covered chambers and is in reasonable agreement with the simulation, given the roughness of the geometrical description, which cannot include the effects of imperfect coverage and openings in the shielding. Adding lead not only increases neutron attenuation but reduces drastically the amount of gamma photons after the shielding to 37 particles.

The addition of lead has proven to be quite efficient at reducing the amount of particles that reach the detectors. We will simulate with double the amount of lead to see how much would have been reasonable to install. Lead is very heavy and is the material that has the biggest effect on the mechanical design of the shielding cassettes that have been installed in the experiment. The results for that configuration show that doubling the lead thickness has a small effect on neutron attenuation by reducing the amount by 6.6% and the gamma radiation by one count over 1000 initial neutrons. With these results the amount of lead that was used, 7 mm, is verified.

Let's try to reduce the amount of borated polyethylene to see the effect on the shielding of neutrons. As can be seen with half the width of borated polyethylene the number of traversing neutrons increases, decreasing the attenuation by 36%. The amount of gamma photons also increases by 18 counts.

Based on the simulations the material configuration for the shielding of 30 mm of borated polyethylene and 7 mm of lead is rather optimal giving the constraints. Boron has a very high impact on neutron attenuation while being relatively light. On the other hand doubling the amount of lead has a small effect on attenuation but a very high cost in mechanical design due to weight.

In order to simulate more accurately the conditions present on inner detectors of the experiment we will add 100 mm of iron, representing the iron yoke that enables the return of the magnetic field present at CMS. The amount of neutrons that reach the inner layers of the experiment is very small, 21 out of 1000, and so we can be certain inner DT stations will not be affected by neutrons coming from the cavern.

Having obtained a reasonable description of the installed MB4 shielding we will evaluate next optimal materials to shield the MB1 inner station from particles coming from the interaction point, with the constraint that only 2 cm thickness is possible to be installed and thus, we are not considering a multi-layered shield as in the MB4s. As can be seen in Figure 2.5 in the MB1 region the radiation field has a larger population of fast particles: neutrons and protons that leak from the inner parts of the CMS detector through the gap between the barrel and the endcap with energies in the range 10-500 MeV, the neutron high energy tail even reaching 1 GeV. On top of the Fluka simulation results there is evidence of a prominent track-like background contribution in the MB1s pointing to the endcap-barrel crack in the data, see Figure 5.7.

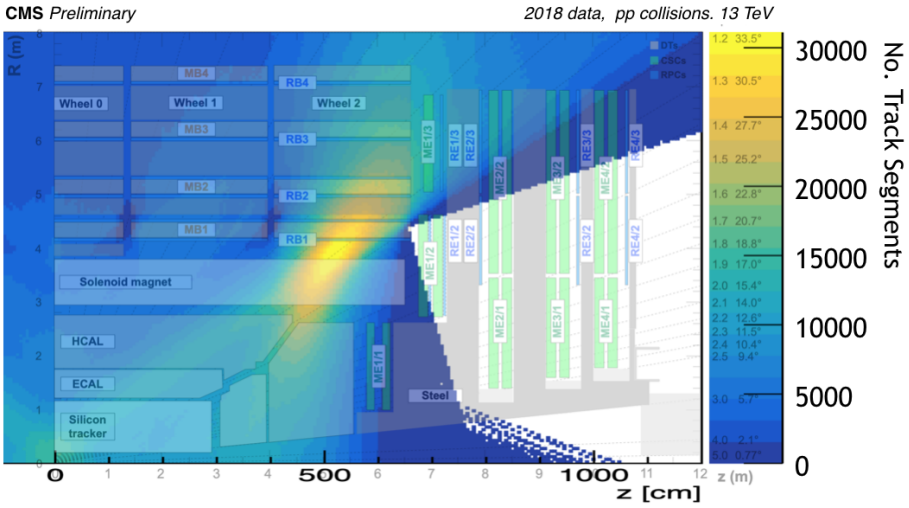

Figure 5.7: Background segments reconstructed in the MB1 station were propagated in the z-R plane in order to observe their position and direction. Figure from [65].

Given the uncertainties in the energy distribution from the Fluka simulation discussed in Chapter 2 and to understand the potential response of typical shielding materials to fast particles we have first simulated with GAMOS incident protons and neutrons in a wide 1 MeV-1 GeV range with an unrealistic flat energy distribution. The results can be seen in in Figure 5.10, from which some relevant observations can be extracted. First, a shielding of 2 cm is effective for protons below 100 MeV, but is transparent for energies above. However, this benefit has to be weighted against the potentially large amounts of secondary neutrons generated by both incident protons and

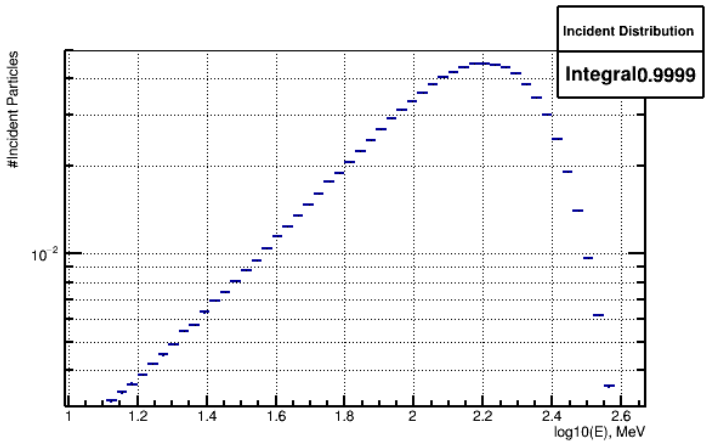

Figure 5.8: Realistic energy distribution of fast protons and neutrons in MB1 Wh±2.

neutrons, the problem being more acute for the latter. Also secondary gammas below 10 MeV are generated in large amounts and have to be taken into account. Finally, the amount of secondary particle varies largely with the shielding material, handicapping the use of heavy-Z materials as Iron or Lead.

Next, we have simulated a realistic incident energy distribution for fast proton and neutrons inspired on Figure 2.5 of Chapter 2. The incident distribution, shown in Figure 5.8 is a Gaussian with an average energy of 100 MeV and a sigma of 100 MeV sampled within the range [10,500] MeV. The results of these simulations are shown in 5.10. In Figure 5.10a the better shielding capabilities for this spectra using iron and lead shields can be observed. With 2 cm thickness available a factor of 2 reduction for this population seem to be within reach if high-Z materials are used. Secondary neutron production from protons is relatively low 5.10c, while the production of fast secondary neutrons (and shielding of fast neutrons, for that matter) remains a concern. In this fast population of incident particles the production of secondary gammas (Figures 5.10e and 5.10f) or secondary protons from neutrons (Figure 5.10d) in the shielding material is negligible.

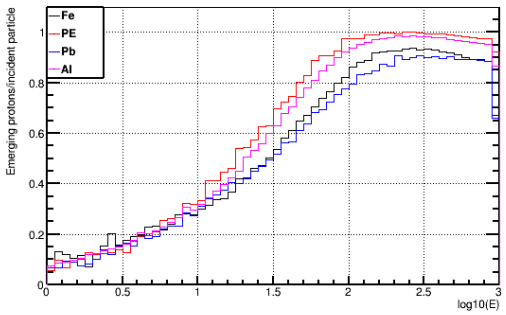

(a) Yield of protons emerging from 2 cm shield per incident proton as a function of the energy.

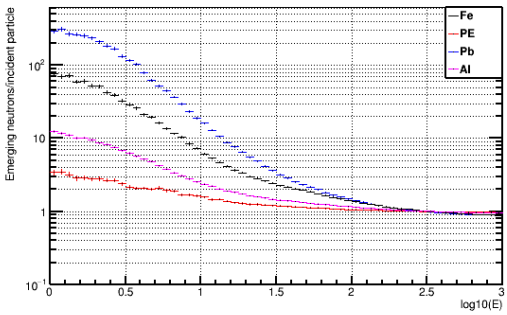

(b) Yield of neutrons emerging from 2 cm shield per incident neutron as a function of the energy.

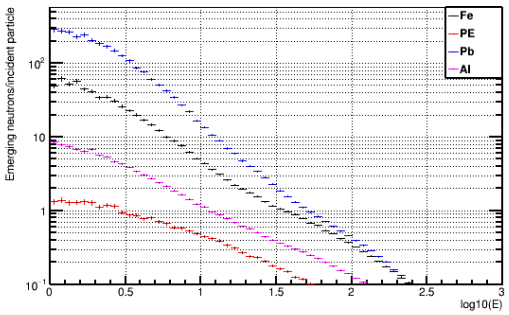

(c) Yield of neutrons emerging from 2 cm shield per incident proton as a function of the energy.

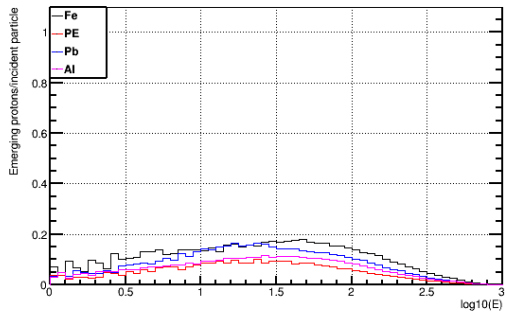

(d) Yield of protons emerging from 2 cm shield per incident neutron as a function of the energy.

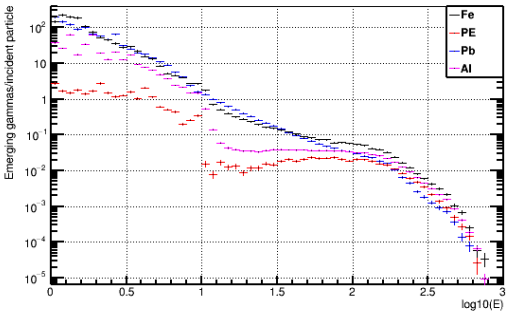

(e) Yield of gammas emerging from 2 cm shield per incident proton as a function of the energy.

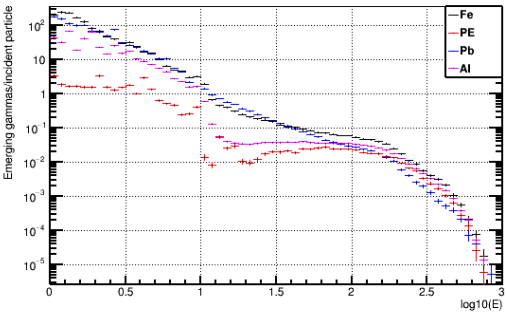

(f) Yield of gammas emerging from 2 cm shield per incident neutron as a function of the energy.

Figure 5.9: GAMOS simulations of 2 cm thick shields using incident protons(left) and neutrons(right) with a flat energy distribution.

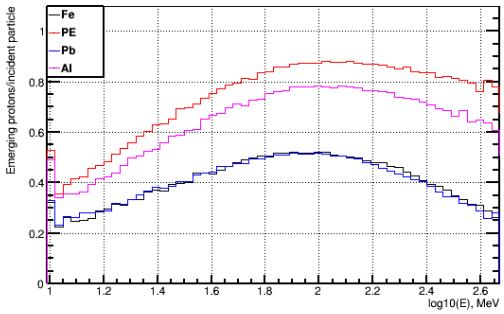

(a) Yield of protons emerging from 2 cm shield per incident proton as a function of the energy.

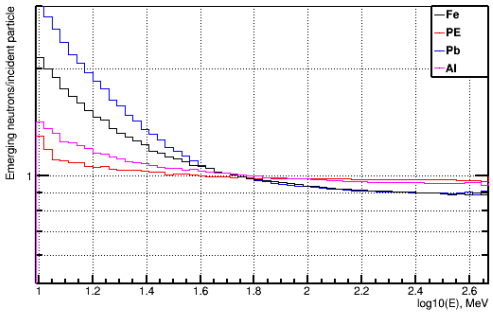

(b) Yield of neutrons emerging from 2 cm shield per incident neutron as a function of the energy.

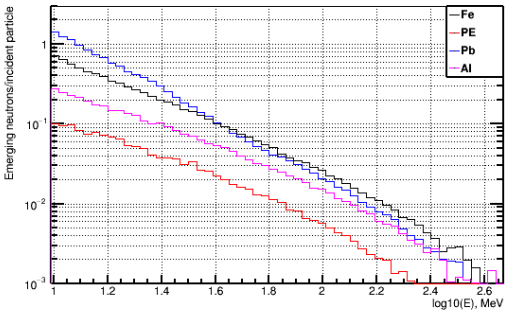

(c) Yield of neutrons emerging from 2 cm shield per incident proton as a function of the energy.

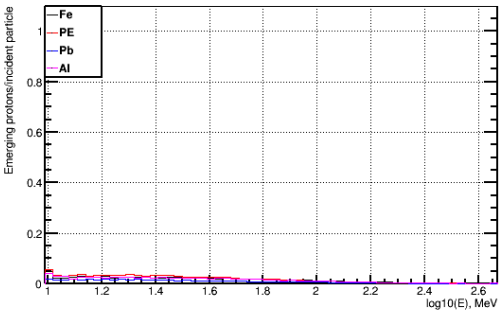

(d) Yield of protons emerging from 2 cm shield per incident neutron as a function of the energy.

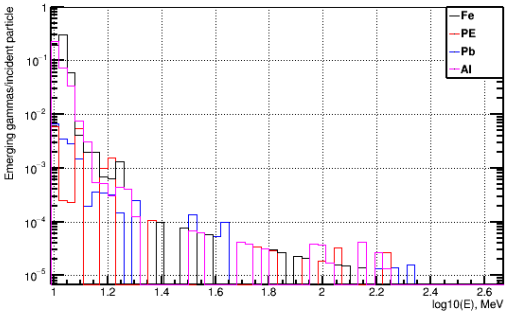

(e) Yield of gammas emerging from 2 cm shield per incident proton as a function of the energy.

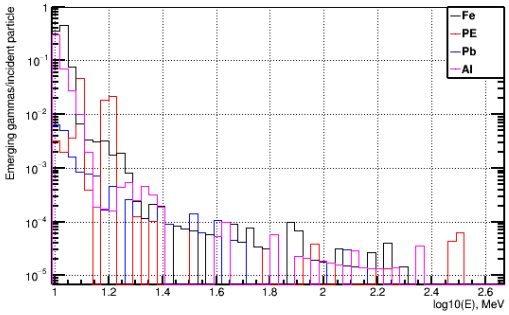

(f) Yield of gammas emerging from 2 cm shield per incident neutron as a function of the energy.

Figure 5.10: GAMOS simulations of 2 cm thick shields using incident protons(left) and neutrons(right) with a realistic energy distribution of the fast particles in MB1 Wh±2.

In summary, high-Z materials are better suited for the fast population but risk generating large amounts of secondary neutrons depending on how many and how energetic the neutron and proton populations are in the MB1 Wh±2 environment.

As mentioned above there is substantial uncertainty in the radiation field present in the MB1s, since these results have not been locally benchmarked to measurements. Additionally, the GAMOS simulations intend to serve as guidance but cannot capture the full geometrical complexity of the setup in CMS the detector and, as a consequence, shielding expectations should be subject to worse performance than predicted due to shielding border effects. Therefore our proposal would be to proceed empirically to decide the trade-off between low-Z (sub-optimal attenuation, less neutron secondary production) and high-Z materials (better attenuation, more neutron secondary production).

The plan is to take the opportunity of a LHC year-end technical stop to install prototype shields. This allows to evaluate their performance in situ as it was done for the MB4 prototypes. Two types of shielding are proposed to cover the two horizontal MB1s in the lower section of the wheel (MB1 S10 Wh−2 and MB1 S10 Wh+2), where mechanical installation is easier:

1. A conservative shield option exclusively made of low-Z material.

2. An aggressive shield option that covers with high-Z material the central part of the chamber of ∼1 m width, where the fast particle population transverse the MB1 chamber, see Figure 5.7.

Regarding the low-Z material choice, Aluminum is preferred for this application due to mechanical and practical reasons related to the deployment in CMS: a polyethylene-only shield is not rigid enough to bridge the full span of the MB1 chamber requiring a central support attached to the external wheel scaffolding and, additionally, encapsulation (or painting) to minimize fire related hazards. If borated, polyethylene would produce additional gammas that we are unable to shield from in the available thickness. Aluminum plates, on the other hand, are extremely simple to build and install, as they can easily bridge the ∼2 m width of the MB1. An Aluminum shield would also provide additional attenuation both for protons and gammas.

The aggressive shield option would be composed of two Aluminum plates of 100 cm width weighting 115 Kg, flanking a central plate of Steel, 60 cm wide ∼200 Kg. Steel plates present substantial practical advantages to using lead: there will be no need of extra support to cover the distance between the supports available on the sides of the station, and no need of encapsulation or cover, which would also be needed for safe handling of the lead.

The Aluminum and Steel prototype widths mentioned above are just an educated guess. The actual design values should be optimized considering all the mechanical and practical installation aspects, together with the width of the region impacted by fast particles that can be measured from the DT occupancy data.

5.5 Summary and Conclusions

The realization from the GIF++ irradiation test that the DT chambers will suffer some performance loss during its operation at HL-LHC launched a series of interventions to minimize its impact. Both operational mitigations and shielding actions have been implemented in the detector. Changes in the HV of the chamber can slow down aging by a factor of 1.5 to 2.25, depending on the location of the chamber in the detector. My contribution to obtaining the results of the expected gain reduction and the performance of the DT chamber when lowering HV and, then, at the end of its lifetime, increasing the HV, was very important to allow the collaboration to proceed with the plan described in this chapter. Modification of the gas system allowed to limit the endangered acceptance to the hot regions of the detector: the MB4 in the top sectors and the MB1s in the external wheels, avoiding cross-contamination to other parts of the detector.

Then, a major mitigating action was implemented in the form of an active protection of the chambers with the installation of a shielding structure to cover the top most exposed DT MB4 chambers. This mitigation is described in this chapter together with the details of the actual shielding structure which has been designed and fabricated at CIEMAT and later on, installed by our team at the CMS detector. The achieved attenuation factors for the MB4 chambers above 2.5 with the installed shielding guaratee its performance during HL-LHC.

Apart from contributing to the construction of this structure, I have performed the simulations detailed in this chapter, with the simulation software GAMOS, in order to evaluate the performance of this shielding under the expected radiation flux at CMS. GAMOS simulations of the installed shielding give a reasonable quantitative description of the achieved attenuation. Likewise, GAMOS has been used to evaluate shielding solutions to be installed in the MB1 station, external wheels, where mechanical constraints and a the presence of a population of fast particles with not very well known energies severely limit achievable attenuation. Within these constraints, two prototype designs have been proposed.

Preliminary evaluation of the impact of these mitigation techniques (gas

open loop, HV gain reduction and MB4 shielding) is that they are offering very good results and will help lengthening the lifetime of the DT detector during HL-LHC. We expect that through prototype testing and comparing with the simulations, shielding will further increase the longevity of the MB1 chambers as it has done for MB4s.

Chapter 6

Radiation Hardness of the DT electronics at CHARM

The on-detector electronics of the CMS DT chambers will need to be replaced for the HL-LHC operation due to the increase of occupancy and trigger rates in the detector, which cannot be sustained by the present system. The main board of this new system is called OBDT and is in charge of the time digitization of the DT chambers signal for further transmission to the new Readout and Trigger electronics.

In the current DT electronics architecture, trigger primitives are generated inside the on-detector electronics and then sent to a concentrator board called TwinMux [66]. The distribution of electronic stages in UXC and USC will be adjusted to take advantage of high bandwidth optical link technologies currently available. By moving part of the processing electronics to USC the system becomes more accessible for maintenance and future upgrades.

The OBDT boards will be located inside some aluminum profiles attached to the DT chambers, inside the CMS volume. These boards will be in charge of performing the $\sim$0.8 ns time digitization of the DT chamber signals and the multiplexing for further transmission through high speed optical links. The OBDT boards will also be in charge of some of the slow-control tasks needed by part of the DT chamber system. There will be a total of 830 boards to readout the 172200 channels from the DT chambers. The installation of this new system will take place during the LHC LS3, which is expected in 2026-2029, right before the start of the HL-LHC phase.

Several stages of prototyping for the OBDT board have taken place, being one of them the OBDTv1 [67] board which was designed to digitize 240 DT channels and included the final FPGA that is intended to be used (Microchip Polarfire [68]). It also included a monitoring chain similar to the

final one, though the high speed transmission architecture did not use the final transceivers and optical transmitters, instead, it used the GBTx ASIC from CERN and commercial optical transmitters. Either case, a firmware pretty close to the final one plus a large fraction of the components used in this version were intended to be used in the final board and, therefore, it was appropiate to perform a first radiation exercise in which the design and the choice of the components could be validated under radiation. The developed test stand and the results obtained in the irradiation tests of the board are presented in this chapter.

The radiation campaign took place at the Cern High-energy AcceleRator Mixed field (CHARM) [69] facility at CERN. This facility has a radiation field that is generated through the interaction of a 24 GeV/c proton beam extracted from the Proton Synchrotron (PS) with a metallic target and allows testing large scale systems. Our system was installed in an overhead conveyor inside CHARM which allowed to obtain a mixed-field radiation environment that resembles the one expected in the CMS experiment during HL-LHC.

6.1 Radiation hardness measurement of phase 2 prototypes at CHARM

6.1.1 The OBDTv1 Board

The OBDTv1 is the prototype board that has been built to validate the design, the global architecture functionality and the main electronics components for the on-detector electronics of the CMS DT chambers for the HL-LHC.

Two types of boards based on the same prototype (OBDTv1), with very similar functionality are foreseen, one board that will process the signals from the phi view of the DT chamber (OBDT-phi) and one for the theta view (OBDT-phi) which require different input connectors.

The signals that arrive to the OBDT come from the Front End Boards (FEB), located inside the DT gas volume. They contain the amplifiers shapers and discriminators of the chambers signals, outputting LVDS-like pulses with 50 ns width for each muon that crosses each drift tube cell. These signals are received as differential pairs at each OBDT.

The OBDTv1 board is built around a MicroSemi Polarfire FPGA MPF300T-1FCG1152E which performs the digitization of up to 240 input signals through a deserialization method implemented inside the FPGA. Each input signal is sampled by a 600 MHz DDR (Double Data Rate) deserializer, and then 0 to

1 transitions are detected in the parallel array of sampled data. The detected transitions are converted to a digital value which includes the coarse count in steps of the LHC bunch crossing (BX), which is 25 ns, and a fine bin size with a least significant bit of 1/30 of a BX. That is, the least significant bit of the Time to Digital Converter (TDC) corresponds to 0.833 ns.

These digital time measurements performed by the OBDTv1 need to be merged into an output serialized stream that is sent through dedicated high speed optical links to the CMS DT backend. The final link implementation is expected to use the lpGBT ASIC [38] and the VTRX+ [37] from CERN at 10.2 Gbps; however, by the time the OBDTv1 was designed, these chips were not available. For the high speed data serialization, the GBTx ASIC has been used and thus, the maximum link speed is reduced to 4.8 Gbps.

Since this GBT link is bidirectional, a commercial optical transceiver of the SFP+ type has been used. This GBTx link is in charge of distributing the clock to the OBDTv1 board, the fast commands and performing the standard slow control and monitoring of the board. It does not perform the output data transmission, since a dedicated link is used for this task.

This data output link is implemented directly through the FPGA which includes the VHDL code of the GBTx protocol. A unidirectional optical transmitter QSFP type is used for this data transmission which is devoted to the digital time measurements stream.

Another ASIC from CERN is used in the OBDTv1, that is the SCA [39], which is in charge of performing the monitoring of the voltages, currents and temperatures, among other tasks.

Summarizing, the main features of the OBDT v1 board are:

- CERN GBTX ASIC: in charge of the CMS clock distribution and fast synchronization commands as well as the slow control of the board for configuration and monitoring.
- CERN SCA ASIC: it includes an ADC to monitor different parameters in the board (temperature, voltages, ...), as well as a DAC, I^2C and GPIO interfaces required by the system. It also allows the generation of the calibration signals and levels required by the DT chambers and remote FPGA reprogramming, among other tasks.
- Optical communication through a pair of commercial transceivers: SFP+ for the GBT link and a dedicated QSFP for the data path to the back-end.
- Linear DC regulators to ensure a low noise power distribution. The OBDTv1 board is powered with two different rails at 5 V (for calibra-

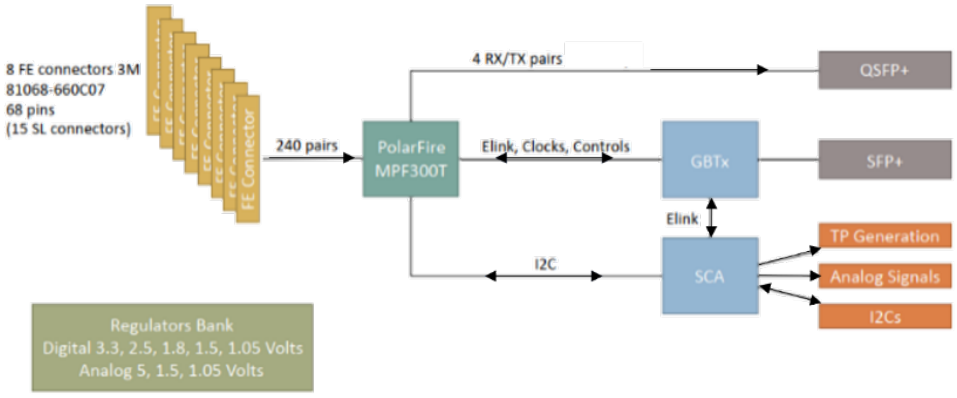

Figure 6.1: Drawing of the OBDTv1 functionality and main components.

tion signals and I^2C communication) and 3.3 V (for the rest of the board's logic). From the 3.3 V rail, the board generates several other voltages required by the different components, that is 2.5 V, 1.8V, 1.5V and 1.05 V.

- A pulsing system generating signals for testing the time calibration of the DT chambers.

The architecture of the OBDTv1 board can be seen in Figure 6.1 and pictures of the board can be seen in Figure 6.2

6.1.2 The CHARM facility

The CHARM facility was built between 2013 and 2014 with the main goal of serving as facility for testing electronics and other instrumentation under the radiation field and doses expected at the LHC (Large Hadron Collider) and HL-LHC (High Luminosity LHC). The expected radiation field is quite specific of hadron colliders and thus, usual worldwide radiation facilities don't provide the doses of neutrons and protons that one could encounter at a proton-proton collider such as LHC. One of the main advantages of CHARM is that it allows testing large scale systems. The facility is largely adaptable, offering a high-penetrating radiation environment with maximum dose rates and fluxes adjustable using different configurations (target, shielding and location). The three main radiation effects of interest (single event effects, total ionizing dose and displacement damage) can be tested simultaneously. The initial proton beam of 24 GeV for CHARM is extracted from the Proton Synchrotron (PS) accelerator from the CERN accelerator's complex. Then

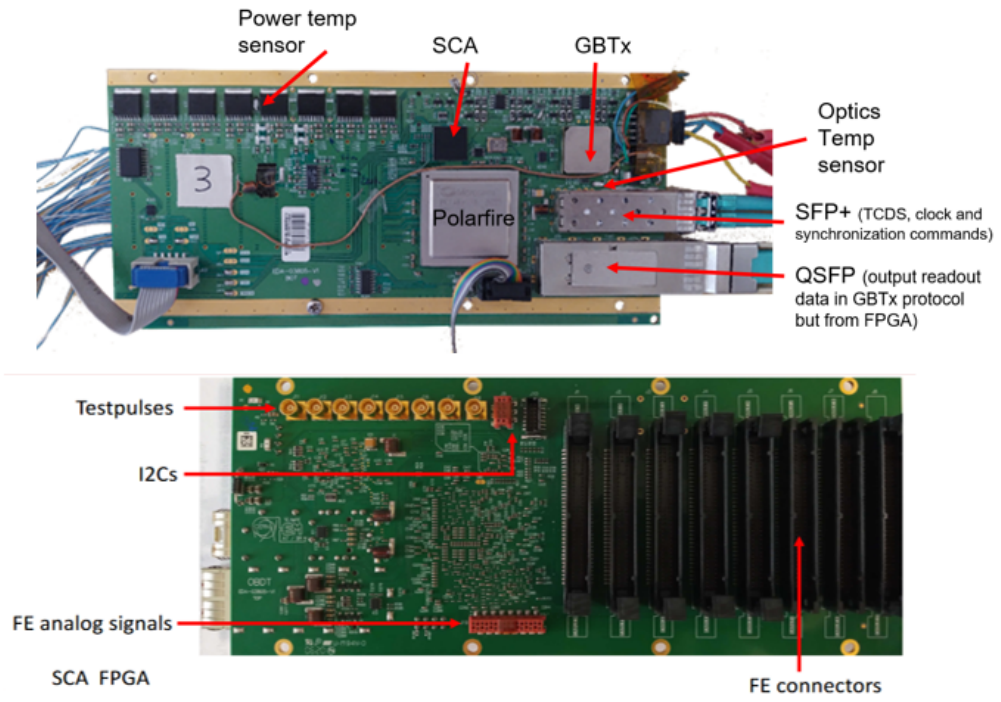

Figure 6.2: Image of the OBDTv1 board top and bottom.

the beam is guided to the experimental area where it hits a cylindrical copper or aluminium target. The resulting secondary mixed radiation field is used to test electronic equipment at predefined test positions. Depending on the test position selected (from 1 to 13), the test equipment is exposed to different particle spectra. In addition, four movable blocks with a thickness of 40 cm and made out of concrete or iron can be placed between the target and the test locations modifying the intensity of the test. The CHARM facility, because of the size of its experimental area can host different user experiments and the irradiation conditions are requested by the primary user, the other users withstand the conditions, during this run we were a secondary user. One key information to perform the radiation characterization is the knowledge of the dose received by the device under test (DUT). The CHARM service provides detailed measurement of this dose after the irradiation campaign is finished, analyzing the dose measurements from the dosimeters installed inside CHARM at the DUT location.

Our test stand was located in the Overhead Conveyor. This is a metallic structure that is hanging from automatized rails and can be taken out of the facility during the installation and removal and then it can be brought

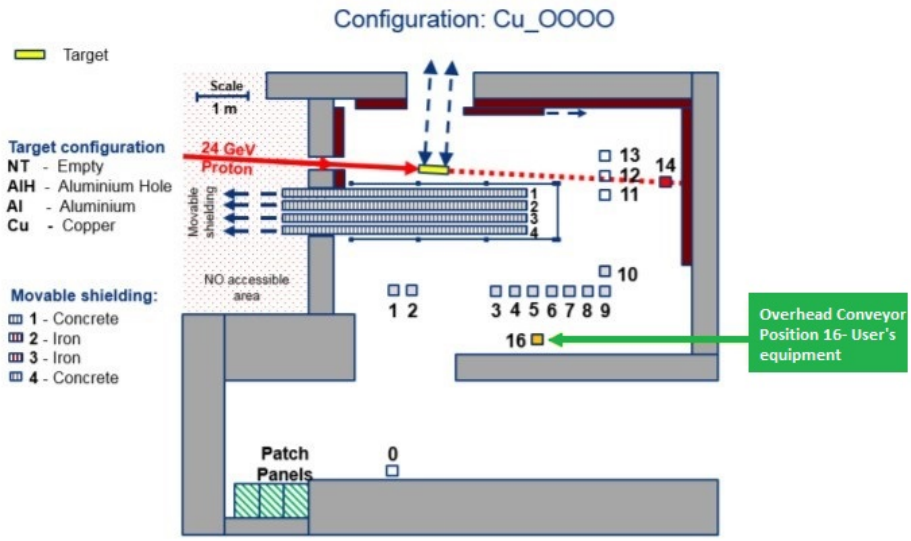

Figure 6.3: CHARM facility layout. The location of the Overhead Conveyor is indicated.

inside of the facility at different locations, obtaining a different intensity depending on the exact location. A nearby room, so called Control Room, is available for installing the equipment that will control the test stand, together with the computers or any other required infrastructure. Cables and fibers interconnect the racks in the Control Room and the different locations of the CHARM racks. The Overhead Conveyor is equipped with an important variety of cables and fibers already laid down and thus, they don't need to be installed for the particular tests, which is highly convenient. The length of these cables is 35 meters.

In addition, there is another room nearby the Control room that is used as preparation area the week before of the irradiation test. In this facility there is a mock-up of both the inside and outside racks, including the Overhead Conveyer. Real length cables interconnect the Conveyer and the racks, allowing for testing the system in realistic conditions and be ready for operation at CHARM as soon as everything is installed.

6.1.3 Test Setup

Figure 6.4: Image of the Overhead Conveyor with our setup inside the CHARM facility.

6.1.3.1 Time Digitization Test Stand

The test setup that is under the radiation field consisted in two OBDTv1 with different firmware, interconnected between them to send signals from one to the other. The one that contains a firmware similar to the one that we expect to operate during HL-LHC is called OBDT. The other board is called PUFO (PUlse Forwarding to Obdt) and contains a firmware devoted to sending pulse hits through 117 differential channels through the FE connectors to the OBDT. These pulses were sent periodically and synchronized with a reference signal that happens once per LHC orbit (at $\sim$ 11 kHz). Since some of the channels at the Polarfire are using the pins from the High Speed Input/Output type banks, we could not generate LVDS outputs through those channels and, therefore, only 117 out of the 240 channels were used.

A Xilinx evaluation board VC707 [70] with an optical extensionFMC

board Faster Technology type FM-S14 [71] is used to generate the system clock and to provide slow control and monitoring of the full setup through several optical links. These two boards were located outside the irradiation bunker. Each OBDT requires one bidirectional optical link that connects to its GBTx for clock reception and slow control monitoring. This link uses an SFP+ transceiver. Then, another unidirectional output link that outputs directly from the Polarfire FPGA, sends the time measurements data stream to the VC707 and uses a QSFP+ transceiver.

The VC707 receives the data stream from the OBDT board which contains the information from the time measurement of the hits detected by the OBDT. Any unexpected value in the number of hits received its time value or the channel information is marked as an error. A calculation of the number of errors detected in this data stream is calculated both internally at the OBDT and also at the VC707, for crosscheck. In addition, a secondary copper communication path to the OBDT and PUFO was implemented through a custom electrical link that allowed the measurement of the firmware Single Event Effects (SEUs) independently from the Bit Error Rates (BER) of the optical path.

Figure 6.5 presents the electrical schematic used for the main logic of this experiment.

Moreover errors detected at the VC707 by the GBT link protocol which contains an auto-correction mechanism, are also counted and allowed to establish the BER of the links. Finally, the VC707 also reads other monitoring information of the OBDTs and PUFO such as voltages, currents or temperatures. Each OBDT requires two rails of voltage for operation:

- 6 V (output voltage 5 V) @ 0.1 Amps: This rail powers I^2C compoments and the calibration logic.
- 3.8 V (output voltage 3.3 V) @ 2.4 Amps: This rail powers the FPGA, the GBTx, the optical transceivers, and all of the important components of the board.

At the maximum power consumption of 2.4 Amps, the OBDT needs to be cooled down not to end up in temperatures higher than 45°C. At CMS this is done with conduction through a water cooling system, but a CHARM, we use fans. Two fans were installed in the setup, to ensure that even if one of them failed under radiation, the other could still keep the system at a reasonable temperature and the test could continue. The fans used were a 12 Volt fan (DC brushless AFC1212DE Delta Electronics) and a three-phase one (AC fan Axial EBMPAPST 4650N).

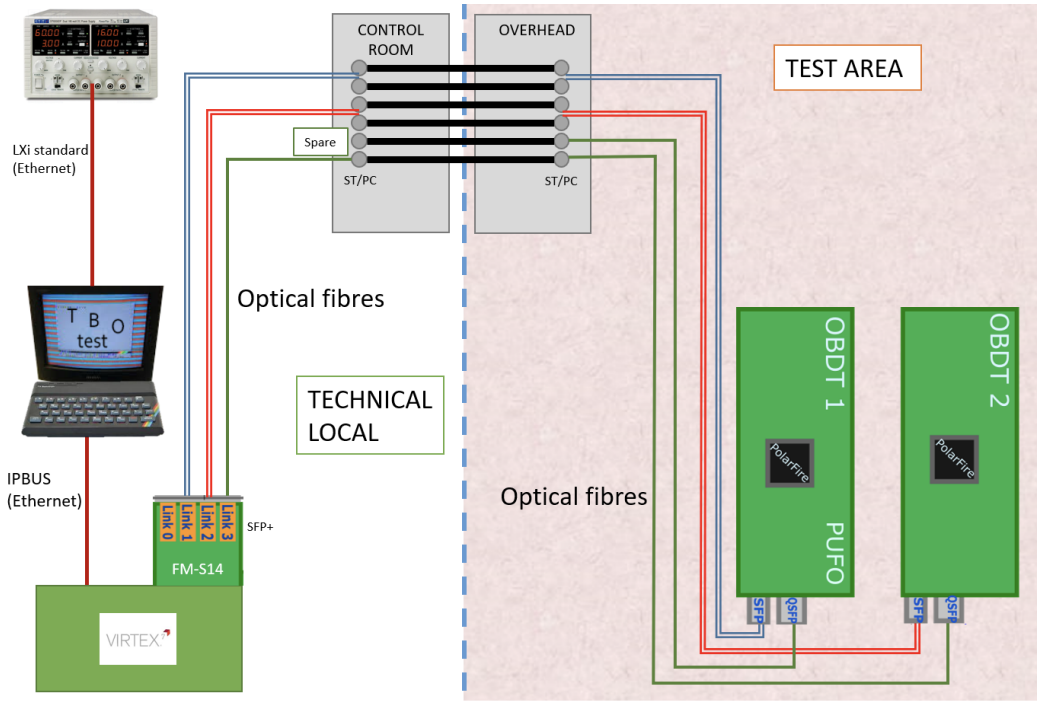

Figure 6.5: Drawing of the Test Stand interconnections for the main test. OBDT and PUFO are located inside CHARM while VC707 is in the Control Room.

The list of integrated circuit part numbers from the OBDTv1 that have been verified during the radiation test is summarized in Table 6.1.

In addition, the commercial optical transceivers that were used during the tests and that have been tested are the ones indicated in Table 6.2. The SFP+ devices were used in the OBDTs to receive the GBTx bidirectional link which carries the clock to the FPGA among others (although also a shared internal clock between OBDTv1 and PUFO can be used). In the QSFP only one transmitter out of the existing four was used to send the output data from the Polarfire FPGA to the VC707.

6.1.3.2 Slow Control Links and FPGA Reprogramming

Since it was already known that the most sensitive component in the boards will be the commercial optical transceiver, a secondary slow control link through copper lines was implemented. This will allow cross-checking the performance of the test separating the potential errors related to a failure in

Part number	Manufacturer	Package	$\frac{\#}{board}$	Function
MPF300T-1FCG1152E	MICROSEMI	BG1152	1	Polarfire FPGA, 512 I/O, 300000 Logic Elements, 1152-Pin FBGA, Extended Commercial Grade
GBT-SCA_REV 6.2	CERN	BGA196	1	Slow Control Adapter ASIC for the GigaBit Transceiver ASIC (GBT)
GBTX ASIC V0.1	CERN	BGA400	1	GigaBit Transceiver ASIC (GBTX)
MT25QL01GBBB8ESF-0SIT	MICRON TECHNOLOGY	SOIC16	1	1Gbit (128 MB), 1.8 V, Multiple I/O Serial Flash Memory
SN74LVC2T45DCTT	TEXAS INSTRUMENTS	TSSOP8	1	Dual-Bit Dual-Supply Bus Transceiver With Configurable Voltage Translation and 3-State Outputs
LTC2052HVCS#PBF	LINEAR TECHNOLOGY	SOIC14	1	Quad Zero-Drift Operational Amplifier
LM340MP-5.0/NOPB	TEXAS INSTRUMENTS	SOT223	1	5 V, 1 A Positive Voltage Regulators
MM3Z5V6B	ON SEMICONDUCTOR	SOD-323F	1	5.6 V 200 mW Zener Voltage Regulator
MM3Z12VB	ON SEMICONDUCTOR	SOD-323F	1	12 V 200 mW Zener Voltage Regulator
1N5819	FAIRCHILD SEMICONDUCTOR	Do-41	3	40 V 1 A Schottky Barrier Rectifier
FXL4TD245BqX	ON SEMICONDUCTORS	QFN16	4	4-Bit Low-Voltage Dual-Supply Signal Translator with Configurable Voltage Supplies and Signal Levels and 3-STATE Outputs
MIC69502WR	MICROCHIP TECHNOLOGY	S-PAK-7	8	Adjustable Low VIN, Low VOUT uCap LDO regulator
P0K1.1206.2P.A	IST (INNOVATIVE SENSOR TECHNOLOGY)	0805	2	-50°C to 150°C, 100 Ohm at 0°C, SM Platinum Temperature sensor

Table 6.1: List of the main components that are part of the OBDTv1 and PUFO boards and that have been irradiated.

DUT name	Function	Usage	Package	Manufacturer
FTLX8574D3BCL	TX/RX	SFP+ PUFO	SFP+	Finisar
AFBR-7099DMZ	TX/RX	SFP+ OBDT	SFP+	Avago
FTL414QB2C	4TX/4RX	QSFP OBDT	QSFP	Finisar
FTL410QD4C	4TX/4RX	QSFP PUFO	QSFP	Finisar

Table 6.2: Optical transceivers used in the OBDTv1 and PUFO boards during irradiation.

the optical transceivers.

The slow control links pathway was:

- Connection between the laptop to the VC707 Xilinx Evaluation board through an Ethernet connection which allowed to implement an IPBUS protocol.
- Primary link: the VC707 had connected the FM-S14 FMC board which included three optical transceivers. Two of them where used to implement a GBTx protocol to the OBDT and to the PUFO. This allowed sending clock and slow control commands. A third optical receiver allowed to receive data from the OBDT under test also through a GBT protocol but implemented directly inside the Polarfire.

- Secondary link: the VC707 had connected a XM105 expansion board which allowed to plug three differential pairs to implement a custom low speed protocol (input, clock and output). This lines were plugged to differential input pins of the PUFO and OBDT boards and were sent through the DB-25 cables between CHARM and the Control Room.

The 35 meters between CHARM and the Control Room were too much to allow that the FlashPro programmer worked satisfactorily in a direct connection. Even if it is implementing a JTAG protocol, the times and the degradation of the TTL signals was too large and it was not working. USB extenders were considered but their radiation tolerance was put under question.

The solution implemented was to build the Flashpro functionality in a Raspberry Pi using the Direct C libraries provided by Microsemi, where we could control the clock frequency and the delays between the commands. And then, we built some expansion boards that performed a TTL to LVDS conversion (and viceversa).

In this way, the JTAG signals were converted to LVDS to be sent through the 35 meters of cable using the DB-25 connections and then some LVDS to TTL conversion was implemented in some boards near the OBDT and PUFO. The LVDS transceivers and receivers DS90LV048 and DS90LV047 had already been validated under radiation and were expected to work fine.

6.1.3.3 SEU-Monitoring Specific Logic

Apart from monitoring the expected OBDT firmware logic in the experiment, a piece of firmware was implemented to perform a comparative measurement of the SEU rate in the Polarfire with respect to the data published by others following techniques detailed in FPGA Radiation test guidelines [72]. Basic flip flop sensitivity to Single-Event Upset (SEU) can be evaluated using shift-registers, by looking at the output of the chain for the expected bit.

The logic implemented consisted on four chains of Flip Flops:

- FF all 1s: One chain where a logic 1 is passed through a chain of 4096 flip-flops and any upset where a 1 is not measured is reported.
- FF all 0s: One chain where a logic 0 is passed through a chain of 4096 flip-flops and any upset where a 0 is not measured is reported.
- CKBRD 40 MHz: a flip-flop chain is feed with a fast checkerboard 1010101 running at 40 MHz. Any change within this pattern is accounted.

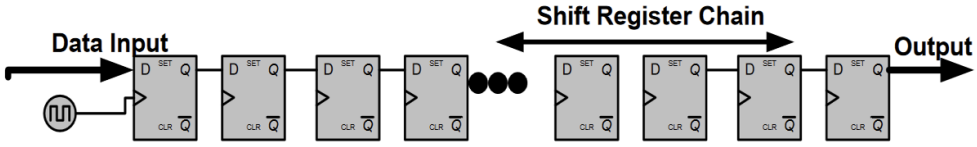

Figure 6.6: Drawing of a flip-flop chain. 4096 elements were used to detect a potential SEU under different logic conditions.

- CKBRD 10 MHz: a flip-flop chain is feed with a fast checkerboard 111100001111000011110000 running at 40 MHz. Any change within this pattern is accounted.

- LSRAM: Errors detected in 17 bit words in a 2^{17} positions RAM memory. Addresses are written as values in the memory. Errors were detected by scrubbing all the RAM continuously.

6.1.4 Dosimetry online and offline at CHARM

The detailed dose measurements at CHARM are made using the LHC Radiation Monitoring System (RADMON) [3]. The RADMON system employs a RADiation-sensitive Field Effect Transistor (RADFET), which is a p-channel MOS transistor that is used to measure the ionizing energy deposition that creates electron-hole pairs in the material. The exposure to ionizing radiation in these transistors increases the positive charge build-up inside the gate oxide (SiO2) layer of the device and this leads to an increase of the threshold voltage. The RadMon detection system provides measurement of the TID by means of these RadFETs but it also provides information about the amount of Displacement Damage (DD) by means of p-i-n diodes, and High Energy Hadrons (HEH) fluence by counting Single Events Upsets (SEU) of SRAM memories. All of these sensors are placed very close to the user's irradiation setup and are measured precisely by the facility personnel. Nevertheless, the data cannot be accessed during irradiation by the user. An online monitoring of the dose rate would be interesting to dynamically identify effects depending on the dose rate in the Device Under Test (DUT) and to understand variation of beam conditions as well as the insertion of the shielding wall. In Appendix B we will explore the possibility of using the safety dosimetry interface accessible through CERN's logging system in order to get online information of the radiation affecting the DUT.

Run	Configuration	POT	TID [Gy]	HEH Fluence [cm-2]	ThN Fluence [cm-2]	1MeV [cm-2]
7_1	CuOOIC	1.54E+15	1.7	4.99E+09	3.76E+10	5.30E+10
7_2	CuOOOO	1.93E+16	108.1	3.28E+11	5.99E+11	1.84E+12

Table 6.3: Configuration used during the irradiation in the two periods and doses and fluences received.

The dosimetry at CHARM which includes the dose and the fluences are obtained by a detailed calibration performed by the CHARM team using the RadMon system and is detailed in here [45]. The irradiation period lasted 9 days and took place between November 3rd and November 12th and it was divided in two periods with different shielding conditions as shown in Table 6.3. A first period where shielding configuration CuOOIC was used and only 1.7 Gy were integrated for around 17 hours and then the second period with configuration CuOOOO for the rest of the irradiation up to a total of 109.8 Gy of collected dose. For reference CuOOIC means: copper target, one block of iron shielding and one of concrete shielding. CuOOOO means copper target and no shielding at all.

Table 6.4 summarizes the total dose and particles fluence of the irradiation session. The hardness factors $H_{50\%}$ and $H_{10\%}$ correspond to the HEH energy values for which the fluxes are 50% and 10% of the total HEH flux, respectively, while the POT is the number of protons impinging the target.

6.2 Results of the Irradiation Campaign

The radiation campaign consisted in a first week of preparation in the nearby room to make sure that all of the equipment was ready and operational in the expected conditions and then nine days of irradiation inside CHARM.

The operation of the set-up could be done fully from remote. A custom Python program was developed to perform the monitoring and control of the set-up. This program allowed to perform all of the usual operations such as configuration of the system, power cycle of the power supplies, reloading of firmware, etc. and then it had a routine that was running continuously in which a loop of actions to monitor the status of the boards was performed (reading and logging the values of the currents, voltages, temperatures of the boards and the values of all of the error counters developed to monitor every quantity that could point to a SEU in the firmware or communication error in the system.

There were two parameters that could not be read remotely: one was the

RADIATION LEVEL	Target inside 03/11/2021 17:23 Configuration change 12-11-21 16:40
Dose (Gy)	109.8
HEH fluence (cm^{-2})	$3.33 \cdot 10^{11}$
ThN fluence (cm^{-2})	$6.37 \cdot 10^{11}$
1MeVneq fluence (cm^{-2})	$1.89 \cdot 10^{12}$
R factor (CuOOIC)	7.54
R factor (CuOOOO)	1.83
Total POT*	$2.08 \cdot 10^{16}$

*POT is the total number of protons hitting the target.

Table 6.4: Total dose and fluence received at CHARM during the irradiation period.

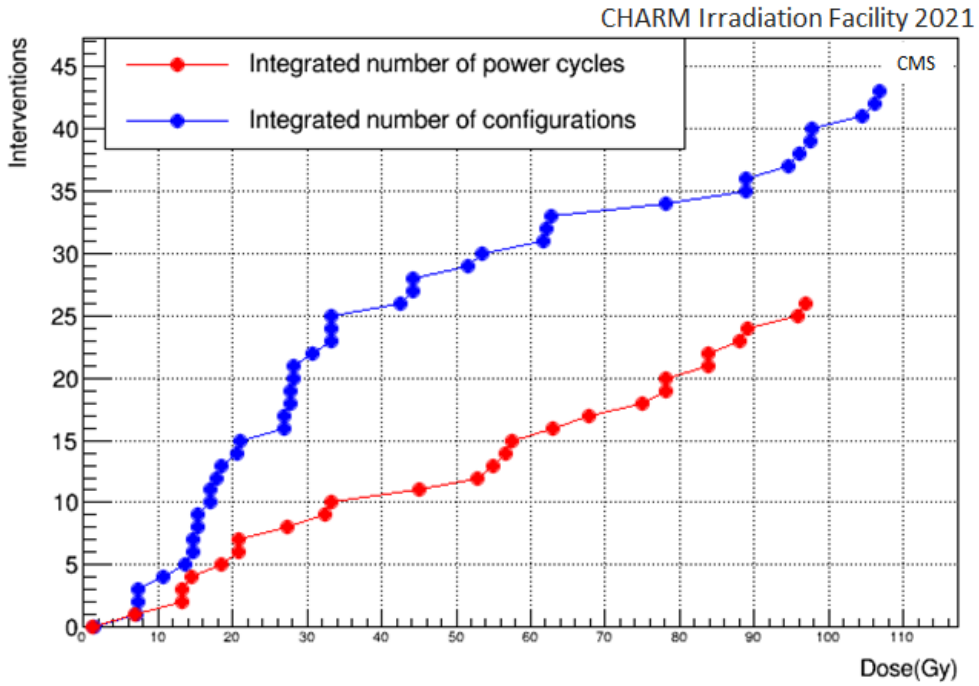

Figure 6.7: Accumulated number of power cycles and reconfigurations performed during the irradiation at CHARM.

current and voltage of the power supply that was powering the DC fan and the other one was the temperature of one of the sensors in the OBDT board. To make sure that we could read the temperature even if all the slow control failed, we cabled one of the PT1000 of the OBDT board to a pair of cables of the DB-25 connector and we were reading the value of this resistor with a multimeter from the control room. Therefore, the temperature could be read, but it was done manually. This was particularly useful to verify the temperature of the board once we suffered a problem with the SCA.

The total number of power cycles and reconfigurations that took place during the test are shown in Figure 6.7.

The power cycles can be classified in two types:

- Interventions (a total of 17) to recover from failures happening where the link was unlocking and providing wrong data. Sometimes they were recovered with a board reconfiguration but the vast majority required a power cycle (and a consequent configuration).

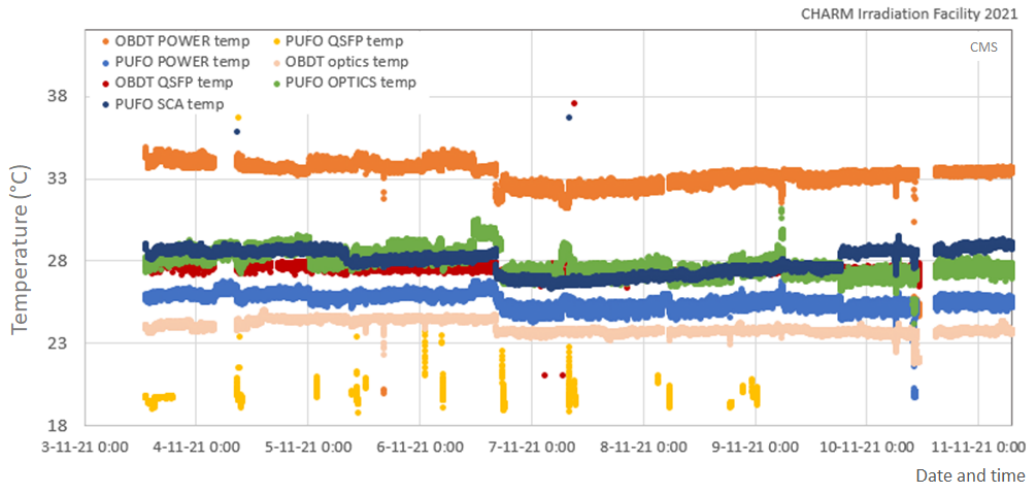

Figure 6.8: Temperatures of all of the OBDT and PUFO board sensors during all the irradiation period.

- Shifters actions for verification of the system not related with system malfunction.

For the dose that we expect in HL-LHC on the OBDT boards if were to operate with these commercial optical transceivers, for a total dose received at CHARM of 109.9 Gy, it would result in 3.67 power cycles/year.

6.2.1 Results from the performance of the fans

As mentioned, two fans were installed in the setup to guarantee redundancy in the cooling to avoid needing to switch off boards. As can be seen in Figure 6.8, the temperature of both boards was pretty stable during the duration of the test and no issue that could be attributed to any of the fans not working or degrading was observed. Both of the worked satisfactorily for the total dose of 109.8 Gy

6.2.2 Results from the Power Supply distribution

The currents of the full setup were measured through the power supplies in both 5V and 3.3 V rails. Only the sum of the currents of both the OBDT and the PUFO per rail was available for monitoring. The results of the currents throughout the period are shown in Table 6.5. As can be seen, both currents experienced a monotonically growth. This has been observed

	3V3 Current	5V Current
START of the Irradiation (A)	4.127	1.653
END of the Irradiation (A)	4.256	1.705
Total Current Increase (A)	0.129	0.052
% Current Increase	3.13	3.15

Table 6.5: Average variation of the test stand currents throughout the irradiation period.

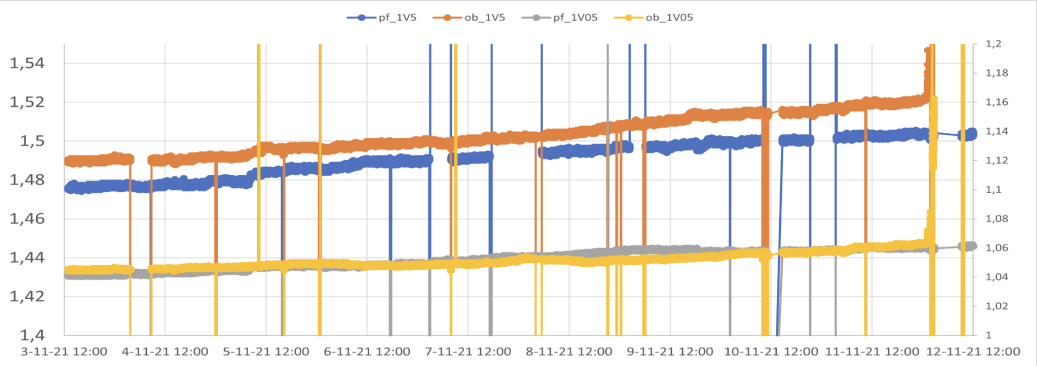

Figure 6.9: Voltages at the output of the linear regulators MIC69502WR in the OBDT and PUFO board during all the irradiation

previously when irradiating these type of regulators and could be due to an increase of the ground current [73]. In average it translates into a current increase in the system of approximately 3%, consistently in both power rails.

The linear regulators at the OBDT board generate different voltages, being the 1.05 V the one used by the PolarfireFPGA. The trends of these voltages can be seen in Figure 6.9. All of these voltages output from the Micrel MIC69502WR regulator and as can be seen there is an increase of approximately 1% of the voltage value throughout the irradiation period. This is also compatible with previous irradiation tests of this technology.

The monotonically ramp has been observed previously with these type of regulators and could be due to the ground current. In average it translates into a current increase in the system of approximately 3% in both power rails.

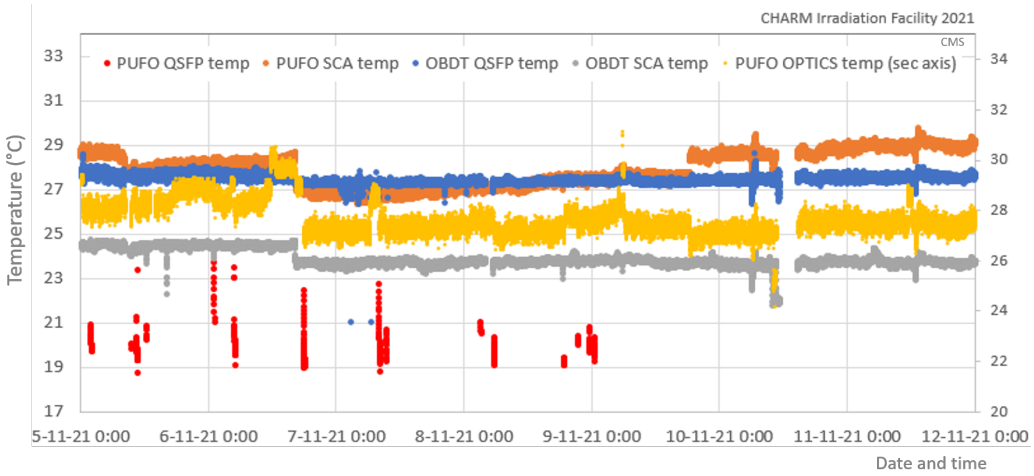

Figure 6.10: Temperatures read from the optical transceivers in the OBDT and PUFO. The temperature sensors of the QSFP are internal to the transceivers and are read through an I^2C interface.

6.2.3 Result from the Optical Transceivers

As shown in Table 6.2, we used four types of optical transceivers during this test. One of them (the QSFP at the PUFO board, which was a Finisar FTL410QD4C) had important problems during the irradiation. In Figure 6.10 the temperatures read out from the different optical transceivers is shown, and as seen, the reading from PUFO QSFP were wrong, with all the digital logic of the transceiver providing invalid data. This effect started right at the beginning of the irradiation and, therefore, it is not due to cumulative effects.

Not only it was not possible to perform the monitoring of the FTL410QD4C temperature, but there were sudden current increases in the system that were related to failures in this transceiver, as they were simultaneous to failures in the data transmission from this device. An example of this can be shown in Figure 6.11, where we can see a sudden increase in the current of the 3.3 V rail which is clearly related with an increase in the temperature sensor closer to the FTL410QD4C. The temperature of the sensor located in the regulators also increased due to the increase of current, but other sensors in the board do not see any increase in temperature. Therefore, it seems clear that very high currents were being drawn by the FTL410QD4C transceiver.

For the optical transceivers that worked correctly, we made an estimation of the failure rate based on two variables:

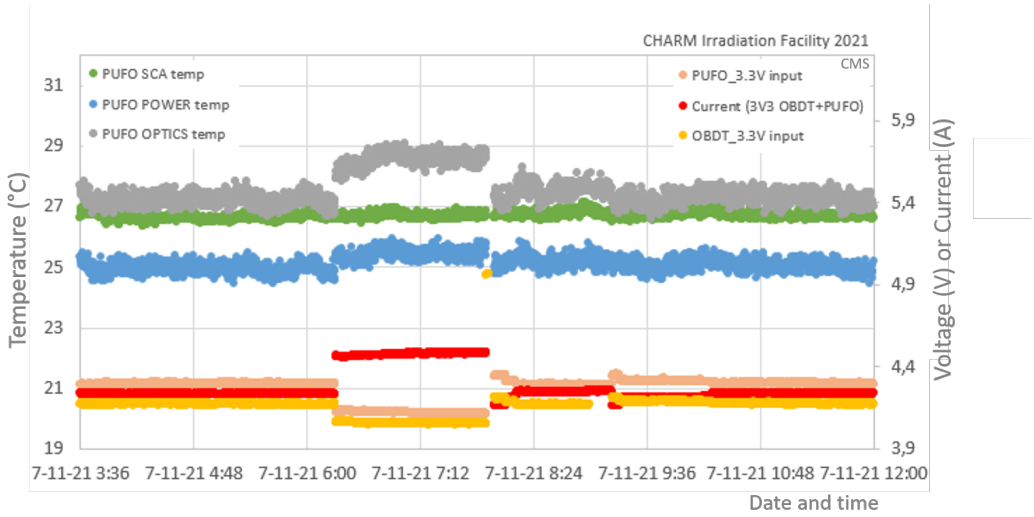

Figure 6.11: Temperatures, currents and voltages in the PUFO board when an increase in current was observed. All the boards functionalities were working properly and the origin of this increase is believed to be in the FTL410QD4C device.

- LOS (Loss of Signal) at the VC707 side, no light arriving to the optical receiver.

- GBT RX_data_error: this is a variable that is activated when the frame of data received had to be corrected due to transmission errors. Under this circumstances, the data received is valid and can be used but it marks that a transmission error took place. This variable is only relevant during periods when LOS is ok.

Some of the LOS events in SFP+ transceivers had a major impact because the clock was lost and a fraction of the monitoring was not reliable. This data has been removed from the estimation of RX_data_errors.

As can be seen in Table 6.6, even if there is a relative large amount of errors during the transmission, and thus, it is not considered safe to operate these devices under radiation, we could still read data correctly through them more than 90% of the time.

	% of the time at 0 errors	
	Loss of Signal	RX_data_errors
SFP+ PUFO, FTLX8574D38CL (Finisar)	91.7	99.5
SFP+ OBDTv1, AFBR-7099DMZ (Avago)	90.3	93.7
QSFP OBDTV1, FTL414QB2C (Finisar	99.5	95.1

Table 6.6: Table with the values of Loss of Signal and *RX_data_error* corrected in the three commercial optical transceivers

6.2.4 Results from the FPGA performance in the reference test

First of all, we present the results from the Polarfire firmware that was devoted to implement a reference test as described in section 6.1.3.3. As mentioned, a piece of firmware was devoted to implement a reference test that could be compared with other publications regarding the Polarfire radiation tolerance.

The number of mismatches in the output values from the flip-flops are counted as SEUs, and the results on each board and test type can be seen in Table 6.7. The formula used to calculate the cross-section is shown in Equation 6.1

$$\sigma(cm^2/bit) = \frac{\#SEUs}{\varphi(\frac{p}{cm^2}) \cdot \#bits} \tag{6.1}$$

	OBDT	PUFO	OBDT	PUFO	Average
	#SEUs	#SEUs	Cross section $(\frac{cm^2}{bit})$	Cross section $(\frac{cm^2}{bit})$	Cross section $(\frac{cm^2}{bit})$
CKBD 40 MHz	60	71	2.08E-14	2.46E-14	2.27E-14
CKBD 10 MHz	33	25	1.14E-14	8.66E-15	1.00E-14
FF All 1s	16	20	5.54E-15	6.93E-15	6.23E-15
FF All 0s	29	22	1.00E-14	7.62E-15	8.83E-15

Table 6.7: Cross sections calculated for the SEU reference test both in the OBDT and PUFO board. Average values are calculated

In addition we, calculated the number of SEU errors detected in the internal RAMs, by scrubbing the 17 bit words data that had been written in

	OBDT	PUFO	OBDT	PUFO	Average
	#SEUs or #MBUs	#SEUs or #MBUs	Cross-section ($\frac{cm^2}{bit}$)	Cross-section ($\frac{cm^2}{bit}$)	Cross-section ($\frac{cm^2}{bit}$)
SEUs	19414	16673	2.08E-14	1.06E-14	1.15E-14
MBUs	1	2	6.37E-19	1.27E-18	9.55E-19

Table 6.8: Cross sections in the RAMs calculated for the SEU reference test both in the OBDT and PUFO board. Average values are calculated.

	Total integrated dose	SEU test integrated dose
Dose (Gy)	109.8	79.82
HEH fluence (cm^{-2})	3.33E+11	2.42E+11
ThN fluence (cm^{-2})	6.37E+11	4.63E+11
1 MeV neq fluence (cm^{-2})	1.89E+12	1.37E+12

Table 6.9: Dose and fluences accumulated when the SEU reference test was operational.

a 2^{17} positions RAM as shown in table 6.8. The firmware was scrubbing all the RAM memory and counting when the word was not the one expected. Few times we could find that the number of SEU counter had a very high value, manifested as a crazy running of this counter. The origin of that is likely to be as a SEU in the part of the logic that affects the SEU-reference counters and the calculation of the address to be read. We are cataloguing those as MBU (Multiple Bit Upsets).

The total dose and fluence used for the cross-sections calculations are lower than the total received because we have removed the periods in which the monitoring was failing. The actual fluence values are shown in Table 6.9

Finally, we show a comparison of this SEU reference test with other radiation tests performed on the Polarfire devices using similar type of logic: Microsemi results for a 10 MeV neutron field [74] and CERN results at PSI with 200 MeV protons in [75]. To compare with previous irradiations found in the literature, we extract cross sections using the combined measured fluence of High Energy Hadrons and Thermanl neutrons as the total fluence of our test. This is done in this way in other places in the literature due to the known content of Boron-10 in the Microsemi Polarfire which makes it susceptible to thermal neutron effects. Our cross sections are a somewhat lower than the ones reported by this other tests but many things were different such as the particle types, energies, clock frequencies and exact firmware

implementations.

	Our Test	PSI CERN	Microsemi LANL 2018
	Cross-section ($\frac{cm^2}{bit}$)	Cross-section ($\frac{cm^2}{bit}$)	Cross-section ($\frac{cm^2}{bit}$)
CKBD 40 MHz	2.27E-14	2.66E-14	1.47E-14
CKBD 10 MHz	1.00E-14	2.31E-14	2.09E-14
FF All 1s	6.23E-15	-	7.39E-15
FF All 0s	8.83E-15	5.31E-15	7.39E-15
LSRAM SEUs	1.15E-14	1.37E-14	1.42E-14
LSRAM MBUs	9.55E-19	<9.5E-18	<5.58E-16

Table 6.10: Comparison of the cross sections in the SEU reference test performed by us at CHARM and by other groups at different facilities.

6.2.5 Results from the FPGA performance in the final firmware test

As described in Section 6.1.3.1 we have also monitored the number of SEUs that could come from a mismatch in the time measurements of the signals between the PUFO and the OBDTv1, that is, representing the final behavior of the logic during operation in CMS. This firmware is expected to be very similar to the one operating during HL-LHC and it has been built using Triple Module Redundancy (TMR) and Cyclic Redundancy Check (CRC) mechanisms in the RAMs. The only part that does not contain TMR is the deserializer logic of the TDCs and the high speed transceivers. The transceivers are out of the scope in these measurements because of the impossibility to distinguish from the errors of the optical transceivers. Indeed, the results presented here are done using the secondary electrical link, to ensure reliable transmission.

As mentioned before, the test consisted in injecting hits from the PUFO into the OBDT, measure the time of the signal and reporting any mismatch. Three Hit Error Counters were built to monitor the mismatches, any of them are accounted as SEU:

- An expected hit it is not received
- The hit is received with wrong timing
- Or there is more than one hit received in a time window

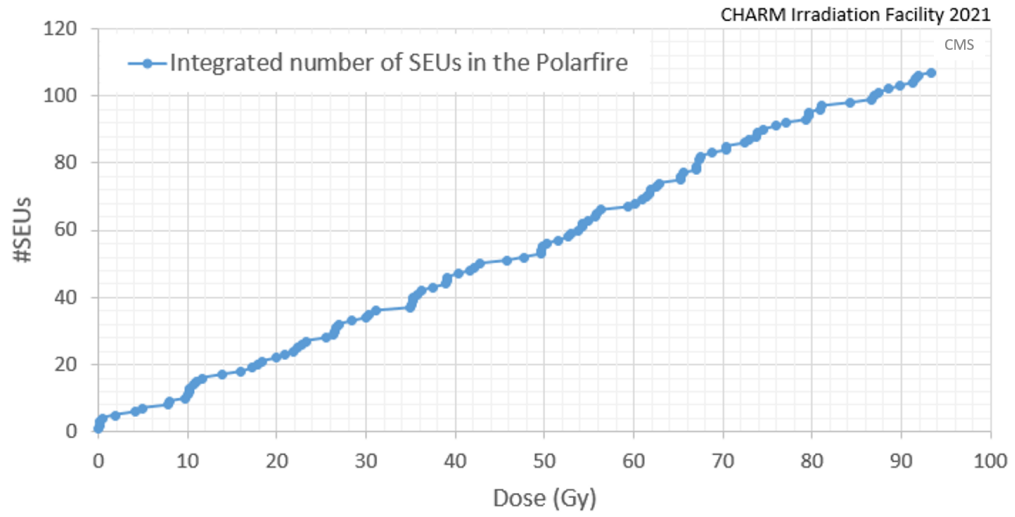

Figure 6.12: Results of the number of SEUs measured in the test stand versus the integrated dose.

These Hit Error Counters are implemented both at the VC707 and inside the OBDT. There are also three ways of reading out the content of this counters:

- A: Hits read through link 3 from OBDT 2 (normal optical readout) and error counters implemented in the VC707
- B: Error counters implemented in Polarfire and read through link 3
- C: Error counters implemented in Polarfire and read through an electrical link

The full system was working correctly during all the test and after the total integrated dose of 109.8 Gy. There were failures attributed to SEUs, but all of them were recoverable automatically. No destructive effect was observed and indeed, no effect that forced to program the FPGA. Sporadic power cycles were happening as mentioned before but they are all attributed to failures in the commercial optical components.

Typically all of the SEUs affected all of the channels simultaneously, meaning, the SEU was not on the time measurement itself but in the BC0 signal, reset distribution or similar logic. Those are counted as 1 SEU. We also crosschecked the counters from the three different monitoring paths, providing coherent result. The electrical path allowed to identify some burst of

errors that were clearly failures in the optical path due to link instabilities. Those errors are clearly not SEUs since their pattern is very different.

The fact that the SEUs affected all of the time measurements simultaneously seems to point to errors in the common logic, particularly what controls the resets. This effect is similar to the ones described in several publications ([76], [77]) and point to the FPGA suffering from radiation-induced resets on the FPGAÂ´s System Controller which is known not to be triplicated. Mitigations exist (disabling the System Controller) to reduce the occurrence of the failure, which cannot be completely suppressed unfortunately. Still, it can be seen that the rate is low. The results show 107 SEUs through all the irradiation campaign. The distribution of those errors versus dose is shown in Figure 6.12.

Taking into account the amount of logic that was used in both devices during the test, the cross-section obtained with these number of failures is $2.33 \times 10^{-15} cm^2/bit$, which seem in the ballpark of previous measurement.

The dose expected in the CMS detector during the HL-LHC is not uniform in the detector, therefore, the extrapolation to the HL-LHC expected failure rates has been separated into different regions according to its expected dose. The results of the number of expected SEUs is shown in Table 6.11. The rest of the failures related to the optical transceivers are not worth extrapolating, since it is clear that different devices will be used in the final system.

Cross sections for the Polarfire FPGA have been measured in a benchmark system and with a version close to the expected firmware. Measured numbers are adequate for our application since the extrapolated number of errors to HL-LHC is below 1 error/day in the full system, which would be the limit of what could imply heavy supervision and recuperation in the system or certain data loss.

6.2.6 Results of the Microsemi Polarfire Remote Reprogramming Firmware

As described before, we built a system to program and verify remotely the Polarfire's FPGA firmware. Before the radiation tests started, but already in the bunker zone, we could verify that the FPGA firmware verification was working fine. However, the first time we tried once the irradiation had started after 15.55 Gy, the firmware verification was not working. IDCODEs were being read properly but the verification was failing in both FPGAs. This was the situation until the end of the test. However, at the end of the irradiation period we were capable of loading the firmware remotely so the programming system seemed to work fine after 109.8 Gy (though still the

	All 840 boards	MB1 externals (72)	MB4 (240)	MB3 (240)
#failures/system	107	107	107	107
#failures/board	53.5	53.5	53.5	53.5
#failures for 840 boards	44940	3852	12840	12840
Total dose integrated at CHARM (Gy)	93.96	93.96	93.96	93.96
Dose at HL-LHC (Gy)	0.505	2.10	0.59	0.06
Dose factor	186.06	44.74	159.25	1566.00
#failures all HL-LHC	241.54	86.09	80.63	8.20
#failures/year	24.15	8.61	8.06	0.82
#failures/day (100 operating days/year)	0.24	0.09	0.08	0.01
#days between failures	4.14	11.62	12.40	121.963

Table 6.11: Extrapolation of the number of failures due to SEUs in the OBDT board expected during HL-LHC if we separate the contribution of each chamber type which has very different expected fluence.

verification procedure was faulty).

6.3 Summary and Conclusions

In this chapter, the tests performed on the HL-LHC electronic prototypes (the OBDTv1) for the CMS DT detector have been presented.

An introduction to the design of the OBDTv1 board is presented, explaining its main characteristics and how it has been designed at CIEMAT to perform the time digitization of the CMS DT chamber signals.

Next, the CHARM facility at CERN, where the electronics has been exposed to an accelerated radiation field, is revisited. The testing system built to test this OBDTv1 board under radiation is described, and the radiation campaign, with the main highlights of the results obtained for the different devices that compose the OBDTv1 are explained.

From the data obtained in this several days campaign, estimations of the performance of the various electronic components of the board can be estimated. Particularly relevant are the results of the performance of the FPGA Microchip Polarfire of the OBDTv1. The interest of the particle

physics community in this device is growing due to its excellent performance under radiation. The results about the SEU cross sections obtained in this radiation exercise are described and compared with what can be obtained in the literature.

Finally, extrapolations to the expected performance of the new designed electronics during its operation in HL-LHC have been performed and show that the new system will be able to operate reliably during all the CMS Phase 2 data taking period, ensuring its optimal performance with minimum downtime.

My contribution to the construction of this testing system, realization of the radiation tests, analysis of the radiation obtained at CHARM and of the results from the radiation campaign, have been critical to perform these tests.

Conclusions

Throughout the different chapters of this thesis, I have aimed at achieving the goal of investigating the reliability of the DT detector during its operation in HL-LHC. The identification and precise tracking of the muon particles will remain of uttermost importance during the operation of the CMS Phase 2, since muons are very clear signatures for a large variety of the physical processes that are to be studied at a proton-proton collider. Ensuring this optimal performance of the muon detector in the barrel region of CMS is challenging at the HL-LHC conditions, since we will have not only a much larger radiation environment but also, we will be dealing with an aged detector that will suffer from the accumulated charge from this radiation field, due to the impossibility of replacing the full DT system.

Accordingly, it was critical to evaluate the performance of the DT chambers under the accumulated integrated charge as well as providing very valuable insight on the performance of electronics under the expected levels of radiation in order to allow for a reliable design of a new system.

The studies performed included detailed simulations and experimental tests at the GIF++ and CHARM facilities at CERN, that reproduced the expected radiation environment, including gamma rays, neutrons, and charged particles. Tests were conducted on both the gaseous detectors and the readout electronics, with a focus on assessing their resilience to radiation damage, and sporadic and long-term impact of radiation exposure. This work evaluated the ability of the DT detectors and their readout electronics to withstand these conditions while maintaining performance in terms of loss of gain, hit efficiency, downtime and operational stability. Additionally, this thesis explored mitigation strategies to enhance the longevity of both the gaseous detector and its electronics, including optimization of gas mixture and the development of radiation-hardened electronics.

A wrap-up of the main conclusions that can be extracted from the work described in previous chapters are:

1. Radiation field at HL-LHC: Through the use of simulations and analy-

sis of the proton-proton collision data, it has been possible to estimate the radiation field and the actual background that will be suffered in the different region of interest of our DT detector and its electronics. These estimations have allowed to perform extrapolations to the instantaneous luminosities foreseen during operation at the HL-LHC.

2. Longevity of the DT gaseous detectors: We observed at the GIF++ facility, using a strong gamma source and muon beams, that the performance of the DT gaseous detectors was much more affected by radiation aging than previously expected. Several irradiation tests allowed to obtain quantitative results about the loss of gain and degradation in the expected hit efficiency with several safety factors. Obtaining a reliable measurement of the collected dose at GIF++, which was my responsibility, was key to perform any type of quantitative assessment and extrapolation of the results obtained irradiating the chambers. After careful analysis, it can be stated that the CMS DT detector could be capable of sustaining the radiation levels expected at the HL-LHC, with some minor degradation in efficiency in the most exposed regions after prolonged exposure. My results from GIF++, Figure 3.16 in particular, are the basis of the DT Upgrade longevity plan, and as such appear in the Phase 2 Muon TDR, being one of the cornerstones of the DT Upgrade. The gas mixture of Ar/CO_2 was found to remain stable under moderate radiation doses, with no significant aging effects that would impede detector performance over time. The DT wires suffer coating of their surface which translates into a loss of detection efficiency which has been quantified, but no other unpleasant effects such as Malter effects have been spotted from the analysis of the currents during the tests. The origin of the coating is not fully confirmed but it seems primarily made of hydrocarbons and also silicon deposits coming from the glue of the electrodes. The results obtained here have been critical to be able to perform estimations of the expected DT detector degradation during its operation at HL-LHC and use this information to create the aged samples to study the performance of improved trigger algorithms for the future operation of CMS.

3. Modeling the aging effects: a model for the aging phenomena that the DT chambers have suffered during its irradiation at the GIF++ facility at CERN has been implemented and described. The model is following the classical expectations for aging in gaseous detectors and addresses the impact on the most sensitive part of the detector, its wire. The degradation of this wire has been modeled through an hypothesis of the

coating surrounding it and the formulation of the resulting equations representing two capacitors and resistors acting in series. Through this mathematical model, the voltage and electrical field in the DT cell can be obtained and results about its expected performance can be obtained numerically. I have compared these simulations with the experimental data acquired during the irradiation at GIF++ of the DT chamber, in order to evaluate if this model can represent the aging effects that we have observed. The conclusion obtained is that the majority of the effects observed at GIF++ on a DT chamber seem to follow well the classical aging phenomena on gaseous detectors with a loss of gain and hit efficiency which is compatible with a coating surrounding the wire of the thickness and relative permittivity studied. As a last remark, the performance of the detector under a high instantaneous radiation field departs from the expected classical behaviour and an hypothesis of what could be happening that explains the measured results is performed.

4. Mitigation strategies: The acknowledgement that the DT detector will suffer some performance loss during its operation at HL-LHC has been critical to launch a series of actions to minimize the impact of this degradation and the most important mitigating actions that we have implemented in the DT detector have been described. The non-recirculation of the gas flow was a relatively straightforward action, but the lowering of the high voltage to reduce the gain of the detector during most of its lifetime required to work with the information provided by the measurements at GIF++ which proved that by lowering the high voltage, the loss of gain was reduced. The nominal operating voltage was 3600 V and results showed that lowering the voltage by 50 V or even 100 V we can keep a reasonable hit reconstruction efficiency while lowering the speed at which the gain decays in the detector. A major mitigating action was implemented in the form of an active protection of the chambers with the installation of a shielding structure to cover the top most exposed DT chambers, which seemed the best way to guarantee a low radiation field in the chambers. The shielding was made out of a 3 cm borated polyethylene sheet and a 7 mm lead sheet that covered all of the MB4 chambers. We have measured the attenuation in situ from the background data rate in the range 2.5-3, results which compares well with the results obtained from currents. Through simulations of the passage of radiation through matter, the actual attenuation factor of the shielding structure has been calculated and compares well with the real attenuation observed at CMS. Poten-

tial shielding options for the now most exposed MB1 chambers in the external wheels have been studied.

5. New electronics for CMS DT at HL-LHC: A first set of tests showed that the legacy DT electronics needed to be substituted when operated at the larger L1 rate needed by CMS during HL-LHC. Accordingly, a new plan for upgrading all the electronics of the CMS DT chambers was developed and this included the fabrication of time digitization electronics using the up-to-date technologies in the market. The OBDTv1 was one of such prototypes and, apart from showing its good performance for the task it was designed, it was required to ensure that it would be optimal also for operation under the harsh environmental conditions expected at HL-LHC. Through dedicated accelerated irradiation tests at CHARM, results about the expected performance of this board at HL-LHC have been obtained. It has been verified that most of its components can stand the expected dose and charged particles flux safely. In particular, the results about the SEU rate in the Microchip FPGA are of importance to the particle physics community. The four optical transceivers tested showed very poor performance and it settled the selection of radiation hard optical transceivers for the final system. An extrapolation of the estimated performance of the system during HL-LHC shows that the expected number of errors and consequent downtime is very minor.

In summary, radiation aging affecting the CMS Drift Tubes has been studied and also modeled from different angles: loss of gain in the detectors, the increase of occupancy from background radiation and the effects on electronics.

While the DT detector system is generally prepared for the HL-LHC's conditions, several *R&D* efforts have been required to improve resilience further, both with mitigating action on the detectors and by fully replacing its electronics. The integration of more robust designs and strategic actions for both the gaseous detectors and electronics will be crucial to meet the long-term demands of the experiment. Future performance of the Drift Tube Chambers is expected to be guaranteed with the changes in design and the application of mitigation techniques.

My personal contributions have included a diversity of aspects. I have worked in all of the activities mentioned in this thesis, which required a variety of expertise. I have personally worked in the installation and operation of the radiation tests, both with the DT chambers and with the electronics prototypes on site at the two facilities at CERN: GIF++ and CHARM. I

have worked in the analysis of the data (particularly the dose and the currents) and I have worked to obtain a reliable estimation of the loss of gain in the detector. A model that represents this aging has been developed and comparison with the data obtained from the experimental tests has allowed to gain insight into the detailed aging mechanisms. In addition I have worked in the simulation of the different shielding structures that could protect the DT chambers from the exposure to the radiation field, cross checking the data obtained at CMS with the results from this simulations and ensuring that a good selection was made. And finally, I have worked in commissioning and evaluating the new electronics prototypes for CMS Phase 2 and in the analysis of the data obtained during radiation tests that allow to obtain extrapolations of its expected performance under HL-LHC and make design decisions for the final version of the boards.

The above contributions have resulted in the following three articles in international journals and a significant contribution to a book chapter:

1. D.D. Redondo Ferrero et al. on behalf of the CMS DT collaboration. *"Irradiation aging of the CMS Drift Tube muon detector"*. Radiation Physics and Chemistry. 2020-07. The contents from this publication are the result of my work performed during the GIF++ irradiation and are fully included in the Chapter 3 of the Thesis.

2. G. Abbiendi, D. D. Redondo (corresponding author) et al., "*Irradiation tests of the OBDTv1 board at CHARM"*. Submitted to JINST with reference JINST_028P_1024. The contents from this publication are the result of my the work during the irradiation at CHARM of the OBDTv1 prototype to validate its performance during HL-LHC and are fully included in the Chapter 6 of the Thesis.

3. C. F. Bedoya, G. Abbiendi; J. Alcaraz Maestre; A. Álvarez Fernández; Barbara Álvarez González; Nicola Amapane; Irene Bachiller; L. Barcellan; C. Baldanza; C. Battilana; M. Bellato et al. *"The Analytical Method algorithm for trigger primitives generation at the LHC Drift Tubes detector"*. Nuclear Instruments and Methods in Physics Research Section A: Accelerators, Spectrometers, Detectors and Associated Equipment. 2023-04. A fraction of the contents from this publication, particularly the results shown in Figure 2 of this paper, come from the results of my work during the GIF++ irradiation. These activities and the results are fully included in the Chapter 3 of the Thesis.

4. CMS collaboration. *"The Phase-2 Upgrade of the CMS Muon Detec-*

tors" 2018. Technical Design Report. CERN-LHCC-2017-012, CMS-TDR-016. This book is the Technical Design Report from the CMS experiment towards the upgrade of the CMS Muon Detector. It has not been published directly in a journal, but is the result of whole collaboration ($>$ 4000 people) review and as such, has been deeply scrutinized. Chapter 3 of this TDR includes plenty of results from this Thesis, as can be seen in full Chapter 3 (for instance pages 87). These results appear also in Chapter 3 of his Thesis.

Finally, I have attended several international conferences in the field.

As a conclusion, this work provides relevant insights into the future operation of the CMS DT detector and sets the groundwork for further improvements in detector and electronics performance in high-radiation environments. The know-how obtained during the development of these activities has allowed to draw a plan for upgrades of the CMS DT detector and to foresee the expected degradation and the failure rate that we can expect from the operation during HL-LHC. In summary, it is expected that this work has helped paving the way towards an efficient and reliable detector from which we can extract the best physics performance and gain insight into the understanding of the subatomic world.

Appendix A

Evaluation of using a Half-Filter for the source at GIF++

Many users with different types of muon detectors place their devices for irradiation at GIF++ and, sometimes, it is difficult to accommodate the different needs regarding filter configuration for everyone. The DT studies at GIF++ require a small dose rate compared to the rest of the detectors on the same region of the bunker. It was discussed to add another filter that only attenuated half of the irradiation cone, without altering the field for the rest of the detectors. For this reason, the Rheinisch-Westfälische Technische Hochschule (RWTH) group from Aachen built a filter made of lead, with the same design as the original GIF++ filters but that only covered half of the source area, allowing to theoretically reduce by a factor 10 the dose received by half of the downstream area. In order to verify the nominal attenuation of the filter and make sure that it did not interfere with the rest of the users some measurements were made as shown in A.1.

The attenuation was lower than expected in most of the irradiation field. One of the possibilities for this discrepancy is the detection of Compton scattered photons that would increase the measured dose. As can be seen in A.1, the area without filter the dose distribution profile remains pretty much like with the filter, however, the other region should have a larger plateau at 10 while it shows a very slow curve. This is likely due to a spherical distribution of the dose instead of a flat one as shown in the simulations [44].

Preliminary results show a different shape for the irradiation field in the non-shielded area that was supposed to be homogeneous in the horizontal plane according to the simulations. The lack of flatness in the half filter regions shows the limitations of this approach for the controlled irradiation or large objects such as a DT chamber. The results have been presented to

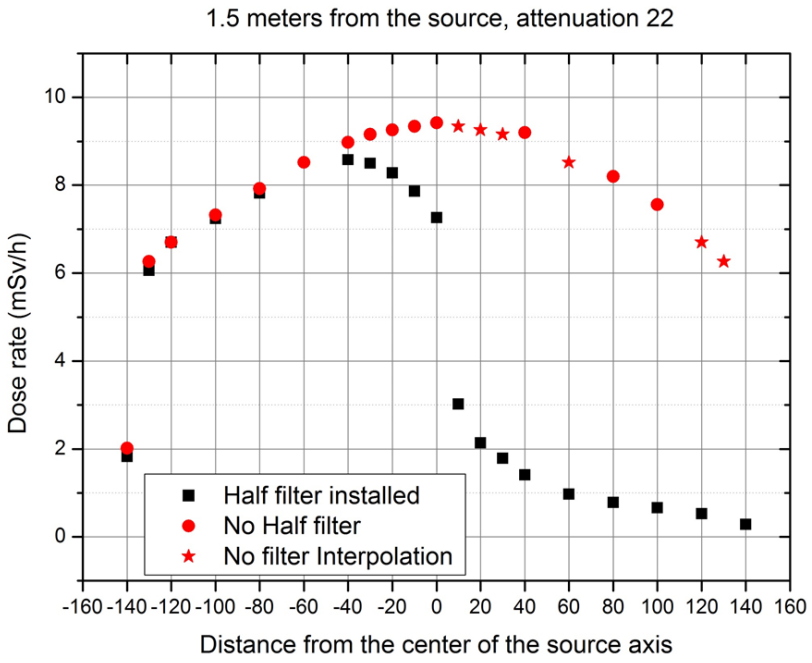

Figure A.1: Dose rate as a function of the distance to the center of the bunker

the GIF++ management in order to further understand the conditions of the irradiation. At the time it was decided that the effects of installing an additional filter to reduce the amount of dose to the DT chamber was not completely understood and the idea was discarded.

Appendix B

Online Dose Monitoring for the CHARM Facility

The variable that we propose to use is the information of the PMIEA822 proportional chamber installed inside the CHARM radiation area. PMIEA821 measurement in location '0' in Figure B.1, behind the shielding. The main advantage is that it can be accessed in real time by TIMBER (the main Web Application which provides access to CERN Accelerator Logging Service data)

Beam Spill Structure

The information from this detector is recorded and is available to the user through the TIMBER interface. An example of the data extracted from TIMBER for the full irradiation period (November 3rd to November 12th 2021) can be seen in Figure B.2. As can be seen, TIMBER provides information of the dose rate of this detector versus time, with rather precise timestamping. Two populations can be seen, one in which the dose rate is very small and one with large dose. We make the hypothesis that the large dose values correspond to a spill hitting the target providing the possibility to derive a "Spill counter" estimator from this measurement. A zoom in of this structure can be seen in Figure B.3.

In order to establish the threshold for discriminating the beam spill "events", a histogram of the distribution of the dose rate was calculated. There is a tail of medium dose rate values that can be associated to ambient dose. The image of the histogram can be seen in Figure B.4 The threshold chosen to consider a beam spill is 5.5 Sv/h, which seems a reasonable value to count spill events.

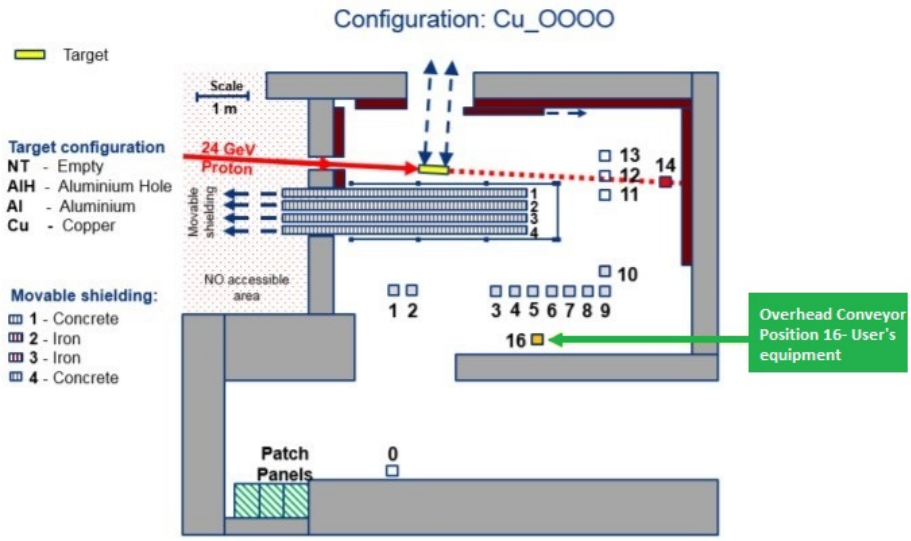

Figure B.1: Drawing of the CHARM facility aerial view with the irradiation locations.

Spill Counter vs Dose Correlation

In what follows, we correlate the values read from TIMBER with the dose provided by the radiation group in our DUT. In Figure B.5 we compare the number of spills, calculated as described previously, to values of the two RADMON sensors provided by the CHARM facility. As can be seen, both measurements follow the same trend in time.

In Figure B.6, the values of the number of spills versus the integrated dose are presented. In that plot two clear slopes can be seen. The large slope from the first part corresponds to the period where the shielding (CuOOIC) was present, requiring a larger number of spills to obtain the same dose in our DUT location. The rest of the irradiation period was performed without shielding (CuOOOO). The correlation of the number of spills and the dose is remarkable, showing the device can provide a relative dose monitoring without any calibration.

If we make the assumption that a constant dose is delivered on each spill, we can obtain the amount of dose for each spill in the different conditions at CHARM. In this way, we could obtain constant calibration factors to allow to providing an instantaneous dose rate monitoring system from the number of spills read from TIMBER. It is clear that the actual dose received

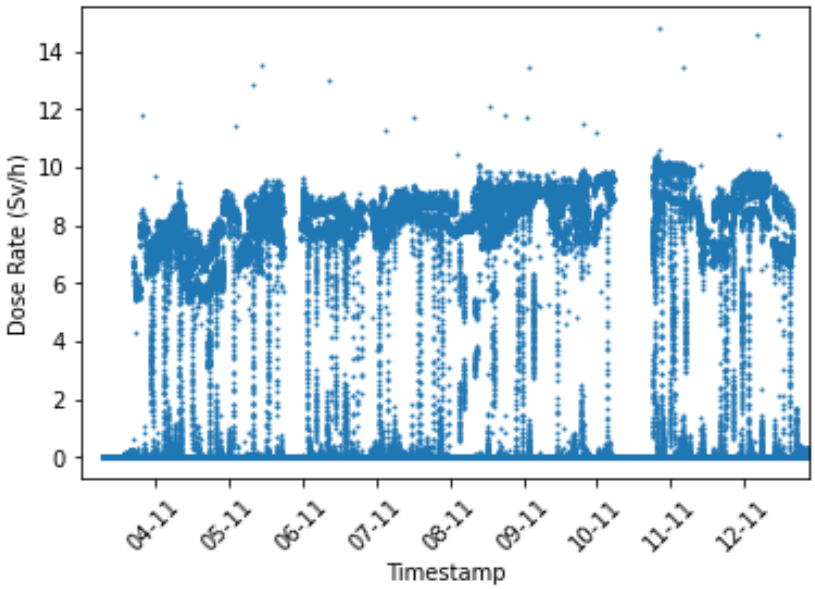

Figure B.2: Representation of the full dataset of the 822 proportional counter information as recorded in TIMBER during the OBDTv1 irradiation period of November 3rd to November 12th 2021.

by each system depends on the location inside the facility. In this case we are providing the results for our DUT which was located on the conveyer. Different correction factors could be calculated from dose vs time data in the different CHARM positions.

We select the region of the data that did not have the shielding as it is the longest part of the irradiation. A linear fit is performed in this data and a strong correlation between the spill number and the integrated dose can be obtained as shown in Figure B.7. The equation of the linear fit is: $y = 348.93x + 674.28$ The coefficient of determination obtained (R2) is = 0.9996

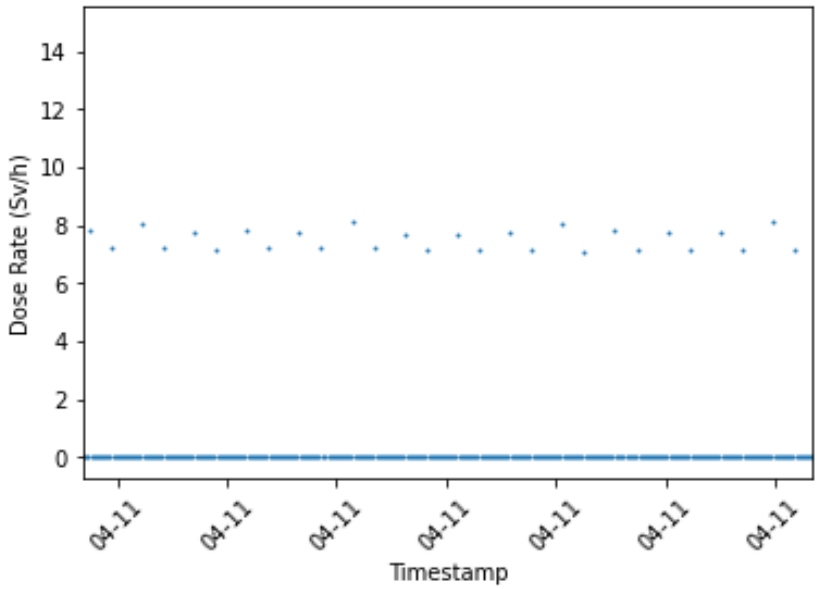

Figure B.3: Figure 3: Zoom in of the TIMBER data for the 822 proportional counter.

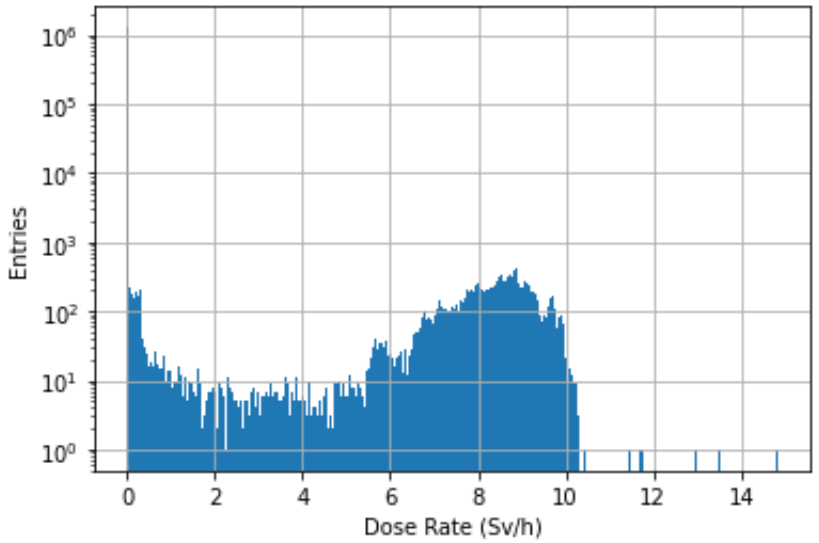

Figure B.4: Histogram of the values of the 822 proportional counter detector as read by TIMBER during all of the radiation period between November 3rd to November 12th 2021.

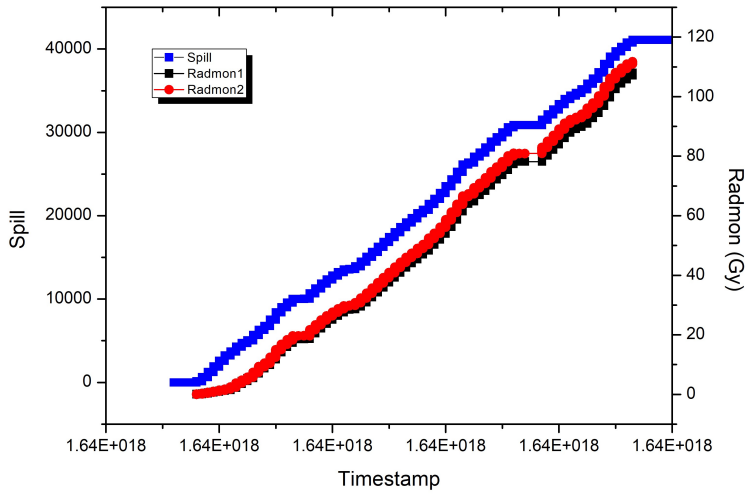

Figure B.5: The number of spills over threshold versus time is represented together with the dose recorded by the two RADMON sensors. As can be seen the behaviour of both measurements is very similar.

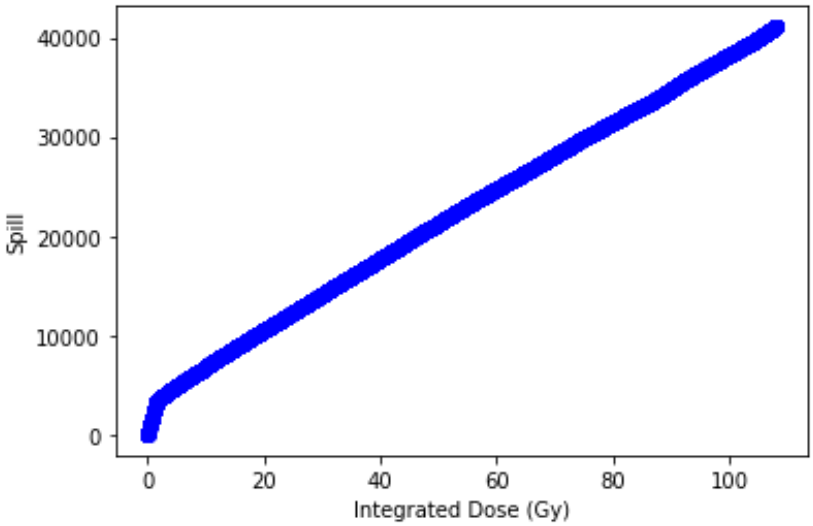

Figure B.6: Representation of the number of spills selected from TIMBER versus the integrated dose provided by RADMON.

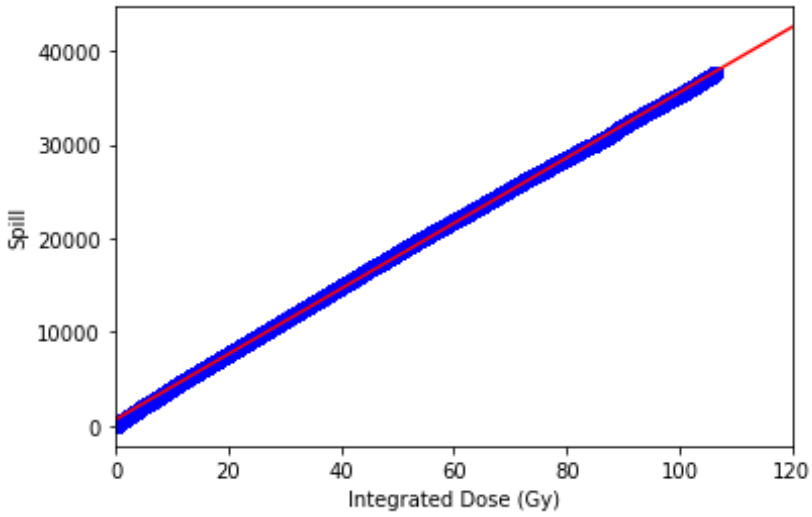

Figure B.7: Representation of the number of spills selected from TIMBER versus the integrated dose provided by RADMON for the period without shielding and the linear fit included.

References

[1] Mary K. Gaillard, Paul D. Grannis, and Frank J. Sciulli. *The Standard Model of particle physics*. *Reviews of Modern Physics*, 71(2), 1999. ISSN 1539-0756. URL http://dx.doi.org/10.1103/RevModPhys.71.S96.

[2] The CMS Collaboration. *The CMS experiment at the CERN LHC*. *Journal of Instrumentation*, 3(08):S08004, 2008. doi: 10.1088/1748-0221/3/08/S08004. URL https://dx.doi.org/10.1088/1748-0221/3/08/S08004.

[3] Oliver Sim Bruning, Paul Collier, P Lebrun, Stephen Myers, Ranko Ostojic, John Poole, and Paul Proudlock. *LHC Design Report*. CERN Yellow Reports: Monographs. CERN, 2004. doi: 10.5170/CERN-2004-003-V-1. URL https://cds.cern.ch/record/782076.

[4] O. Aberle, I Bejar Alonso, O Bruning, P Fessia, L Rossi, L Tavian, and others. *High-Luminosity Large Hadron Collider (HL-LHC): Technical design report*. CERN Yellow Reports: Monographs. CERN-2020-010. CERN, 2020. doi: 10.23731/CYRM-2020-0010. URL https://cds.cern.ch/record/2749422.

[5] *The LEP project*. CERN-PU-ED-80-01. CERN, 1980. URL https://cds.cern.ch/record/445031.

[6] ATLAS collaboration. *ATLAS high-level trigger, data-acquisition and controls: Technical Design Report*. CERN-LHCC-2003-022. CERN, 2003. URL https://cds.cern.ch/record/616089.

[7] ALICE collaboration. *ALICE: Technical proposal for a Large Ion collider Experiment at the CERN LHC*. CERN-LHCC-95-71. CERN, 1995. URL https://cds.cern.ch/record/293391.

[8] LHCb collaboration. *LHCb : Technical Proposal*. CERN-LHCC-98-004. CERN, 1998. URL https://cds.cern.ch/record/622031.

[9] CMS collaboration. *The CMS muon project: Technical Design Report*. Technical design report. CMS. CERN-LHCC-97-032. CERN, 1997. URL https://cds.cern.ch/record/343814.

[10] *CAEN SY4527 Universal Multichannel Power Supply System*. Technical report. URL https://www.caen.it/products/sy4527/.

[11] F Gonella and M Pegoraro. *"The MAD", a Full Custom ASIC for the CMS Barrel Muon Chambers Front End Electronics*. Proceedings of the 7th Workshop on Electronics for LHC Experiments, pp.204-208, 2001. doi: 10.5170/CERN-2001-005.204. URL https://cds.cern.ch/record/529411.

[12] Syed B. Huq. John Goldie. *An Overview of LVDS Technology*. Technical report, 1998. URL https://www.ti.com/lit/an/snla165/snla165.pdf.

[13] J M Cela, G Dellacasa, Cristina Fernandez-Bedoya, J Marin, V Monaco, J C Oller, P De Remigis, A Staiano, and C Willmott. *CMS Drift Tube Chambers Read-Out Electronics*. Proceedings of the Topical Workshop on Electronics for Particle Physics, pp.190-194. CMS-CR-2008-018, 2007. doi: 10.5170/CERN-2007-007.190. URL https://cds.cern.ch/record/1089265.

[14] J. Christiansen. *HPTDC High Performance Time to Digital Converter*. Technical report, CERN, 2004. URL https://cds.cern.ch/record/1067476.

[15] Texas Instruments. *DS92LV1021 and DS92LV1210 16-40 MHz 10 Bit Bus LVDS Serializer and Deserializer*. Technical report. URL https://www.farnell.com/datasheets/1761189.pdf.

[16] Andrea on behalf of the CMS collaboration Triossi. *The CMS Barrel Muon Trigger Upgrade*. *Journal of instrumentation*, (12 C01095): Proceedings of the Topical Workshop on Electronics for Particle Physics (TWEPP 2016), 2017. doi: 10.1088/1748-0221/12/01/C01095. URL https://cds.cern.ch/record/2252301.

[17] *Advance Mezzanine Card Base Specification AMC.0 R2.0*. Technical report. URL https://www.picmg.org/advanced-mezzanine-card-base-specification-amc-0-r2-0/.

[18] *AMD Virtex 7 FPGA*. Technical report. URL https://www.amd.com/en/products/adaptive-socs-and-fpgas/fpga/virtex-7.html.

[19] A. Navarro-Tobar, A. Triossi, C. Fernandez-Bedoya, I. Redondo, D. Redondo, J. Sastre, J.M. Cela-Ruiz, and L. Esteban. *Phase 1 upgrade of the CMS drift tubes read-out system*. 2017 Journal of Instrumentation 12 C03070, Proceedings of the Topical Workshop on Electronics for Particle Physics (TWEPP 2016). doi: 10.1088/1748-0221/12/03/C03070. URL https://iopscience.iop.org/article/10.1088/1748-0221/12/03/C03070.

[20] CMS Collaboration. *CMS The TriDAS Project: Technical Design Report, Volume 2: Data Acquisition and High-Level Trigger. CMS trigger and data-acquisition project.* Technical design report. CMS. CERN-LHCC-2002-026. CERN, 2002. URL https://cds.cern.ch/record/578006.

[21] RD5 collaboration et al. *Bunch crossing identification at LHC using a mean-timer technique*. *Nuclear Instruments and Methods in Physics Research Section A: Accelerators, Spectrometers, Detectors and Associated Equipment*, 336(1):91–97, 1993. ISSN 0168-9002. doi: https://doi.org/10.1016/0168-9002(93)91082-X. URL https://www.sciencedirect.com/science/article/pii/016890029391082X.

[22] J. Ero, I. Evangelou, G. Flouris, C. Foudas, L. Guiducci, N. Loukas, N. Manthos, I. Papadopoulos, E. Paradas, S. Sotiropoulos, P. Sphicas, A. Triossi, and C. Wulz. *The CMS Level-1 Trigger Barrel Track Finder*. *Journal of Instrumentation*, 11(03):C03038. Proceedings of the Topical Workshop on Electronics for Particle Physics (TWEPP2015), 2016. doi: 10.1088/1748-0221/11/03/C03038. URL https://dx.doi.org/10.1088/1748-0221/11/03/C03038.

[23] CMS collaboration. *Technical Proposal for the Phase-II Upgrade of the CMS Detector*. Technical Report CERN-LHCC-2015-010, LHCC-P-008, CMS-TDR-15-02, 2015. URL https://cds.cern.ch/record/2020886.

[24] A Ferrari, Paola R Sala, A Fasso, and Johannes Ranft. *FLUKA: A multi-particle transport code (program version 2005)*. CERN Yellow Reports: Monographs. CERN-2005-010. CERN, 2005. URL https://cds.cern.ch/record/898301.

[25] CMS collaboration. *The Phase-2 Upgrade of the CMS Muon Detectors*. Technical Report CERN-LHCC-2017-012, CMS-TDR-016, CERN, 2017. URL https://cds.cern.ch/record/2283189.

[26] Michel Tytgat, Amany Muhammad, G. Lentdecker, Jordan Jaramillo, L. Moureaux, L. Petre, et al. *Measurement of the background in the CMS muon detector in pp-collisions at* $\sqrt{s} = 13TeV$. *The European Physical Journal C*, 84, 2024. doi: https://doi.org/10.1140/epjc/s10052-024-13077-x.

[27] G. Charpak, H.G. Fisher, C.R. Gruhn, A. Minten, F. Sauli, G. Plch, and G. Flugge. *Time degeneracy of multiwire proportional chambers*. *Nuclear Instruments and Methods*, 99(2):279–284, 1972. ISSN 0029-554X. doi: https://doi.org/10.1016/0029-554X(72)90787-2. URL `https://www.sciencedirect.com/science/article/pii/0029554X72907872`.

[28] John A Kadyk. *Workshop on Radiation Damage to Wire Chambers proceedings*. Lawrence Berkeley Nat. Lab., 1986. URL `https://cds.cern.ch/record/110508`.

[29] Marcus Hohlmann, Cristobal Padilla, Norbert Tesch, and Maxim Titov. *International Workshop on Aging Phenomena in Gaseous Detectors proceedings*. 2003. URL `https://cds.cern.ch/record/490181`.

[30] M. Capeans. *Aging of gaseous detectors: Assembly materials and procedures*. *ICFA Instrum. Bull.*, 24:85–109, 2002. URL `https://inspirehep.net/literature/42724`.

[31] C. Garabatos F. Sauli K. Silander R. Bouclier, M. Capeans. *Effects of outgassing from some materials on gas chamber aging*. *Nucl. Instrum. Meth. A*, 350, 1994.

[32] Carsten Niebuhr. *Aging effects in gas detectors*. *Nuclear Instruments and Methods in Physics Research Section A: Accelerators, Spectrometers, Detectors and Associated Equipment*, 566(1):118–122, 2006. ISSN 0168-9002. doi: https://doi.org/10.1016/j.nima.2006.05.130. URL `https://www.sciencedirect.com/science/article/pii/S0168900206007935`. TIME 2005.

[33] C Albajar, N Amapane, P Arce, C Autermann, M Bellato, M Benettoni, Alberto C Benvenuti, M Bontenackels, and J et al. Caballero. *Test beam analysis of the first CMS drift tube muon chamber*. *Nucl. Instrum. Methods Phys. Res., A*, 525:465–484, 2004. doi: 10.1016/j.nima.2004.01.080. URL `https://cds.cern.ch/record/816639`.

[34] G. Iles ´O. Sahin P. A. Bausson A. Tsirou G. Fedi P. G. Verdini L. Ardilla M. Balzer T. Schuh T. Williams A. Thea K. Harder S.

Dugad R. Shukla I. Mirza A. Rose, D. Parker. *The CMS experiment at the CERN LHC*. *Proceedings of Topical Workshop on Electronics for Particle Physics (TWEPP2018)*, Antwerp, Belgium. 2018. URL https://pos.sissa.it/343/115/pdf.

[35] I Bestintzanos, K Adamidis, I Euaggelou, C Fernandez Bedoya, C Foudas, A Lymperakis, N Manthos, A Navarro, I Papadopoulos, I Redondo, S Sotiropoulos, P Sphicas, and K Vellidis. *An ATCA processor for Level-1 trigger primitive generation and readout of the CMS barrel muon detectors*. *JINST*, 18(02):C02039, 2023. doi: 10.1088/1748-0221/18/02/C02039. URL https://cds.cern.ch/record/2861849.

[36] Jeroen Guido Hegeman, Jean-marc Olivier Andre, Ulf Behrens, James Branson, Olivier Chaze, and Cittolinet al. *The CMS Timing Control and Distribution System*. Technical Report CMS-CR-2015-321, CERN, 2016. URL https://cds.cern.ch/record/2110277.

[37] Jan Troska, Alexander Brandon-Bravo, Stephane Detraz, Andrea Kraxner, Lauri Olantera, et al. The VTRx+, an Optical Link Module for Data Transmission at HL-LHC. *PoS*, TWEPP-17:048, 2018. doi: 10.22323/1.313.0048.

[38] N Guettouche, S Baron, S Biereigel, D Hernandez Montesinos, S Kulis, P Vicente Leitao, J Mendez, P Moreira, D Porret, and K Wyllie. The lpGBT production testing system. *JINST*, 17(03):C03040, 2022. doi: 10.1088/1748-0221/17/03/C03040. URL https://cds.cern.ch/record/2823942.

[39] A Caratelli, S Bonacini, K Kloukinas, A Marchioro, P Moreira, R De Oliveira, and C Paillard. *The GBT-SCA, a radiation tolerant ASIC for detector control and monitoring applications in HEP experiments*. *JINST*, 10(03):C03034, 2015. doi: 10.1088/1748-0221/10/03/C03034. URL https://cds.cern.ch/record/2158969.

[40] Muhammad Bilal Kiani. *Upgrade of the Drift Tube (DT) Muon System for the CMS Detector at the HL-LHC*. Technical Report CMS-CR-2022-230, CERN, 2023. URL https://cds.cern.ch/record/2841566.

[41] P Moreira, J Christiansen, K Wyllie, Paulo Moreira, Sophie Baron, Sandro Bonacini, Jorgen Christiansen, Philippe Farthouat, Sebastian Feger, Rui Francisco, Tullio Grassi, Ping Gui, Magnus Hansen, Kostas Kloukinas, Pedro Leitao, Alessandro Marchioro, Manoel Marin, David Porret,

Jose Silva, Filip Tavernier, Jan Troska, Francois Vasey, and Ken Wyllie. *GBTX manual; V0.18 draft.* 2021. URL `https://cds.cern.ch/record/2809057`.

[42] E Conti and F Gasparini. *Test of the wire ageing induced by radiation for the CMS barrel muon chambers*. *Nucl. Instrum. Methods Phys. Res., A*, 465(2-3):472–81, 2001. doi: 10.1016/S0168-9002(01)00690-8. URL `https://cds.cern.ch/record/516813`.

[43] Roberto Guida. *GIF++: A new CERN Irradiation Facility to test large-area particle detectors for the High-Luminosity LHC program*. *PoS*, ICHEP2016:260, 2016. doi: 10.22323/1.282.0260. URL `https://cds.cern.ch/record/2265093`.

[44] Dorothea Pfeiffer, Georgi Gorine, Hans Reithler, Bartolomej Biskup, Alasdair Day, Adrian Fabich, et al. *The radiation field in the New Gamma Irradiation Facility GIF++ at CERN. The radiation field in the New Gamma Irradiation Facility (GIF++) at CERN*. *Nucl. Instrum. Methods Phys. Res., A*, 866:91–103, 2017. doi: 10.1016/j.nima.2017.05.045. URL `https://cds.cern.ch/record/2229386`.

[45] Ch. Ilgner A. Macpherson A. Oh T. Pritchard F. Ravotti R. Stone E. Tsesmelis S. Worm L. Fernandez-Hernando, M. Glaser. *The Radiation Monitoring System for the LHC Experiments and Experimental Areas*. (TS-Note-2004-006), 2004.

[46] L. Scibile G. Segura Millan, D. Perrin. *RAMSES: The LHC Radiation Monitoring System for the Environment and Safety*. pages Proceedings of EPAC 2004, Lucerne, Switzerland, 2005. URL `http://accelconf.web.cern.ch/e04/PAPERS/WEPLT033.PDF`.

[47] Adrien Ledeul, Gustavo Segura, Riku-Pekka Silvola, Bartlomiej Styczen, and Daniel Vasques Ribeira. *REMUS: The new CERN Radiation and Environment Monitoring Unified Supervision*. page TUD3O03, 2015. doi: 10.18429/JACoW-ICALEPCS2015-TUD3O03. URL `https://cds.cern.ch/record/2213488`.

[48] *Conversion Coefficients for use in Radiological Protection against External Radiation. Annals of the ICRP 74*, 1996.

[49] Mika Huhtinen. *The radiation environment at the CMS experiment at the LHC*. (HU-SEFT-R-1996-14), 1996. URL `https://cds.cern.ch/record/308251`.

[50] F. Gasparini A. T. Meneguzzo G. Mocellin, F. Gonella. *Report on the construction and performances of four drift cells of the muon chambers of CMS for aging effects studies at LNL*. Technical Report INFN-LNL-245, 2016. URL https://userswww.pd.infn.it/~ameneg/GIF/Report_DTbicells_LNL.pdf.

[51] Enrico Conti. *Measurement of the Wire Gain of Cells of the Barrel Muon Drift Chambers*. Technical Report CMS-NOTE-2002-002, CERN, 2002. URL https://cds.cern.ch/record/687392.

[52] M. C. Fouz J. Puerta L. Romero C. Willmott M. Cerrada, N. Colino. *Construcción y pruebas de un prototipo para el detector central de muones de CMS. XXVIII Reunión Bienal de la RSEF*. URL http://wwwae.ciemat.es/bienalae/bienal01/pdf_files/fae20.pdf.

[53] C. Heidemann H. Reithler D. Teyssier G. Altenhofer, T. Hebbeker. *The drift velocity monitoring system of the CMS barrel muon chambers. Nucl. Instrum. Meth. A*, 888, 2018. doi: https://doi.org/10.1016/j.nima.2017.12.032.

[54] Isidro Gonzalez et al. for the CMS Muon Group. *Study of the effects of radiation on the CMS Drift Tubes Muon Detector for the HL-LHC*. (CMS CR-2019/159 Proceedings of iWoriD 2019 21st International Workshop on Radiation Imaging Detectors), 2019. doi: 10.1088/1748-0221/14/12/C12010. URL https://cds.cern.ch/record/2705998.

[55] *Garfield ++ Toolkit*. URL https://garfieldpp.web.cern.ch/garfieldpp/about/.

[56] Maxim P. Titov, M. Hohlmann, C. Padilla, and N. Tesch. *Summary and Outlook of the International Workshop on Aging Phenomena in Gaseous Detectors (DESY, Hamburg, October, 2001)*.

[57] Walter Blum, Werner Riegler, and Luigi Rolandi. *Particle Detection with Drift Chambers*. Springer, 2008. doi: https://doi.org/10.1007/978-3-540-76684-1.

[58] *MAGBOLTZ Software*. URL https://magboltz.web.cern.ch/magboltz/.

[59] Isidro Gonzalez Caballero on behalf of the CMS Muon Group. Longevity studies for the CMS Drift Tubes towards HL-LHC. (CMS-CR-2024-048

Proceedings of Aging 2023 International Conference on Detector Stability and Aging Phenomena in Gaseous Detectors), 2024. doi: 10.1016/j.nima.2024.169512. URL https://cds.cern.ch/record/2890672.

[60] Adrian Alvarez Fernandez. Measurement of Higgs boson production via gluon fusion in the H WW decay channel with the CMS experiment. PhD thesis, Universidad Complutense de Madrid, 2021. URL https://docta.ucm.es/entities/publication/b2d3308e-3abd-497b-996f-cbd126f2ce31.

[61] M Capeans-Garrido. *The transition radiation tracker of the ATLAS experiment*. *IEEE Trans. Nucl. Sci.*, 51:994–1000, 2004. doi: 10.1109/TNS.2004.829486. URL https://cds.cern.ch/record/816797.

[62] Sergio Pulido Ferrero. *Diseño del sistema de blindaje de protección radioactiva del colisionador CMS, utillaje para su instalación y procedimiento para el transporte hasta el colisionador en el CERN*. Master's thesis, Universidad Rey Juan Carlos, 2018.

[63] Pedro Arce, Juan Ignacio Lagares, Laura Harkness, et al. *Gamos: A framework to do Geant4 simulations in different physics fields with an user-friendly interface*. *Nuclear Instruments and Methods in Physics Research Section A: Accelerators, Spectrometers, Detectors and Associated Equipment*, 735:304–313, 2014. ISSN 0168-9002. doi: https://doi.org/10.1016/j.nima.2013.09.036. URL https://www.sciencedirect.com/science/article/pii/S0168900213012709.

[64] S. Agostinelli, J. Allison, K. Amako, J. Apostolakis, H. Araujo, P. Arce, et al. *Geant4,a simulation toolkit*. *Nuclear Instruments and Methods in Physics Research Section A: Accelerators, Spectrometers, Detectors and Associated Equipment*, 506(3):250–303, 2003. ISSN 0168-9002. doi: https://doi.org/10.1016/S0168-9002(03)01368-8. URL https://www.sciencedirect.com/science/article/pii/S0168900203013688.

[65] CMS collaboration. *Background Measurements in the CMS DT chambers during LHC Run 2, CMS DP-2020/011*. Technical report, 2020. URL https://cds.cern.ch/record/2710126.

[66] Andrea Triossi. *A New Data Concentrator for the CMS Muon Barrel Track Finder*. Technical Report CMS-CR-2014-104, CERN, 2014. URL https://cds.cern.ch/record/1712905.

[67] Javier Sastre Alvaro. *The OBDT board: A prototype for the Phase 2 Drift Tubes on-detector electronics*. Technical Report CMS-CR-2019-207, CERN, 2020. URL https://cds.cern.ch/record/2797780.

[68] *Microsemi, PolarFire FPGA Product Overview*. Technical report. URL https://www.microsemi.com/products/fpga-soc/fpga/polarfire-fpga#documentation.

[69] J Mekki, M Brugger, R G Alia, A Thornton, N C Dos Santos Mota, and S Danzeca. *CHARM: A Mixed Field Facility at CERN for Radiation Tests in Ground, Atmospheric, Space and Accelerator Representative Environments*. *IEEE Trans. Nucl. Sci.*, 63(4):2106–2114, 2016. doi: 10.1109/TNS.2016.2528289. URL https://cds.cern.ch/record/2265305.

[70] *Xilinx. VC707 Evaluation Board*. Technical report. URL https://www.xilinx.com/products/boards-and-kits/ek-v7-vc707-g.html.

[71] *Faster Technology, FM-S14 Quad SFP/SFP+ transceiver FMC Modular*. Technical report. URL https://www.xilinx.com/products/boards-and-kits/ek-v7-vc707-g.html.

[72] Melanie D. Berg. *Field Programmable Gate Array (FPGA) Single Event Effect (SEE) Radiation Testing*. 2012. URL https://api.semanticscholar.org/CorpusID:12545721.

[73] Cristina Bedoya. Design, construction and validation of the drift tubes read-out electronics for the CMS experiment. PhD thesis, Universidad Complutense de Madrid, 2009. URL https://cds.cern.ch/record/1308710.

[74] Stephen Varela Paco Mok Alex Cai Nadia Rezzak, J. J. Wang. *Polarfire Neutron Testing Report*. 2018. URL https://ww1.microchip.com/downloads/aemdocuments/documents/fpga/ProductDocuments/SupportingCollateral/polarfire_lanl_neutron_see_test_report_09272019.pdf.

[75] Panagiotis Gkountoumis Rudi Ferraro, Matteo Brucoli. *Microsemi Polarfire MPF300TS FPGA PSI Radiation Test Report*. 2020. URL https://edms.cern.ch/document/2475661/1.

[76] Antonio Scialdone, Rudy Ferraro, Ruben Garcia Alia, Luca Sterpone, Salvatore Danzeca, and Alessandro Masi. *FPGA Qualification and Failure Rate Estimation Methodology for LHC Environments Using Bench-*

marks Test Circuits, volume 69 of *IEEE Transactions on Nuclear Science*. 2022. doi: 10.1109/TNS.2022.3162037.

[77] Ken O'Neill. *Polarfire FPGAs*. Technical report. URL `https://ww1.microchip.com/downloads/aemDocuments/documents/AERO/ProductDocuments/SupportingCollateral/2019-Space-ForumRT-PolarFire-Update.pdf`.